

## Curved jets of viscous fluid : interactions with a moving wall

**Citation for published version (APA):**

Hlod, A. V. (2009). *Curved jets of viscous fluid : interactions with a moving wall*. [Phd Thesis 1 (Research TU/e / Graduation TU/e), Mathematics and Computer Science]. Technische Universiteit Eindhoven.  
<https://doi.org/10.6100/IR644274>

**DOI:**

[10.6100/IR644274](https://doi.org/10.6100/IR644274)

**Document status and date:**

Published: 01/01/2009

**Document Version:**

Publisher's PDF, also known as Version of Record (includes final page, issue and volume numbers)

**Please check the document version of this publication:**

- A submitted manuscript is the version of the article upon submission and before peer-review. There can be important differences between the submitted version and the official published version of record. People interested in the research are advised to contact the author for the final version of the publication, or visit the DOI to the publisher's website.
- The final author version and the galley proof are versions of the publication after peer review.
- The final published version features the final layout of the paper including the volume, issue and page numbers.

[Link to publication](#)

**General rights**

Copyright and moral rights for the publications made accessible in the public portal are retained by the authors and/or other copyright owners and it is a condition of accessing publications that users recognise and abide by the legal requirements associated with these rights.

- Users may download and print one copy of any publication from the public portal for the purpose of private study or research.
- You may not further distribute the material or use it for any profit-making activity or commercial gain
- You may freely distribute the URL identifying the publication in the public portal.

If the publication is distributed under the terms of Article 25fa of the Dutch Copyright Act, indicated by the "Taverne" license above, please follow below link for the End User Agreement:

[www.tue.nl/taverne](http://www.tue.nl/taverne)

**Take down policy**

If you believe that this document breaches copyright please contact us at:

[openaccess@tue.nl](mailto:openaccess@tue.nl)

providing details and we will investigate your claim.

# **Curved Jets of Viscous Fluid: Interactions with a Moving Wall**

Copyright ©2009 by Andriy Hlod, Eindhoven, The Netherlands.

All rights are reserved. No part of this publication may be reproduced, stored in a retrieval system, or transmitted, in any form or by any means, electronic, mechanical, photocopying, recording or otherwise, without prior permission of the author.

Printed by Printservice Technische Universiteit Eindhoven

Cover design by Oranje Vormgevers

A catalogue record is available from the Eindhoven University of Technology Library

ISBN 978-90-386-1951-4

NUR 919

Subject headings: boundary value problems; free boundary problems; hyperbolic problems; characteristic directions; viscous jets; gravity; centrifugal force; Coriolis force; fiber spinning; rotor fiber spinning; numerical methods / shooting method

2000 Mathematics Subject Classification: 76-05, 76M20, 76M25, 76M55, 65M25, 65N06, 35L50, 35L65, 35R35, 34B15

# Curved Jets of Viscous Fluid: Interactions with a Moving Wall

PROEFSCHRIFT

ter verkrijging van de graad van doctor aan de  
Technische Universiteit Eindhoven, op gezag van de  
rector magnificus, prof.dr.ir. C.J. van Duijn, voor een  
commissie aangewezen door het College  
voor Promoties in het openbaar te verdedigen  
op woensdag 16 september 2009 om 16.00 uur

door

Andriy Vasyliovich Hlod

geboren te Boryslav, Oekraïne

Dit proefschrift is goedgekeurd door de promotor:

prof.dr. M.A. Peletier

# Contents

<b>1</b>	<b>Introduction</b>	<b>1</b>
1.1	A piece of sweet science . . . . .	1
1.2	Viscous jets in industrial applications . . . . .	4
1.2.1	Rotary spinning process . . . . .	4
1.2.2	Thermal isolation . . . . .	4
1.2.3	Three-dimensional polymeric mats . . . . .	5
1.2.4	Glass wool . . . . .	5
1.3	Problem setting . . . . .	5
1.3.1	Drag spinning . . . . .	6
1.3.2	Rotary spinning . . . . .	7
1.4	Literature overview . . . . .	7
1.5	Modeling of thin jets . . . . .	9
1.6	Main results and thesis layout . . . . .	12
1.6.1	Boundary conditions . . . . .	12
1.6.2	Drag spinning . . . . .	13
1.6.3	Rotary spinning . . . . .	14
1.6.4	Numerical method for dynamic jet . . . . .	14
<b>2</b>	<b>Boundary conditions</b>	<b>15</b>
2.1	Equations and boundary conditions . . . . .	15
2.2	Boundary conditions for the position vector $\mathbf{r}$ . . . . .	19
2.3	Jet orientation . . . . .	23
2.4	Conclusions . . . . .	25
<b>3</b>	<b>Drag spinning</b>	<b>27</b>
3.1	Algebraic equation . . . . .	27
3.2	Parameter regions for the three flow regimes . . . . .	34
3.3	Viscous jet . . . . .	36
3.4	Viscous-inertial jet . . . . .	39
3.5	Inertial jet . . . . .	43
3.6	Existence and uniqueness for the three flow regimes . . . . .	47
3.7	Inertial jet with upwards pointing nozzle . . . . .	55
3.8	Results . . . . .	57
3.9	Conclusions . . . . .	65
<b>4</b>	<b>Experiments of drag spinning and comparison with theory</b>	<b>67</b>

---

4.1	Experimental setup and parameter choice . . . . .	68
4.1.1	Experimental setup . . . . .	68
4.1.2	Parameter choice . . . . .	69
4.2	Results . . . . .	70
4.2.1	Jet shape . . . . .	70
4.2.2	Touchdown point . . . . .	72
4.2.3	Influences of $v_{\text{nozzle}}$ and $L$ . . . . .	72
4.2.4	Unsteady jet for upwards pointing nozzle . . . . .	74
4.3	Comparison between model and experiments . . . . .	76
4.3.1	Comparison of touchdown point . . . . .	76
4.3.2	Comparison of jet shapes . . . . .	79
4.3.3	Discussion about differences and similarities . . . . .	80
4.4	Summary of the three flow regimes . . . . .	82
4.5	Concluding remarks . . . . .	84
<b>5</b>	<b>Rotary fiber spinning</b> . . . . .	<b>87</b>
5.1	Derivation of equations . . . . .	87
5.2	Analysis . . . . .	91
5.3	Results . . . . .	96
5.4	Rotating coagulator and viscous jet . . . . .	104
5.5	Remark: jet does not reach the coagulator . . . . .	110
5.6	Conclusions . . . . .	112
<b>6</b>	<b>A numerical method for the dynamic jet</b> . . . . .	<b>113</b>
6.1	Numerical method . . . . .	113
6.1.1	Equations for dynamic jet in drag spinning . . . . .	113
6.1.2	Relaxation forms of some equations and boundary conditions . . . . .	117
6.1.3	Numerical scheme for the dynamic jet in drag spinning . . . . .	118
6.1.4	Equations for dynamic jet in rotary spinning . . . . .	122
6.1.5	Relaxation forms of some equations and boundary conditions . . . . .	126
6.1.6	Numerical scheme for dynamic jet in rotary spinning . . . . .	127
6.2	Numerical simulations . . . . .	130
6.2.1	Results for dynamic jet in drag spinning . . . . .	130
6.2.2	Results for dynamic jet in rotary spinning . . . . .	145
6.3	Conclusions . . . . .	156
<b>7</b>	<b>Conclusions and outlook</b> . . . . .	<b>157</b>
<b>A</b>	<b>Surfaces <math>S_1</math> and <math>S_2</math></b> . . . . .	<b>161</b>
A.1	Surface $S_1$ . . . . .	161
A.2	Surface $S_2$ . . . . .	163
<b>B</b>	<b>Proof of lemmas from Chapter 3</b> . . . . .	<b>167</b>
B.1	Proof of Lemma 3.4 . . . . .	167
B.2	Proof of Lemmas 3.6, 3.9, 3.10, and 3.11 . . . . .	169
B.3	Proof of Lemmas 3.18 and 3.22 . . . . .	171
<b>C</b>	<b>Experimental measurements</b> . . . . .	<b>177</b>

***CONTENTS***

---

---

**vii**

<b>Bibliography</b>	<b>189</b>
<b>Index</b>	<b>197</b>
<b>Summary</b>	<b>201</b>
<b>Samenvatting</b>	<b>203</b>
<b>Acknowledgments</b>	<b>205</b>
<b>Curriculum Vitae</b>	<b>207</b>



# Chapter 1

## Introduction

### 1.1 A piece of sweet science

When a falling viscous fluid (e.g. honey) hits a motionless horizontal surface (e.g. pancake) a rich variety of behaviors can be observed. In case the falling fluid forms a thin thread (e.g. pouring from a bottle high above the pancake) the fluid thread coils at the surface as if it were a rope; see Figure 1.1.



**Figure 1.1:** *Coiling of thread.*



**Figure 1.2:** *Thread's fluid flows away.*

On the other hand, when the fluid forms a film (e.g. pouring from a wide-mouthed jar) it folds by flipping back and forward instead of coiling; see Figure 1.3. However, when the falling velocity at the surface is small (e.g. the bottle is close to the pancake) the fluid hits the surface slowly enough to simply flow away and form a puddle; see Figure 1.2. For a low viscosity fluid (e.g. water) the puddle formation is also observed

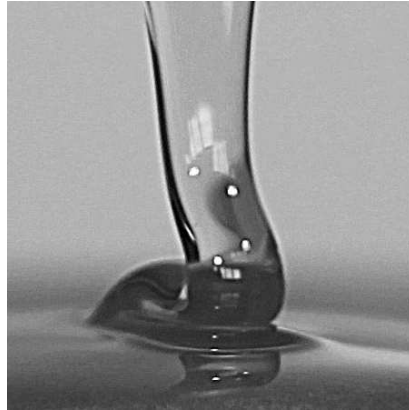
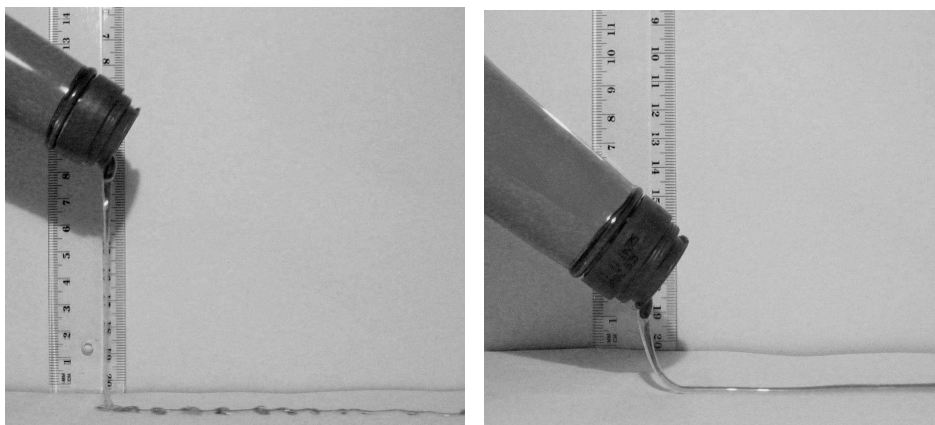


**Figure 1.3:** *Folding of viscous film*

regardless of the falling height. For a detailed description of the examples above we refer to [53, p. 7]. Thus we see that for sure the falling height, the thread shape, and the fluid viscosity influence the way the fluid hits the immovable surface.

Next we consider a surface moving with respect to the thread (e.g. syrup falls from the bottle that moves over the pancake) [98]. In this case for small surface velocity the shape of the thread beside a small part near the surface is vertical; see Figure 1.4(a). An increase of the velocity results in a transformation of the initially vertical thread in a completely curved one; see Figure 1.4(b). The thread resembles a string sagging under gravity, and touches the surface tangentially. From this, we conclude that the surface velocity not only affects the local behaviour but the shape of the whole thread.



(a) Vertical thread.

(b) Curved thread.

**Figure 1.4:** *The thread of syrup hitting a moving surface*

So far we considered only gravity as the driving force for the fluid to reach a horizontal surface. Another possibility for the fluid to reach a surface is by centrifugal and

Coriolis forces. This situation one can encounter in a cotton candy machine ([63, p. 157] and [91]). This machine consists of a cylindrical extruder with holes on its lateral surface. The cylinder is placed into a large circular pan. The extruder rotates around its axis and the molten sugar is thrown through the holes in all the directions hitting the pan to make cotton candy. Parameters which influence the candy spinning are the distance between the extruder and the pan and the angular velocity of the extruder.

Another relevant parameter, in all the examples above, is the exit velocity of the fluid through the bottleneck or the extruder hole. Its influence on the shape of the resulting fluid thread can be illustrated by considering water pumping through a syringe. In this case the water leaves the syringe in the same direction as the syringe end, and the water jet resembles a ballistic trajectory; see Figure 1.5. However, if the exit velocity becomes



**Figure 1.5:** *Ballistic trajectory of water jet*



**Figure 1.6:** *Water falls vertically down*

very small (low pressure) the water falls vertically down regardless of the syringe orientation; see Figure 1.6. In order to obtain a ballistic trajectory using honey instead of water, one needs to create a larger exit velocity for the honey than for the water. Therefore, to predict the orientation of the exit velocity of the fluid one has to consider the magnitude of the exit velocity and the viscosity of the fluid.

All the examples presented above can be generalized as follows. Consider a jet of viscous fluid extruded from a circular nozzle that hits a moving surface under the influence of external forces. In this thesis we study the effects of following parameters:

1. the distance between the nozzle and the surface,
2. the magnitude of the exit velocity from the nozzle,
3. the velocity of the surface,
4. the viscosity of the fluid,
5. the specific external forces i.e gravity, or centrifugal and Coriolis forces,

on the jet between the nozzle and the moving surface.

## 1.2 Viscous jets in industrial applications

In this section we present industrial processes in which a viscous jet hits a moving surface. In all these processes a liquid jet emerges from a nozzle and is driven by gravity or centrifugal and Coriolis forces towards a moving surface. The performance of the processes strongly depends on the features of the jet between the nozzle and the moving surface. The theory developed in this thesis is of importance for modeling these processes.

### 1.2.1 Rotary spinning process

A rotary spinning device consists of a rotor and a coagulator [28, 57]. Both the coagulator and the rotor have the form of a vertical cylinder. A water curtain falls along the coagulator's inner wall; see Figure 1.7. Inside the coagulator the rotor is placed so that

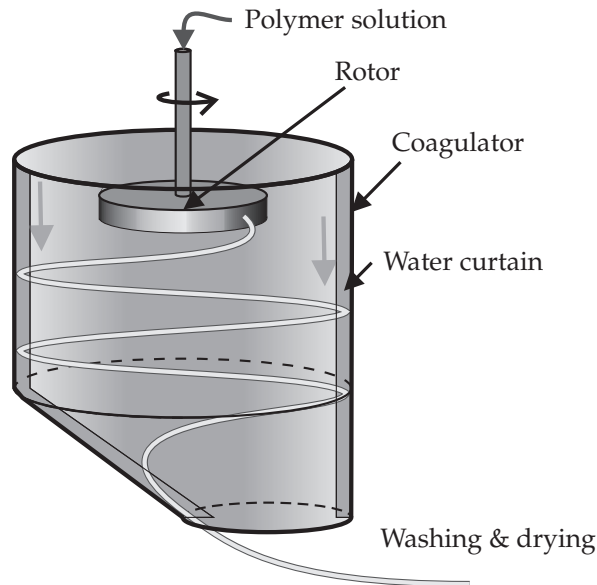


**Figure 1.7:** Rotary spinning process

the symmetry axes of the rotor and the coagulator coincide. The rotor rotates counter-clockwise and has small nozzles in its lateral surface. Hot polymer solution is pumped through the rotor's nozzles, flows to the coagulator under the influence of Coriolis and centrifugal forces, and hits the water curtain at the coagulator wall. The resulting fiber is transported away by the water, then it is washed and cut into small pieces to get pulp.

### 1.2.2 Thermal isolation

One way of making a high-temperature thermal isolation is by means of fibers [10]. Such kind of isolation is used in furnaces, aeroengines, domestic appliances, fire protection systems and other applications. The product from the process consists of the fibres

that are the desired output, and also unfiberised material, mainly shot particles. In the

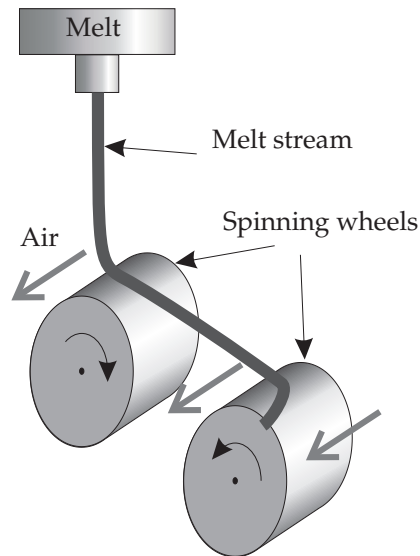


**Figure 1.8:** *The fiberisation process in the production of thermal isolation*

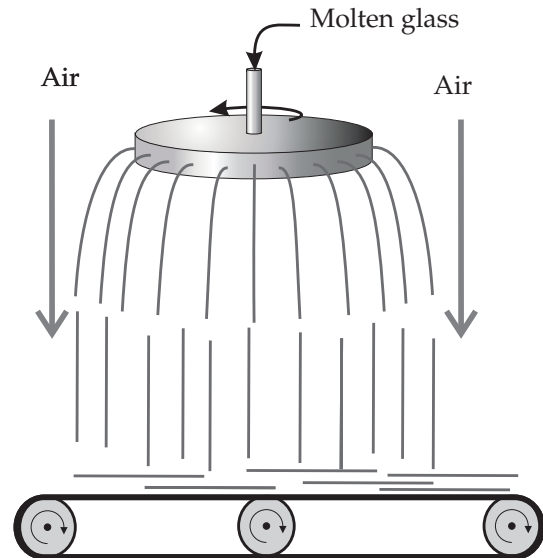


**Figure 1.9:** *The centrifugal spinning process in the production of glass wool*

manufacturing process, a melt stream is extruded from a circular nozzle, and falls on two successive spinning wheels which are used for fiberisation. The resulting material is blown away by an air stream parallel to the wheels. A model of such a process considers a viscous jet sequentially hitting two wheels; see Figure 1.8.

### 1.2.3 Three-dimensional polymeric mats

To produce a three-dimensional polymeric mat a line of parallel jets of molten polymer falls onto a moving pattern surface [4]. Near the surface the jets coil and overlap each other. After solidifying this creates a rigid 3D mat. Three-dimensional polymeric mats are used as protective layers on vulnerable erosion-prone areas.

### 1.2.4 Glass wool

Glass wool is often used for thermal insulation in buildings, and it is of increasing industrial importance [77]. It is also produced by a centrifugal spinning process. In this process molten glass is pressed through small nozzles of a rotating drum; see Figure 1.9. Thin jets are formed that break into pieces due to the surrounding air streams, and they hit a conveyor belt to form a web.

## 1.3 Problem setting

The origin of this study lies in the rotary spinning process. In this process para-aramid fibres are produced with an average length less than one meter due to breakage, whereas

arbitrary long fibers are desired. It is also possible to observe unsteady jets between the rotor and the coagulator. Reasons for the breakage and unsteadiness are unknown, however one expects that they can be related. Another issue is that the jets do not leave the nozzles of the rotor radially, as one would expect. A study of rotary spinning requires understanding of the behaviour of the jet between the nozzle at the rotor and the contact with the water curtain at the coagulator.

### 1.3.1 Drag spinning

However, before dealing with rotary spinning, we start with an experimental and theoretical study of a similar but simpler problem, i.e. a steady jet falling under gravity from a nozzle onto a horizontal moving belt to which we refer as a drag spinning<sup>1</sup>; see Figure 1.10. Advantages of drag spinning are the constant body force and an accessible experimental study of the jet. In this system a jet of viscous Newtonian fluid leaves the

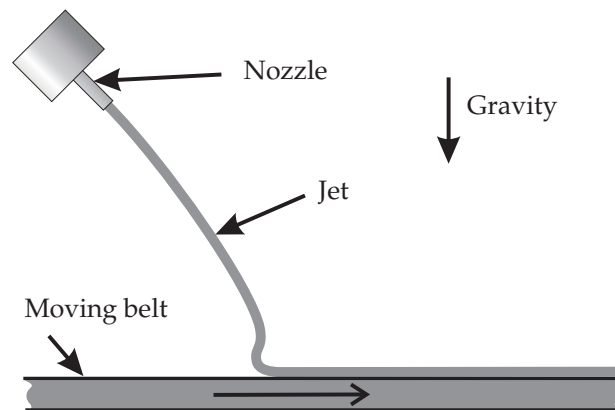


**Figure 1.10:** Drag spinning, a jet fall onto the moving surface from the oriented nozzle under gravity.

nozzle and falls under gravity onto the horizontally moving belt. When hitting the belt, the jet sticks to the belt making the material particle velocity at the contact with the belt equal to that of the belt. The nozzle is placed above the belt and the nozzle orientation can vary between the vertically down (gravity) direction and the horizontal. The horizontal nozzle orientation coincides with the direction of motion of the belt.

In this setup we distinguish three flow regimes. In the first one the jet shape between the nozzle and the belt is convex and the jet touches the belt tangentially; as in Figure 1.4(b). In the second one the jet is pure vertical; as in Figure 1.4(a). In the last one the jet shape is concave, comparable to a ballistic trajectory, and the nozzle orientation becomes determinant; as in Figure 1.5.

<sup>1</sup>The term “drag spinning” is used to indicate that the jet is dragged by the moving belt. The term “drag” is not related to the effect of aerodynamic drag.

### 1.3.2 Rotary spinning

As the next step, we apply the knowledge about the modeling of the three flow regimes in the drag spinning to model the rotary spinning process. The situation is simplified by neglecting gravity and disregarding the water curtain at the coagulator. This allows us to consider the jet in the horizontal plane that contains the nozzle; see Figure 1.11. In ro-

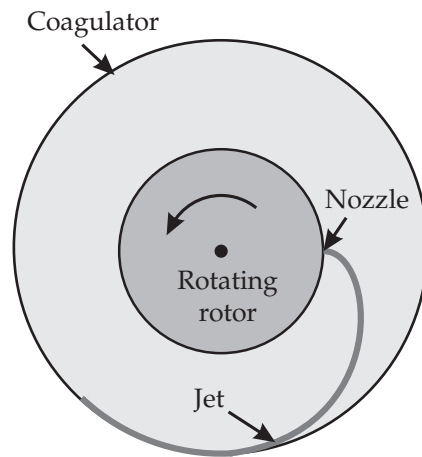


**Figure 1.11:** *The rotary spinning process in two dimensions (view from the top).*

tary spinning, the jet originates from the rotating nozzle of the rotor and flows towards the motionless coagulator under centrifugal and Coriolis forces. At the coagulator the jet sticks to it (i.e the material particle velocity at the contact with the coagulator is zero). By modeling this system, we describe possible situations for the jet in the rotary spinning process.

## 1.4 Literature overview

In this section, we give an overview of the literature related to the subject of this thesis. First, we present the relevant problems and later the specific references. Finally, we mention and discuss the publications which gave birth to this study.

One of the simplest cases is a vertically falling fluid jet. The jet shape is straight and the jet is one-dimensional. The jet cross-section might not be circular; planar jets or sheets of fluid with a cross-section comparable to an elongated rectangle are often considered as well. The fluid can vary from the simplest viscous Newtonian fluid to a nonlinear viscoelastic one with temperature-dependent properties. Other effects that are commonly considered are inertia, gravity, surface tension, and surrounding air flow.

Relevant issues related to this study are:

- Instabilities of jets of viscous fluid hitting a stationary surface;
- Influence of the nozzle on the shape of a jet;
- Influence of the moving surface on the shape of a jet;

- Curved jets.

Vertically falling jets have been widely studied experimentally; see for example [14, 99], as well as numerically and theoretically [2, 15, 16, 25, 36, 62, 97]. Vertical jets of molten polymer in fiber spinning processes are studied in [37, 49, 73, 109, 117, 118]. The vertical jet can become unstable due to surface tension causing the Plateau-Rayleigh instability leading to droplet formation [11, 12, 31, 41–44, 60, 73, 84, 115].

When a jet of viscous fluid hits a stationary solid surface the jet can buckle or coil transforming its kinetic energy into bending. Also these processes have been extensively studied experimentally [7, 8, 19, 20, 45, 47, 48, 68, 89] as well as numerically and theoretically [20–23, 45, 66, 67, 75, 87–89, 101, 102, 114]. A similar coiling effect is observed when an elastic rope hits a stationary surface [46, 64]. Similarly, but two-dimensional, effects of buckling and folding occur when a sheet of viscous fluid hits a solid surface [24, 86, 100, 104–106, 114, 116]. For thin elastic sheets folding is possible as well; see [65].

The influence of the nozzle on the overall shape of the jet is present in the teapot effect: when one pours tea from a pot the stream of tea can bend backwards to the side of the pot [54, 56]; see Figure 1.12. A related example, worth to mention in this context,



**Figure 1.12:** *The teapot effect: if one fast pours water from a teapot the water stream resembles a ballistic trajectory (left photo); if water pours a bit slower the water stream is vertical (middle photo); if water pours very slowly, the water clings to the underside of the teapot lip (right photo);*

is a viscous catenary, where a filament of an incompressible highly viscous fluid that is supported at its ends sags under the influence of gravity [59, 93, 103].

Other causes of the curved jet shape can be a non vertical nozzle orientation and external forces other than gravity. Spiralling liquid jets (a 2D jet under the influence of centrifugal and Coriolis forces and surface tension), and jets curved by gravity are extensively studied with the focus on instabilities and droplet formation; see [27, 79–81, 108, 110, 113]. Jets in 3D under the influence of gravity or centrifugal and Coriolis forces are studied in [71, 77, 78].

So far we have considered only a stationary surface, or no surface at all. An industrial process of curtain coating [55, vol. 6, p. 312], where a liquid curtain falls onto a moving surface to uniformly cover it, is studied in [3, 30, 35, 95, 112]. In this process, the curtain is mostly vertical except for a bending region close to the moving surface. Modeling of a curved curtain due to a moving surface is described in [30] and due to a pressure difference in [35]. The situation with the curved curtain in [30] is very similar to the convex jet shape in Figure 1.4(b).



Mathematical models of a fiber lay-down process incorporating the influence of turbulent air flow with application to the production of nonwoven and glass wool, are studied in [9, 39, 69, 70].

The rotary spinning problem was presented at the 48th European Study Group Mathematics with Industry in Delft (15/3/2004 - 19/3/2004) [28]. At that workshop the following questions were posed:

1. Can we describe the situation (process and geometry) in which continuous filaments can be generated?
2. Can we determine the circumstances (process and geometry) in which the length of a broken filament can be predicted?
3. Can we determine the effect of processing conditions in the present operating situation in order to achieve a robust production process?

To tackle these questions, the string model was used (see Section 1.5 for the model description). At that time, the equations were not solved due to the assumption that the jet always leaves the nozzle radially. In the conclusions, a suggestion was made to first consider the problem of a polymer dropping down from a horizontal nozzle on a conveyer belt.

The second study of the rotary spinning process was done in [57, 58]. It has been shown there that the jet orientation at the nozzle is determined by the jet itself. However, understanding why the jet orientation can not be prescribed at the nozzle was missing.

At the beginning of this work no public study of drag spinning had been available. Later on studies of drag spinning with the nozzle oriented vertically down have been published in [13, 74, 90]. In [13, 74] an extensive set of experiments on steady and unsteady viscous jet behaviour were performed. The case of steady flow was modeled both in [13], using a model of string type with surface tension, and in the later publication [90], using a model with shear and bending. In [13, 90] the steady/unsteady boundaries for different belt velocities and falling heights were obtained approximately. However, the mechanism why the jet in drag spinning can have either convex or vertical shapes was not understood. Some models have been solved for vertical [2, 15] or convex [13] jets, but concave jets have not been studied at all. The questions of existence and uniqueness of a steady jet in drag spinning have been left unanswered. A thorough mathematical study of rotary spinning has not been done yet. Hence, the subject of this thesis, defined in Section 1.3, was not covered in the literature at the beginning of this study and there has been no overlap with publications that appeared during this study.

The results of this study for drag spinning are published in [50–52]. In the next section, we will give an overview of the modeling of thin viscous jets.

## 1.5 Modeling of thin jets

To model a thin viscous jet one makes use of its slenderness (i.e. a typical jet length is much larger than a characteristic size of its cross-section); see [20, 32, 33, 71, 77, 78, 85, 92, 111, 114]. In this case the jet is described as a curve. The flow profile in a jet cross-section perpendicular to the curve is assumed to be uniform. Effects that are often incorporated to model a jet are:

- Inertia of the fluid.
- External body forces.
- Rheology of the fluid.
- Temperature-dependent fluid properties.
- Compressibility of the fluid.
- Surface tension.
- Influence of the surrounding medium.

The model equations follow from the conservation laws of mass, momentum, and angular momentum. Models to which we refer as “string type” are based on the conservation of mass and momentum; see [20,71,77,78,92]. Models based on the conservation of mass, momentum, and angular momentum are called “rod type”; see [32,33,85,111]. Here, we employ the classification introduced in [71], which follows from the analogy to the elastic string and rod models [5].

In this study, we use a model of string type including effects of inertial, viscous, and external body forces (gravity for drag spinning and centrifugal and Coriolis for rotary spinning). We refer to this model as the string model. We neglect effects of surface tension and air drag. This allows us to avoid considering possible instabilities caused by these effects. The fluid is assumed to be Newtonian, isothermal, and incompressible.

Next, for convenience of the reader we present a formal way of deriving the model equations. These equations also follow from the publication presented above. In doing so, we consider the conservation of mass and momentum for an infinitesimally small segment of the jet of length  $2\partial_s$ ; see Figure 1.13. The position of the jet centerline is

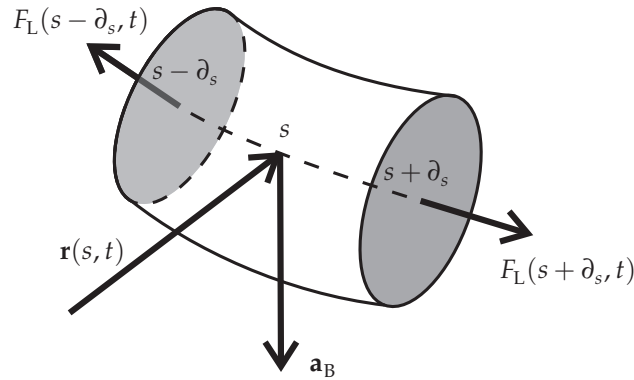


**Figure 1.13:** An infinitesimally small part of the jet

described by a vector  $\mathbf{r}(s, t)$ , with  $s$  being the arc-length (the distance to the nozzle along the jet) and  $t$  time. The cross-sectional area of the jet is  $\mathcal{A}$ . The forces acting on the jet segment are the body force  $\rho\mathbf{a}_B$  and two longitudinal forces at the segment ends:  $F_L(s - \partial_s, t)$  and  $F_L(s + \partial_s, t)$ . The intrinsic flow velocity across the jet cross-section is assumed to be uniform (at first order of slenderness) across the whole cross-section,

with in-flow at the side  $s - \partial_s$  and out-flow at the side  $s + \partial_s$ . The intrinsic flow velocity is directed along the centerline with  $v(s, t)$  being its magnitude.

We start with the conservation of mass for the jet segment. The segment volume can be approximated by a cylinder of height  $2\partial_s$  and cross-sectional area  $\mathcal{A}(s, t)$

$$\mathcal{V}(s, t) \approx 2\partial_s \mathcal{A}(s, t).$$

Here, and further on in this section, by  $\approx$  it is meant an equality up to first order of slenderness. A change of the volume is only due to in- and out-flow through the sides, so

$$\mathcal{V}_t(s, t) \approx \mathcal{A}(s - \partial_s, t)v(s - \partial_s, t) - \mathcal{A}(s + \partial_s, t)v(s + \partial_s, t), \quad (1.1)$$

where the subindex  $t$  stands for the time derivative. By dividing (1.1) by  $2\partial_s$  and letting  $\partial_s$  go to zero, we arrive at

$$\mathcal{A}_t(s, t) + (\mathcal{A}(s, t)v(s, t))_s = 0, \quad (1.2)$$

where the index  $s$  stands for the derivative with respect to  $s$ .

The acceleration of the fluid in the jet segment is approximated by the acceleration at the point  $s$  and is denoted by  $\mathbf{a}(s, t)$ . The equation of conservation of momentum for the jet segment has the following form:

$$\rho\mathcal{V}(s, t)\mathbf{a}(s, t) \approx -F_L(s - \partial_s, t)\mathbf{r}_s(s - \partial_s, t) + F_L(s + \partial_s, t)\mathbf{r}_s(s + \partial_s, t) + \rho\mathcal{V}(s, t)\mathbf{a}_B. \quad (1.3)$$

Here we use the unit vector  $\mathbf{r}_s$  directed along the jet to describe the direction of the longitudinal forces. The condition

$$|\mathbf{r}_s| = 1, \quad (1.4)$$

follows from  $s$  being the arc-length parameter. The acceleration  $\mathbf{a}$  is written in Euler coordinates as

$$\mathbf{a} = \mathbf{r}_{tt} + (v_t + vv_s)\mathbf{r}_s + v^2\mathbf{r}_{ss} + 2v\mathbf{r}_{st}. \quad (1.5)$$

By dividing (1.3) by  $2\partial_s$ , taking the limit  $\partial_s \rightarrow 0$ , and using (1.5), we arrive at

$$\rho\mathcal{A}(\mathbf{r}_{tt} + (v_t + vv_s)\mathbf{r}_s + v^2\mathbf{r}_{ss} + 2v\mathbf{r}_{st}) = (F_L\mathbf{r}_s)_s + \rho\mathcal{A}\mathbf{a}_B. \quad (1.6)$$

For a Newtonian fluid, we have

$$F_L = 3\nu\rho\mathcal{A}v_s. \quad (1.7)$$

The term  $3\nu$  is called the Trouton viscosity [107], and we refer to [20, pp. 25-30] for the derivation of (1.7) for a straight jet. Equation (1.6) together with (1.7) gives

$$\mathbf{r}_{tt} + (v_t + vv_s)\mathbf{r}_s + v^2\mathbf{r}_{ss} + 2v\mathbf{r}_{st} = 3\nu\frac{(\mathcal{A}v_s\mathbf{r}_s)_s}{\mathcal{A}} + \mathbf{a}_B, \quad (1.8)$$

which by use of the fluid particle velocity  $\mathbf{v}$  can be rewritten as

$$\mathbf{v}_t + v\mathbf{v}_s = 3\nu\frac{(\mathcal{A}v_s\mathbf{r}_s)_s}{\mathcal{A}} + \mathbf{a}_B, \quad (1.9)$$

$$\mathbf{v} = \mathbf{r}_t + v\mathbf{r}_s. \quad (1.10)$$

A rigorous derivation of (1.2) and (1.9)-(1.10) is given in [77,78].

For a steady jet the equation of conservation of mass (1.2) becomes

$$(\mathcal{A}v)_s = 0, \quad (1.11)$$

and the equation of conservation of momentum (1.8) with use of (1.11),

$$((v - 3\nu v_s/v)\mathbf{r}_s)_s = \frac{1}{v}\mathbf{a}_B. \quad (1.12)$$

In the next section, we explain how boundary conditions for  $v$  and  $\mathbf{r}$ , can be obtained.

## 1.6 Main results and thesis layout

In this section, we present the main results of this thesis and its layout. We start with a nontrivial result for the boundary conditions for the jet flow which determine the jet shape. Next, we reveal our main findings from the study of steady jets in drag and rotary spinnings and we conclude with the outcome of a numerical method for the dynamic jet in both situations.

In this thesis, we study a jet of viscous fluid hitting a moving surface in two different setups: drag spinning and rotary spinning; see Section 1.3. To describe the jet we use the string model; see Section 1.5.

### 1.6.1 Boundary conditions

The key issue for the string model is the derivation of boundary conditions for  $\mathbf{r}$  (see Chapter 2). To derive these boundary conditions, we treat the conservation of momentum equation for the dynamic jet (1.8) as a semi-linear hyperbolic PDE for the shape  $\mathbf{r}$  provided that the jet is under tension ( $v_s > 0$ ):

$$\mathbf{r}_{tt} + 2v\mathbf{r}_{st} + v\xi\mathbf{r}_{ss} = \tilde{\mathbf{f}}, \quad (1.13)$$

where

$$\xi = v - 3\nu v_s/v, \quad (1.14)$$

and  $\tilde{\mathbf{f}} = (3\nu(\mathcal{A}v_s)_s/\mathcal{A} - v_t - vv_s)\mathbf{r}_s + \mathbf{a}_B$ . The variable  $\xi$  is proportional to the net momentum flux through a jet cross-section (2.22), which is due to inertia and viscosity. When  $\xi > 0$  the momentum flux due to inertia is larger than that due to viscosity, and for a negative sign otherwise. Boundary conditions for  $\mathbf{r}$  follow from the number of BC at some point on the boundary, which should be equal to the number of the characteristics directed into the domain at this point. The directions of the characteristics are determined by the sign of  $\xi$ . By this, we arrive at three cases for boundary conditions and a classification of the jet flow regimes (see Figure 1.14):

1. In the case of the **viscous jet** one characteristic points to the left and one to the right at each end; see Figure 1.14(a). Therefore, we have to prescribe one boundary condition for  $\mathbf{r}$  at each end. At the nozzle we prescribe the nozzle position and at the surface we prescribe the tangency with the surface.

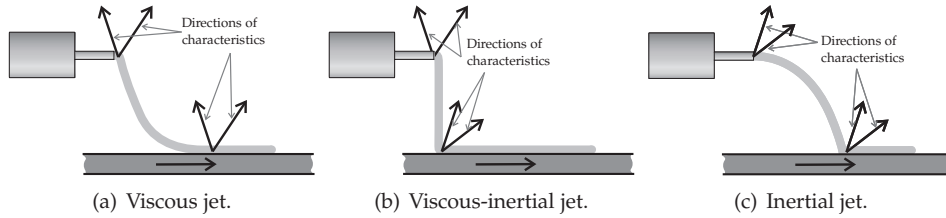


**Figure 1.14:** Characteristics directions for the three flow regimes in drag spinning.

2. In the case of the **viscous-inertial jet** one characteristic points to the left and one to the right at the nozzle, and two characteristics point to the right at the surface; see Figure 1.14(b). Therefore, we can only prescribe one BC at the nozzle, i.e. the nozzle position.
3. In the case of the **inertial jet** two characteristics point to the right at the nozzle and at the surface; see Figure 1.14(c). Therefore, we prescribe two boundary conditions at the nozzle, i.e. the nozzle position and orientation, and none at the surface.

The names of the flow regimes (viscous, viscous-inertial, and inertial) refer to the dominant effect in the momentum flux. We prescribe the boundary conditions for the steady jet in accordance with those for the dynamic one. For the steady viscous-inertial jet an extra condition is prescribed at the point where  $\xi = 0$ : the jet at this point should be aligned with the direction of the external force at that point.

When the jet is under compression ( $v_s < 0$ ), equation (1.13) changes its type and the string model equations for the dynamic jet become ill-posed. This can be avoided by considering a rod type model.

The remaining boundary conditions are the flow velocity at the nozzle and the surface, and a geometrical constraint (i.e. the distance between the nozzle and the belt in drag spinning, and the distance between the rotor and the coagulator in rotary spinning).

## 1.6.2 Drag spinning

A theory for drag spinning using the string model is developed in Chapter 3. The drag spinning model is described by three dimensionless numbers. We succeeded in finding the 3D regions of the dimensionless numbers for the three flow regimes. Moreover, we show that for all the admissible parameters the steady jet solution exists and indicate when it is unique. When uniqueness is violated, up to two inertial jet solutions exist together with one either viscous or viscous-inertial jet solution. Finally, we present and analyse the results of the string model in drag spinning. In Section 3.7 we shortly describe the string model for the upwards pointing nozzle.

In Chapter 4, we present the experimental investigation of drag spinning. In the experiments for steady jets we obtain the three flow regimes shown in Figure 1.15, and apart from the classification above we alternatively classify them by the convexity of the main part of the jet. For further comparison with theory, we measure the position of the touchdown point for different belt velocities. For the cases where a steady jet is not observed we measure the evolution of the touchdown point in time. A comparison

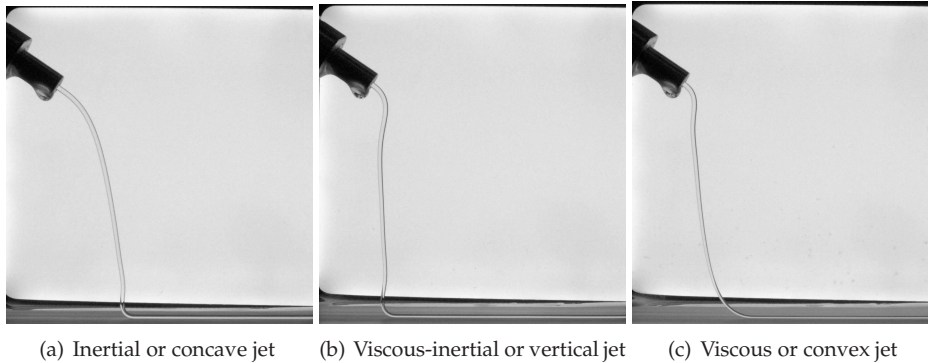


**Figure 1.15:** *The three flow regimes in the drag spinning experiment*

with experiments shows qualitative agreement; see Section 4.3. Non-uniqueness of the steady jet solution can result in an unsteady jet in the experiments (see Section 4.2.4). A discussion about a quantitative difference between the model and the experiments in drag spinning and summary of the three flow regimes are done in Section 4.3.

### 1.6.3 Rotary spinning

In the rotary spinning process the string model indicates three possible situations: the viscous-inertial jet, the inertial jet, and one non-existing case in which a solution satisfying the model boundary conditions does not exist (see Chapter 5). Remarkable is that a viscous jet is not possible in the present rotary spinning setup. It is only possible when the coagulator rotates in the same direction as the rotor with an angular velocity of at least half that of the rotor (see Section 5.4). An example of the steady jet not reaching the coagulator is given in Section 5.5.

### 1.6.4 Numerical method for dynamic jet

A numerical method for the dynamic jet in drag and rotary spinning is developed by using an upwind scheme (see Chapter 6). The boundary conditions for the jet orientation in the viscous and inertial flow regimes, and the geometrical constraint when the jet touches the surface tangentially are relaxed by replacing them by ordinary differential equations in time. The method works as long as the jet is under tension for all  $s$  and  $t$ . Otherwise, the equation conservation of momentum changes its type and this method does not work any more. The dynamic jet correctly evolves to the appropriate steady jet flow regime. When in rotary spinning no steady jet exists the jet starts to oscillate.

## Chapter 2

# Boundary conditions

In this chapter we derive the boundary conditions for the model equations describing dynamic and steady jets. We do this first for the general case of a jet hitting a moving surface, and after that we specify for the drag or rotary spinning process. First, we state boundary conditions for the flow velocity  $v$  and the cross-sectional area  $\mathcal{A}$ . The equation for the position vector  $\mathbf{r}$  is hyperbolic if the whole jet is under tension and elliptic when the whole jet is under compression. In case of a hyperbolic equation the boundary conditions for  $\mathbf{r}$  follow from the characteristic directions and depend on the sign of the momentum flux through a jet cross-section. In case of an elliptic equation, the Cauchy problem is known to be ill posed and therefore we disregard this case when considering the dynamic jet.

The boundary conditions for the steady jet are prescribed in the same way as for the dynamic jet (i.e. the steady jet solution is treated as a stationary solution of the dynamic jet equations). It is shown that for the steady jet there are only three possible choices of boundary conditions for  $\mathbf{r}$ . This provides a criteria for jet flow characterization between the three flow regimes. Finally, we confirm our choice of the boundary conditions for  $\mathbf{r}$  using momentum conservation at the nozzle and at the contact with the belt.

### 2.1 Equations and boundary conditions

The dynamic jet model consists of the conservation of momentum and mass, (1.8) and (1.2), and the arc length relation (1.4),

$$\mathbf{r}_{tt} + (v_t + vv_s)\mathbf{r}_s + v^2\mathbf{r}_{ss} + 2v\mathbf{r}_{st} = 3v\frac{(\mathcal{A}v_s\mathbf{r}_s)_s}{\mathcal{A}} + \mathbf{a}_B, \quad (2.1)$$

$$\mathcal{A}_t + (\mathcal{A}v)_s = 0, \quad (2.2)$$

$$|\mathbf{r}_s| = 1, \quad (2.3)$$

with  $s \in (0, s_{\text{end}}(t))$  and  $t > 0$ .

Here,  $t$  is time and  $s$  is arc length, and subscripts  $s$  and  $t$  represent the derivatives with respect to  $s$  and  $t$ , respectively. At the nozzle  $s = 0$  and at the contact with the surface  $s = s_{\text{end}}(t)$ . The unknowns in these equations are: the two-dimensional position vector

$\mathbf{r}(s, t)$ , the flow velocity in the jet  $v(s, t)$ , and the cross-sectional area of the jet  $\mathcal{A}(s, t)$ . In addition to these unknowns, we have an extra scalar unknown  $s_{\text{end}}(t)$ , the length of the jet between the nozzle and the moving surface.

When we wish to solve the full dynamic system (2.1)-(2.3) we need initial conditions. These conditions must supply the values of  $\mathbf{r}$ ,  $\mathbf{r}_t$ ,  $\mathcal{A}$  and  $v$ , the initial position, velocity, cross-section, and flow velocity in the jet, for all  $s \in (0, s_{\text{end}}(0))$ . As for the boundary conditions<sup>1</sup>, we note that the following conditions are obvious: at the nozzle,  $s = 0$ , we prescribe the position  $\mathbf{r}_{\text{nozzle}}$ , the flow velocity  $v_{\text{nozzle}}$  and the cross-sectional area  $\mathcal{A}_{\text{nozzle}}$ , while at the contact with the surface (i.e. the belt or the coagulator) the fluid sticks to the surface and in case of a steady jet the flow velocity then equals the surface velocity  $v_{\text{surface}}$ . For, an unsteady jet the boundary condition for the flow velocity at the surface is derived below. In addition, a geometric constraint is formulated which accounts for the prescribed distance from the nozzle to the surface.

To derive a boundary condition for  $v(s_{\text{end}}(t), t)$ , we consider a very small piece of the dynamic jet at the surface at times  $t$  and  $t + \delta t$ , where  $\delta t$  is small enough so the surface shape is approximated as flat (in case of the curved coagulator surface); see Figure 2.1. Consider a material point  $\mathcal{A}$  of the jet having at times  $t$  and  $t + \delta t$  the positions  $S_a(t)$

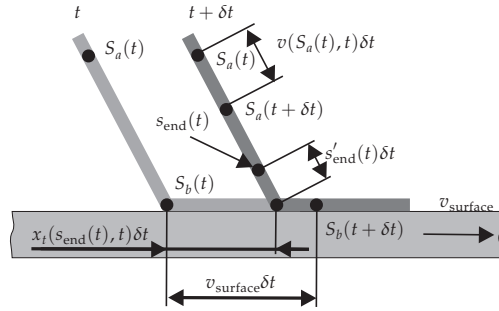


**Figure 2.1:** A small piece of the dynamic jet at the surface, and two jet particles  $S_a$  and  $S_b$  at times  $t$  and  $t + \delta t$ .

and  $S_a(t + \delta t)$ , respectively, which are just above the contact with the surface. Take another point  $\mathcal{B}$  having at times  $t$  and  $t + \delta t$  positions  $S_b(t) = s_{\text{end}}(t)$  and  $S_b(t + \delta t)$ , respectively, which are in contact with the belt in both times. The values of  $S_a$  and  $S_b$  represent the distance to the nozzle along the jet<sup>2</sup>. Because of continuity of the flow velocity in the jet, the distances<sup>3</sup> between  $\mathcal{A}$  and  $\mathcal{B}$  at times  $t$  and  $t + \delta t$  should differ on  $O(\Delta s \delta t)$

$$S_b(t) - S_a(t) = S_b(t + \delta t) - S_a(t + \delta t) + O(\Delta s \delta t), \quad (2.4)$$

where  $\Delta s = S_b(t) - S_a(t)$  denotes the initial distance between the points  $\mathcal{A}$  and  $\mathcal{B}$ .

<sup>1</sup>Here we mean boundary conditions directly following from the modeling. However, more boundary conditions for  $\mathbf{r}$  are possible. This will be explained by the hyperbolic nature of the equation for  $\mathbf{r}$  (i.e. the number of boundary conditions depends on the number of the incoming characteristics at the domain boundaries); see Section 2.2 for the explanation.

<sup>2</sup>In this derivation we extend the jet by adding the path the fluid makes on the surface after hitting it. Whereas everywhere else we consider the jet between the nozzle and the contact with the surface only.

<sup>3</sup>Here we mean the distance along the jet.



Although the flow velocity in the jet should be continuous, because the longitudinal force  $F_L$ , and thus also  $v_s$  (see (1.7)) along the jet is bounded, the fluid particle velocity in the jet is discontinuous if the jet changes its orientation from non-tangent to tangent with the surface at the contact point with the surface. The position of  $\mathcal{A}$  in the jet is changed due to the flow velocity  $v(S_a(t), t)$  according to

$$S_a(t + \delta t) = S_a(t) + v(S_a(t), t)\delta t + o(\delta t), \quad (2.5)$$

and the position of  $\mathcal{B}$  in the jet from  $t$  to  $t + \delta t$  is changed due to the horizontal movement of the jet end  $x_t(s_{\text{end}}(t), t)\delta t$ , the change of the jet length  $s'_{\text{end}}(t)\delta t$ , and the surface displacement  $v_{\text{surface}}\delta t$ , yielding

$$S_b(t + \delta t) = S_b(t) + v_{\text{surface}}\delta t - x_t(s_{\text{end}}(t), t)\delta t + s'_{\text{end}}(t)\delta t + o(\delta t); \quad (2.6)$$

see Figure 2.1 for details. After substituting (2.5) and (2.6) into (2.4) and dividing the latter by  $\delta t$  and letting  $\delta t \rightarrow 0$ ,

$$\begin{aligned} v_{\text{surface}} - x_t(s_{\text{end}}(t), t) + s'_{\text{end}}(t) + O(\Delta s) &= v(S_a, t) = \\ &= v(S_b(t), t)(1 + O(\Delta s)) = v(s_{\text{end}}(t), t)(1 + O(\Delta s)), \end{aligned} \quad (2.7)$$

which by letting  $\Delta s \rightarrow 0$  results in

$$v(s_{\text{end}}(t), t) = v_{\text{surface}} - x_t(s_{\text{end}}(t), t) + s'_{\text{end}}(t), \quad (2.8)$$

the aimed boundary condition for  $v$  at the surface for the dynamic jet. If the jet is steady, (2.8) becomes

$$v(s_{\text{end}}) = v_{\text{surface}}. \quad (2.9)$$

That we indeed have to prescribe boundary conditions for  $v$  both at the begin and at the end point of the jet follows from (2.1), as we shall show now. By taking the inner product of (2.1) with  $\mathbf{r}_s$  and using (2.3), we obtain

$$v_t - 3\nu v_{ss} + \left[ \left( v - 3\nu \frac{\mathcal{A}_s}{\mathcal{A}} \right) v_s + (\mathbf{r}_{tt} - \mathbf{a}_B, \mathbf{r}_s) \right] = 0. \quad (2.10)$$

The equation (2.10) is a parabolic PDE in  $v$  [18, p. 422-423]. In this case, both in the begin and end points of the jet, one boundary condition for  $v$  should be prescribed.

The boundary condition for  $\mathcal{A}$  must be prescribed in the begin point of the jet, as follows from the characteristic direction of (2.2) when  $v > 0$ , which is a hyperbolic PDE in  $\mathcal{A}$ .

We proceed by giving the explicit formulations for these boundary conditions for the drag and rotary spinning process separately. A scheme of the drag spinning process is depicted in Figure 2.2. In this process, the fluid leaves the nozzle with velocity  $v_{\text{nozzle}}$  and falls under gravity onto a horizontal belt. The belt moves with velocity  $v_{\text{belt}}$  and we assume that the fluid sticks to the belt (i.e the particle velocity at contact with the belt is  $v_{\text{belt}}$ ). The distance between the belt and the nozzle is  $L$ , and the angle between the horizontal and the nozzle orientation is  $\alpha_{\text{nozzle}}$  (positive for the nozzle pointing upwards and negative otherwise). For drag spinning, we use a cartesian coordinate system  $\{\mathbf{Oe}_x, \mathbf{e}_y\}$  with the origin  $O$  at the nozzle to describe the position vector  $\mathbf{r} = (x, y)$  and

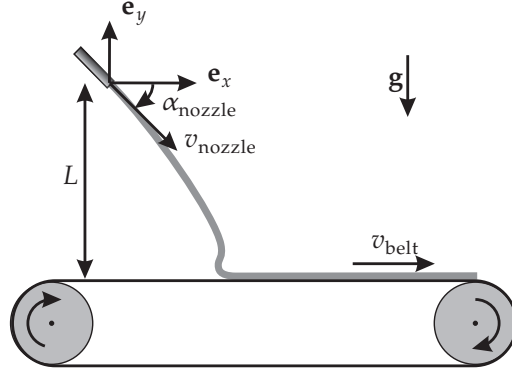


Figure 2.2: Drag spinning.

consequently  $\mathbf{r}_{\text{nozzle}} = \mathbf{0}$ . Boundary conditions in drag spinning are thus

$$v(0, t) = v_{\text{nozzle}}, \quad (2.11)$$

$$v(s_{\text{end}}(t), t) = v_{\text{belt}} - x_t(s_{\text{end}}(t), t) + s'_{\text{end}}(t), \quad (2.12)$$

$$\mathbf{r}(0, t) = \mathbf{r}_{\text{nozzle}} = \mathbf{0}, \quad (2.13)$$

$$\mathcal{A}(0, t) = \mathcal{A}_{\text{nozzle}}, \quad (2.14)$$

$$y(s_{\text{end}}(t), t) = -L. \quad (2.15)$$

The last condition is the geometric constraint in case of drag spinning.

In rotary spinning the jet moves from the rotor to the coagulator. The radii of the rotor and the coagulator are  $R_{\text{rot}}$  and  $R_{\text{coag}}$ , respectively, and the rotor rotates counterclockwise with angular velocity  $\Omega$ ; see Figure 2.3. In rotary spinning, we use a co-

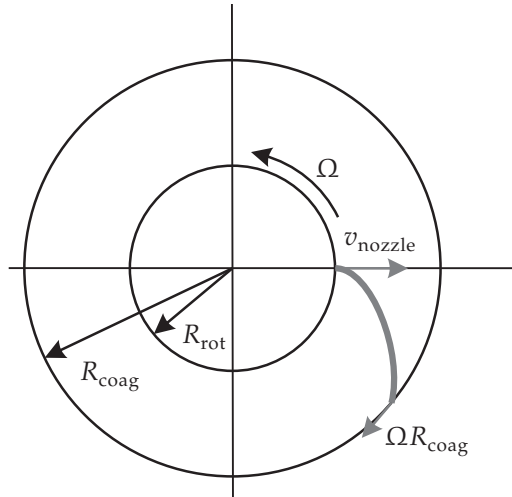


Figure 2.3: The rotary spinning process in two dimensions.

rotating reference frame  $\{O\tilde{\mathbf{e}}_x, \tilde{\mathbf{e}}_y\}$  connected to the rotor with the origin  $O$  at the center of the rotor; see Figure 5.1. The nozzle at the rotor is radially orientated, and the flow velocity at the nozzle is  $v_{\text{nozzle}}$ . At the coagulator, the fluid sticks to the fixed surface and then the particle velocity in the rotating frame is  $\Omega R_{\text{coag}}$ . The position vector is given  $\mathbf{r} = (x, y)$ , with respect to  $\{O\tilde{\mathbf{e}}_x, \tilde{\mathbf{e}}_y\}$ . The nozzle position is  $\mathbf{r}_{\text{nozzle}} = (R_{\text{rot}}, 0)$ . Boundary conditions in rotary spinning are thus

$$v(0, t) = v_{\text{nozzle}}, \quad (2.16)$$

$$v(s_{\text{end}}(t), t) = R_{\text{coag}} (\Omega + \beta_t(s_{\text{end}}(t), t)) + s'_{\text{end}}(t), \quad (2.17)$$

$$\mathbf{r}(0, t) = \mathbf{r}_{\text{nozzle}}, \quad (2.18)$$

$$\mathcal{A}(0, t) = \mathcal{A}_{\text{nozzle}}, \quad (2.19)$$

$$|\mathbf{r}(s_{\text{end}}(t), t)| = R_{\text{coag}}, \quad (2.20)$$

where  $\beta(s, t) = \arctan(y(s, t)/x(s, t))$ , the polar angle. The last condition is the geometric constraint in case of rotary spinning.

The equations (2.1) and (2.2) are of second order in  $s$  for  $v$  and  $\mathbf{r}$ , and of the first order for  $\mathcal{A}$ . Up to now we have two boundary conditions for  $v$  ((2.11), (2.12) or (2.16), (2.17)), one boundary condition for  $\mathbf{r}$  ((2.13) or (2.18)), and one boundary condition for  $\mathcal{A}$  ((2.14) or (2.19)). The geometric constraints (2.15) and (2.20) are used to determine  $s_{\text{end}}(t)$  in drag and rotary spinning, respectively. However, because (2.1) is hyperbolic<sup>4</sup> in  $\mathbf{r}$  we need to know its characteristic directions to determine boundary conditions for  $\mathbf{r}$ . This issue we will treat in the next section.

## 2.2 Boundary conditions for the position vector $\mathbf{r}$

As follows from [40], demanding the alignment of the jet at the nozzle with the nozzle orientation leads to non-existence of the solution for certain model parameters; see Figures 1.5 and 1.6 for illustration. Figures 1.4(a) and 1.4(b) suggest that tangency at the surface should be prescribed as a boundary condition in the second case, but not in the first. In this section we derive a criterion how to prescribe boundary conditions for  $\mathbf{r}$ .

To determine the boundary conditions for  $\mathbf{r}$ , we write the dynamic conservation of momentum equation (2.1) as a semi-linear partial differential equation for  $\mathbf{r}$  of the form

$$\mathbf{r}_{tt} + 2v\mathbf{r}_{st} + v^2\mathbf{r}_{ss} - 3vv_s\mathbf{r}_{ss} = \mathbf{r}_{tt} + 2v\mathbf{r}_{st} + v\xi\mathbf{r}_{ss} = \tilde{\mathbf{f}}, \quad (2.21)$$

with  $\xi = v - 3vv_s/v$ , and  $\tilde{\mathbf{f}} = (3v(\mathcal{A}v_s)_s/\mathcal{A} - v_t - vv_s)\mathbf{r}_s + \mathbf{a}_B$ . According to the classification [18, p. 422-423] the equation (2.21) is hyperbolic when  $v_s > 0$ , parabolic when  $v_s = 0$ , and elliptic when  $v_s < 0$ .

The sign of the variable  $\xi$  plays a crucial role in this equation. The quantity

$$\rho\mathcal{A}v\xi = \rho\mathcal{A}v^2 - 3v\rho\mathcal{A}v_s \quad (2.22)$$

represents the net momentum flux (i.e. the momentum transfer per unit of time) through

<sup>4</sup>In the analysis of this chapter we restrict ourselves to the situations when the whole jet is under tension and the equation for  $\mathbf{r}$  is hyperbolic, see Section 2.2 for explanation.

a cross-section due to inertia  $\rho \mathcal{A} v^2$  and viscosity  $3\nu\rho \mathcal{A} v_s$ . For a positive sign of  $\xi$ , the momentum flux due to inertia is larger than that due to viscosity, and for a negative sign it is the other way around.

Let us consider only the case  $v_s > 0$  throughout the jet, so that (2.21) is hyperbolic. We comment on the case  $v_s < 0$  in Remark 2.3 at the end of this section.

For hyperbolic equations it is well-known that the number of boundary conditions at some point of the boundary should be equal to the number of the characteristics directed into the domain at this point [38, p. 417] and [29, 61]. An easy way to understand this follows from the concept of “domain of dependence” [18, p. 438-449].

The characteristic equation [26, p. 57] for (2.21) is

$$z^2 - 2vz + v^2 - 3\nu v_s = 0, \quad (2.23)$$

where  $z$  is the velocity of a characteristic curve. Equation (2.23) has the solutions

$$z_1 = v + \sqrt{3\nu v_s}, \quad z_2 = v - \sqrt{3\nu v_s}. \quad (2.24)$$

Therefore, the directions of the characteristics of (2.21) depend on the sign of  $\xi$  as follows:

1. If  $\xi < 0$  then  $z_1 > 0$  and  $z_2 < 0$ , i.e. one characteristic points to the left and one to the right.
2. If  $\xi = 0$  then  $z_1 > 0$  and  $z_2 = 0$ , i.e. one characteristic points to the right and one is stationary.
3. If  $\xi > 0$  then  $z_1 > 0$  and  $z_2 > 0$ , i.e. both characteristics point to the right.

In this problem the characteristic  $z_1$  is identified with the information about the jet position and the characteristic  $z_2$  is identified with the information about the jet orientation. The way we identify the angle is confirmed by (2.28) further on.

Next we will state the monotonic properties of  $\xi(s)$  for the steady jet. We will use these properties to determine the characteristic directions of the dynamic jet equations for  $\mathbf{r}$  (2.21) at both jet ends. From this the boundary conditions for  $\mathbf{r}$  directly follow.

Now let us consider the steady jet. By taking the inner product of (1.12) with  $\mathbf{r}_s$  and using (2.3), we obtain

$$\xi'(s) = (\mathbf{a}_B(s), \mathbf{r}'(s))/v(s), \quad (2.25)$$

where by  $'$  we denote the derivative with respect to  $s$ . For the drag and rotary spinning parameters that we consider the term  $(\mathbf{a}_B(s), \mathbf{r}'(s))/v(s)$  is always positive, and thus the function  $\xi(s)$  is strictly increasing. As a consequence there are three possibilities for the sign of  $\xi(s)$ :

1.  $\xi(s) < 0$  for  $s \in [0, s_{\text{end}}]$ . According to (2.22), viscous momentum flux dominates inertial flux everywhere in the jet. Because of that we call this flow regime **viscous**.
2.  $\xi(s) < 0$  for  $s \in [0, s^*)$  and  $\xi(s) > 0$  for  $s \in (s^*, s_{\text{end}}]$ , where  $\xi(s^*) = 0$  and  $s^* \in [0, s_{\text{end}}]$ . According to (2.22), viscous momentum flux dominates at the nozzle and inertial flux dominates at the surface. Because of that we call this flow regime **viscous-inertial**.

3.  $\xi(s) > 0$  for  $s \in [0, s_{\text{end}}]$ . According to (2.22), inertial momentum flux dominates viscous flux everywhere in the jet. Because of that we call this flow regime **inertial**.

Thus, the sign of  $\xi$  provides a classification of the three flow regimes for the jet flow.

Next, we select the boundary conditions for  $\mathbf{r}$  in case of the steady jet. To do this we treat a solution of the steady jet equations as a stationary solution of the dynamic jet equations. Doing this for (2.21), we obtain the boundary conditions for  $\mathbf{r}$  from the characteristic directions of (2.21), which are determined by the sign of  $\xi$ . In (2.21) we use that  $\xi(s, t) = \xi(s)$  is strictly increasing in  $s$ . The boundary conditions obtained in this way are used for the steady jet equations. Next, we treat the three jet flow regimes separately:

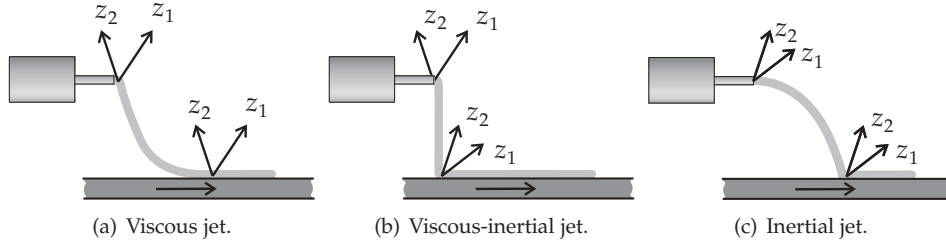


**Figure 2.4:** Characteristics directions for the three flow regimes in drag spinning.

1. In the case of the **viscous jet**, both at the nozzle and at the surface one characteristic  $z_2$  points to the left and one  $z_1$  to the right; see Figure 2.4(a). Therefore, we have to prescribe one boundary condition for  $\mathbf{r}$  at each end. At the nozzle ( $s = 0$ ) we prescribe the nozzle position (as already done in (2.13) and (2.18) and at the surface we prescribe the tangency with the surface ( $s = s_{\text{end}}$ ). The latter provides the extra missing boundary condition.
2. In the case of the **viscous-inertial jet**, at the nozzle one characteristic  $z_2$  points to the left and one  $z_1$  to the right, and two characteristics  $z_1$  and  $z_2$  point to the right at the surface; see Figure 2.4(b). Therefore, we can only prescribe one boundary condition at the nozzle ( $s = 0$ ), namely the nozzle position (as already done in (2.13) and (2.18). The missing condition will be formulated in (2.26) further on.
3. In the case of the **inertial jet**, two characteristics  $z_1$  and  $z_2$  point to the right, both at the nozzle and at the surface; see Figure 2.4(c). Therefore, we prescribe two boundary conditions at the nozzle, i.e the nozzle position (as already done in (2.13) and (2.18) and orientation. The latter condition is new and provides the missing boundary condition.

Hence, for the steady jet we appoint the nozzle position as a boundary condition for all the three flow regimes, the tangency with the surface for the viscous flow, and the nozzle orientation for the inertial flow.

**Remark 2.1.** *The method of prescribing the boundary conditions for  $\mathbf{r}$  according to the direction of characteristic determined by the sign of  $\xi$  described above does not cover the situation if the jet or its part is under compression. For the jet under compression the equation for  $vr$  is elliptic and*

the method described above is not applicable. We extend the mechanism of prescribing boundary conditions for the steady jet fully or partly under compression and prescribe the boundary conditions for  $\mathbf{r}$  according to the sign of  $\xi$ , in the same way as described above.

Note that for the viscous-inertial jet, we prescribe only one boundary condition for the second-order differential equation (2.21) for  $\mathbf{r}$ . An extra condition follows from  $\xi(s^*) = 0$ , expressing that at  $s = s^*$  the jet should be aligned with the direction of the external force at this point, or, as follows from (1.12),

$$\mathbf{r}_s = \frac{1}{v\xi_s} \mathbf{a}_B \quad \text{at } s = s^*. \quad (2.26)$$

The analysis of characteristics, as directions of information propagation, explains why the nozzle orientation influences the jet shape only in the inertial flow, and why the surface orientation influences the jet shape only in the viscous flow. In this respect, we see that:

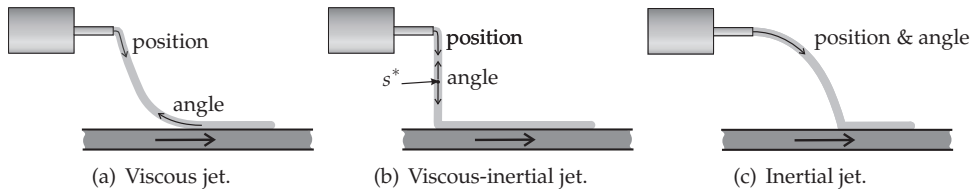


**Figure 2.5:** Directions of information propagations for the three flow regimes in drag spinning.

- In viscous flow, one characteristic points into the domain at the nozzle and one at the surface. Hence, information about the direction of the surface orientation influences the jet shape; see Figure 2.5(a). Therefore, the surface orientation becomes relevant in viscous flow, whereas the nozzle orientation is irrelevant for the viscous jet.
- In viscous-inertial flow, only one characteristic (at the nozzle) points into the domain. Therefore, no information about the nozzle orientation or the flow orientation at the surface influences the jet shape; see Figure 2.5(b). Thus, in viscous-inertial flow the nozzle and the surface orientations are irrelevant for the jet. The information about the orientation travels from the point  $s^*$  towards the nozzle and the surface.
- In inertial flow, the information about the jet shape travels from the nozzle to the surface. Therefore, not only the nozzle position but also the nozzle orientation is relevant for the jet; see Figure 2.5(c). In addition, no information on the flow orientation travels back from the surface.

As we have seen before the belt velocity always influences the jet because of the parabolic nature of the equation for  $v$ , (2.10). Hence, by changing the belt velocity it is possible to change the jet flow regime as well.

**Remark 2.2.** For the dynamic jet under tension, boundary conditions for  $\mathbf{r}$  are prescribed as follows:

- We always prescribe the nozzle position at  $s = 0$ .
- If  $\xi(0, t) > 0$  we prescribe the nozzle orientation at  $s = 0$ .
- If  $\xi(s_{\text{end}}(t), t) < 0$  we prescribe tangency with the surface at  $s = s_{\text{end}}(t)$ .

**Remark 2.3.** The dynamic equation for  $\mathbf{r}$ , (2.21), becomes elliptic when  $v_s < 0$ , and in reality a steady jet might not exist [101]. In this situation the conservation of momentum (2.1) becomes elliptic for  $\mathbf{r}$ . In case  $v_s < 0$ , everywhere in the jet, one has to solve a Cauchy problem for the elliptic equation. Such kind of problems are expected to be ill-posed. Analogy can be made with Hadamard's example [34, p. 234]. This example shows that a solution to a Cauchy problem for the Laplace equation does not continuously depend on the initial datum in any Sobolev norm. For arbitrarily small initial data, the solution can be arbitrary large. Because of this the string model does not adequately describe the jet because it is unstable.

## 2.3 Jet orientation

In this section, we will first give an alternative explanation of the information propagation about the jet orientation to the one found in Section 2.2, and secondly we justify the demand of the tangency with the surface if  $\xi(s_{\text{end}}(t), t) < 0$ , and of the jet alignment with the nozzle orientation if  $\xi(0, t) > 0$ .

Let  $\theta(s, t)$  be the angle between the unit tangent vector  $\mathbf{r}_s$  and some fixed reference direction ( $\theta$  describes thus the orientation of the jet), such that

$$\mathbf{r}_{ss} = \theta_s \mathbf{r}_s^\perp, \quad \mathbf{r}_{st} = \theta_t \mathbf{r}_s^\perp, \quad (2.27)$$

where  $\mathbf{r}_s^\perp$  is the normal vector at  $s$  on the jet. Multiplying (2.1) by  $\mathbf{r}_s^\perp$ , we obtain

$$2v\theta_t + v\xi\theta_s = (\mathbf{a}_B - \mathbf{r}_{tt}, \mathbf{r}_s^\perp). \quad (2.28)$$

The right-hand side of (2.28) will depend on integrals in  $\theta$ ,  $(\theta_t)^2$ , and  $\theta_{tt}$ , but we assume that we can neglect these influences for the determination of the characteristics. In that case, the left-hand side of (2.28) forms the principal part of a first-order wave equation, having  $(s - \frac{\xi}{2}t)$  as characteristic variable. This implies that the direction of information propagation is determined by the sign of  $\xi$ : the information propagates in positive  $s$ -direction if  $\xi > 0$ , and in negative  $s$ -direction if  $\xi < 0$ . Consequently, the orientation  $\theta(s, t)$  must be prescribed at  $s > 0$  if  $\xi > 0$ , and at  $s = s_{\text{end}}(t)$  if  $\xi < 0$ . This agrees completely with the results of Section 2.2.

We proceed with justifying that the jet must touch the surface tangentially in  $s = s_{\text{end}}(t)$  if  $\xi(s_{\text{end}}(t), t) < 0$ . We do this for the more general dynamic case, but it is evident that the results also hold for the steady case. For this, let us consider an infinitesimally small segment of the jet at the surface as sketched in Figure 2.6. The rate of momentum of the segment is the total of the three forces: the internal longitudinal force  $\mathbf{F}_L$  at  $s_1$  ( $\mathbf{F}_L = F_L \mathbf{r}_s$ , see (1.7)), the normal and friction force of the surface,  $\mathbf{F}_N$  and  $\mathbf{F}_f$ , respectively, plus the momentum in- and out-flow  $(\rho \mathcal{A} v)(s_1, t)v(s_1, t)$  and  $(\rho \mathcal{A} v)(s_{\text{end}}, t)v(s_{\text{end}}, t)$  through the cross-sections  $s_1$  and  $s_{\text{end}}$ , respectively. Here, we may neglect the external and inertial body forces, because the volume can be made arbitrary small by taking the length of the segment small enough. Moreover we consider

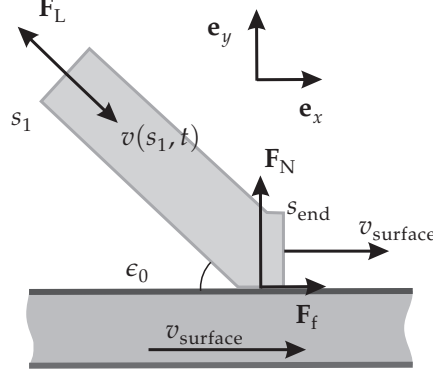


**Figure 2.6:** The infinitesimally small jet segment at the surface

the surface to be flat. We introduce a local  $x, y$  coordinate system with  $\mathbf{e}_x$  and  $\mathbf{e}_y$  tangent and normal to the surface, respectively. We denote the touchdown angle by  $\epsilon_0$ , i.e. the angle between the direction of the jet at  $s = s_1$ , just before it reaches the surface, and the surface. Conservation of momentum states that the total rate of momentum change of the segment must be zero, yielding, with  $v(s_{\text{end}}(t), t) = v_{\text{surface}}$

$$\rho \mathcal{A}(s_1, t) v(s_1, t)^2 \mathbf{r}_s - \mathbf{F}_L + \rho \mathcal{A}(s_{\text{end}}(t), t) v_{\text{surface}}^2 \mathbf{e}_x + \mathbf{F}_N + \mathbf{F}_f = 0. \quad (2.29)$$

Projecting (2.29) onto  $\mathbf{e}_y$ , and using (1.7) and (2.22), we obtain

$$F_N - \rho \mathcal{A}(s_1, t) v(s_1, t) \xi(s_1, t) \sin(\epsilon_0) = 0. \quad (2.30)$$

Noting that always  $F_N \geq 0$ , we see that if  $\xi(s_1, t) < 0$ , then (2.30) only has a solution when  $\epsilon_0 = 0$ . Hence, the jet should touch the surface tangentially if  $\xi(s_1, t) < 0$ . On the other hand if  $\xi(s_1, t) > 0$ , (2.30) can be satisfied for  $\epsilon_0 \neq 0$ .

We also justify the demand of the jet alignment with the nozzle at  $s = 0$  if  $\xi(0, t) > 0$ . To do this consider an infinitesimally small segment of the jet at the nozzle as sketched in Figure 2.7. The rate of momentum change of the segment is the total of the two

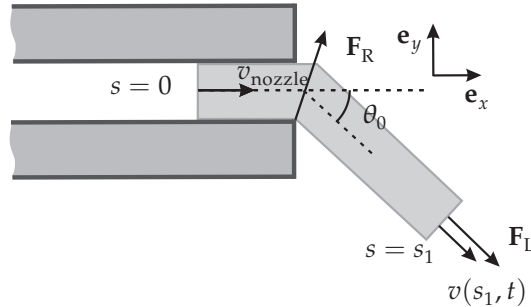


**Figure 2.7:** The infinitesimally small jet segment at the nozzle

forces: the internal longitudinal force  $\mathbf{F}_L$  at  $s_1$  and the reaction force of the nozzle  $\mathbf{F}_R$ ,



plus the momentum in- and out-flow  $(\rho \mathcal{A} v)(0, t)v(0, t)$  and  $(\rho \mathcal{A} v)(s_1, t)v(s_1, t)$  through the cross-section  $s = 0$  and  $s = s_1$ , respectively. Using the same reasoning as for the jet segment at the nozzle, we may neglect the external and inertial body forces. We introduce a local  $x, y$ -coordinate system with  $\mathbf{e}_x$  and  $\mathbf{e}_y$  tangent and normal to the nozzle orientation, respectively. The angle between the direction of the jet at  $s = s_1$ , just after it leaves the nozzle, and  $\mathbf{e}_x$ , we denote by  $\theta_0$ . Conservation of momentum states that the total rate of momentum change of the segment must be zero, yielding, with  $v(0, t) = v_{\text{nozzle}}$

$$\rho \mathcal{A}_{\text{nozzle}} v_{\text{nozzle}}^2 \mathbf{e}_x + \mathbf{F}_L - \rho \mathcal{A}(s_1, t)v(s_1, t)^2 \mathbf{r}_s + \mathbf{F}_R = 0. \quad (2.31)$$

Projecting (2.31) onto  $\mathbf{e}_y$ , and using (1.7) and (2.22), we obtain

$$F_{R,y} + \rho \mathcal{A}(s_1, t)v(s_1, t)\xi(s_1, t) \sin(\theta_0) = 0, \quad (2.32)$$

where  $F_{R,y}$  is the  $y$ -component of  $\mathbf{F}_R$ . Noting that always  $F_{R,y} \geq 0$ , we see that if  $\xi(s_1, t) > 0$ , then (2.32) only has a solution for  $\theta_0 = 0$ . Hence, the jet should be aligned with the nozzle if  $\xi(s_1, t) > 0$ . On the other hand, if  $\xi(s_1, t) < 0$ , (2.32) can be satisfied for  $\theta_0 \neq 0$ .

## 2.4 Conclusions

In this chapter, we have discussed the way we prescribe the boundary conditions for the model equations (2.1)-(2.3). The boundary conditions for the flow velocity of the jet  $v$ , and its cross-sectional area  $\mathcal{A}$ , together with an extra condition for the jet length  $s_{\text{end}}$ , naturally follow from the model. The boundary conditions for the position vector  $\mathbf{r}$  follow from the conservation of momentum (2.1), if it is treated as an hyperbolic equation for  $\mathbf{r}$ . This is true when the jet is under tension ( $v_s > 0$ ). In this case, for the steady jet three types of boundary conditions exists, which are determined by the sign of the momentum flux through the jet cross-section. This leads us to a classification of three steady jet flow regimes: viscous, viscous-inertial, and inertial. The choice of the characteristic direction for the jet orientation is confirmed by the corresponding equation (2.28). The tangency condition at the belt if  $\xi < 0$  and the alignment with the nozzle if  $\xi > 0$  also follow from the momentum conservation.

When the whole jet, or a part of it, is under compression equation (2.1) for  $\mathbf{r}$  becomes elliptic and the problem is ill-posed. This not only causes difficulties to solve (2.1) numerically, but, more important, the dynamic jet model does not adequately describes the jet which could be unstable.



## Chapter 3

# Drag spinning

This chapter is dedicated to a theoretical study of the string model of the steady jet in drag spinning as derived in Section 1.5 (i.e. the jet falls under gravity from an oriented nozzle onto a moving belt). In first instance, we partly solve the model equations so that we end up with one first-order ODE with two unknown parameters. Then we reformulate the resulting problem into one algebraic equation. In such a way, solving the algebraic equation becomes equivalent to solving the whole problem.

Next we determine the parameter regions for the three flow regimes, i.e. viscous, viscous-inertial, and inertial. For each flow regime we prove existence and investigate uniqueness. This leads to existence of a solution to the original problem for all the admissible model parameters. We shortly describe a situation when the nozzle points upwards.

Finally we analyse the partitioning of the parameter space between three flow regimes and present the jet shape as one of the dimensional parameters is changed so the regime is changed from viscous to viscous-inertial, or from inertial to viscous-inertial.

### 3.1 Algebraic equation

In this section we partly solve the steady jet equations in drag spinning and make the analysis showing that the jet can have only three possible shapes: convex, vertical and concave, which correspond to viscous, viscous-inertial, and inertial regimes, respectively. This allows to reformulate the problem by deriving an equivalent algebraic equation which is convenient for further analysis. We start with the model description.

The jet is modeled as a curve in  $2D$  of unknown length  $s_{\text{end}}$ ; see Figure 3.1. The curve is parameterized by its arc length  $s$ , with the origin  $s = 0$  at the nozzle and  $s = s_{\text{end}}$  at the touchdown point at the belt. The position of a certain point  $s$  of the thin jet at time  $t$  is described by its position vector  $\mathbf{r} = \mathbf{r}(s)$  with respect to the origin  $0$ , which is chosen at the nozzle point.

A local coordinate system in a point  $s$  having as basis the tangent and normal vectors  $\mathbf{e}_t, \mathbf{e}_n$  is constructed at each point of the jet. The angle between the tangent vector and horizontal direction is  $\theta$ , negative for the tangent pointing downwards. The nozzle orientation is determined by the angle between the nozzle direction and the horizontal

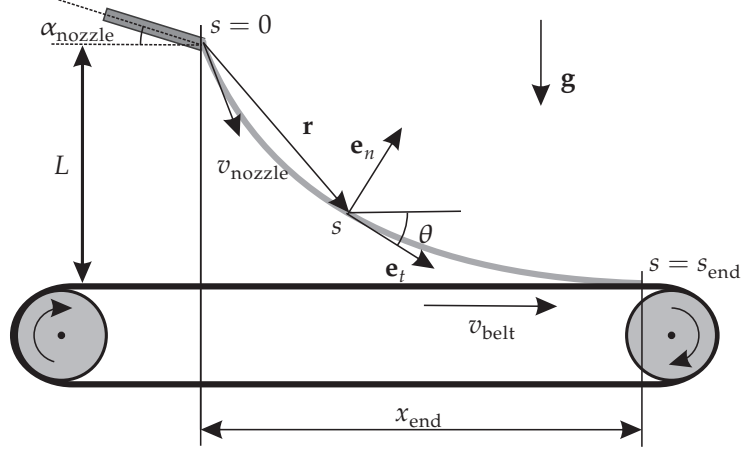


Figure 3.1: Steady jet model in drag spinning.

$\alpha_{\text{nozzle}}$  which is allowed to vary between the vertically down direction  $\alpha_{\text{nozzle}} = \pi/2$  and the horizontal  $\alpha_{\text{nozzle}} = 0$ . The horizontal distance between the nozzle and the touchdown point at the belt is  $x_{\text{end}}$ . The flow velocity in a point  $s$  of the jet is  $v = v(s)$ , and the cross-sectional area is  $\mathcal{A}(s)$ . The jet at the touchdown point has the same velocity as the belt  $v_{\text{belt}}$ , and the flow velocity at the nozzle is  $v_{\text{nozzle}}$ .

The system of equations describing a thin jet follows from the laws of conservation of momentum and mass (1.12) and (1.11) together with the condition for  $s$  as the arc length (1.4)

$$\mathcal{A}(\mathbf{r}_s v v_s + v^2 \mathbf{r}_{ss}) = 3v(v_s \mathcal{A} \mathbf{r}_s)_s + \mathcal{A} \mathbf{g}, \quad (3.1)$$

$$(\mathcal{A}v)_s = 0, \quad (3.2)$$

$$|\mathbf{r}_s| = 1. \quad (3.3)$$

Here we took gravity as an acceleration of the external force  $\mathbf{a}_B = \mathbf{g}$ . Thus, we have three differential equations, (3.1)-(3.3), for the unknowns  $\mathbf{r}$ ,  $v$  and  $\mathcal{A}$ . Next we describe boundary conditions which follow from (2.11)-(2.15).

For the velocity  $v$  we prescribe two boundary conditions: at  $s = 0$ , the flow velocity at the nozzle is

$$v(0) = v_{\text{nozzle}}, \quad (3.4)$$

while at  $s = s_{\text{end}}$  the jet sticks to the belt, so

$$v(s_{\text{end}}) = v_{\text{belt}}. \quad (3.5)$$

The boundary condition for  $\mathcal{A}$  follows from the known cross-sectional area of the nozzle as

$$\mathcal{A}(0) = \frac{\pi}{4} d_{\text{nozzle}}^2, \quad (3.6)$$

where  $d_{\text{nozzle}}$  is the nozzle diameter. The fixed vertical distance between the nozzle and

the belt gives the additional constraint

$$\int_0^{s_{\text{end}}} \sin(\theta(s)) ds = -L. \quad (3.7)$$

As it is shown in Section 2.2 the number of boundary conditions for  $\mathbf{r}$  at the jet ends should be equal to the number of the characteristics of the equation (1.12) pointing inside the domain. According to the analysis made in Section 2.2 directions of the characteristics are determined by  $\xi$

$$\xi = v - 3\nu \frac{v_s}{v}, \quad (3.8)$$

which stands for the momentum transfer through a jet cross-section and plays a crucial role in our further analysis; see also (2.22). In such a way at the nozzle we always prescribe the nozzle position

$$\mathbf{r}(0) = \mathbf{0}, \quad (3.9)$$

whereas boundary conditions for the jet orientation  $\theta$  depend on the sign  $\xi$  at the nozzle and at the belt; see Section 2.2. If at the nozzle  $\xi > 0$  we prescribe the nozzle orientation

$$\text{if } \xi(0) > 0 \text{ then } \theta(0) = \alpha_{\text{nozzle}}. \quad (3.10)$$

If at the belt  $\xi < 0$  we prescribe the tangency with the belt

$$\text{if } \xi(s_{\text{end}}) < 0 \text{ then } \theta(s_{\text{end}}) = 0. \quad (3.11)$$

The equations (3.1)-(3.3) and the boundary conditions (3.4)-(3.11) form a system for the unknown functions  $\mathbf{r}$ ,  $v$  and  $\mathcal{A}$ , and the scalar unknown  $s_{\text{end}}$  which we investigate further.

By integrating (3.2), using (3.4) and (3.6), we find that

$$\mathcal{A}(s) = \frac{F}{v(s)\rho},$$

where the mass flux  $F = \rho v_{\text{nozzle}} \pi d_{\text{nozzle}}^2 / 4$ . We eliminate  $\mathcal{A}$  from (3.1) to obtain

$$\mathbf{r}_s v_s + v \mathbf{r}_{ss} = 3\nu (\mathbf{r}_s v_s / v)_s + \mathbf{g} / v. \quad (3.12)$$

By use of  $\xi$  we write (3.12) as

$$(\xi \mathbf{r}_s)_s = \frac{\mathbf{g}}{v}. \quad (3.13)$$

Using  $\mathbf{e}_t = \mathbf{r}_s$ , and  $(\mathbf{e}_t)_s = -\theta_s \mathbf{e}_n$ , we can write out (3.13) in components as

$$\xi_s = -\frac{g \sin(\theta)}{v}, \quad (3.14)$$

and

$$\theta_s = \frac{g \cos(\theta)}{\xi v}. \quad (3.15)$$

Equation (3.15) requires a boundary condition for  $\theta$ ; this is related to the question of boundary conditions for  $\mathbf{r}$ .

We scale the system as follows: the length  $s$  is scaled with respect to  $3\nu/v_{\text{nozzle}}$  and the velocity  $v$  with respect to  $v_{\text{nozzle}}$ . Then, (3.14), (3.15), (3.8), (3.4), (3.5), (3.10), (3.11) and (3.7) successively become

$$\xi_s = -\frac{A \sin(\theta)}{v}, \quad (3.16)$$

$$\theta_s = \frac{A \cos(\theta)}{\xi v}, \quad (3.17)$$

$$\xi = v - \frac{v_s}{v}, \quad (3.18)$$

$$v(0) = 1, \quad (3.19)$$

$$v(s_{\text{end}}) = \text{Dr}, \quad (3.20)$$

$$\text{if } \xi(0) > 0 \text{ then } \theta(0) = \alpha_{\text{nozzle}}, \quad (3.21)$$

$$\text{if } \xi(s_{\text{end}}) < 0 \text{ then } \theta(s_{\text{end}}) = 0, \quad (3.22)$$

$$\int_0^{s_{\text{end}}} \sin(\theta(s)) ds = -\text{Re}. \quad (3.23)$$

Here,  $A = 3g\nu/v_{\text{nozzle}}^3$ ,  $\text{Re} = v_{\text{nozzle}}L/(3\nu)$  is the Reynolds number,  $\text{Dr} = v_{\text{belt}}/v_{\text{nozzle}}$  is the draw ratio, and the scaled  $s_{\text{end}}$  becomes  $s_{\text{end}}v_{\text{nozzle}}/(3\nu)$ . The dimensionless number  $A$  is related to the Froude number  $\text{Fr} = v_{\text{nozzle}}/\sqrt{gL}$  and  $\text{Re}$  as  $A = 1/(\text{ReFr}^2)$ . After scaling the system is described in terms of three positive dimensionless numbers, which define an admissible parameter space  $\mathcal{P}$  as

$$\mathcal{P} := \{(A, \text{Re}, \text{Dr}) : A > 0, \text{Re} > 0, \text{Dr} > 0\}. \quad (3.24)$$

By replacing the material coordinate  $s$  by the time variable  $\tau$ , according to

$$ds = v(\tau)d\tau, \quad (3.25)$$

the system (3.16)-(3.23) becomes

$$\xi_\tau = -A \sin(\theta), \quad (3.26)$$

$$\theta_\tau = \frac{A \cos(\theta)}{\xi}, \quad (3.27)$$

$$\xi = v - \frac{v_\tau}{v^2}, \quad (3.28)$$

$$v(0) = 1, \quad (3.29)$$

$$v(\tau_{\text{end}}) = \text{Dr}, \quad (3.30)$$

$$\text{if } \xi(0) > 0 \text{ then } \theta(0) = \alpha_{\text{nozzle}}, \quad (3.31)$$

$$\text{if } \xi(\tau_{\text{end}}) < 0 \text{ then } \theta(\tau_{\text{end}}) = 0, \quad (3.32)$$

$$\int_0^{\tau_{\text{end}}} \sin(\theta(\tau))v(\tau)d\tau = -\text{Re}. \quad (3.33)$$

Here,  $\tau_{\text{end}}$  is the result of the coordinate transformation (3.25) and of

$$s_{\text{end}} = \int_0^{\tau_{\text{end}}} v(\tau)d\tau.$$

Next, we solve (3.26) and (3.27), using the first integral

$$\xi \sin(\theta) = -A\tau - c_1, \quad (3.34)$$

to obtain

$$\xi = \pm \sqrt{A^2\tau^2 + 2Ac_1\tau + c_2}, \quad (3.35)$$

$$\theta = \mp \arcsin \left( \frac{A\tau + c_1}{\sqrt{A^2\tau^2 + 2Ac_1\tau + c_2}} \right). \quad (3.36)$$

Here,  $c_1$  and  $c_2$  are unknown constants to be determined later.

In the analysis we restrict ourselves to solutions with  $\theta \in [0, \pi/2]$ . Then, we conclude from (3.26) that  $\xi$  is a strictly increasing function. Therefore, as in Section 2.2, we distinguish three possible situations for the sign of  $\xi$ : always negative, changes sign from negative to positive, and always positive, i.e.

$$\xi(0) < \xi(\tau_{\text{end}}) < 0. \quad (3.37)$$

$$\xi(0) \leq 0 \leq \xi(\tau_{\text{end}}), \quad (3.38)$$

$$0 < \xi(0) < \xi(\tau_{\text{end}}), \quad (3.39)$$

This gives us a characterization of the three flow regimes.

A term **viscous jet** is defined as a solution to the problem (3.1)-(3.11) for which (3.37) holds. The term viscous is used because the viscosity is the dominant effect in the momentum transfer through the jet cross-section everywhere in the jet. We define a subset  $\mathcal{P}_{\text{visc}}$  of the parameter region  $\mathcal{P}$  so that if for  $(A, \text{Re}, \text{Dr}) \in \mathcal{P}_{\text{visc}}$  an viscous jet solution exists.

If (3.37) holds, then it follows from (3.27) that  $\theta$  is a strictly decreasing function for  $\theta < \pi/2$ . In this case the jet has a convex shape. This corresponds to the viscous jet and according to the arguments in Chapter 2, we may require tangency for the jet at the belt, i.e.

$$\theta(\tau_{\text{end}}) = 0. \quad (3.40)$$

Then

$$\xi = -\sqrt{A^2\tau(\tau - 2\tau_{\text{end}}) + c_2}, \quad (3.41)$$

$$\theta = -\arcsin \left( \frac{A(\tau_{\text{end}} - \tau)}{\sqrt{A^2\tau(\tau - 2\tau_{\text{end}}) + c_2}} \right). \quad (3.42)$$

A term **viscous-inertial jet** is defined as a solution to the problem (3.1)-(3.11) for which (3.38) holds. The term viscous-inertial is used because the viscosity is the dominant effect in the momentum transfer through the jet cross-section near the nozzle, whereas inertia near the belt. We define a subset  $\mathcal{P}_{\text{v-i}}$  of the parameter region  $\mathcal{P}$  so that if for  $(A, \text{Re}, \text{Dr}) \in \mathcal{P}_{\text{v-i}}$  an viscous-inertial jet solution exists.

For (3.38) to hold, there must exist a  $\tau^* \in [0, \tau_{\text{end}}]$  so that  $\xi(\tau^*) = 0$ . Then from (3.27), it follows that  $\theta(\tau^*) = -\pi/2$ . Substituting  $\tau^*$  in (3.36), we have

$$\frac{A\tau^* + c_1}{\sqrt{A^2(\tau^*)^2 + 2Ac_1\tau^* + c_2}} = 1, \quad (3.43)$$

giving  $c_1^2 = c_2$ . This implies that

$$\theta \equiv -\pi/2, \quad (3.44)$$

for all  $\tau \in [0, \tau_{\text{end}}]$ , and hence the jet is vertical. For  $\xi$  obeying (3.38), we obtain

$$\xi(\tau) = A\tau + c_1 = A\tau - \sqrt{(c_2)^2}. \quad (3.45)$$

Note, that for the viscous-inertial jet, as it is shown in Section 2.2, no boundary condition for  $\theta$  is necessary.

A term **inertial jet** is defined as a solution to the problem (3.1)-(3.11) for which (3.39) holds. The term inertial is used because the inertia is the dominant effect in the momentum transfer through the jet cross-section everywhere in the jet. We define a subset  $\mathcal{P}_{\text{inert}}$  of the parameter region  $\mathcal{P}$  so that if for  $(A, \text{Re}, \text{Dr}) \in \mathcal{P}_{\text{inert}}$  an inertial jet solution exists with  $\alpha_{\text{nozzle}} = -\pi/2$ . Here we restrict ourself only to  $\alpha_{\text{nozzle}} = -\pi/2$  because as it will follow later for  $\alpha_{\text{nozzle}} > -\pi/2$  an inertial jet solution can coexist with the viscous-inertial or viscous jet, whereas for the parameters from  $\mathcal{P}_{\text{inert}}$  the inertial jet solution exists for all admissible  $\alpha_{\text{nozzle}}$ .

If (3.39) holds, then it follows from (3.27) that  $\theta$  is a strictly increasing function for  $\theta < \pi/2$ , implying that the jet has a concave shape. This corresponds to the inertial jet and according to the arguments in Chapter 2 we prescribe the nozzle orientation angle as the boundary condition for  $\theta$ , i.e.

$$\theta(0) = \alpha_{\text{nozzle}}. \quad (3.46)$$

Substitution of (3.46) into (3.35)-(3.36) gives

$$\xi = \sqrt{A^2\tau^2 - 2A\sqrt{c_2}\sin(\alpha_{\text{nozzle}})\tau + c_2}, \quad (3.47)$$

$$\theta = -\arcsin\left(\frac{A\tau - \sqrt{c_2}\sin(\alpha_{\text{nozzle}})}{\sqrt{A^2\tau^2 - 2A\sqrt{c_2}\sin(\alpha_{\text{nozzle}})\tau + c_2}}\right). \quad (3.48)$$

By substituting the found solutions for  $\xi$  and  $\theta$  into (3.28)-(3.33) for the three situa-



tions (3.39)-(3.37), we successively obtain

$$v - \frac{v_\tau}{v^2} = \begin{cases} w\sqrt{A^2\tau(\tau - 2\tau_{\text{end}})/w^2 + 1} & \text{viscous jet,} \\ w + A\tau & \text{viscous-inertial jet,} \\ \sqrt{A^2\tau^2 + w^2 - 2A\tau w \sin(\alpha_{\text{nozzle}})} & \text{inertial jet,} \end{cases} \quad (3.49)$$

$$v(0) = 1, \quad (3.50)$$

$$v(\tau_{\text{end}}) = \text{Dr}, \quad (3.51)$$

$$\text{Re} = \begin{cases} \int_0^{\tau_{\text{end}}} \frac{A(\tau_{\text{end}} - \tau)}{\sqrt{A^2\tau(\tau - 2\tau_{\text{end}}) + w^2}} v(\tau) d\tau & \text{inertial jet,} \\ \int_0^{\tau_{\text{end}}} v(\tau) d\tau & \text{viscous-inertial jet,} \\ \int_0^{\tau_{\text{end}}} \frac{A\tau - w \sin(\alpha_{\text{nozzle}})}{\sqrt{A^2\tau^2 + w^2 - 2A\tau w \sin(\alpha_{\text{nozzle}})}} v(\tau) d\tau & \text{inertial jet,} \end{cases} \quad (3.52)$$

where  $w = \xi(0)$ .

For given  $w \in \mathbb{R}$  and a flow regime, the problem (3.49)-(3.51) has a solution  $v(\tau; w)$  and  $\tau_{\text{end}}(w)$ , where  $\tau_{\text{end}}(w)$  satisfies (3.51). Here, we assume that for any  $w$ , (3.51) has only one solution, which is not always true. However, this allows us to illustrate a solution procedure.

Substituting  $v(\tau; w)$  and  $\tau_{\text{end}}(w)$  into the integrals (3.52), we obtain the functions of  $w$ :

$$\begin{aligned} I_{\text{inert}}(w) &= \int_0^{\tau_{\text{end}}(w)} \frac{A\tau - w \sin(\alpha_{\text{nozzle}})}{\sqrt{A^2\tau^2 + w^2 - 2A\tau w \sin(\alpha_{\text{nozzle}})}} v_{\text{inert}}(\tau; w) d\tau && \text{inertial jet,} \\ I_{\text{v-i}}(w) &= \int_0^{\tau_{\text{end}}(w)} v_{\text{v-i}}(\tau; w) d\tau && \text{viscous-inertial jet,} \\ I_{\text{visc}}(w) &= \int_0^{\tau_{\text{end}}(w)} \frac{A(\tau_{\text{end}}(w) - \tau)}{\sqrt{A^2\tau(\tau - 2\tau_{\text{end}}(w)) + w^2}} v_{\text{visc}}(\tau; w) d\tau && \text{viscous jet.} \end{aligned} \quad (3.53)$$

Here, we denote by  $v_{\text{visc}}(\tau; w)$ ,  $v_{\text{v-i}}(\tau; w)$  and  $v_{\text{inert}}(\tau; w)$  the solution of (3.49) for a viscous, viscous-inertial, and inertial jet, respectively. According to (3.39)-(3.37),  $I_{\text{visc}}(w)$  and  $I_{\text{v-i}}(w)$  are defined for  $w \leq 0$ , and  $I_{\text{inert}}(w)$  for  $w > 0$ . With (3.53), solving (3.49)-(3.52) is equivalent to solving the algebraic equation

$$\text{find } r \in \{\text{inert, v-i, visc}\} \text{ and } w, \text{ so that } I_r(w) = \text{Re}. \quad (3.54)$$

Therefore, a study of existence and uniqueness of a jet solution results into a study of the existence and uniqueness of a solution to the algebraic equation (3.54).

At this point, we like to shortly recapitulate the main steps in our solution procedure. We do this, as an example for the inertial flow; the other cases are completely analogous. The steps are:

1. Solve  $v = v_{\text{inert}}(\tau; w)$  from (3.49)<sub>1</sub>, with use of the boundary condition (3.50).
2. Find  $\tau_{\text{end}}(w)$  from (3.51) as  $v_{\text{inert}}(\tau_{\text{end}}(w); w) = \text{Dr}$ .
3. Calculate  $I_{\text{inert}}(w)$  from (3.53).
4. Solve  $w$  from (3.54).

The partitioning of the parameter space  $\mathcal{P}$  into the regions of viscous  $\mathcal{P}_{\text{visc}}$ , viscous-inertial  $\mathcal{P}_{\text{v-i}}$  and inertial  $\mathcal{P}_{\text{inert}}$  jets is done in the next section.

### 3.2 Parameter regions for the three flow regimes

In this section we determine the parameter regions for the three flow regimes. First we show that by changing any model parameter continuously the flow type can only change between the viscous and viscous-inertial, and between the viscous-inertial and inertial flow regimes. Then we find the parameter region for the inertial flow  $\mathcal{P}_{\text{inert}}$ . This together with the parameter region of the viscous flow  $\mathcal{P}_{\text{visc}}$  determines the parameter region for the viscous-inertial jet  $\mathcal{P}_{\text{v-i}}$ , and thus we have a characterization for the whole parameter space.

**Lemma 3.1.** *When the model parameters are changed continuously so that the jet solution behaves in the following way: a)  $\xi(0)$  changes sign, or b)  $\xi(\tau_{\text{end}})$  changes sign, then we have correspondingly a) transition between the viscous-inertial and inertial flow regime, or b) transition between the viscous and viscous-inertial flow regime.*

*Proof.* To prove the lemma we use a lower estimate for  $\xi(\tau_{\text{end}}) - \xi(0) \geq C(A, \text{Re}, \text{Dr}) > 0$ . From this follows that in case of a transition from inertial to viscous-inertial flow,  $\xi(0)$  changes sign from positive to negative, while  $\xi(\tau_{\text{end}})$  remains positive if  $\xi(0) > -C(A, \text{Re}, \text{Dr})$ . The similar situation occurs in case of a transition from viscous to viscous-inertial;  $\xi(\tau_{\text{end}})$  changes sign from negative to positive and  $\xi(0)$  remains negative if  $\xi(\tau_{\text{end}}) < C(A, \text{Re}, \text{Dr})$ .

The estimate for  $\xi(\tau_{\text{end}}) - \xi(0)$  follows from (3.26) and (3.33) as

$$\xi(\tau_{\text{end}}) - \xi(0) = A \int_0^{\tau_{\text{end}}} \sin(\theta) d\tau \geq \frac{A \text{Re}}{\max\{\text{Dr}, 1, \xi\}} \geq \frac{A \text{Re}}{\max\{\text{Dr}, 1, \xi(\tau_{\text{end}})\}}.$$

Here we used that  $v$  is continuous and at the local maximum  $v = \xi$  (3.28), from which, together with the boundary conditions (3.29) and (3.30) and monotonicity of  $\xi \leq \xi(\tau_{\text{end}})$ , we infer that

$$v(\tau) \leq \max\{\text{Dr}, 1, \xi(\tau_{\text{end}})\}.$$

□

Next we determine the parameter regions for the three flow regimes in terms of the three dimensionless parameters  $A$ ,  $\text{Dr}$  and  $\text{Re}$ . By Lemma 3.1, we know that there exist borders between  $\mathcal{P}_{\text{inert}}$  and  $\mathcal{P}_{\text{v-i}}$ , and  $\mathcal{P}_{\text{visc}}$  and  $\mathcal{P}_{\text{v-i}}$ , and no border between  $\mathcal{P}_{\text{inert}}$  and  $\mathcal{P}_{\text{visc}}$ . Since during transition between the inertial and viscous-inertial flow regime the sign of  $\xi(0)$  changes, the border between  $\mathcal{P}_{\text{inert}}$  and  $\mathcal{P}_{\text{v-i}}$  is defined by the solution of (3.26)-(3.33) for  $\xi(0) = 0$ . The surface for which the above is true is defined as follow

$$S_1 = \left\{ (A, \text{Dr}, \text{Re}) : \text{Dr} = v_{\text{v-i}}(\tau; 0, A) \text{ and } \text{Re} = \int_0^{\tau} v_{\text{v-i}}(\bar{\tau}; 0, A) d\bar{\tau} \right\},$$

or in terms of the space variable  $s$

$$S_1 = \{(A, \text{Dr}, \text{Re}) : \text{Dr} = v_{\text{v-i}}(\text{Re}; 0, A)\}. \quad (3.55)$$

Similarly we the border between  $\mathcal{P}_{\text{visc}}$  and  $\mathcal{P}_{\text{v-i}}$  is defined by solutions of (3.26)-(3.33) for which  $\xi(\tau_{\text{end}}) = 0$ . The surface is for which above is true is defined as follow

$$S_2 = \left\{ (A, \text{Dr}, \text{Re}) : \text{Dr} = v_{\text{v-i}}(\tau; -\tau_{\text{end}}/A, A) \text{ and } \text{Re} = \int_0^\tau v_{\text{v-i}}(\bar{\tau}; -\tau_{\text{end}}/A, A) d\bar{\tau} \right\},$$

or, in terms of the space variable  $s$ ,

$$S_2 = \{(A, \text{Dr}, \text{Re}) : \text{Dr} = v_{\text{v-i}}(\text{Re}; -\tau_{\text{end}}/A, A)\},$$

where we take  $w = -\tau_{\text{end}}/A$  so  $\xi(\tau_{\text{end}}) = 0$  see (3.41). We proceed with the determination of  $\mathcal{P}_{\text{inert}}$  for  $\alpha_{\text{nozzle}} = -\pi/2$ .

**Lemma 3.2.** *Let  $(\xi, v_{\text{inert}}, \theta)$  be a solution for the inertial jet (3.26)-(3.33) with  $\alpha_{\text{nozzle}} = -\pi/2$ . If  $v_{\text{inert}}(\text{Re}; 0, A)$  is defined, as  $v_{\text{inert}}(\text{Re}; 0, A) = \lim_{w \rightarrow 0} v_{\text{inert}}(\text{Re}; w, A)$ , then*

$$\text{Dr} < v_{\text{inert}}(\text{Re}; 0, A). \quad (3.56)$$

*Proof.* Because  $v_{\text{inert}}(s; w)$  is decreasing in  $w$  for  $\alpha_{\text{nozzle}} = -\pi/2$ , from Lemma 3.18 we have that

$$\text{Dr} = v_{\text{inert}}(\text{Re}; w) < v_{\text{inert}}(\text{Re}; 0),$$

where  $w > 0$ . □

**Lemma 3.3.** *Let  $(\xi, v_{\text{v-i}}, \theta)$  be a solution for the viscous-inertial jet (3.26)-(3.33). Then*

$$\text{Dr} \geq v_{\text{v-i}}(\text{Re}; 0, A) = v_{\text{inert}}(\text{Re}; 0, A) \quad (3.57)$$

*Proof.* Because  $v_{\text{inert}}(s; w, A)$  is decreasing in  $w$ , from Lemma 3.13 we have that

$$\text{Dr} = v_{\text{v-i}}(\text{Re}; w, A) \geq v_{\text{v-i}}(\text{Re}; 0, A),$$

where  $w \leq 0$ . □

**Lemma 3.4.** *The solution  $v_{\text{v-i}}(s; 0, A) \in C^1$  exists and is unique for  $A \geq 0$ .*

1. *The function  $A \mapsto v_{\text{v-i}}(s; 0, A)$  is  $C^1$  (in  $A$ ) at any  $s$  so that  $v_{\text{v-i}}(s; 0, A)$  is finite*
2.  *$v_{\text{v-i}}(s; 0, A)$  strictly decreases as  $A$  increases.*
3. *There are three possible kinds of asymptotic behaviour for  $v_{\text{v-i}}(s; 0, A)$*

$$(a) \quad \lim_{s \rightarrow M_s} v_{\text{v-i}}(s; 0, A) = \infty, \text{ for } M_s < \infty; \quad (3.58)$$

$$(b) \quad \lim_{s \rightarrow \infty} v_{\text{v-i}}(s; 0, A) = \infty; \quad (3.59)$$

$$(c) \quad \lim_{s \rightarrow Z_s} v_{\text{v-i}}(s; 0, A) = 0, \text{ for } Z_s < \infty. \quad (3.60)$$

4. If  $A$  is so that (3.58) and (3.59) holds, then  $v_{v-i}(s; 0, A)$  increases in  $s$ ; and if (3.60) holds, then  $v_{v-i}(s; 0, A)$  first increases in  $s$  and then decreases and reaches zero at finite  $s$ .
5. the value  $A = A^*$ , for which asymptotic behavior (3.59) holds, is unique.

The proof of this lemma is done in Appendix B.1.

Summarizing the Lemmas above, we conclude that  $\mathcal{P}_{\text{inert}}$  lies below the surface  $S_1$ , and  $\mathcal{P}_{\text{visc}}$  and  $\mathcal{P}_{v-i}$  lie above the surface  $S_1$ ; see Figure 3.2. Then,  $\mathcal{P}_{\text{inert}}$  is redefined as

$$\mathcal{P}_{\text{inert}} := \begin{cases} \text{Re} < s_0 \text{ and } \text{Dr} < v_{v-i}(\text{Re}; 0, A), & \text{for } A > A^*, \\ (\text{Re} < s_\infty \text{ and } \text{Dr} < v_{v-i}(\text{Re}; 0, A)) \text{ or } (\text{Re} \geq s_\infty), & \text{for } A < A^*, \\ \text{Dr} < v_{v-i}(\text{Re}; 0, A), & \text{for } A = A^*, \end{cases} \quad (3.61)$$

see Appendix A.1 for details. Here  $s_0 = \min\{s > 0 : v_{v-i}(s; 0, A) = 0\}$  and  $s_\infty = \min\{s > 0 : \lim_{\bar{s} \rightarrow s} v_{v-i}(\bar{s}; 0, A) = \infty\}$ .

The surface  $S_2$  separating  $\mathcal{P}_{\text{visc}}$  and  $\mathcal{P}_{v-i}$  is obtained in Section 3.3.

**Lemma 3.5.** • The function  $A \mapsto v_{v-i}(\text{Re}; -\tau_{\text{end}}/A, A)$  is  $C^1$  if  $v_{v-i}(\text{Re}; -\tau_{\text{end}}/A, A)$  is finite.

- The function  $\text{Re} \mapsto v_{v-i}(\text{Re}; -\tau_{\text{end}}/A, A)$  is strictly increasing and it blows up for finite  $\text{Re}$  for all  $A$ .

•

$$\mathcal{P}_{\text{visc}} := \{(A, \text{Dr}, \text{Re}) : \text{Dr} > v_{v-i}(\text{Re}; -\tau_{\text{end}}/A, A)\}. \quad (3.62)$$

The proof of this lemma follows from Lemmas 3.6-3.11 in Section 3.3. A proof of continuity is similar to the proof of part 1 of Lemma 3.18

Summarizing the results of the lemmas above the parameter region for the viscous-inertial jet lies between the surfaces  $S_1$  and  $S_2$ , i.e.

$$\mathcal{P}_{v-i} := \{(A, \text{Re}, \text{Dr}) : (A, \text{Re}, \text{Dr}) \notin \mathcal{P}_{\text{inert}} \cup \mathcal{P}_{\text{visc}}\}. \quad (3.63)$$

The regions  $\mathcal{P}_{\text{inert}}$ ,  $\mathcal{P}_{v-i}$  and  $\mathcal{P}_{\text{visc}}$ , and the borders between them,  $S_1$  and  $S_2$ , are illustrated in Figure 3.2. Note, that the regions of model parameters:  $\mathcal{P}_{\text{inert}}$ ,  $\mathcal{P}_{v-i}$  and  $\mathcal{P}_{\text{visc}}$  do not intersect and cover the admissible parameter space  $\mathcal{P}$ .

Summarizing, the parameter regions for the three flow regimes are determined in terms of three dimensionless numbers  $A$ ,  $\text{Re}$  and  $\text{Dr}$ . Further analysis of the the parameter regions is done in Section 3.8. In the next three sections we investigate the uniqueness and existence of the jet solution in each flow regime. A summary of the existence and uniqueness results is presented in Section 3.6.

### 3.3 Viscous jet

For a study of the viscous jet on the basis of (3.49)-(3.52), it is convenient to transfer the origin of  $\tau$ , to the contact point with the belt by  $\hat{\tau} = \tau_{\text{end}} - \tau$ . Also, it is convenient to scale  $\hat{v}$  with respect to  $v_{\text{belt}}$  instead of  $v_{\text{nozzle}}$ , which was used above. In such a way the

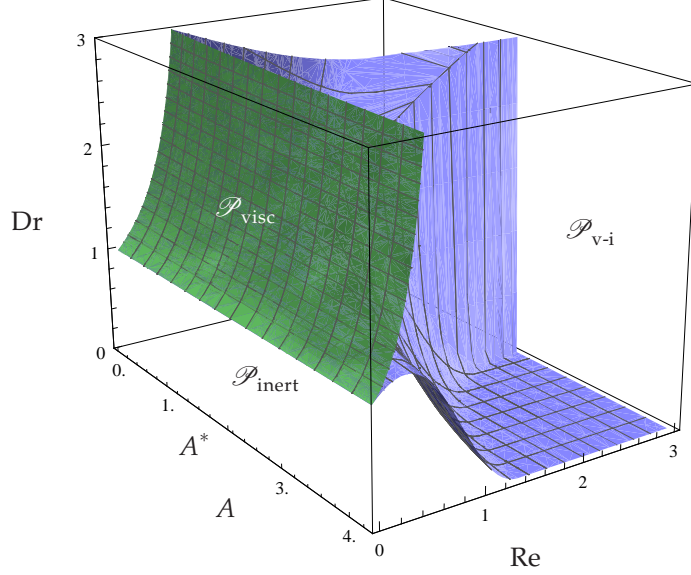


**Figure 3.2:** Parameter regions for three flow regimes  $\mathcal{P}_{\text{inert}}$ ,  $\mathcal{P}_{\text{v-i}}$  and  $\mathcal{P}_{\text{visc}}$ . The border between  $\mathcal{P}_{\text{inert}}$  and  $\mathcal{P}_{\text{v-i}}$  is  $S_1$  (bluish surface) and the border between  $\mathcal{P}_{\text{visc}}$  and  $\mathcal{P}_{\text{v-i}}$  is  $S_2$  (greenish surface).

dimensionless numbers used in this section are

$$\hat{A} = \frac{3g\nu}{v_{\text{belt}}^3} = \frac{A}{\text{Dr}^3}, \quad \hat{\text{Re}} = \frac{v_{\text{belt}}L}{3\nu} = \text{Re Dr}, \quad \text{and} \quad \hat{\text{Dr}} = \frac{v_{\text{nozzle}}}{v_{\text{belt}}} = \frac{1}{\text{Dr}}. \quad (3.64)$$

Also, throughout this section we omit the indices ‘visc’ and use another definition for  $I_{\text{visc}}$ . Then, the system (3.49)-(3.52) becomes

$$\hat{v}'(\hat{\tau}) = -\hat{v}^2(\hat{\tau})(\sqrt{\hat{A}^2\hat{\tau}^2 + \hat{w}} + \hat{v}(\hat{\tau})), \quad (3.65)$$

$$\hat{v}(0) = 1, \quad (3.66)$$

$$\hat{v}(\hat{\tau}_{\text{end}}) = \hat{\text{Dr}}, \quad (3.67)$$

$$\int_0^{\hat{\tau}_{\text{end}}} \frac{\hat{A}\hat{\tau}\hat{v}(\hat{\tau})}{\sqrt{\hat{A}^2\hat{\tau}^2 + \hat{w}}} d\hat{\tau} = \hat{\text{Re}}. \quad (3.68)$$

Here  $\hat{v}(\hat{\tau}) = v(\tau)$ ,  $\hat{w} = (\xi(\tau_{\text{end}})/\text{Dr})^2$  and  $\hat{\tau}_{\text{end}} = \tau_{\text{end}}$ .

We reformulate the problem (3.65–3.68) as an algebraic equation for the parameter  $\hat{w}$ . To this end we first formulate properties of a solution  $\hat{v}(\cdot, \hat{w})$  of the initial-value problem (3.65–3.66) for given  $\hat{w} \geq 0$ .

**Lemma 3.6.** For any  $\hat{w} \geq 0$ , equation (3.65) has a unique solution  $\hat{v}(\cdot, \hat{w}) : [0, \infty) \rightarrow (0, 1]$  satisfying (3.66) with  $\hat{v}(\cdot, \hat{w}) \in C^1([0, \infty))$ .

In addition,

1.  $\hat{v}(\hat{\tau}; \hat{w})$  is a strictly decreasing function of  $\hat{\tau}$  for fixed  $\hat{w}$  and a strictly decreasing function

of  $\hat{w}$  for fixed  $\hat{\tau}$ .

2.

$$\hat{v}(\hat{\tau}; \hat{w}) < \frac{2}{2 + \hat{\tau}\sqrt{\hat{A}^2\hat{\tau}^2 + \hat{w}}}. \quad (3.69)$$

3. The operator  $\hat{w} \mapsto \hat{v}(\cdot, \hat{w})$  is continuous from  $[0, \infty)$  to  $L^\infty(0, \infty)$ .

The proof of this lemma is done in Appendix B.2.

In order to solve (3.65)-(3.68) we need to find  $\hat{w}$  for which (3.67)-(3.68) are satisfied. Knowing a correct value of  $\hat{w}$ , we can obtain a solution  $\hat{v}(\hat{\tau})$ , which leads to a solution of the viscous jet. Therefore, next we concentrate on finding a correct  $\hat{w}$ .

**Definition 3.7.** We define a function  $I : [0, \infty) \rightarrow [0, \infty)$  in the following way. For given  $\hat{w} \in [0, \infty)$  let  $\hat{v}(\cdot, \hat{w})$  be the solution of (3.65–3.66) given by Lemma 3.6. By items 1 and 2 of Lemma 3.6 there exists a unique  $\hat{\tau}_{\text{end}}(\hat{w}) \geq 0$  satisfying

$$v(\hat{\tau}_{\text{end}}(\hat{w}); \hat{w}) = \hat{D}r. \quad (3.70)$$

Define  $I(\hat{w})$  as

$$I(\hat{w}) = \int_0^{\hat{\tau}_{\text{end}}(\hat{w})} \frac{\hat{A}\hat{\tau}\hat{v}(\hat{\tau}; \hat{w})}{\sqrt{\hat{A}^2\hat{\tau}^2 + \hat{w}}} d\hat{\tau}. \quad (3.71)$$

By Lemma 3.6, part 2, the integrable function is bounded from above and the integral converges.

**Corollary 3.8.** Solving (3.65–3.68) is equivalent to finding a  $\hat{w} \geq 0$  that satisfies

$$I(\hat{w}) = \hat{R}e. \quad (3.72)$$

The curve  $\mathcal{C}_{\text{visc}}$ , which we use to prove global existence and uniqueness in Section 3.6, is defined as

$$\mathcal{C}_{\text{visc}} := \left\{ \left( \frac{-\sqrt{\hat{A}^2\hat{\tau}_{\text{end}}(\hat{w})^2 + \hat{w}}}{\hat{D}r}, \frac{I(\hat{w})}{\hat{D}r} \right) : \hat{w} > 0 \right\}. \quad (3.73)$$

In the next three lemmas we will show some properties of  $I(\hat{w})$ , which lead to a characterization of existence and uniqueness of a solution to (3.72). The proofs of these lemmas are done in Appendix B.2.

**Lemma 3.9.**  $I(\hat{w})$  is a strictly decreasing function of  $\hat{w}$ .

**Lemma 3.10.**  $I(\hat{w})$  is continuous.

**Lemma 3.11.**  $\lim_{\hat{w} \rightarrow \infty} I(\hat{w}) = 0$ .

Summarizing the results of the previous lemmas, we formulate a theorem of existence and uniqueness of a solution to the viscous jet.

**Theorem 3.12.** There exists a solution to the viscous jet if and only if

$$I(0; \hat{A}, \hat{D}r) > \hat{R}e. \quad (3.74)$$

If it exists, the solution is unique.

The theorem follows simply from Lemmas 3.9, 3.10, and 3.11.

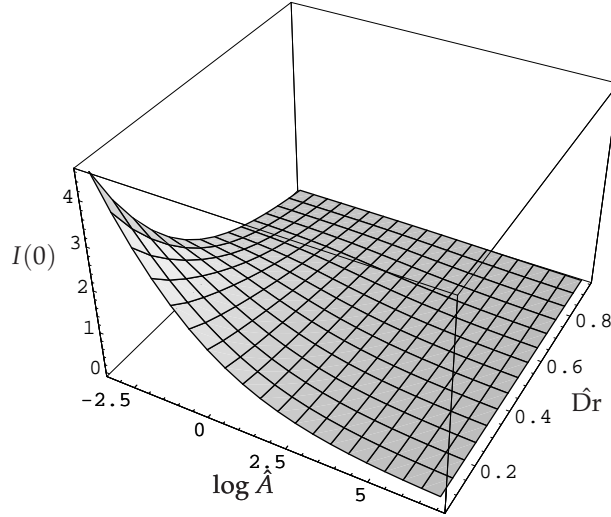


Figure 3.3: Surface  $I(0; \hat{A}, \hat{D}r)$ .

As a consequence of Theorem 3.12, a solution to the viscous jet exists only if the point  $(\hat{A}, \hat{D}r, \hat{R}e)$  is below the surface  $I(0; \hat{A}, \hat{D}r)$ ; see Figure 3.3. In Appendix A.2 we present a way how to calculate  $I(0; \hat{A}, \hat{D}r)$ .

### 3.4 Viscous-inertial jet

In this section we treat the viscous-inertial flow in detail. We show that for each parameter set from  $\mathcal{P}_{v-i}$  the viscous-inertial jet solution exists and is unique.

In case of viscous-inertial flow, the jet shape is straight vertical, and therefore the length of the jet is known in advanced  $s_{\text{end}} = Re$ . The equation for  $v(s)$  (which follow from (3.1) in case of a viscous-inertial jet) has an analytic solution [15]. However, this solution is cumbersome and difficult to analyze. Therefore, we proceed with the equations for  $v(\tau)$ , following from (3.49)-(3.52),

$$v_{\tau} = v^2(v - (A\tau + w)), \quad (3.75)$$

$$v(0) = 1, \quad (3.76)$$

$$v(\tau_{\text{end}}) = Dr, \quad (3.77)$$

$$Re = \int_0^{\tau_{\text{end}}} v(\tau) d\tau. \quad (3.78)$$

The initial-value problem (3.75) can be solved analytically, [82], however the expressions are bulky and difficult to work with. Therefore, we use the same approach as in the

previous section.

For a given  $w \leq 0$  the initial-value problem (3.75)-(3.76) has a solution  $v(\tau; w)$ . We consider this solution only up to that value of  $\tau$  when it becomes zero or infinite, so

$$\mathcal{D}(v(\cdot; w)) = (0, M_\tau) \text{ where } 0 < M_\tau \leq \infty$$

and

$$M_\tau = \sup\{M > 0 : 0 < v(\tau; w) < \infty, \tau \in (0, M)\}.$$

The properties of  $v(\tau; w)$  are summarized in the following lemma.

**Lemma 3.13.** *For  $\forall w \leq 0$ ,  $v(\tau; w)$  exists, is unique and has regularity  $C^1$  in the domain of definition.*

*Following holds for  $v(\tau; w)$*

1. *The function  $w \mapsto v(\tau; w)$  is  $C^1$  if  $v(\tau; w)$  is finite.*
2.  *$v(\tau; w)$  strictly decreases as  $w$  increases.*
3. *There are three possible kinds of asymptotic behaviour for  $v(\tau; w)$ :*

(a)

$$\lim_{\tau \rightarrow M_\tau} v(\tau; w) = \infty, \text{ for } M_\tau < \infty.$$

(b)

$$\lim_{\tau \rightarrow \infty} (v(\tau; w) - A\tau - w) = 0.$$

(c)

$$\lim_{\tau \rightarrow \infty} v(\tau; w) = 0.$$

4. *The value  $w = w_{\text{crit}}$ , for which asymptotic behavior 3b holds, is unique and exists for  $A \geq A^*$ .*

The proof of this Lemma is analogous to the proof of Lemma 3.18. One difference with the concave case is that  $w_{\text{crit}}$  exists for  $A \geq A^*$  in the case of the viscous-inertial jet and for  $A < A^*$  in the case of the concave jet. There are three possibilities for monotonic and asymptotic behaviors of  $v(\tau; w)$ , which follow from the balance between the terms  $v(\tau; w)$  and  $A\tau + w$  in the equation (3.75):

1.  $v(\tau; w)$  is a strictly increasing function and has a vertical asymptote 3a for  $w < w_{\text{crit}}$ .
2. In case  $A \geq A^*$ ,  $v(\tau; w)$  is a strictly increasing function and has an asymptote 3b for  $w = w_{\text{crit}}$ .
3. In case  $A > A^*$ ,  $v(\tau; w)$  first strictly increases until it reaches its maximum and then strictly decreases to zero 3c for  $w_{\text{crit}} < w \leq 0$ .

Each of the monotonic behaviors is possible for  $A > A^*$ , only the first two  $A = A^*$ , and only the first one for  $A < A^*$ . This is illustrated in Figures 3.4 and 3.5 for  $A > A^*$  and  $A < A^*$ , respectively.



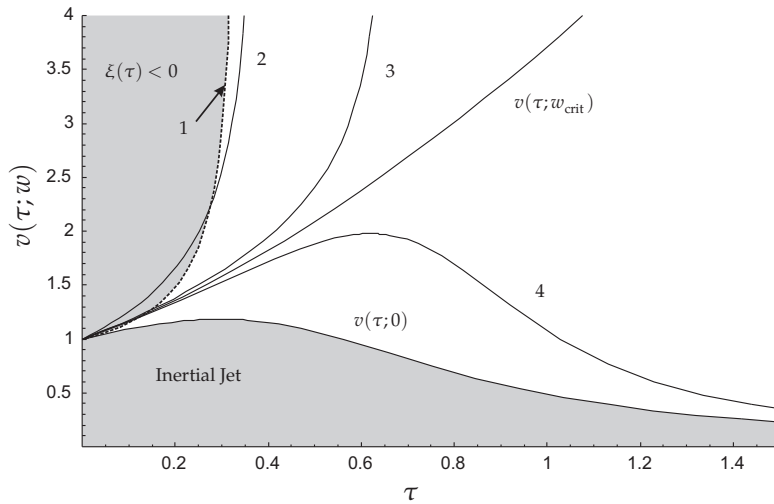


**Figure 3.4:** For  $A > A^*$   $v(\tau; w)$  can be: i) strictly increasing function with vertical asymptote (curves 2 and 3) for  $w < w_{\text{crit}}$ ; ii) strictly increasing function with oblique asymptote (curve  $v(\tau; w_{\text{crit}})$ ) for  $w = w_{\text{crit}}$ ; iii) first increasing function until it reaches a maximum and then decreasing with horizontal asymptote  $v = 0$  (curves 4 and  $v(\tau; 0)$ ) for  $w < w_{\text{crit}}$ . A part of  $v(\tau; w)$ , line 2, can lie in the region  $\xi(\tau) < 0$ , the grey area above the dashed line 1.

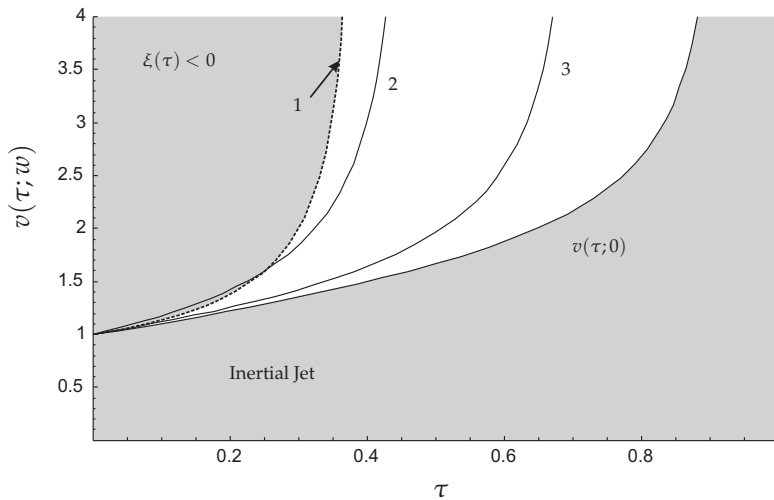


**Figure 3.5:** Velocity  $v(\tau; w)$  is strictly increasing function and has vertical asymptote (curves 2, 3 and  $v(\tau; 0)$ ) for  $A < A^*$ . A part of  $v(\tau; w)$ , line 2, can lie in the region  $\xi(\tau) < 0$ , a grey area above the dashed line 1.

Next we study a solution to the equation

$$v(\tau; w) = \text{Dr}, \quad \tau \geq -w/A, \quad (3.79)$$

which may have one solution  $\tau_{\text{end}}(w)$ , or two solutions for strictly increasing and decreasing parts of  $v(\tau; w)$ , which are denoted as  $\tau_{\text{end},1}(w)$  and  $\tau_{\text{end},2}(w)$ , respectively. Here we demand that for a solution of (3.79) the condition of viscous-inertial jet for  $\xi \geq 0$  should be fulfilled:  $\tau \geq -w/A$ . In Figures 3.4 and 3.5 the grey area above the dashed line 1 corresponds to the region in which  $\xi < 0$ .

A value of  $w$  for which  $\tau_{\text{end},1}(w) = -w/A$  is denoted by  $w_{\text{visc}}$ . It is unique, because  $\tau_{\text{end},1}(w)$  increases (part 2 of Lemma 3.13) and  $-w/A$  strictly decreases. For  $w < w_{\text{visc}}$  (3.79) does not have a solution.

The value  $w \leq 0$ , for which  $\max_{\tau} v(\tau; w) = \text{Dr}$ , is denoted by  $w_{\text{max}}$  and it is unique by part 2 of Lemma 3.13. This  $w_{\text{max}}$  exists in case  $A > A^*$  and  $\text{Dr} > \max_{\tau} v(\tau; 0)$ .

Using (3.79) we compute  $\mathcal{C}_{v-i}$  as

$$\mathcal{C}_{v-i} := \left\{ \left( w, \int_0^{\tau_{\text{end}}} v(\tau; w) d\tau \right) : v(\tau_{\text{end}}; w) = \text{Dr} \right\}, \quad (3.80)$$

The curve  $\mathcal{C}_{v-i}$  is described using one or two functions:

$$I_{v-i}(w) := \int_0^{\tau_{\text{end}}(w)} v(\tau; w) d\tau,$$

when  $\tau_{\text{end}}(w)$  is defined or similarly  $I_{v-i,1}(w)$  and  $I_{v-i,2}(w)$  are calculated using  $\tau_{\text{end},1}(w)$  and  $\tau_{\text{end},2}(w)$ .

**Remark 3.14.** From the definition of  $I_{v-i}$  it follows that the existence and uniqueness of a solution to the concave jet is equivalent to existence and uniqueness of the following algebraic equation:

$$I_{v-i}(w) = \text{Re}. \quad (3.81)$$

If  $I_{v-i,1}(w)$  and  $I_{v-i,2}(w)$  exist for the same  $w$  then we consider existence and uniqueness for only one function. In other words a solution to the concave jet exists and is unique if the horizontal line  $\text{Re}$  crosses the curve  $\mathcal{C}_{v-i}$  only once.

Next we formulate properties of  $\mathcal{C}_{v-i}$ .

**Lemma 3.15.** Following properties holds for  $\mathcal{C}_{v-i}$ :

1.  $\mathcal{C}_{v-i}$  is continuous.
2. For the cases (3.94) and (3.95)

$$\lim_{w \rightarrow +w_{\text{crit}}} I_{v-i,2}(w) = \infty.$$

3.  $I_{v-i,1}(w)$  is a strictly increasing function.
4.  $I_{v-i,2}(w)$  is a strictly decreasing function.
5. For  $w \in \mathcal{D}(I_{v-i,1}(w)) \cup \mathcal{D}(I_{v-i,2}(w))$  it holds  $I_{v-i,2}(w) > I_{v-i,1}(w)$ .

The proof of this lemma follows from the same arguments as the proof of Lemma 3.22.

**Lemma 3.16.** *A solution of (3.81) exists and is unique for all parameters from  $\mathcal{P}_{v-i}$ .*

The proof of this lemma follows from the continuity and monotonicity properties of  $\mathcal{C}_{v-i}$  described in Lemma 3.15. In Section 3.6 we describe all possible shapes of  $\mathcal{C}_{v-i}$  in detail.

Finally we formulate the theorem about existence and uniqueness of a solution for the viscous-inertial jet:

**Theorem 3.17.** *A viscous-inertial jet solution exists and is unique for all parameters from  $\mathcal{P}_{v-i}$ .*

### 3.5 Inertial jet

In this section we show that for each parameter set from the region of concave flow,  $\mathcal{P}_{\text{inert}}$ , a concave jet solution exists and we investigate uniqueness. We start with formulating the properties of  $v(\tau; w)$ , being a solution of the initial-value problem, which follows from (3.49)-(3.50),

$$v_\tau = v^2(v - f(\tau, w)), \quad (3.82)$$

$$v(0) = 1, \quad (3.83)$$

where

$$f(\tau, w) = \sqrt{A^2\tau^2 + w^2 - 2A\tau w \sin(\alpha_{\text{nozzle}})}, \quad (3.84)$$

and  $\alpha_{\text{nozzle}} \geq 0$ . Next we investigate a solution to

$$v(\tau_{\text{end}}; w) = \text{Dr}, \quad (3.85)$$

which follows from (3.51). Using (3.52) we compute  $\mathcal{C}_{\text{inert}}$  as

$$\mathcal{C}_{\text{inert}} := \left\{ \left( w, \int_0^{\tau_{\text{end}}} g(\tau, w) v(\tau; w) d\tau \right) : v(\tau_{\text{end}}; w) = \text{Dr} \right\}, \quad (3.86)$$

where  $g(\tau, w) = (A\tau - w \sin(\alpha_{\text{nozzle}}))/f(\tau, w)$ . We formulate the properties of  $\mathcal{C}_{\text{inert}}$  which allows us to show that  $\Pi(\mathcal{C}_{\text{inert}}) \supset \mathcal{L}_{\text{inert}}^1$ , and using monotonic properties of  $\mathcal{C}_{\text{inert}}$ , we state the cases for which a concave jet solution is unique.

For a given  $w \geq 0$ , the differential equation (3.82) - (3.83) has a solution  $v(\tau; w)$ , which is considered up to a point when  $v$  becomes infinity or zero, i.e.

$$\mathcal{D}(v) = [0, M_\tau) \text{ so that for } \tau \in [0, M_\tau), 0 < v(\tau; w) < \infty.$$

The properties of  $v(\tau; w)$  are formulated in the following Lemma, which we prove in Appendix B.3.

**Lemma 3.18.** *The solution  $v(\tau; w) \in C^1$  exists and is unique.*

<sup>1</sup>Here  $\Pi$  is the projection operator  $\Pi((x, y)) = y$ .

1. The function  $w \mapsto v(\tau; w)$  is  $C^1$  if  $v(\tau; w)$  is finite.
2.  $v(\tau; w)$  strictly decreases as  $w$  increases.
3. There are three possible forms of asymptotic behavior for  $v(\tau; w)$

$$(a) \quad \lim_{\tau \rightarrow M_\tau} v(\tau; w) = \infty, \text{ for } M_\tau < \infty. \quad (3.87)$$

$$(b) \quad \lim_{\tau \rightarrow \infty} (v(\tau; w) - f(\tau, w)) = 0. \quad (3.88)$$

$$(c) \quad \lim_{\tau \rightarrow \infty} v(\tau; w) = 0. \quad (3.89)$$

4. The  $w = w_{\text{crit}}$  for which asymptotic behavior 3b holds, is unique and exists for  $A < A^*$ .

The possible monotonic behaviour of  $v(\tau; w)$  follows from the previous lemma and from the fact that  $v(\tau; w)$  strictly increases when  $v(\tau; w) > f(\tau, w)$ , has a maximum when  $v(\tau; w) = f(\tau, w)$ , and strictly decreases when  $v(\tau; w) < f(\tau, w)$ . Therefore, there are 4 possibilities for monotonic and asymptotic behaviour of  $v(\tau; w)$  (see Figures 3.6 and 3.7):

1. In case  $A < A^*$  and  $w < w_{\text{crit}}$   $v(\tau; w)$  is a strictly increasing function and has the vertical asymptote (3.87).
2. In case  $A \leq A^*$  and  $w = w_{\text{crit}}$   $v(\tau; w)$  is a strictly increasing function and has the asymptote (3.88).
3. In case  $A \leq A^*$  and  $w_{\text{crit}} < w < 1$ , or  $A > A^*$  and  $w < 1$ ,  $v(\tau; w)$  first strictly increases until it reaches its maximum and then strictly decreases with the horizontal asymptote (3.89).
4. In case  $w \geq 1$ ,  $v(\tau; w)$  strictly decreases with the horizontal asymptote (3.89).

Note that all 4 monotonic behaviour is possible when  $A < A^*$ , first is not possible when  $A = A^*$  and only last two are possible when  $A > A^*$ .

**Definition 3.19.** On the range of  $w \geq 0$  for which the solution of (3.85) exists, we define  $\tau_{\text{end}}(w) = \tau_{\text{end}}$ . In case two solutions are possible we denote  $\tau_{\text{end},1}(w)$  as a solution of (3.85) on a non-decreasing part of  $v(\tau; w)$  and  $\tau_{\text{end},2}(w)$  on a strictly decreasing part.

**Definition 3.20.** The value  $w$  for which

$$\max_{\tau} v(\tau; w) = \text{Dr}$$

holds, is called  $w_{\text{max}}$ .

The value  $w_{\text{max}}$  is unique, as follows from part 2 of Lemma 3.18. The curve  $\mathcal{C}_{\text{inert}}$  is described using one or two functions

$$I_{\text{inert}}(w) := \int_0^{\tau_{\text{end}}(w)} \frac{g(\tau, w)v(\tau; w)}{f(\tau, w)} d\tau, \quad (3.90)$$

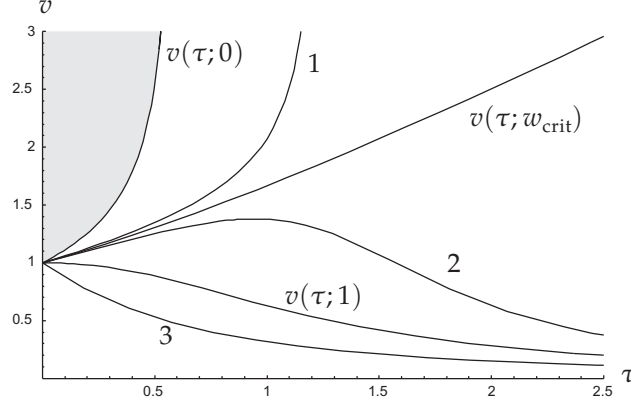


**Figure 3.6:**  $v(\tau; w)$  for different  $w$  and  $A < A^*$ . Curve 1 for  $0 < w < w_{\text{crit}}$ , curve 2 for  $w_{\text{crit}} < w < 1$  and curve 3 for  $w > 1$ . No solutions exist in the grey area above  $v(\tau; 0)$ .

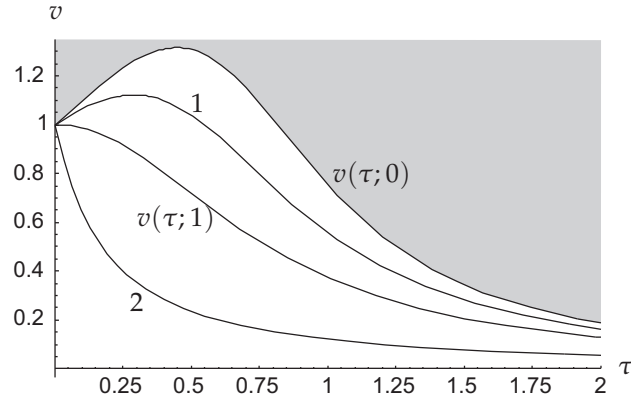


**Figure 3.7:**  $v(\tau; w)$  for different  $w$  and  $A > A^*$ . Curve 1 for  $0 < w < 1$  and curve 2 for  $w > 1$ . No solutions exist in the grey area above  $v(\tau; 0)$ .

when  $\tau_{\text{end}}(w)$  is defined or similarly  $I_{\text{inert},1}(w)$  and  $I_{\text{inert},2}(w)$  are calculated using  $\tau_{\text{end},1}(w)$  and  $\tau_{\text{end},2}(w)$ . Further in this section and in Appendix B.3, we do not distinguish between  $I_{\text{inert},1}(w)$  and  $I_{\text{inert},2}(w)$  and write  $I_{\text{inert}}(w)$ , except when it is necessary.

**Remark 3.21.** From the definition of  $I_{\text{inert}}$  it follows that existence and uniqueness of a solution to the concave jet is equivalent to existence and uniqueness of the following algebraic equation

$$I_{\text{inert}}(w) = \text{Re}. \quad (3.91)$$

If  $I_{\text{inert},1}(w)$  and  $I_{\text{inert},2}(w)$  exist for the same  $w$ , then we consider existence and uniqueness for only one function.

The properties of  $I_{\text{inert}}(w)$  are formulated in the following Lemma, which we prove in Appendix B.3.

**Lemma 3.22.** 1.  $C_{\text{inert}}$  is continuous for  $w \geq 0$ .

2. For the cases (3.93) and (3.96)

$$\lim_{w \rightarrow +w_{\text{crit}}} I_{\text{inert},2}(w) = \infty.$$

3. For the cases (3.96) and (3.97)

$$\lim_{w \rightarrow \infty} I_{\text{inert},2}(w) = 0.$$

4.  $I_{\text{inert},1}(w)$  is a strictly increasing function if  $\alpha_{\text{nozzle}} = -\pi/2$ .

5.  $I_{\text{inert},2}(w)$  is a strictly decreasing function.

6.  $I_{\text{inert},2}(w) > I_{\text{inert},1}(w)$  for  $w \in \mathcal{D}(I_{\text{inert},1}) \cup \mathcal{D}(I_{\text{inert},2})$ .

Using the properties of  $I(w)$  from Lemma 3.22 we get existence for (3.91) and we can specify the cases when the solution is unique.

**Lemma 3.23.** *A solution of (3.91) exists for all parameters from  $\mathcal{P}_{\text{inert}}$ . It is unique when one of the following conditions is fulfilled:*

- $\text{Dr} < 1$ .
- $\text{Dr} > 1$  and  $\alpha_{\text{nozzle}} = -\pi/2$ .
- $\text{Dr} > 1$  and  $\text{Re} > \max_w I_{\text{inert},1}(w)$ .

The proof of uniqueness is done by showing that  $\Pi(\mathcal{C}_{\text{inert}}) \supset \mathcal{L}_{\text{inert}}$ . For this, we use continuity and asymptotic behaviour of  $\mathcal{C}_{\text{inert}}$  shown in the previous lemma and described in detail in Section 3.6. The uniqueness follows from the monotonicity properties of  $I_{\text{inert},1}(w)$  and  $I_{\text{inert},2}(w)$  shown in the previous lemma.

**Remark 3.24.** *In case  $\text{Dr} > 1$  and  $\alpha_{\text{nozzle}} > -\pi/2$ ,  $I_{\text{inert},1}(w)$  might not be a strictly increasing function. The earlier proof of part 4 of Lemma 3.22 for  $\alpha_{\text{nozzle}} = -\pi/2$  fails because  $g(\tau, w)$  is strictly decreasing in  $w$  for  $\alpha_{\text{nozzle}} > -\pi/2$ . However, numerical experiments suggest that  $I_{\text{inert},1}(w)$  is strictly convex. Therefore, at most two solutions of (3.91) might be possible; see parts  $\mathcal{C}_{\text{inert}}^1$  in Figures 3.13(a) and 3.13(b). This gives us a condition for uniqueness of the solution of (3.91) as*

$$(I_{\text{inert},1})_w(0) \geq 0.$$

*Detailed investigation of convexity of  $I_{\text{inert},1}(w)$  lies outside of the scope of this thesis.*

**Remark 3.25.** *When  $(I_{\text{inert},1})_w(0) < 0$  a part of  $\Pi(\mathcal{C}_{\text{inert}})$ , lies outside  $\mathcal{P}_{\text{inert}}$ . This results in the existence of one or two concave jet solutions and either vertical or convex jet solutions for the same model parameters.*

We summarize the results of this section in a theorem about existence and uniqueness for the concave jet.

**Theorem 3.26.** *A concave jet solution exists for all parameters from  $\mathcal{P}_{\text{inert}}$ . It is unique when one of the following conditions is fulfilled:*

- $\text{Dr} < 1$ .
- $\text{Dr} > 1$  and  $\alpha_{\text{nozzle}} = -\pi/2$ .
- $\text{Dr} > 1$  and  $\text{Re} > \max_w I_{\text{inert},1}(w)$ .

### 3.6 Existence and uniqueness for the three flow regimes

In this section we show that for all admissible values of the dimensionless parameters  $\alpha_{\text{nozzle}} \geq 0$ ,  $A > 0$ ,  $\text{Dr} > 0$  and  $\text{Re} > 0$ , a jet solution exists and we investigate its uniqueness. By defining a curve

$$\mathcal{C}_I := \{(w, \text{Re}) : (\theta, v, \xi) \text{ is a jet solution at } (A, \text{Re}, \text{Dr}) \text{ with } w = \xi(0) \text{ for some } A, \text{Dr}\}. \quad (3.92)$$

existence of a solution to (3.54) becomes equivalent to

$$\Pi(\mathcal{C}_I) = (0, \infty),$$

which is shown in Lemma 3.27, below. The curve  $\mathcal{C}_I$  consist of the curves

$$\mathcal{C}_I = \mathcal{C}_{\text{inert}} \cup \mathcal{C}_{\text{v-i}} \cup \mathcal{C}_{\text{visc}}$$

where the curves  $\mathcal{C}_{\text{visc}}$ ,  $\mathcal{C}_{\text{v-i}}$  and  $\mathcal{C}_{\text{inert}}$  are defined by (3.73), (3.80) and (3.86), respectively.

Later on we will show that  $\mathcal{C}_I$  is a curve, which can be constructed from the functions  $I_2(w)$  (sometimes we refer to a part of  $\mathcal{C}_I$ , which is a function  $I(w)$ ).

Next, we study the structure of  $\mathcal{C}_I$  and show that  $\Pi(\mathcal{C}_{\text{inert}}) \subset \mathcal{P}_{\text{inert}}$  for  $\alpha_{\text{nozzle}} = -\pi/2$ ,  $\Pi(\mathcal{C}_{\text{v-i}}) \subset \mathcal{P}_{\text{v-i}}$  and  $\Pi(\mathcal{C}_{\text{visc}}) \subset \mathcal{P}_{\text{visc}}$ , which proves the characterization of the parameter space given in Section 3.2. The uniqueness follows from monotonicity properties of  $\mathcal{C}_I$ , which is always true for  $\alpha_{\text{nozzle}} = -\pi/2$ . If  $\alpha_{\text{nozzle}} \neq -\pi/2$ , numerical experiments suggests that a solution of (3.54) might not be unique. The properties of the curves  $\mathcal{C}_{\text{visc}}$ ,  $\mathcal{C}_{\text{v-i}}$  and  $\mathcal{C}_{\text{inert}}$  are treated in Sections 3.3, 3.4 and 3.5, respectively.

**Lemma 3.27.** *For  $\mathcal{C}_I$ , the following statements hold*

- $\mathcal{C}_I$  is continuous.

- 

$$\lim_{w \rightarrow -\infty} I(w) = 0, \text{ and } \lim_{w \rightarrow w_{\text{crit}}^-} I(w) = \infty \text{ for } \text{Dr} > 1,$$

$$\lim_{w \rightarrow \infty} I(w) = 0, \text{ and } \lim_{w \rightarrow w_{\text{crit}}^+} I(w) = \infty \text{ for } \text{Dr} < 1,$$

and

$$I(1) = 0, \text{ and } \lim_{w \rightarrow w_{\text{crit}}^+} I(w) = \infty \text{ for } \text{Dr} = 1.$$

- $\Pi(\mathcal{C}_I) = (0, \infty)$ .

*Proof.* The curve  $\mathcal{C}_I$  is continuous. Each part of  $\mathcal{C}_I$ , ( $\mathcal{C}_{\text{inert}}$ ,  $\mathcal{C}_{\text{v-i}}$  and  $\mathcal{C}_{\text{visc}}$ ) is continuous. And for the connections between  $\mathcal{C}_{\text{inert}}$  and  $\mathcal{C}_{\text{v-i}}$  at  $w = 0$ , and between  $\mathcal{C}_{\text{visc}}$  and  $\mathcal{C}_{\text{v-i}}$  at  $w = w_{\text{visc}}$  it holds

$$\lim_{w \rightarrow 0^+} I_{\text{inert}}(w) = I_{\text{v-i}}(w) \text{ and } \lim_{w \rightarrow w_{\text{visc}}^-} I_{\text{visc}}(w) = I_{\text{v-i}}(w_{\text{visc}}).$$

The asymptotical properties of  $\mathcal{C}_I$  follow from Lemmas (3.11), (3.15) and (3.22), see Figure 3.10. For  $\text{Dr} = 1$ , the vertical asymptote remains and the horizontal transforms into

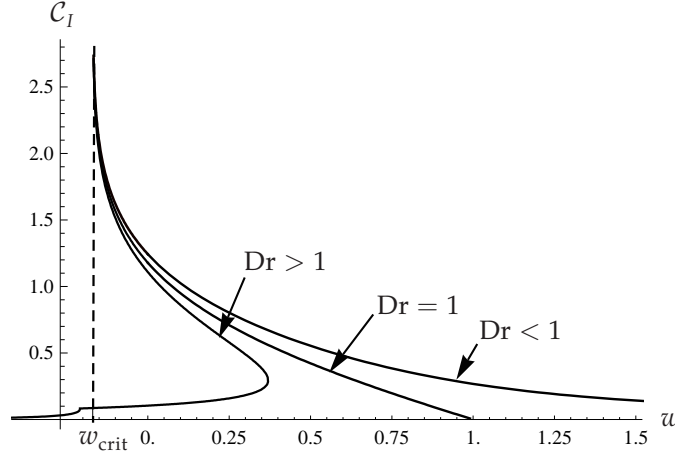


**Figure 3.8:** The asymptotic behaviour of the curves  $\mathcal{C}_I$  for the cases  $Dr > 1$  ( $v_{\text{belt}} = 1.1$  m/s),  $Dr = 1$  ( $v_{\text{belt}} = 1$  m/s), and  $Dr < 1$  ( $v_{\text{belt}} = 0.9$  m/s) and the same  $A$  ( $v_{\text{nozzle}} = 1$  m/s,  $\nu = 0.09$  m<sup>2</sup>/s,  $\alpha_{\text{nozzle}} = -\pi/2$ ).

$\lim_{w \rightarrow 1} I(w) = 0$ ; see Figure 3.8.

The asymptotic behaviour of  $\mathcal{C}_I$  together with the continuity gives

$$\Pi(\mathcal{C}_I) = (0, \infty).$$

□

Next we look at typical partitions of  $\mathcal{C}_I$  into  $\mathcal{C}_{\text{inert}}$ ,  $\mathcal{C}_{\text{v-i}}$  and  $\mathcal{C}_{\text{visc}}$  and how this fits with the parameter regions  $\mathcal{P}_{\text{inert}}$ ,  $\mathcal{P}_{\text{v-i}}$  and  $\mathcal{P}_{\text{visc}}$ . We define a line in the parameter space along which  $\text{Re}$  varies from 0 to  $\infty$ , while  $A$  and  $Dr$  are fixed:

$$\mathcal{L}(A, Dr) = \{(A, \text{Re}, Dr) : \text{Re} \in (0, \infty)\}.$$

The line  $\mathcal{L}$  is partitioned into  $\mathcal{L}_{\text{visc}} := \mathcal{L} \cap \mathcal{P}_{\text{visc}}$ ,  $\mathcal{L}_{\text{v-i}} := \mathcal{L} \cap \mathcal{P}_{\text{v-i}}$  and  $\mathcal{L}_{\text{inert}} := \mathcal{L} \cap \mathcal{P}_{\text{inert}}$ . There are 5 typical possibilities how  $\mathcal{L}$  can be partitioned, which is illustrated by the lines  $a$ ,  $b$ ,  $c$ ,  $d$  and  $e$  for fixed  $A$  in the typical  $(A, \text{Re})$  diagrams for fixed  $Dr > 1$  on the left and  $Dr \leq 1$  on the right in Figure 3.9. Also there are 5 typical ways how  $\mathcal{C}_I$  is constructed from  $\mathcal{C}_{\text{inert}}$ ,  $\mathcal{C}_{\text{v-i}}$  and  $\mathcal{C}_{\text{visc}}$ , see Figures 3.10 and 3.11, which depends on the values  $A$  and  $Dr$ .

Next, we consider each of these 5 possibilities separately. We use that  $\Pi(\mathcal{C}_{\text{visc}}) = \mathcal{L}_{\text{visc}}$ ,  $\Pi(\mathcal{C}_{\text{v-i}}) = \mathcal{L}_{\text{v-i}}$  and, if  $\alpha_{\text{nozzle}} = -\pi/2$ ,  $\Pi(\mathcal{C}_{\text{inert}}) = \mathcal{L}_{\text{inert}}$ . In each of these 5 situations we describe the monotonic behaviour of  $\mathcal{C}_{\text{inert}}$  and  $\mathcal{C}_{\text{v-i}}$ . The curve  $\mathcal{C}_{\text{visc}}$  is presented in the first 3 cases and has the same monotonic behaviour. Starting from the connection point with  $\mathcal{C}_{\text{v-i}}$  at  $w = w_{\text{visc}}$ ,  $\mathcal{C}_{\text{visc}}$  first decreases as  $w$  increases in a very small region (see Figure 3.12) then it decreases as  $w$  decreases and goes asymptotically to 0 as  $w$  goes to  $-\infty$ ; see the curves  $\mathcal{C}_{\text{visc}}$  in Figure 3.10.

1. In case

$$A \leq A^* \text{ and } Dr > 1, \tag{3.93}$$



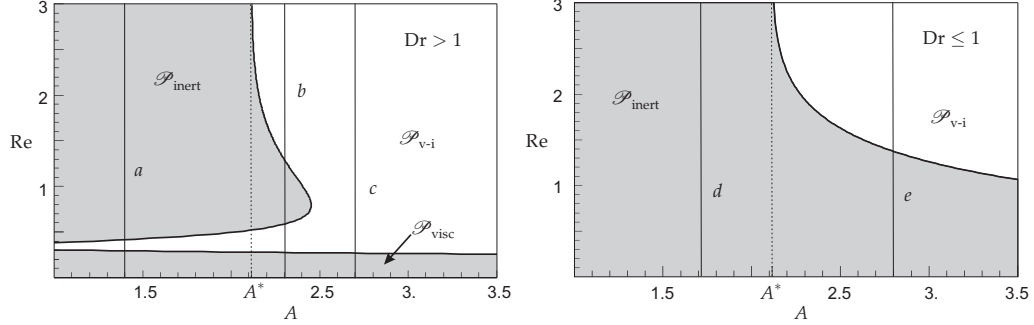


**Figure 3.9:** The typical shapes of the diagrams for three flow regimes for the parameters  $A$  and  $Re$ , and for the cases  $Dr > 0$  (left) and  $Dr \leq 0$  (right). The lines  $a$ ,  $b$ ,  $c$ ,  $d$  and  $e$  illustrate the typical possibilities for partitioning, in different flow regimes, for the corresponding cases (3.93)-(3.97).

(corresponds to line  $a$  in Figure 3.9) then

$$\mathcal{L}(A, Dr) = \mathcal{L}_{\text{visc}} \cup \mathcal{L}_{\text{v-i}} \cup \mathcal{L}_{\text{inert}}$$

the structure of  $\mathcal{C}_I$  (see Figure 3.10(a)) is  $\mathcal{C}_I = \mathcal{C}_{\text{visc}} \cup \mathcal{C}_{\text{v-i}} \cup \mathcal{C}_{\text{inert}}$  and

$$\Pi(\mathcal{C}_I) = \Pi(\mathcal{C}_{\text{visc}} \cup \mathcal{C}_{\text{v-i}} \cup \mathcal{C}_{\text{inert}}) = \mathcal{L}_{\text{visc}} \cup \mathcal{L}_{\text{v-i}} \cup \mathcal{L}_{\text{inert}} = (0, \infty),$$

where  $\mathcal{C}_{\text{inert}} = \mathcal{C}_{\text{inert}}^1 \cup \mathcal{C}_{\text{inert}}^2$ . In this case  $\mathcal{C}_{\text{inert}}^1$  is defined by an increasing function  $I_{\text{inert},1}(w)$  with  $\mathcal{D}(I_{\text{inert},1}) = (0, w_{\text{max}}]$ ;  $\mathcal{C}_{\text{inert}}^2$  is defined by a decreasing function  $I_{\text{inert},2}(w)$  with a vertical asymptote at  $w = w_{\text{crit}}$ ,  $\mathcal{D}(I_{\text{inert},2}) = (w_{\text{crit}}, w_{\text{max}})$  and  $I_{\text{inert},2}(w) > I_{\text{inert},1}(w)$ ; and  $\mathcal{C}_{\text{v-i}}$  is defined by an increasing function  $I_{\text{v-i}}(w)$  with  $\mathcal{D}(I_{\text{v-i}}) = [w_{\text{visc}}, 0]$ . In Figure 3.10(a) we illustrate how the projections of the parts of  $\mathcal{C}_I$  agree with the partitioning of the line  $a$  in Figure 3.9.

2. In case

$$A > A^* \text{ and } Dr > 1 \text{ and } \max \mathcal{P}_{\text{v-i}}(\tau; 0) < Dr \quad (3.94)$$

(corresponds to line  $b$  in Figure 3.9) then

$$\mathcal{L}(A, Dr) = \mathcal{L}_{\text{visc}} \cup \mathcal{L}_{\text{v-i}}^1 \cup \mathcal{L}_{\text{inert}} \cup \mathcal{L}_{\text{v-i}}^2,$$

the structure of  $\mathcal{C}_I$  (see Figure 3.10(b)) is  $\mathcal{C}_I = \mathcal{C}_{\text{visc}} \cup \mathcal{C}_{\text{v-i}}^1 \cup \mathcal{C}_{\text{inert}} \cup \mathcal{C}_{\text{v-i}}^2$  and

$$\begin{aligned} \Pi(\mathcal{C}_I) &= \Pi(\mathcal{C}_{\text{visc}} \cup \mathcal{C}_{\text{v-i}}^1 \cup \mathcal{C}_{\text{inert}} \cup \mathcal{C}_{\text{v-i}}^2) \\ &= \mathcal{L}_{\text{visc}} \cup \mathcal{L}_{\text{v-i}}^1 \cup \mathcal{L}_{\text{inert}} \cup \mathcal{L}_{\text{v-i}}^2 = (0, \infty), \end{aligned}$$

where  $\mathcal{C}_{\text{inert}} = \mathcal{C}_{\text{inert}}^1 \cup \mathcal{C}_{\text{inert}}^2$ . In this case  $\mathcal{C}_{\text{inert}}^1$  is defined by an increasing function  $I_{\text{inert},1}(w)$  with  $\mathcal{D}(I_{\text{inert},1}) = (0, w_{\text{max}}]$ ;  $\mathcal{C}_{\text{inert}}^2$  is defined by a decreasing function  $I_{\text{inert},2}(w)$  with  $\mathcal{D}(I_{\text{inert},2}) = (0, w_{\text{max}})$  and  $I_{\text{inert},2}(w) > I_{\text{inert},1}(w)$ ;  $\mathcal{C}_{\text{v-i}}^1$  is defined by an increasing function  $I_{\text{v-i},1}(w)$  with  $\mathcal{D}(I_{\text{v-i},1}) = [w_{\text{visc}}, 0]$ ; and  $\mathcal{C}_{\text{v-i}}^2$  is defined by

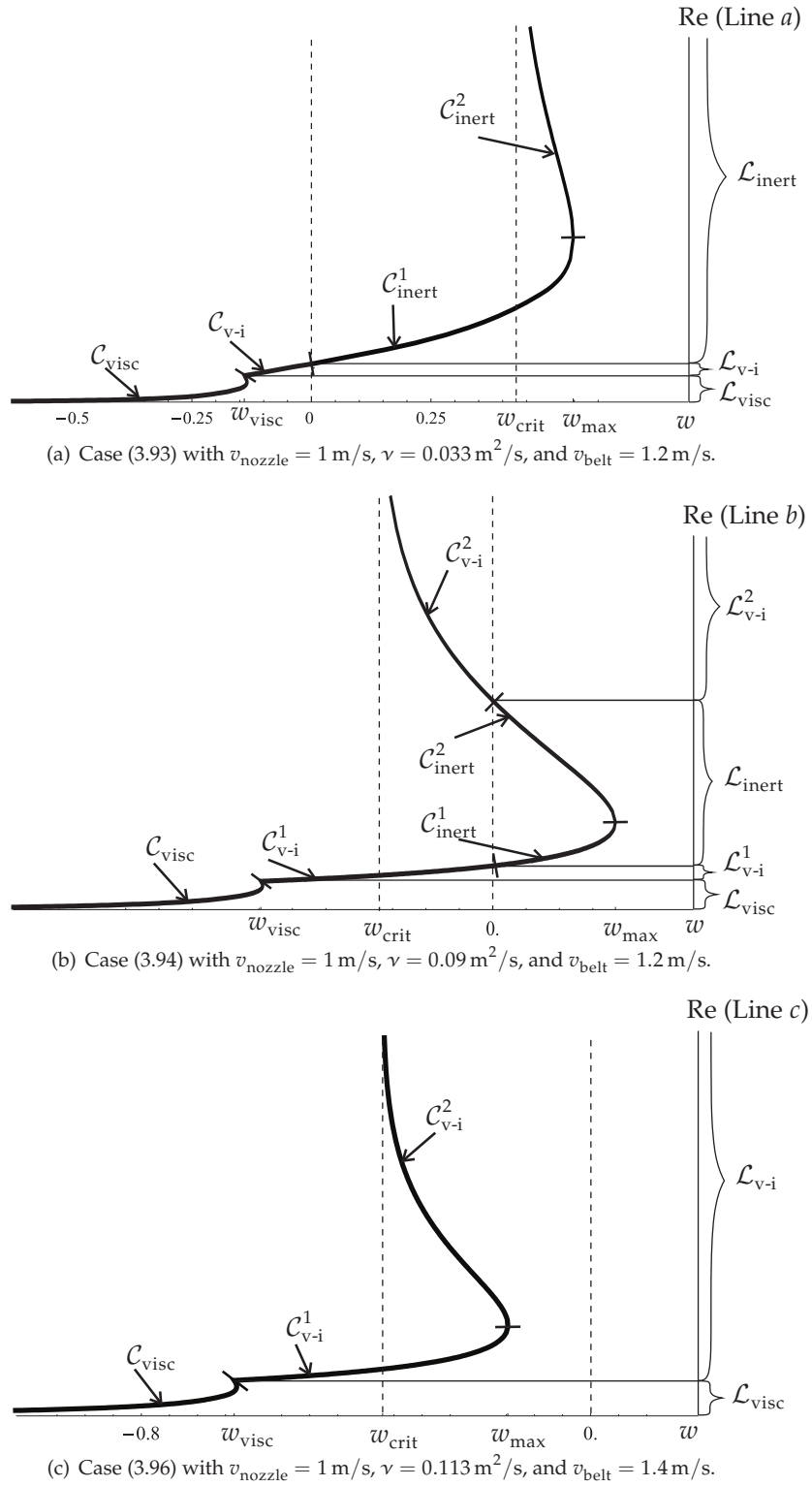
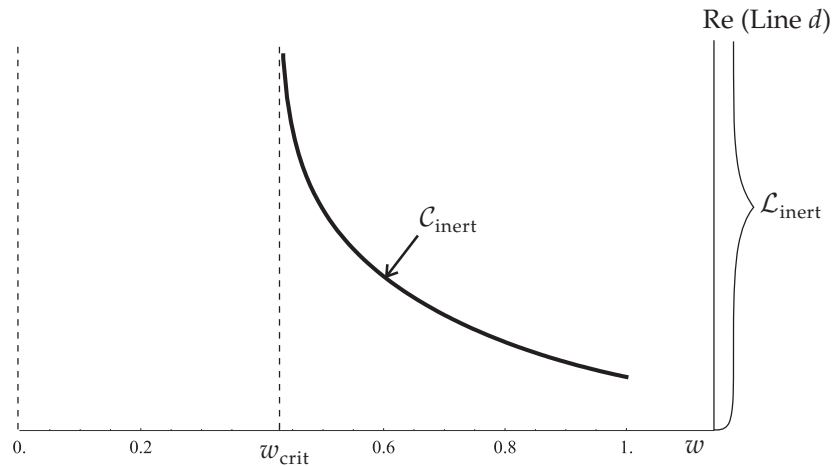
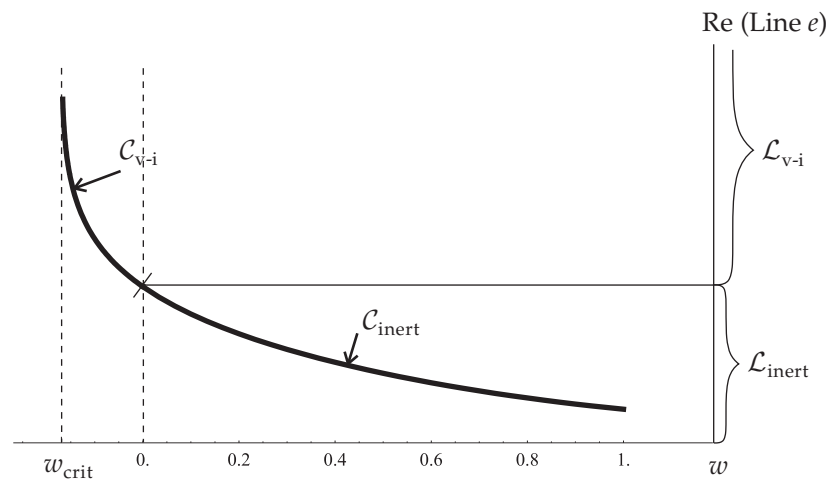


**Figure 3.10:** The typical shapes of the curves  $C_1$  and the projection  $\Pi$  of the  $C_1$ -structure onto a line  $\mathcal{L}$  for the cases (3.93)-(3.95) and  $\alpha_{\text{nozzle}} = -\pi/2$ .



(a) Case (3.97) with  $v_{nozzle} = 1$  m/s,  $\nu = 0.033$  m<sup>2</sup>/s, and  $v_{belt} = 0.9$  m/s.



(b) Case (3.95) with  $v_{nozzle} = 1$  m/s,  $\nu = 0.09$  m<sup>2</sup>/s, and  $v_{belt} = 0.9$  m/s.

**Figure 3.11:** The typical shapes of the curves  $C_1$  and the projection  $\Pi$  of the  $C_1$ -structure onto a line  $\mathcal{L}$  for the cases (3.96)-(3.97) and  $\alpha_{nozzle} = -\pi/2$ .

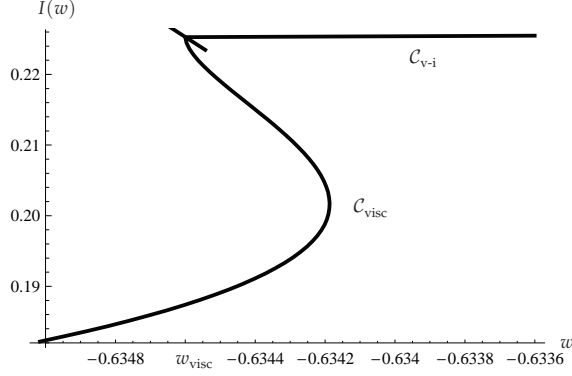


**Figure 3.12:** A typical, zoomed in shape of  $\mathcal{C}_I$  at the non-smooth connection between  $\mathcal{C}_{\text{visc}}$  and  $\mathcal{C}_{\text{v-i}}$  ( $v_{\text{nozzle}} = 1 \text{ m/s}$ ,  $\nu = 0.113 \text{ m}^2/\text{s}$ ,  $v_{\text{belt}} = 1.4 \text{ m/s}$ ).

an increasing function  $I_{\text{v-i},2}(w)$  with a vertical asymptote at  $w = w_{\text{crit}}$ ,  $\mathcal{D}(I_{\text{v-i},2}) = [w_{\text{crit}}, 0]$  and  $I_{\text{v-i},2}(w) > I_{\text{v-i},1}(w)$ . In Figure 3.10(b) we illustrate how the projections of the parts of  $\mathcal{C}_I$  agree with the partitioning of the line  $b$  in Figure 3.9.

3. In case

$$A > A^* \text{ and } \text{Dr} > 1 \text{ and } \max \mathcal{P}_{\text{v-i}}(\tau; 0) \geq \text{Dr}, \quad (3.95)$$

(corresponds to line  $c$  in Figure 3.9) then

$$\mathcal{L}(A, \text{Dr}) = \mathcal{L}_{\text{visc}} \cup \mathcal{L}_{\text{v-i}},$$

the structure of  $\mathcal{C}_I$  (see Figure 3.10(c)) is  $\mathcal{C}_I = \mathcal{C}_{\text{visc}} \cup \mathcal{C}_{\text{v-i}}$  and

$$\Pi(\mathcal{C}_I) = \Pi(\mathcal{C}_{\text{visc}} \cup \mathcal{C}_{\text{v-i}}) = \mathcal{L}_{\text{visc}} \cup \mathcal{L}_{\text{v-i}} = (0, \infty),$$

where  $\mathcal{C}_{\text{v-i}} = \mathcal{C}_{\text{v-i}}^1 \cup \mathcal{C}_{\text{v-i}}^2$ . In this case  $\mathcal{C}_{\text{v-i}}^1$  is defined by an increasing function  $I_{\text{v-i},1}(w)$  with  $\mathcal{D}(I_{\text{v-i},1}) = [w_{\text{visc}}, w_{\text{max}}]$ ; and  $\mathcal{C}_{\text{v-i}}^2$  is defined by an increasing function  $I_{\text{v-i},2}(w)$  with a vertical asymptote at  $w = w_{\text{crit}}$ ,  $\mathcal{D}(I_{\text{v-i},2}) = [w_{\text{crit}}, w_{\text{max}})$  and  $I_{\text{v-i},2}(w) > I_{\text{v-i},1}(w)$ . In Figure 3.10(c) we illustrate how the projections of the parts of  $\mathcal{C}_I$  agree with the partitioning of the line  $c$  in Figure 3.9.

4. In case

$$A \leq A^* \text{ and } \text{Dr} \leq 1 \quad (3.96)$$

(corresponds to line  $d$  in Figure 3.9) then

$$\mathcal{L}(A, \text{Dr}) = \mathcal{L}_{\text{inert}}$$

the structure of  $\mathcal{C}_I$  (see Figure 3.11(a)) is  $\mathcal{C}_I = \mathcal{C}_{\text{inert}}$

$$\Pi(\mathcal{C}_I) = \Pi(\mathcal{C}_{\text{inert}}) = \mathcal{L}_{\text{inert}} = (0, \infty).$$

Here  $\mathcal{C}_{\text{inert}}$  is defined by a decreasing function  $I_{\text{inert}}(w)$  with vertical asymptote at  $w = w_{\text{crit}}$ , horizontal asymptote  $I = 0$  and  $\mathcal{D}(I_{\text{inert}}) = (w_{\text{crit}}, \infty)$ . In Figure 3.11(a)

we illustrate how the projections of the parts of  $\mathcal{C}_I$  agree with the partitioning of the line  $d$  in Figure 3.9.

5. In case

$$A > A^* \text{ and } \text{Dr} \leq 1 \quad (3.97)$$

(corresponds to line  $e$  in Figure 3.9) then

$$\mathcal{L}(A, \text{Dr}) = \mathcal{L}_{\text{inert}}$$

the structure of  $\mathcal{C}_I$  (see Figure 3.11(b)) is  $\mathcal{C}_I = \mathcal{C}_{\text{inert}} \cup \mathcal{C}_{\text{v-i}}$  and

$$\Pi(\mathcal{C}_I) = \Pi(\mathcal{C}_{\text{inert}} \cup \mathcal{C}_{\text{v-i}}) = \mathcal{L}_{\text{inert}} \cup \mathcal{L}_{\text{v-i}} = (0, \infty).$$

Here  $\mathcal{C}_{\text{inert}}$  is defined by a decreasing function  $I_{\text{inert}}(w)$  with horizontal asymptote  $I = 0$  and  $\mathcal{D}(I_{\text{inert}}) = (0, \infty)$  and  $\mathcal{C}_{\text{v-i}}$  is defined by a decreasing function  $I_{\text{v-i}}(w)$  with vertical asymptote at  $w = w_{\text{crit}}$  and  $\mathcal{D}(I_{\text{v-i}}) = (w_{\text{crit}}, 0]$ . In Figure 3.11(b) we illustrate how the projections of the parts of  $\mathcal{C}_I$  agree with the partitioning of the line  $e$  in Figure 3.9.

The above analysis of 5 typical cases of  $\mathcal{C}_I$  shows that the regions  $\mathcal{P}_{\text{inert}}$ ,  $\mathcal{P}_{\text{v-i}}$  and  $\mathcal{P}_{\text{visc}}$  agree with partitioning of  $\mathcal{C}_I$  if  $\alpha_{\text{nozzle}} = -\pi/2$ . The monotonic properties of the curve  $\mathcal{C}_I$  in the cases imply uniqueness of a jet solution. All this we summarize in the following Lemma.

**Lemma 3.28.** *If  $\alpha_{\text{nozzle}} = -\pi/2$ , a jet solution is unique for all model parameters and the viscous, viscous-inertial, or inertial jet solution exists if  $(A, \text{Re}, \text{Dr})$  lies in the corresponding region  $\mathcal{P}_{\text{visc}}$  or  $\mathcal{P}_{\text{v-i}}$  or  $\mathcal{P}_{\text{inert}}$ .*

Next we look at a nozzle angle  $\alpha_{\text{nozzle}} \in (-\pi/2, 0]$ . Then, the curves  $\mathcal{C}_{\text{v-i}}$  and  $\mathcal{C}_{\text{visc}}$  remain the same, but the curve  $\mathcal{C}_{\text{inert}}$  changes. For cases (3.96) and (3.97) the functions  $I_{\text{inert}}(w)$  remain decreasing with the same asymptote. The same is true for the functions  $I_{\text{inert}}^2(w)$  in cases (3.93) and (3.94). However, we can not prove that the functions  $I_{\text{inert}}^1(w)$  in cases (3.93) and (3.94) increase. Moreover, numerical experiments suggests that  $I_{\text{inert}}^1(w)$  can first decrease and then increase, but  $I_{\text{inert}}^1(w)$  remains positive; see Figures 3.13(a) and 3.13(b) for  $\alpha_{\text{nozzle}} = 0$ . This leads to the following lemma.

**Lemma 3.29.** *If  $\alpha_{\text{nozzle}} \in (-\pi/2, 0]$  a jet solution is unique for all model parameters except for*

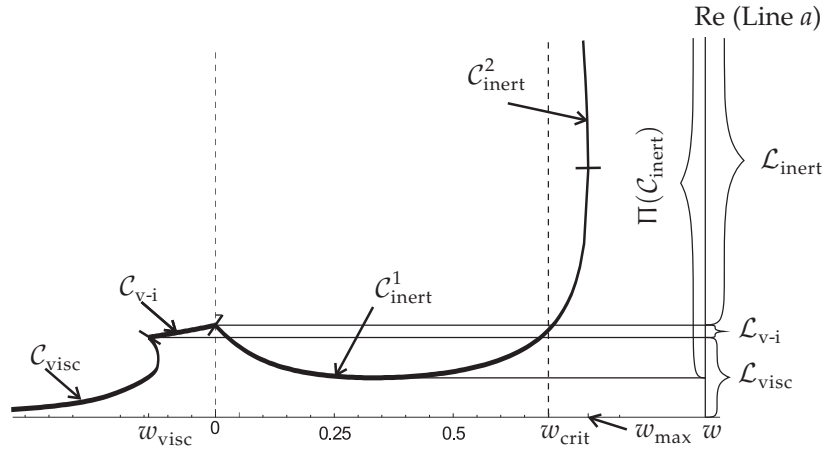
$$\text{Re} \notin \Pi(\mathcal{C}_{\text{inert}}^1) \cup (\Pi(\mathcal{C}_{\text{inert}}^2) \cap (\mathcal{L}_{\text{v-i}} \cup \mathcal{L}_{\text{visc}})),$$

for the cases (3.93) and (3.94).

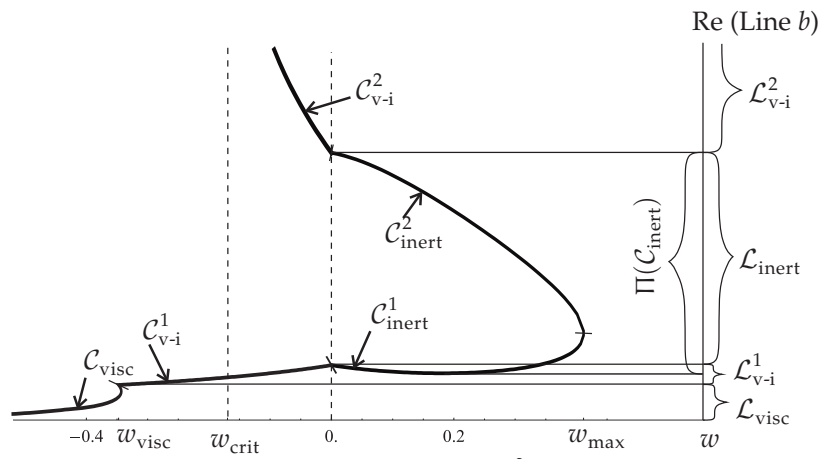
*The viscous or viscous-inertial jet solution exists iff  $(A, \text{Re}, \text{Dr})$  lies in the corresponding region  $\mathcal{P}_{\text{visc}}$  or  $\mathcal{P}_{\text{v-i}}$ . If  $(A, \text{Re}, \text{Dr}) \in \mathcal{P}_{\text{inert}}$ , then inertial jet solution exists.*

The numerical experiments for  $\alpha_{\text{nozzle}} = 0$  show that in the case (3.93)  $\Pi(\mathcal{C}_{\text{inert}}^1) \cap (\mathcal{L}_{\text{v-i}} \cup \mathcal{L}_{\text{visc}}) \neq \emptyset$  and in the case (3.94)  $\Pi(\mathcal{C}_{\text{inert}}^1) \cap (\mathcal{L}_{\text{v-i}}^1) \neq \emptyset$ . Therefore, two inertial jet solutions are possible and either a viscous or inertial jet solution is possible. The parameter region for the inertial jet depends on  $\alpha_{\text{nozzle}}$  and is larger then  $\mathcal{P}_{\text{inert}}$ .

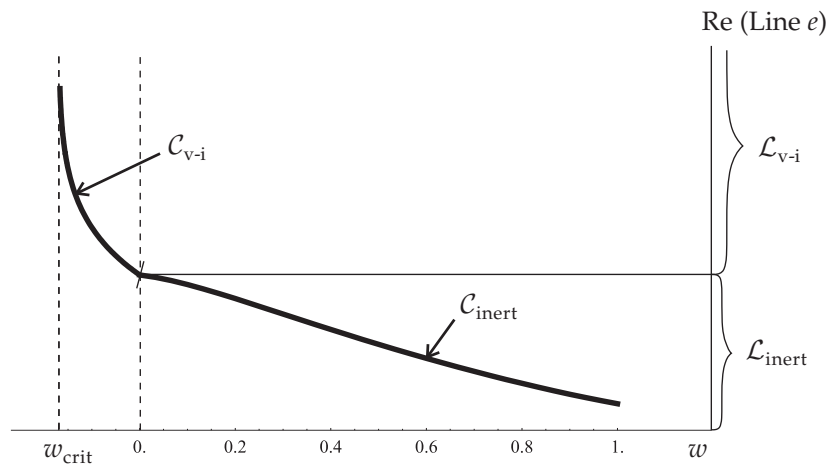
The curve  $\mathcal{C}_I$  is not smooth at the transition between  $\mathcal{C}_{\text{visc}}$  and  $\mathcal{C}_{\text{v-i}}$ , see Figures 3.10(a), 3.10(b) and 3.10(c), and see Figure 3.12 for zoomed in  $\mathcal{C}_I$  at  $w = w_{\text{visc}}$ . This happens



(a) Case (3.93) with  $v_{\text{nozzle}} = 1 \text{ m/s}$ ,  $\nu = 0.033 \text{ m}^2/\text{s}$ , and  $v_{\text{belt}} = 1.2 \text{ m/s}$ .



(b) Case (3.94) with  $v_{\text{nozzle}} = 1 \text{ m/s}$ ,  $\nu = 0.0766 \text{ m}^2/\text{s}$ , and  $v_{\text{belt}} = 1.2 \text{ m/s}$ .



(c) Case (3.97) with  $v_{\text{nozzle}} = 1 \text{ m/s}$ ,  $\nu = 0.09 \text{ m}^2/\text{s}$ , and  $v_{\text{belt}} = 0.9 \text{ m/s}$ .

**Figure 3.13:** The typical shapes of  $C_I$  when  $\alpha_{\text{nozzle}} = 0$  and the projection  $\Pi$  of the  $C_I$ -structure onto a line  $\mathcal{L}$ , for the cases (3.93), (3.94) and (3.97).

because the jet shape changes from straight vertical to the tangential to the belt at the contact with the belt. The transition between  $\mathcal{C}_{v-i}$  and  $\mathcal{C}_{inert}$  is smooth in case  $\alpha_{nozzle} = -\pi/2$  because the shape of the jet remains straight vertical for inertial and viscous-inertial jets; see Figures 3.10(a), 3.10(b) and 3.11(b). For  $\alpha_{nozzle} \in (-\pi/2, 0]$  the inertial jet shape is aligned with the nozzle and behaves strictly inertial in contrast to the straight vertical shape for the viscous-inertial jet case. Therefore, the transition between  $\mathcal{C}_{v-i}$  and  $\mathcal{C}_{inert}$  is not smooth; see Figure 3.13 for  $\alpha_{nozzle} = 0$ .

The uniqueness and existence analysis of a jet solution is summarized in the following theorem.

**Theorem 3.30.** *A jet solution exists for all admissible values of the model parameters. It is unique for all model parameters except for*

$$\text{Re} \notin \Pi(\mathcal{C}_{inert}^1) \cup (\Pi(\mathcal{C}_{inert}^2) \cap (\mathcal{L}_{v-i} \cup \mathcal{L}_{visc})) \text{ and } \alpha_{nozzle} \in (-\pi/2, 0],$$

for the cases (3.93) and (3.94).

### 3.7 Inertial jet with upwards pointing nozzle

In this section we shortly discuss the inertial jet with the nozzle pointing upwards. We discuss the behavior of  $v(\tau; w)$ . Investigation of the monotonic behavior of the curve  $\mathcal{C}_I$  for different  $A$  and  $Dr$  reveals the possibility of non-unique solutions for (3.91).

In the same way as in the previous section we consider a solution  $v(\tau; w)$  of (3.82) and (3.85) up to a point when  $v(\tau; w)$  becomes infinite or zero. From (3.82) it follows that monotonicity of  $v(\tau; w)$  is given by the balance between  $v(\tau; w)$  and  $f(\tau, w)$ :

- When  $v(\tau; w) > f(\tau, w)$  then  $v(\tau; w)$  increases.
- When  $v(\tau; w) < f(\tau, w)$  then  $v(\tau; w)$  decreases.
- When  $v(\tau; w) = f(\tau, w)$  then  $v(\tau; w)$  has a maximum or minimum.

For a nozzle pointing upward,  $\alpha_{nozzle} > 0$ , the function  $f(\tau, \cdot)$  (3.84) first decreases and then increases with a minimum at the point  $\tau = \tau_{fm}$  and  $f(\cdot, w)$  is not monotonic in  $w$ . This implies that the graphs of  $f(\tau, w)$  for different  $w$  cross each other. Therefore, the monotonic behavior of  $v(\tau; w)$  and the analysis are more complicated than for  $\alpha_{nozzle} \leq 0$ . A detailed analysis of the properties of the functions  $v(\tau; w)$ ,  $I(w)$  and the equation (3.85) is outside the scope of this paper. However, we will discuss the monotonic behavior of  $v(\tau; w)$  and the possible solutions of (3.85), which leads to the shape of  $\mathcal{C}_I$ .

Depending on  $A$  and  $w$ , the following possibilities for  $v(\tau; w)$  and the the solutions of (3.85) exists:

- For  $w > 1$ ,  $v(\tau; w) < f(\tau, w)$  and thus  $v$  always decreases, (see Figure 3.14(a) curve 5 and Figure 3.14(b) curve 4) and moreover (3.85) has one solution for  $Dr < 1$ , see Figure 3.15(a).
- While decreasing  $w$ , we find a point  $w = w_1^* < 1$  where  $v(\tau; w_1^*) < f(\tau, w_1^*)$  for all  $\tau$  except  $\tau_{fm}$ . At the point  $\tau_{fm}$ ,  $f(\tau_{fm}, w_1^*) = v(\tau_{fm}; w_1^*)$  and  $v_{\tau}(\tau_{fm}; w_1^*) = 0$ ;

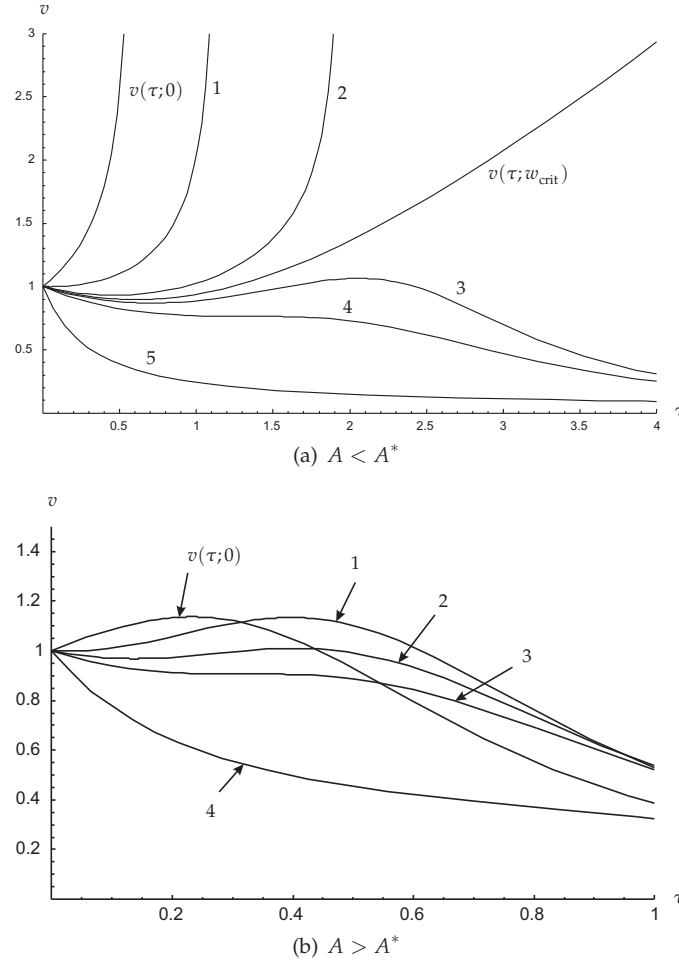


**Figure 3.14:** Velocities  $v(\tau; w)$  for different values of  $w$ , and for the cases  $A < A^*$  and  $A > A^*$

see Figure 3.14(a) curve 4 and Figure 3.14(b) curve 3. In this case, (3.85) has one solution for  $Dr < 1$ ; see Figure 3.15(b).

- Consider  $w$  so that  $\max\{w_{\text{crit}}, 1\} > w > w_1^*$  for  $A \leq A^*$ , or  $1 > w > w_1^*$  for  $A > A^*$ . Then first  $v(\tau; w) < f(\tau, w)$  until it crosses  $f(\tau, w)$  at  $\tau = \tau_{fm}$ , next  $v(\tau; w) > f(\tau, w)$  for some interval until it crosses  $f(\tau, w)$  at  $\tau > \tau_{fm}$  and then  $v(\tau; w) < f(\tau, w)$ . Therefore,  $v(\tau; w)$  first decreases, has a local minimum, then increases until it hits a local maximum and then decreases; see Figure 3.14(a) curve 3 and Figure 3.14(b) curve 2. As a consequence the equation (3.85) can have: one (see Figures 3.15(d) and 3.15(g)), two (see Figures 3.15(c) and 3.15(f)), three (see Figure 3.15(e)) or no solutions.
- In case  $A \leq A^*$  and  $w_{\text{crit}} > 1$  for  $w_{\text{crit}} \geq w > 1$  first  $v(\tau; w) < f(\tau, w)$  until it crosses the line  $f(\tau, w)$  at  $\tau = \tau_{fm}$  and then  $v(\tau; w) > f(\tau, w)$ . Therefore, the ve-



locity  $v(\tau; w)$  first decreases and has a global minimum at some  $\tau < \tau_{fm}$  and then increases; see Figure 3.14(a) curves 2 and  $v(\tau; w_{\text{crit}})$ . In this case the equation (3.85) has 2 solutions for  $\min v(\tau; w) < \text{Dr} < 1$ , (see Figure 3.15(i)) and one solution for  $\min v(\tau; w) = \text{Dr}$  or  $\text{Dr} > 1$ ; see Figures 3.15(h), 3.15(j) and 3.15(l) for  $w = w_{\text{crit}}$ .

- In case  $A \leq A^*$  and  $0 \geq w \geq \min\{w_{\text{crit}}, 1\}$ ,  $v(\tau; w) > f(\tau, w)$  and the velocity  $v(\tau; w)$  strictly increases, see Figure 3.14(a) curves 1 ( $v(\tau; 1)$ ) and  $v(\tau; 0)$ . Therefore, only one solution of (3.85) is possible for  $\text{Dr} > 1$ ; see Figure 3.15(k).
- For  $A > A^*$  and  $0 \geq w \geq 1$ , or  $A < A^*$  with  $w_{\text{crit}} < 1$  and  $w_{\text{crit}} > w \geq 1$ , first  $v(\tau; w) > f(\tau, w)$ , until it crosses  $f(\tau, w)$  at  $\tau = \tau_{fm}$ , and afterwards  $v(\tau; w) > f(\tau, w)$ . The velocity  $v(\tau; w)$  first increases, reaches its global maximum and then decreases; see Figure 3.14(a) curves 2 and Figure 3.14(b) curves 1, ( $v(\tau; 1)$ ), and  $v(\tau; 0)$ . The equation (3.85) has two solutions for  $1 < \text{Dr} < \max v(\tau; w)$ , (see Figure 3.15(n)), and one solution for  $\text{Dr} = \max v(\tau; w)$  (see Figure 3.15(m)) and  $\text{Dr} < 1$  (see Figure 3.15(o)).

In the discussion above,  $w_{\text{crit}}$  has the same meaning as for the case  $\alpha_{\text{nozzle}} \leq 0$ . From this discussion above we obtain a global picture of  $\tau_{\text{end}}(w)$ , which leads us to the shapes of the curves  $cSI$ . In Figure 3.16 we present an example of possible shapes of  $\mathcal{C}_I$  in the cases (3.93), (3.94), (3.96) and (3.97). Here  $w_2^*$  corresponds to the situation depicted in Figure 3.15(c) and  $w_3^*$  corresponds to the situation depicted in Figure 3.15(f).

The asymptotical behavior of  $\mathcal{C}_I$  is the same as in the case  $\alpha_{\text{nozzle}} \leq 0$ . If  $A \leq A^*$ ,  $\mathcal{C}_I$  has a vertical asymptote at  $w = w_{\text{crit}}$ . If  $\text{Dr} < 1$ ,  $\mathcal{C}_I$  has a horizontal asymptote  $\text{Re} = 0$ , and  $\mathcal{C}_I$  approaches to this asymptote from below. Because the nozzle points upwards, the equation (3.85) can have solutions for  $\text{Re} < 0$ . The monotonic behavior of  $\mathcal{C}_I$  is more complicated for upwards pointing nozzle and multiple solutions of the equation (3.85) are possible. This leads to multiple solutions for the stationary inertial jet. The detailed study of inertial jet with upwards pointing nozzles is outside the range of this investigation.

The curves  $\mathcal{C}_I$  calculated for the upwards pointing nozzle  $\alpha_{\text{nozzle}} > 0$  are depicted in Figure 3.16. Equation (3.54) has a solution for  $\text{Re} < 0$  (the belt is above the nozzle) in the inertial regime. Therefore, in case  $\text{Dr} > 1$  and  $0 < \text{Re} < I(0)$  three multiple solutions are possible, two in the inertial regime and one in the viscous-inertial or inertial regimes; see Figures 3.16(a) and 3.16(b). For  $v_{\text{belt}} < 1$  the part of  $I(w)$  for the inertial regime has a loop which results in multiple solutions as well; see Figures 3.16(c) and 3.16(d).

## 3.8 Results

In this section we present some results from our model concerning the partitioning of the parameter space. We investigate changes of the flow type if one of the dimensional parameters ( $L, \nu, v_{\text{belt}}, v_{\text{nozzle}}$ ) is varied. We describe the trajectories of the process parameters in the parameter space  $\mathcal{P}$ , and we illustrate the jet shape evolution. Note that the only possible transitions between flow types are between  $\mathcal{P}_{v-i}$  and  $\mathcal{P}_{\text{visc}}$  and between  $\mathcal{P}_{v-i}$  and  $\mathcal{P}_{\text{inert}}$ ; see Figure 3.2.

The projection of the regions for the three flow regimes onto the  $(A, \text{Re})$ -plane is depicted in Figure 3.17, and what follows is valid for all values of  $\text{Dr}$ . We observe a region  $\{A < A^*, \text{Re} > \mathcal{R}_1(A)\}$  where the jet is inertial, and a region  $\{A > A^*, \text{Re} > \mathcal{R}_2(A)\}$

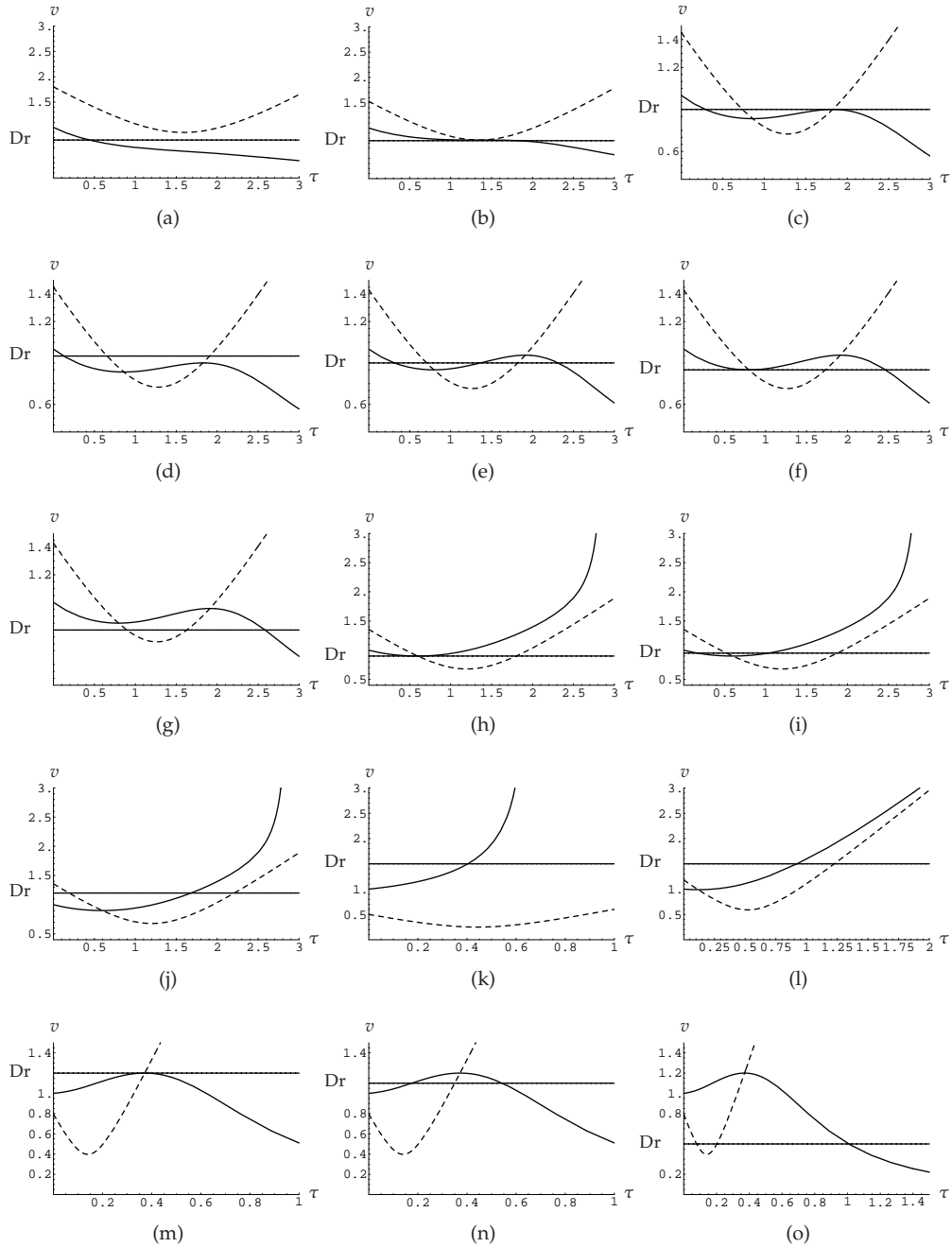
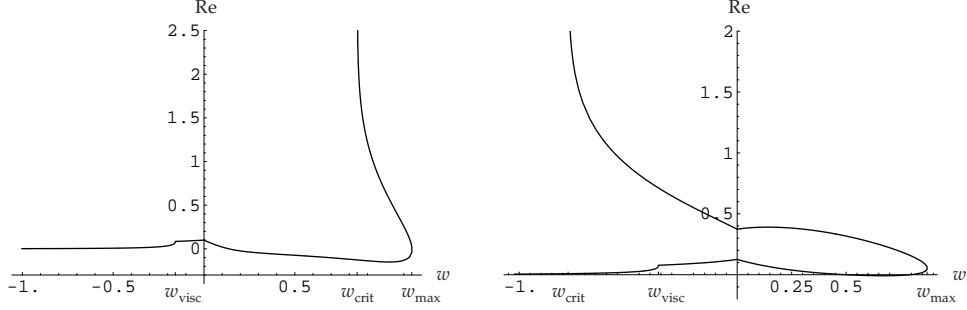
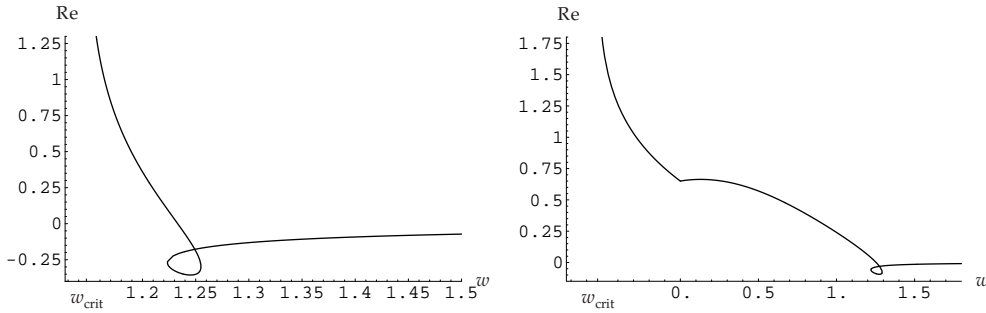


**Figure 3.15:** Possibilities for solutions of (3.85). The horizontal lines indicate the possible values of  $Dr$ , solid lines stand for  $v(\tau; w)$  and dotted lines stand for  $f(\tau, w)$ .



(a) Case (3.93) with  $v_{\text{nozzle}} = 1 \text{ m/s}$ ,  $\nu = 0.066 \text{ m}^2/\text{s}$ , and  $v_{\text{belt}} = 1.1 \text{ m/s}$ .  
 (b) Case (3.94) with  $v_{\text{nozzle}} = 1 \text{ m/s}$ ,  $\nu = 0.166 \text{ m}^2/\text{s}$ , and  $v_{\text{belt}} = 1.1 \text{ m/s}$ .



(c) Case (3.96) with  $v_{\text{nozzle}} = 1 \text{ m/s}$ ,  $\nu = 0.033 \text{ m}^2/\text{s}$ , and  $v_{\text{belt}} = 0.95 \text{ m/s}$ .  
 (d) Case (3.97) with  $v_{\text{nozzle}} = 1 \text{ m/s}$ ,  $\nu = 0.133 \text{ m}^2/\text{s}$ , and  $v_{\text{belt}} = 0.99 \text{ m/s}$ .

**Figure 3.16:** The typical shapes of the curves  $C_1$  when  $\alpha_{\text{nozzle}} = \pi/4 > 0$ , for the cases (3.93), (3.94), (3.96) and (3.97). The curves  $C_1$  are not continuously differentiable at the transition points between the viscous and viscous-inertial regimes,  $w = w_{\text{visc}}$ , and between the viscous-inertial and inertial regimes  $w = 0$  due to the change of the boundary condition. The shapes of the curves  $C_1$  in the inertial regime ( $w > 0$ ) indicate the possibility of multiple solutions of (3.54) for all the cases presented in this figure.

where it is viscous-inertial. In the region between  $\mathcal{R}_1$ ,  $\mathcal{R}_2$  and  $\mathcal{R}_3$  inertial or viscous-inertial flow, but no viscous flow, is possible. Finally, in the region  $\{A > 0, \text{Re} < \mathcal{R}_3(A)\}$ , all three flow regimes are possible. Hence, it is only in the latter region, where  $\text{Re} < \mathcal{R}_3(A) < 1$ , that a viscous jet can occur.

The parameter regions projection onto the  $(A, \text{Dr})$ -plane is depicted in Figure 3.18; and what follows holds for all  $\text{Re}$ . We observe that for  $\{A > A^*, \text{Dr} < 1\}$  only an inertial jet is possible, while inertial or viscous-inertial flow is possible for  $\{A > A^*, \text{Dr} < 1\}$ . In the region  $\{A > A^*, \text{Dr} > \mathcal{D}(A)\}$  viscous or viscous-inertial flow is possible, while in the rest of region  $\{\text{Dr} > 1\}$  all three flow regimes are possible. Hence, a viscous jet can only occur if  $1 < \text{Dr} < \mathcal{D}(A) (= \infty, \text{ for } A < A^*)$ .

Next, we study the evolution of the jet if one of the dimensional parameters varies as to change the flow type from viscous to viscous-inertial. For a reference configuration we take the dimensional parameters  $L = 1 \text{ cm}$ ,  $\nu = 0.047 \text{ m}^2/\text{s}$ ,  $v_{\text{belt}} = 1.4 \text{ m/s}$ , and  $v_{\text{nozzle}} = 1 \text{ m/s}$ , for which the jet is viscous. If we increase  $L$ , decrease  $\nu$ , decrease  $v_{\text{belt}}$ ,

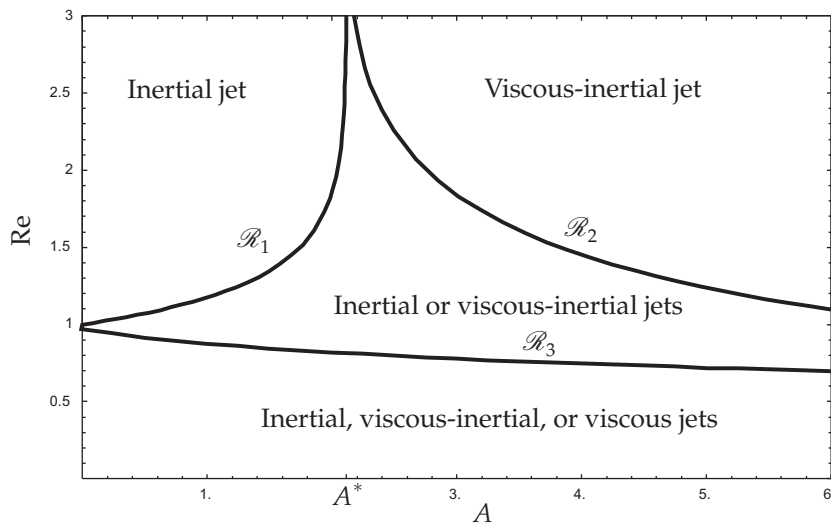


**Figure 3.17:** Regions of  $A$  and  $Re$  for which, for all  $Dr$ , different flow regimes exist. In the region  $\{A < A^*, Re > \mathcal{R}_1(A)\}$ , only inertial jets are possible, in  $\{A > A^*, Re > \mathcal{R}_2(A)\}$  only viscous-inertial jets, while in  $\{A > 0, Re < \mathcal{R}_3(A)\}$  all flow regimes are possible. In the remaining region between  $\mathcal{R}_1$ ,  $\mathcal{R}_2$  and  $\mathcal{R}_3$  inertial and viscous-inertial jets, but no viscous jets, are possible.

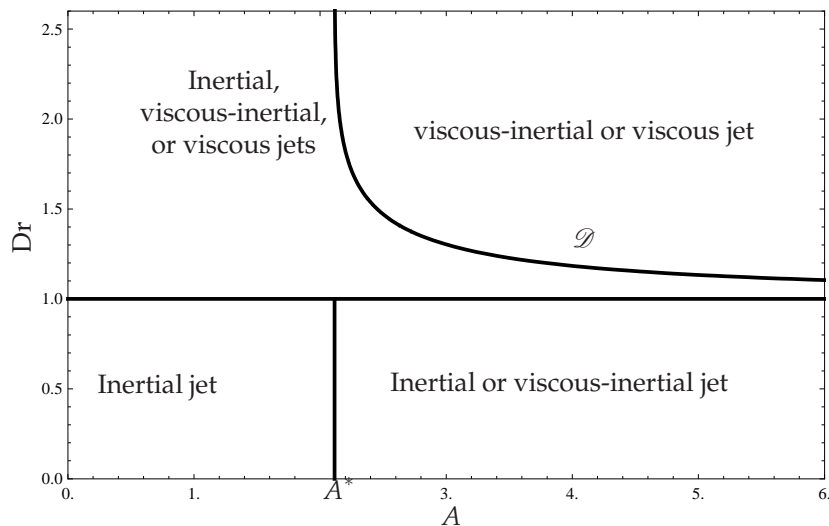


**Figure 3.18:** Regions of  $A$  and  $Dr$  for which, for all  $Re$ , different flow regimes exist. In the region  $\{A < A^*, Dr < 1\}$  only inertial jets are possible, in  $\{A > A^*, Dr < 1\}$  inertial and viscous-inertial jets (no viscous jets), and in  $\{A > A^*, Dr > \mathcal{D}(A)\}$  viscous and viscous-inertial jets (no inertial jets). In the remaining region between  $Dr = 1$  and  $\mathcal{D}$ , all flow regimes are possible.

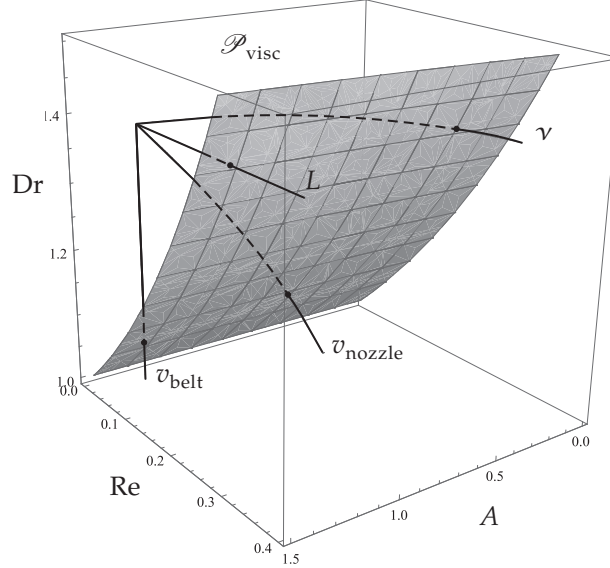


**Figure 3.19:** Traces of the point  $(A, Re, Dr)$  as we change one of the dimensional parameters ( $L$  increases,  $\nu$  decreases,  $v_{\text{belt}}$  decreases,  $v_{\text{nozzle}}$  increases). The curves originate at the same point in the region  $\mathcal{P}_{\text{visc}}$  and eventually leave  $\mathcal{P}_{\text{visc}}$ , entering  $\mathcal{P}_{\text{v-i}}$ , by crossing the separating gray surface at the points indicated by the dots.

or increase  $v_{\text{nozzle}}$ , eventually the jet flow changes from viscous to viscous-inertial. The corresponding curves in the parameter space  $\mathcal{P}$  are indicated in Figure 3.19.

Changes of the jet shape while only one of the dimensional parameters  $L$ ,  $\nu$ ,  $v_{\text{belt}}$  or  $v_{\text{nozzle}}$  varies as described above are shown in Figures 3.20(a), 3.20(b), 3.20(c), and 3.20(d), respectively. In Figures 3.19 and 3.20 we see that if the point  $(A, Re, Dr)$  approaches the boundary of  $\mathcal{P}_{\text{visc}}$ , the jet shape becomes vertical. If  $(A, Re, Dr)$  is very close to the boundary of  $\mathcal{P}_{\text{visc}}$  the jet shape is almost vertical, except for the small region near the belt where the jet rapidly bends to the horizontal belt direction.

The analysis of the parameter region for the inertial jet is more complex than that for the viscous jet. In case  $\{A > A^*, Dr < 1\}$  (“Inertial jet” in Figure 3.18), the flow is inertial for all  $L$ . Similar, if  $\{A < A^*, Re > \mathcal{R}_1(A)\}$  (“Inertial jet” in Figure 3.17), the flow is inertial for all  $v_{\text{belt}}$ . In a situation when  $\nu$  decreases or  $v_{\text{nozzle}}$  increases,  $A$  approaches zero and  $Re$  approaches infinity, since  $A = 3g\nu/v_{\text{nozzle}}^3$  and  $Re = v_{\text{nozzle}}L/(3\nu)$ . Thus, eventually the point  $(A, Re)$  enters the “Inertial jet” region in Figure 3.17. Hence, if the jet is not in the inertial flow regime, decreasing  $\nu$  or increasing  $v_{\text{nozzle}}$  makes the jet to become inertial eventually.

To illustrate the change of flow from inertial to viscous-inertial, while only one of the parameters  $L$ ,  $\nu$ ,  $v_{\text{belt}}$  and  $v_{\text{nozzle}}$  varies, we take the reference values  $L = 30$  cm,  $\nu = 0.2$  m<sup>2</sup>/s,  $v_{\text{belt}} = 2$  m/s, and  $v_{\text{nozzle}} = 1.5$  m/s. If we decrease  $L$ , increase  $\nu$ , increase  $v_{\text{belt}}$  or decrease  $v_{\text{nozzle}}$  eventually the jet flow changes from inertial to viscous-inertial. The curves in the parameter space  $\mathcal{P}$  are indicated in Figure 3.21.

Changes of the jet shape for  $\alpha_{\text{nozzle}} = -\pi/4$ , while only one of the dimensional parameters  $L$ ,  $\nu$ ,  $v_{\text{belt}}$  or  $v_{\text{nozzle}}$  varies as described above are shown in Figures 3.22(a),

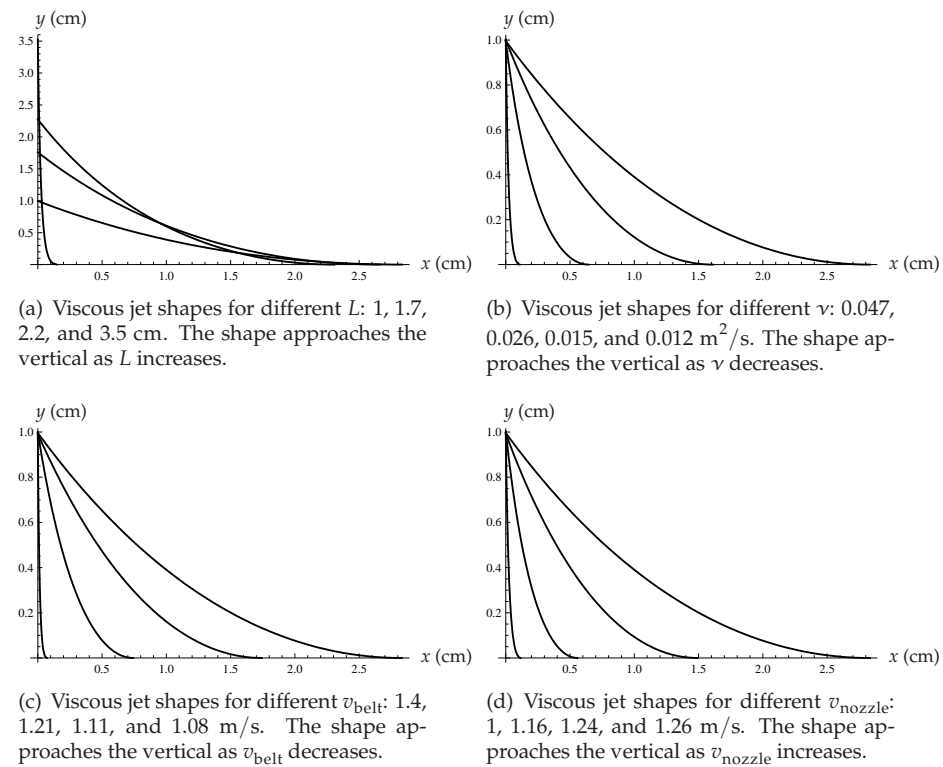


**Figure 3.20:** Shapes of the viscous jet for different values of  $L$ ,  $\nu$ ,  $v_{\text{belt}}$  and  $v_{\text{nozzle}}$ . The reference values are  $L = 1 \text{ cm}$ ,  $\nu = 0.047 \text{ m}^2/\text{s}$ ,  $v_{\text{belt}} = 1.4 \text{ m}/\text{s}$ , and  $v_{\text{nozzle}} = 1 \text{ m}/\text{s}$ .

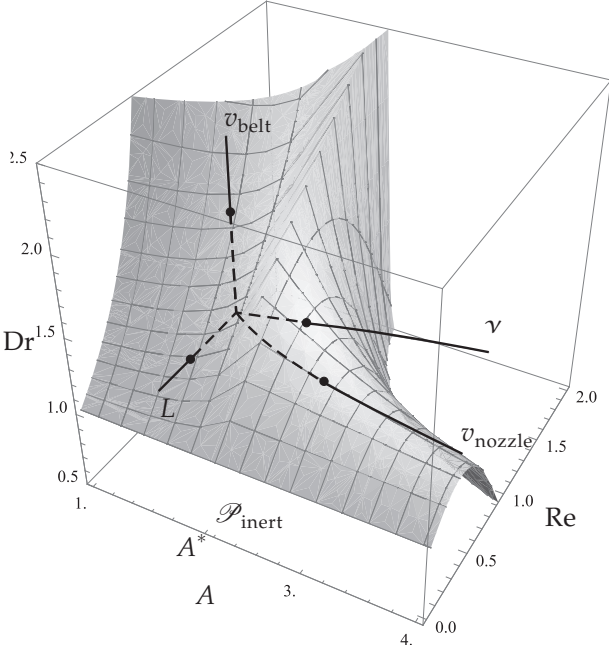
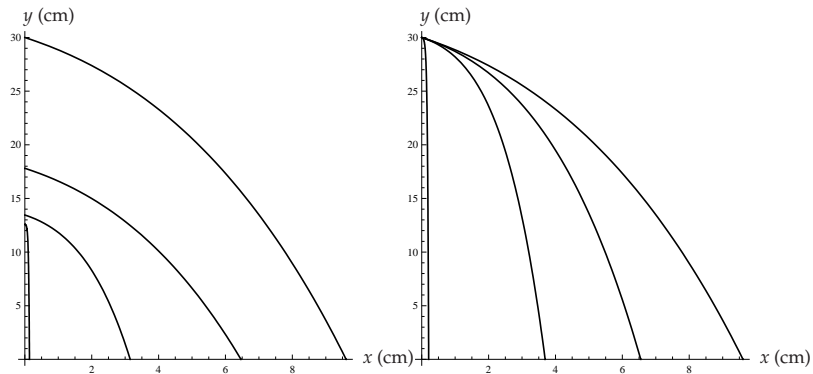
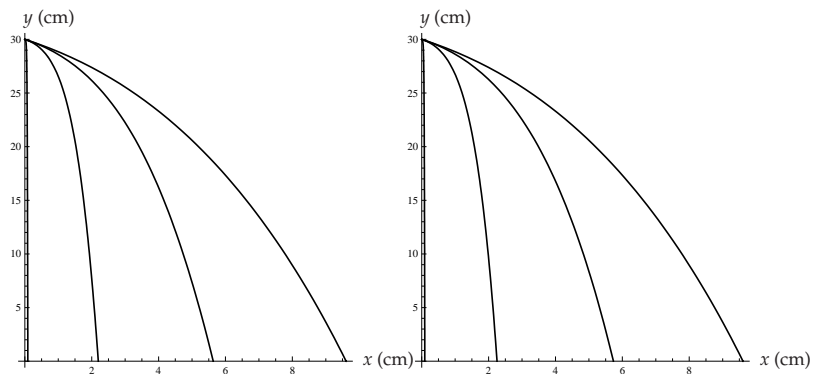


**Figure 3.21:** Curves in the parameter space  $\mathcal{P}$  as we change one of the parameters ( $L$  decreases,  $\nu$  increases,  $v_{\text{belt}}$  increases,  $v_{\text{nozzle}}$  decreases). The curves originates at the same point in the region  $\mathcal{P}_{\text{inert}}$  and eventually leave  $\mathcal{P}_{\text{inert}}$  by crossing the separating surface at the points indicated by the dots.



(a) Inertial jet shapes for different  $L$ : 30, 18, 13, and 12 cm. The shape approaches the vertical as  $L$  decreases.

(b) Inertial jet shapes for different  $\nu$ : 0.2, 0.26, 0.3, and 0.32  $\text{m}^2/\text{s}$ . The shape approaches the vertical as  $\nu$  increases.



(c) Inertial jet shapes for different  $v_{\text{belt}}$ : 2, 2.57, 2.86, and 2.95 m/s. The shape approaches the vertical as  $v_{\text{belt}}$  increases.

(d) Inertial jet shapes for different  $v_{\text{nozzle}}$ : 1.5, 1.4, 1.36, and 1.34 m/s. The shape approaches the vertical as  $v_{\text{nozzle}}$  decreases.

**Figure 3.22:** Shapes of the inertial jet for different values of  $L$ ,  $\nu$ ,  $v_{\text{belt}}$ ,  $v_{\text{nozzle}}$ . The reference values are  $L = 30$  cm,  $\nu = 0.2$   $\text{m}^2/\text{s}$ ,  $v_{\text{belt}} = 2$  m/s, and  $v_{\text{nozzle}} = 1.5$  m/s. The nozzle orientation is  $\alpha_{\text{nozzle}} = -\pi/4$ .



3.22(b), 3.22(c), and 3.22(d), respectively. In Figures 3.21 and 3.22 we see that if the point  $(A, Re, Dr)$  approaches the boundary of  $\mathcal{P}_{\text{inert}}$ , the jet shape becomes more vertical. If  $(A, Re, Dr)$  is very close to the boundary of  $\mathcal{P}_{\text{inert}}$  the jet shape is almost vertical except for the small region near the belt where the jet rapidly bends from the nozzle direction to an almost vertical one.

The analysis above shows that the transition between the viscous and the inertial flow regimes as parameters continuously vary is only possible via the viscous-inertial flow.

### 3.9 Conclusions

In this chapter we investigate uniqueness and existence of a solution to the steady jet model from Section 1.5 in drag spinning; see Section 1.3. We simplify the model equations (3.1)-(3.3) by solving them partly analytically to reduce them to one first-order ODE for  $v(\tau)$ , containing two unknown parameters (3.49)-(3.52). This system is reformulated as an algebraic equation, (3.54), which is equivalent to the original model equations (3.1)-(3.3).

For this situation we distinguish three flow regimes, which are characterized by the dominant term in the momentum transfer through the jet cross-section,  $\xi$ , i.e. viscous, viscous-inertial, and inertial regimes having convex, vertical, and concave jet shape, respectively. The model is described by three dimensionless parameters, which are partitioned between the three flow regimes.

For all three flow regimes we prove existence and investigate uniqueness. A jet solution is unique for the viscous and viscous-inertial jets. The solutions for the inertial jet, with  $\alpha_{\text{nozzle}} \neq -\pi/2$ , might not be unique. For some settings of parameters, up to two inertial jet solutions exist together with one viscous-inertial or viscous jet solution. In this case the region of the inertial jet regime depends on the nozzle orientation, and overlaps with the viscous-inertial and, possibly, the viscous jet regime.

If the nozzle points upwards, inertial jet solutions exist, even for the belt placed above the nozzle.



## Chapter 4

# Experiments of drag spinning and comparison with theory

In this chapter we describe our experiments of the fall of a thin jet of a Newtonian fluid onto a moving belt and compare their results with the theoretical results obtained in Chapter 3. Our purpose is to compare experimentally observed jet shape between the nozzle and the belt with the theoretical results according to our model studied in Chapter 3. This comparison with theory is done in Section 4.3. The experiments are meant to confirm our theoretical result, but this experimental observation of the jet in drag spinning does not aim at a perfect match with the model. We rather hope and expect to see similar changes in jet behaviour if the process parameters are varied as the model predicts i.e. qualitative agreement. To reach this goal we study dependencies between the belt velocity and the position of the touchdown point of the jet with the belt and the shape properties, which characterize the jet flow regimes in drag spinning (e.g. convexity of the major part of the jet shape).

Because of our goal above, which is also dictated by the restricted experimental possibilities we had, we do not repeat our experiments and do not measure errors. Moreover, we do not focus on local effects at the nozzle and at the belt. The local effects at the belt are reported in the papers about a ‘fluid-mechanical sewing machine’ [13,90].

We compare the relations between the position of the touchdown point and the belt velocity obtained experimentally and theoretically, and we notice that they show qualitative agreement. Comparisons of the shapes obtained experimentally and theoretically highlight quantitative differences.

This chapter is organized as follow: first we describe the experimental setup, then we analyze the results, compare them with the theoretical ones, and finally we draw some conclusions.

## 4.1 Experimental setup and parameter choice

### 4.1.1 Experimental setup

A viscous fluid, polybutene Indopol H-100, is pumped through a nozzle and allowed to fall from the nozzle onto a moving belt; see Figure 4.1. The belt is wrapped around two parallel horizontal cylinders at the same height. The left cylinder is connected to an electric motor, to move the horizontal belt from the left to the right with a constant speed.

Parameter name		Value	Unit
belt velocity	$v_{\text{belt}}$	0 – 5	m/s
flow velocity at nozzle	$v_{\text{nozzle}}$	0.4 – 1.2	m/s
distance between belt and nozzle	$L$	0.01 – 0.07	m
nozzle orientation	$\alpha_{\text{nozzle}}$	$-38 - 17.2^\circ$	
kinematic viscosity of fluid	$\nu$	0.047	$\text{m}^2/\text{s}$
fluid density	$\rho$	880	$\text{kg}/\text{m}^3$
nozzle diameter	$d_{\text{nozzle}}$	1 or 0.4	mm

**Table 4.1:** Values of the experimental parameters

The nozzle is placed above the belt. The distance  $L$  between the nozzle and the belt and the nozzle orientation  $\alpha_{\text{nozzle}}$ <sup>1</sup> can be varied. A screw pump producing a constant flow rate is connected to the nozzle. The flow rate was measured by weighing the fluid collected from the nozzle during 30 s. In the experiments, two different nozzles were used, with diameters of 1 mm and 0.4 mm.

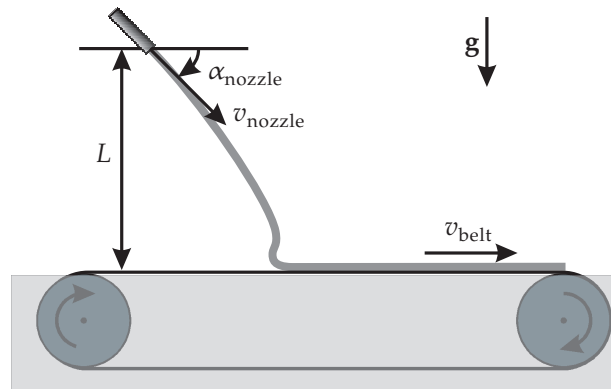


**Figure 4.1:** Scheme of the experimental setup for a jet falling onto a moving belt.

The experimental setup allows changing nozzle position and orientation, belt velocity, and flow velocity from the nozzle. For all experiments the same fluid is used. The

<sup>1</sup>The angle between the nozzle orientation and the horizontal direction, negative for downwards-pointing nozzle.

values of the experimental parameters are given in Table 4.1.

#### 4.1.2 Parameter choice

In the next section we describe the experimental results, which are used for comparison with those of our theoretical model in Section 4.3. To obtain a good agreement, we have to minimize the influences of the effects which are not incorporated in our model. In this respect we motivate our parameter choice below.

In our jet model (see Section 1.5) we incorporate the effects of longitudinal viscosity, inertia, and gravity, but we neglect surface tension, viscous bending and shear, and air drag. We try to use parameter values so that influences of the effects, not included in our model, are minimized. Analysis of a model with surface tension in [13, Section 4] shows that surface tension has less influence when the jet is thick and flow velocity in the jet is large. From a model with viscous shear and bending [90] we conclude that these effects are more manifest for thicker jets. During our experiments we have observed that for a nozzle diameter of 0.4 mm the jet is more vulnerable to external air flow than for a nozzle diameter of 1 mm.

Apart from all that, to get a concave jet shape for  $v_{\text{belt}}$  close to zero, we need large flow velocity at the nozzle, which keeps the effect of surface tension small. Our choice is to use the thinner nozzle with 0.4 mm in diameter for most of our experiments. A reason supporting our preference of the thinner nozzle is that in this case the boundary effects due to viscous bending and shear are smaller, and the jet shape more clearly exhibits convexity of its main part which is very essential for our flow characterization. However, this introduces larger air drag causing more discrepancy with the model.

In total we have performed 88 experiments where a steady jet was observed, and 2 experiments in which an unsteady jet was observed. We mainly focus on the description of the steady jet; see Appendix C for the parameter values and the experimental pictures. The 88 experiments with steady jets are divided into 10 sets. In each set the parameters  $v_{\text{nozzle}}$ ,  $d_{\text{nozzle}}$ ,  $\alpha_{\text{nozzle}}$ , and  $L$  are fixed; see Table 4.2. The belt velocity  $v_{\text{belt}}$  is allowed to vary within a set; see Appendix C for the values of  $v_{\text{belt}}$  in the experiments. The unsteady jets are shortly discussed in Section 4.2.4

Set N.	$v_{\text{nozzle}}$ m/s	$d_{\text{nozzle}}$ mm	$\alpha_{\text{nozzle}}$	$L$ cm
1	1.148	0.4	-5	6.8
2	1.147	0.4	-5	4.1
3	0.934	0.4	+9	3
4	0.934	0.4	-29.7	3.6
5	0.934	0.4	-2.6	6.1
6	0.934	0.4	-2.6	1.6
7	0.723	0.4	-38	3.4
8	0.723	0.4	-38	5.2
9	0.482	0.4	-38	5.2
10	1.061	1	-37.3	5.4

**Table 4.2:** Parameter values for the sets of the experiments with the steady jet.

## 4.2 Results

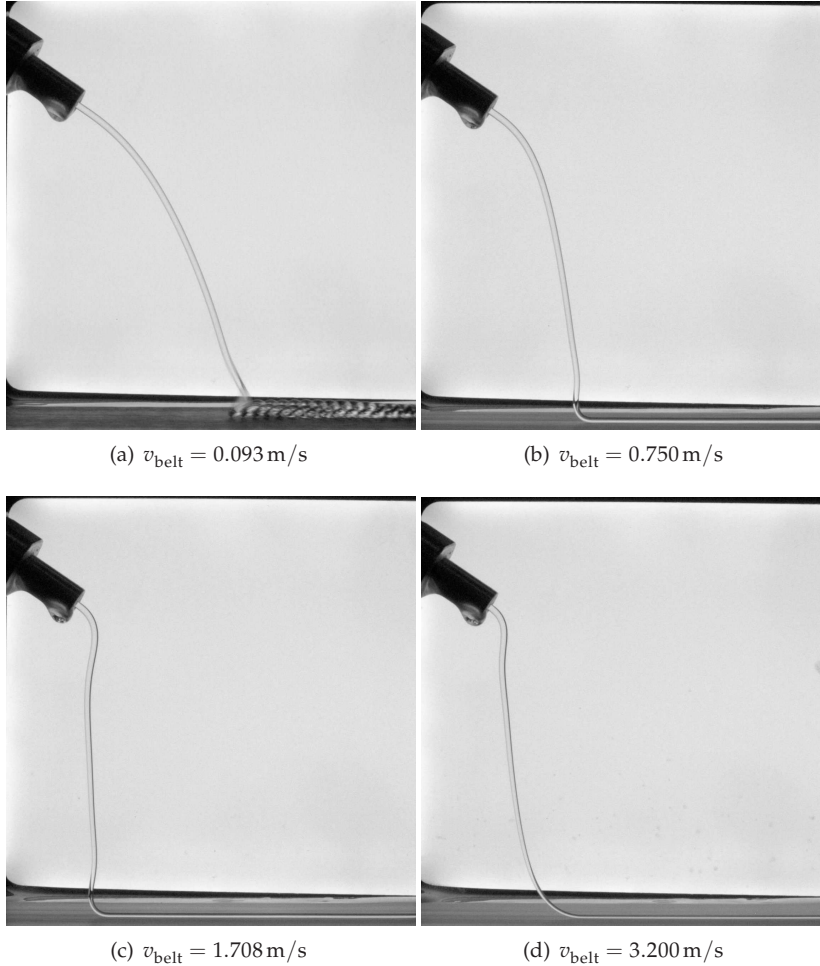


**Figure 4.2:** Jet shapes for a set of experiments for varying  $v_{\text{belt}}$  with  $d_{\text{nozzle}} = 1 \text{ mm}$ ,  $v_{\text{nozzle}} = 1.061 \text{ m/s}$ ,  $L = 0.054 \text{ m}$  and  $\alpha_{\text{nozzle}} = -37.3^\circ$ . The belt moves from the left to the right. The jet shape changes from concave (Figures 4.2(a) and 4.2(b)) to vertical (Figure 4.2(c)), and from vertical to convex (Figure 4.2(d)), while  $v_{\text{belt}}$  is increased.

### 4.2.1 Jet shape

We start with the description of a typical sequence of experiments. We take  $v_{\text{belt}}$  close to zero and choose  $L$  and  $v_{\text{nozzle}}$  so that the shape of the jet is concave, resembling a ballistic trajectory; see Figure 4.2(a). To obtain the concave jet shape the nozzle should not point down vertically, and therefore we take  $\alpha_{\text{nozzle}} > -\pi/2$ . Next, we gradually increase  $v_{\text{belt}}$  and analyze the evolution of the jet shape. For small  $v_{\text{belt}}$  the jet shape is

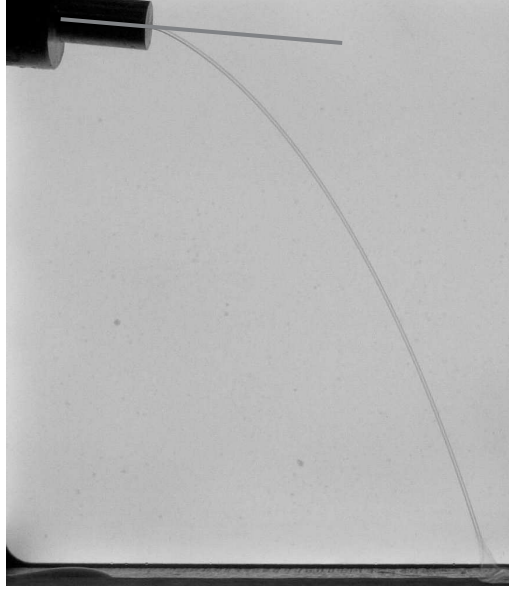


**Figure 4.3:** Experiment with  $d_{\text{nozzle}} = 0.4$  mm,  $v_{\text{nozzle}} = 1.188$  m/s,  $v_{\text{belt}} = 0.1$  m/s,  $L = 0.068$  m and  $\alpha_{\text{nozzle}} = -5^\circ$ . The jet has a concave shape, which is not aligned with the nozzle orientation.

concave with an unsteady region near the belt; see Figure 4.2(a). By increasing  $v_{\text{belt}}$ , we observe that the unsteady region near the belt transforms into a steady bending region<sup>2</sup>, where the jet bends to the horizontal belt direction; see Figure 4.2(b). The jet shape in this region resembles the backward-pointing heel, reported for the vertically falling jet in [13].

Upon increasing  $v_{\text{belt}}$ , the jet shape becomes more vertical. In this case, the contact point with the belt approaches the vertical projection of the nozzle position. As a result, for  $v_{\text{belt}}$  large enough, the main part of the jet between the belt and the nozzle is purely vertical; see Figure 4.2(c). The bending region near the belt remains, and a new bending region near the nozzle appears, where the jet bends from the nozzle orientation to the vertical direction.

Still further increase in  $v_{\text{belt}}$  results in the disappearing of the bending region near the belt. The jet shape becomes convex everywhere, except for a bending region near the nozzle, in which the jet steeply changes from the nozzle direction to a more vertical one; see Figure 4.2(d). Close to the belt, the direction of the jet becomes smoothly tangent to the belt (no bending region). The touchdown point moves away from the nozzle in the direction of motion of the belt as  $v_{\text{belt}}$  increases.

Summarizing, we observe a concave jet shape for small  $v_{\text{belt}}$ , except for a small bending or unsteady region near the belt. With increasing  $v_{\text{belt}}$  the jet shape becomes vertical, except for small bending regions near the nozzle and the belt. Further increase of  $v_{\text{belt}}$  leads to a convex jet shape, except for a small bending region near the nozzle. This

<sup>2</sup>By the term “bending region” we refer to a small steady part of the jet at the nozzle or at the belt in which the jet sharply changes its orientation.

gives a characterization of the jet flow by its shape, i.e. concave, vertical and convex. The characterization based of the jet shape is convenient in drag spinning; while as we shall see in Chapter 5 a flow characterization based on the jet shape is not possible in rotary spinning. Therefore, we mostly stick to the flow characterization based on the sign of the momentum flux through the jet cross-section  $\xi$ , introduced in Chapter 2. In Chapter 3 we showed that the concave shape corresponds to the inertial jet, the vertical shape to the viscous-inertial jet, and the convex shape to the viscous jet.

For the concave jet in Figures 4.2(a) and 4.2(b), where the nozzle diameter is 1 mm, the jet near the nozzle is aligned with the nozzle orientation. When the nozzle diameter is 0.4 mm, the jet is not aligned with the nozzle orientation. This can be seen in Figure 4.3, where the jet near the nozzle points more downwards than the nozzle.

## 4.2.2 Touchdown point

A convenient measurement to characterize the jet behaviour is the horizontal position  $x_{\text{end}}$  of the touchdown point with the belt, relative to the nozzle position. For each of the 10 sets, into which the experiments are divided, the values of the fixed parameters are given in Table 4.2. The values of  $x_{\text{end}}$  for different  $v_{\text{belt}}$  for each set are presented in Figures 4.4 and 4.5. Below, we describe a typical relation between  $s_{\text{end}}$  and  $v_{\text{belt}}$  on an example of Set 2.

A typical behaviour of the jet while  $v_{\text{belt}}$  increases is the following one. For the concave jet with  $v_{\text{belt}}$  close to zero the contact point is away from the nozzle in the direction of the pointing nozzle. With increasing  $v_{\text{belt}}$ , the touchdown point moves first towards the nozzle position ( $x_{\text{end}}$  decreases) until the jet becomes vertical ( $x_{\text{end}} = 0$ ), stays vertical over some range of values for  $v_{\text{belt}}$ , and then moves away from the nozzle position in the direction of motion of the belt ( $x_{\text{end}}$  increases). In Figure 4.4(b), and from the experimental pictures in Appendix C, we see that in Set 2 the first five dots are in the inertial (concave) flow regime, the sixth and seventh<sup>3</sup> with  $x_{\text{end}}$  close to 0, represent the viscous-inertial (vertical) flow, and the remaining ones (8th and higher) are in the viscous (convex) flow regime.

This type of non-monotonic behaviour of  $x_{\text{end}}$  as  $v_{\text{belt}}$  increases we expect to see also from the results of our model, which will be confirmed by the comparison to be present in Section 4.3. The minimum, close to zero, values of  $x_{\text{end}}$  occurring for the viscous-inertial (vertical) jet are of especial interest for us, because they indicate transitions between the flow regimes. In Figures 4.4 and 4.5, we see that transitions between the flow regimes while  $v_{\text{belt}}$  changes continuously is only possible between the inertial and viscous-inertial regimes.

## 4.2.3 Influences of $v_{\text{nozzle}}$ and $L$

A detailed experimental investigation of the influence of  $L$ ,  $v_{\text{nozzle}}$ ,  $d_{\text{nozzle}}$ , and  $\alpha_{\text{nozzle}}$  on the jet beyond the scope of this work. However, we like to describe some trends in the influence of  $v_{\text{nozzle}}$  and  $L$  that could be observed from the  $x_{\text{end}}$  versus  $v_{\text{belt}}$  mea-

<sup>3</sup>To distinguish a viscous-inertial flow regime we use existence of clearly exhibited bending regions at the belt and at the nozzle with the straight vertical jet part connecting them; see experimental pictures in Appendix C. It may happen that the sizes of these regions are not the same, which causes  $x_{\text{end}}$  be a bit away from zero.



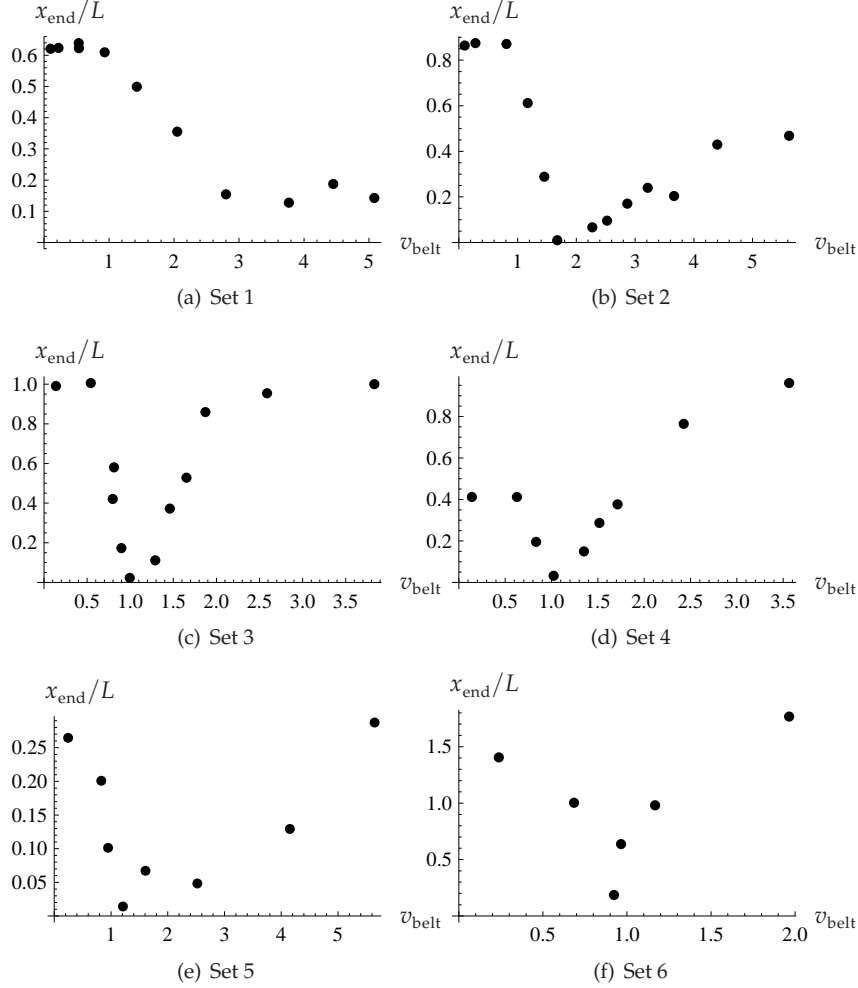


**Figure 4.4:**  $x_{\text{end}}/L$  for different  $v_{\text{belt}}$  in Sets 1-6

measurements of the experiment with  $d_{\text{nozzle}} = 0.4$  mm in Sets 1-9. In Set 10 we have  $d_{\text{nozzle}} = 1$  mm and it is used for comparison with the theory in Section 4.3. We use a quantity  $x_{\text{end}}/L$  instead of  $x_{\text{end}}$  to characterize the jet because it is more representative in describing how close the jet shape is to the vertical one. As follows from the jet shape simulations in Section 3.8 the closer the jet shape is to the vertical one the nearer the parameters are to the border of the viscous-inertial regime.

In our experiments we have used 4 values of  $v_{\text{nozzle}}$ <sup>4</sup>. Independently of  $L$  and  $\alpha_{\text{nozzle}}$  for Sets 1-6, with larger  $v_{\text{nozzle}}$ , the values of  $x_{\text{end}}/L$  for the inertial jet are less than in Sets 1 and 2, or of the same order, as those for the viscous jet. For Sets 7-9 with smaller  $v_{\text{belt}}$  shown in Figure 4.5, the values of  $x_{\text{end}}/L$  are much closer to zero for the inertial jet than

<sup>4</sup> $v_{\text{nozzle}} = 1.148$  m/s in Sets 1-2,  $v_{\text{nozzle}} = 0.934$  m/s in Sets 3-6,  $v_{\text{nozzle}} = 0.723$  m/s in Sets 7-8, and  $v_{\text{nozzle}} = 0.482$  m/s in Set 9

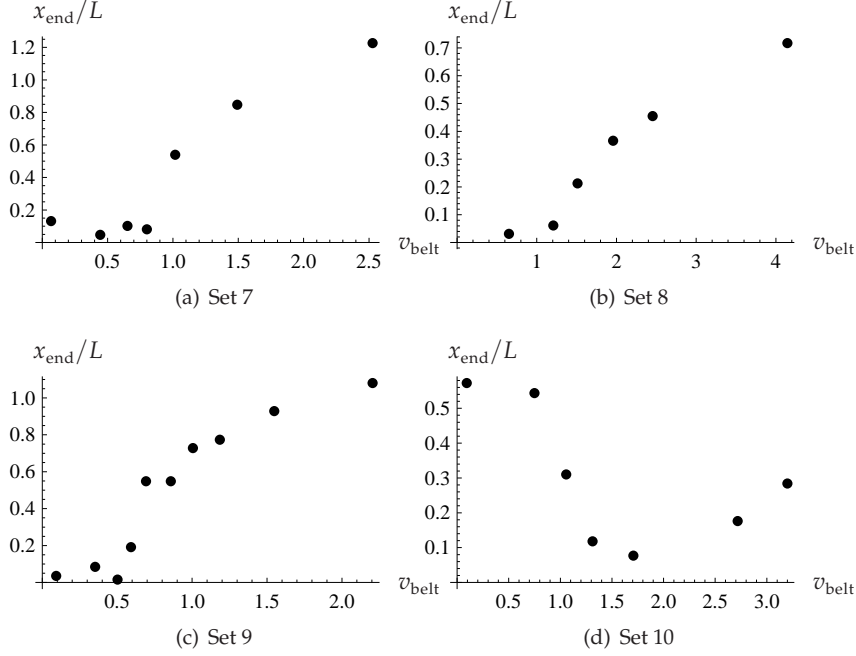


Figure 4.5:  $x_{\text{end}}/L$  for different  $v_{\text{belt}}$  in Sets 7-10

those for the viscous jet. In Sets 8-9 we have changed only  $v_{\text{nozzle}}$  and we observe that  $x_{\text{end}}/L$  in the viscous regime is larger for the smaller  $v_{\text{nozzle}}$ ; see Figures 4.5(b) and 4.5(c).

The influence of  $L$  can be observed in Sets 1-2, Sets 5-6, and Sets 7-8, where two values of  $L$  were used for the same  $v_{\text{nozzle}}$ . An observation shows that  $x_{\text{end}}/L$  increases as  $L$  decreases, so the jet is closer to the vertical one for larger  $L$  (see Figures 4.4(a) and 4.4(b), Figures 4.4(e) and 4.4(f), and Figures 4.5(a) and 4.5(b)).

The above observation of the influences of  $v_{\text{nozzle}}$  and  $L$  on the jet shape agree with some theoretical results of Section 3.8.

- The viscous jet shape approaches to the vertical one if  $v_{\text{nozzle}}$  decreases; see Figure 3.20(d) for experimental results.
- The viscous jet shape approaches to the vertical one if  $L$  increases; see Figure 3.20(a) for experimental results.
- The inertial jet shape approaches to the vertical one if  $v_{\text{nozzle}}$  decreases; see Figure 3.22(d) for experimental results.

#### 4.2.4 Unsteady jet for upwards pointing nozzle

In the experiments with  $d_{\text{nozzle}} = 1$  mm and the nozzle pointing upwards with  $\alpha_{\text{nozzle}} = 17.2$ , we observed unsteady jets. We did two experiments with different belt velocities keeping the other parameters the same. During these experiments, we recorded videos

Exp N.	$v_{\text{nozzle}}$ m/s	$v_{\text{belt}}$ m/s	$d_{\text{nozzle}}$ mm	$\alpha_{\text{nozzle}}$	$L$ cm
89	1.061	1.227	1	17.2	4.4
90	1.061	1.345	1	17.2	4.4

**Table 4.3:** Parameter values for the experiments with the unsteady jet.

of the unsteady jets. The jet shape was always concave, though sometimes approaching the vertical. We analyzed the videos by splitting them into frames. We detected the position of the touchdown points by comparing the pixels values and applying a threshold. Thus, we obtained the evolution of  $x_{\text{end}}$  in time; see Figure 4.6(a) and 4.7(a).

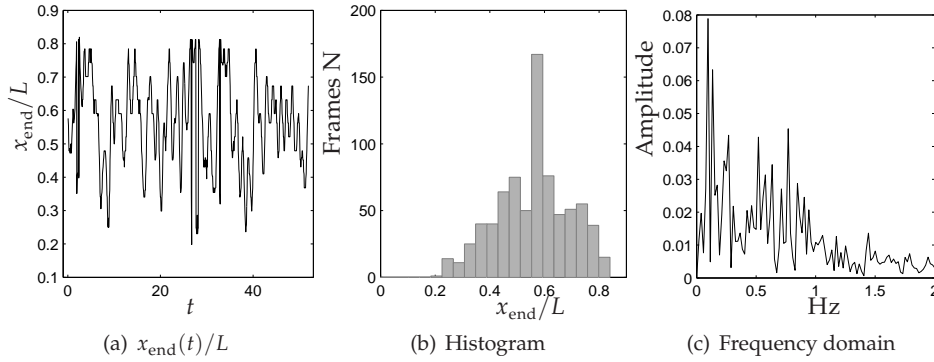


**Figure 4.6:** Unsteady jet in the experiment 89.

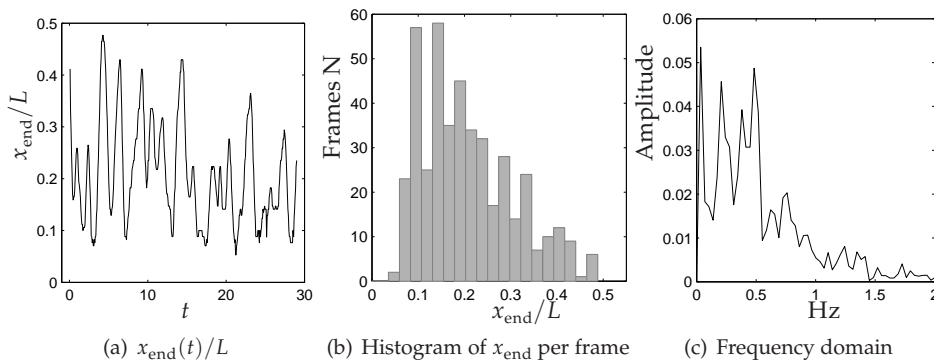


**Figure 4.7:** Unsteady jet in the experiment 90.

In Figures 4.6(a) and 4.7(a) we see that the evolution of  $x_{\text{end}}$  appears to have no periodicity. In the frequency domain we see no clear peaks and the evolution of  $x_{\text{end}}$  mostly consists of the frequencies lower than 1 Hz; see Figures 4.6(c) and 4.7(c). To

obtain a frequency domain we use the input signal

$$\frac{x_{\text{end}}(t)}{L} - \frac{1}{LT} \int_0^T x_{\text{end}}(t) dt,$$

where  $T$  is the length of the signal. Figures 4.6(b) and 4.7(b) show histograms in which we plot the number of frames versus  $x_{\text{end}}/L$ . We see that for the smaller  $v_{\text{belt}}$  in the experiment 89, the values of  $x_{\text{end}}/L$  are between 0.2 to 0.8, with the maximum peak at 0.6. For the larger  $v_{\text{belt}}$  in experiment 90, the values of  $x_{\text{end}}/L$  are between 0.05 to 0.46, with the maximum peak at 0.15. Therefore, for smaller  $v_{\text{belt}}$  the value of  $x_{\text{end}}$  is mostly larger. This is in agreement with the observations for the steady jet in the inertial regime described in Subsection 4.2.2, where we observe the larger values for  $x_{\text{end}}$  for smaller  $v_{\text{belt}}$ . Further investigation of the unsteady jet is beyond the scope of this study.

### 4.3 Comparison between model and experiments

In this section we validate our model using the results of the experiments described in the preceding section. We do this by comparing the corresponding relations between  $x_{\text{end}}$  and  $v_{\text{belt}}$  and the jet shapes from experiments and model. Finally, we discuss differences and similarities for the jets in viscous and inertial flow regimes.

#### 4.3.1 Comparison of touchdown point

Comparison of the relations between  $x_{\text{end}}$  and  $v_{\text{belt}}$  obtained from the experiments and from the theory for Sets 1-10 are depicted in Figures 4.8 and 4.9. In these figures the solid curves  $\mathcal{C}(x_{\text{end}}, v_{\text{belt}})$  represent the relation between  $v_{\text{belt}}$  and  $x_{\text{end}}/L$  as obtained from the model, whereas the dots represent the experimental results. The vertical lines divide the axis  $v_{\text{belt}}$  into the three flow regimes. The interval  $v_{\text{belt}}$  from zero to the first vertical line, to which we refer as  $v_1$ , stands for the inertial regime  $\mathcal{P}_{\text{inert}}$ . The interval  $v_{\text{belt}}$  between the two lines  $v_1$  and  $v_2$ , indicates the viscous-inertial regime  $\mathcal{P}_{\text{v-i}}$ . The range of  $v_{\text{belt}}$  larger than  $v_2$  indicates the viscous regime  $\mathcal{P}_{\text{visc}}$ . Hence, for small  $v_{\text{belt}}$  the flow is inertial, for increasing  $v_{\text{belt}}$  viscous-inertial, and for even larger  $v_{\text{belt}}$  viscous.

Next we describe in detail the comparison of the model predictions of the touchdown point with the ones obtained from the experiments from Set 2 in Figure 4.8(b). A curve  $\mathcal{C}(x_{\text{end}}, v_{\text{belt}})$ , describing the relation between  $x_{\text{end}}$  and  $v_{\text{belt}}$  as obtained from the model (solid curve in Figure 4.8(b)) consists of three parts:

- **Inertial jet part.** For  $v_{\text{belt}}$  close to 0,  $x_{\text{end}}$  increases as  $v_{\text{belt}}$  increases, till  $\mathcal{C}(x_{\text{end}}, v_{\text{belt}})$  reaches its maximum. For further increasing  $v_{\text{belt}}$ ,  $x_{\text{end}}$  decreases till  $\mathcal{C}(x_{\text{end}}, v_{\text{belt}})$  becomes vertical (at  $v_{\text{belt}} > v_2$ ). After this point,  $\mathcal{C}(x_{\text{end}}, v_{\text{belt}})$  bends back and  $x_{\text{end}}$  decreases to zero; during this phase  $v_{\text{belt}}$  decreases to  $v_1$ . At this point where  $x_{\text{end}}$  becomes zero, the jet becomes vertical; in the preceding part of  $\mathcal{C}(x_{\text{end}}, v_{\text{belt}})$  the jet is concave.
- **Viscous-inertial jet part.** This part of  $\mathcal{C}(x_{\text{end}}, v_{\text{belt}})$  is horizontal with  $x_{\text{end}} = 0$ , while  $v_{\text{belt}}$  increases from  $v_1$  to  $v_2$ . In this part, the flow is vertical.
- **Viscous jet part.** This part of  $\mathcal{C}(x_{\text{end}}, v_{\text{belt}})$  starts at  $x_{\text{end}} = 0$  and  $v_{\text{belt}} = v_2$ , after which both  $x_{\text{end}}$  and  $v_{\text{belt}}$  increase. In this part the jet is convex.

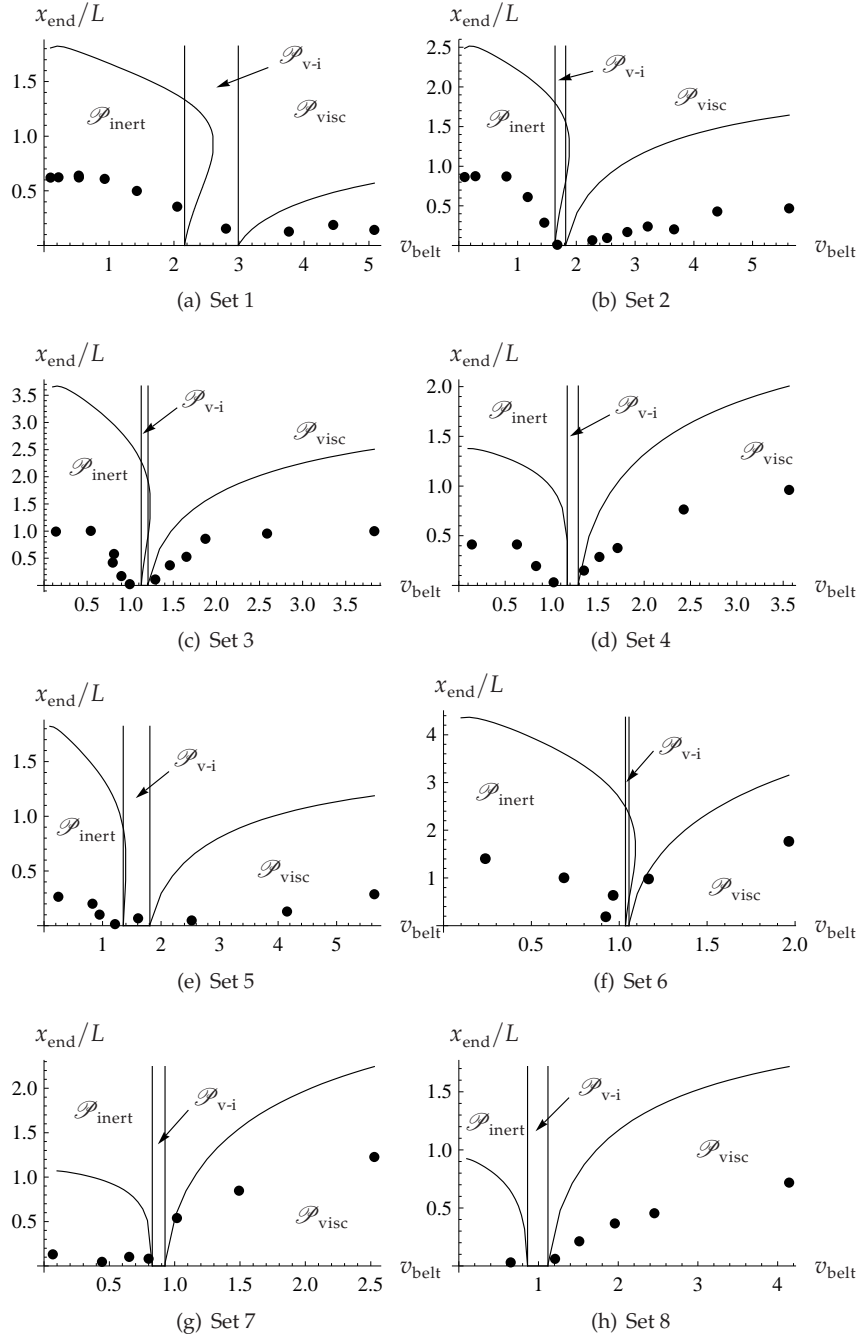


**Figure 4.8:** Comparison of the relations between  $v_{\text{belt}}$  (m/s) and  $x_{\text{end}}/L$  as obtained from the model  $\mathcal{C}(x_{\text{end}}, v_{\text{belt}})$  (solid line) and from the experiment (dots) for the sets 1-8

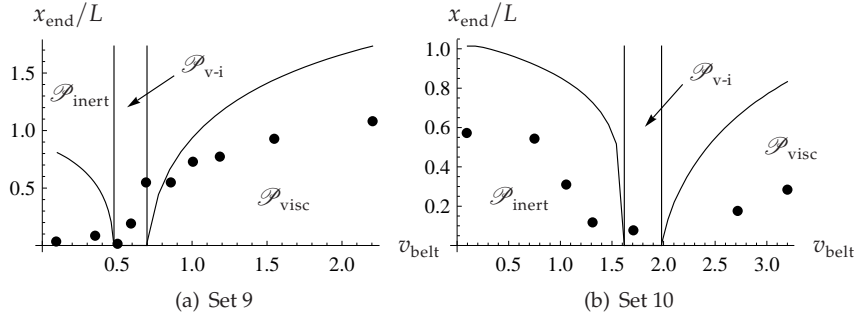


**Figure 4.9:** Comparison of the relations between  $v_{\text{belt}}$  (m/s) and  $x_{\text{end}}/L$  as obtained from the model  $\mathcal{C}(x_{\text{end}}, v_{\text{belt}})$  (solid line) and from the experiment (dots) for the sets 9-10

Looking at the inertial part of the curve  $\mathcal{C}(x_{\text{end}}, v_{\text{belt}})$  in Figure 4.8(b) within the region  $v_{\text{belt}} > v_1$ , we notice that the solution is non-unique there: two inertial and one viscous-inertial, for  $v_{\text{belt}} \leq v_2$ , or one viscous for  $v_{\text{belt}} > v_2$ , solutions exist there. This illustrates the non-uniqueness of the jet solution for  $\alpha_{\text{nozzle}} > -\pi/2$ . However, as we see in Figures 4.8 and 4.9 the curves  $\mathcal{C}(x_{\text{end}}, v_{\text{belt}})$  for Sets 4 and 7-10 do not show this non-uniqueness of the jet solution for  $\alpha_{\text{nozzle}} < -29.7^\circ$ . In the remaining sets the jet solution can be non-unique.

The experimental results have qualitatively the same tendency as the theoretical ones from our model. For  $v_{\text{belt}}$  close to zero (the first three experimental values) the small maximum, or a kind of plateau, is found too and after that the values monotonically decrease till  $x_{\text{end}}$  becomes zero. This represents the transition from the inertial to the viscous-inertial jet regime. The following observation points all lie in the viscous jet regime and they show a monotonic increase of  $x_{\text{end}}$  with  $v_{\text{belt}}$ . Hence, the behavior of the experimental data agrees, in general, with that predicted by the model. The only difference is (non-)monotonicity of the inertial part of  $\mathcal{C}(x_{\text{end}}, v_{\text{belt}})$  in the small region of  $v_{\text{belt}} > v_1$  where the model has multiple solutions; see sets 1-3 and 5-6 in Figure 4.8.

Although the theoretical and experimental results agree in a qualitative sense, quantitatively significant differences are found. The values of  $x_{\text{end}}$  predicted by the model for viscous and inertial flows are substantially larger than the values obtained experimentally. We comment on this in the next subsection.

Using Figures 4.10 and 4.11 we compare the predictions of the parameter regions in the  $(v_{\text{belt}}, L)$ -plane for flow regimes obtained from the model with those from the experiments. To determine the type of flow regime from the experimental data, we observe the behavior of  $x_{\text{end}}$  as  $v_{\text{belt}}$  increases: for the inertial flow  $x_{\text{end}}$  decreases, for the viscous-inertial flow  $x_{\text{end}}$  is close to zero, and for the viscous flow  $x_{\text{end}}$  increases. The results for two different values of  $L$  and fixed value of  $vn$  are presented in Figure 4.10, and for four different values of  $L$  and fixed value of  $vn$  in Figure 4.11. For the smaller  $L$  in Figure 4.10 and for all  $L$  in Figure 4.11 we clearly see that in the inertial regime  $x_{\text{end}}$  decreases, stays close to zero in the viscous-inertial regime, and increases in the viscous jet region as  $v_{\text{belt}}$  increases. A similar behavior of  $x_{\text{end}}$  is observed for the larger  $L$  in Figure 4.10, except that in the viscous regime the increase of  $x_{\text{end}}$  is less significant. Summarizing, we conclude that the experimental results for the parameter regions for

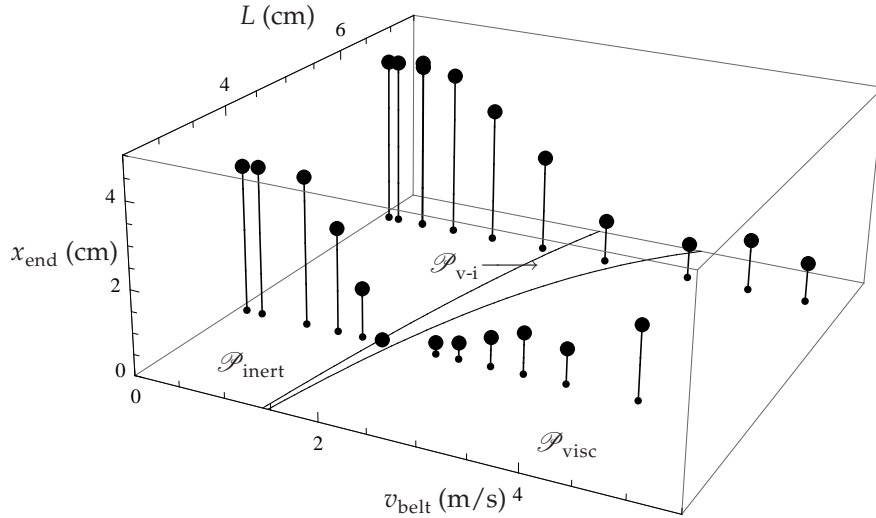


**Figure 4.10:** The regions of  $v_{\text{belt}}$  and  $L$  for the three flow regimes (solid lines; from the model) and the experimental values of  $x_{\text{end}}$  from Sets 1 and 2. Here, two values of  $L$  are used 4.1 cm and 6.8 cm. The other parameters are  $\nu = 0.047 \text{ m}^2/\text{s}$ ,  $v_{\text{nozzle}} = 1.147 \text{ m/s}$ ,  $d_{\text{nozzle}} = 0.4 \text{ mm}$ , and  $\alpha_{\text{nozzle}} = -5^\circ$ .

the three flow regimes in the  $(v_{\text{belt}}, L)$ -plane agree with the theoretical ones.

### 4.3.2 Comparison of jet shapes

Theoretically and experimentally obtained jet shapes are presented in Figures 4.12 and 4.13 for an inertial and a viscous jet, respectively. The experimental shapes are obtained from photos using an image-analysis program. For a viscous-inertial jet the only difference between the experimental and theoretical shapes is due to bending regions near the nozzle and the belt in the experiments. Therefore, we do not discuss the viscous-inertial jet here.

Using Figure 4.12, we compare the jet shapes for the inertial flow. The experimental shape bends steeper down at the nozzle than the one from the model, and is more curved. This results in a smaller  $x_{\text{end}}$  from the experiment than predicted theoretically. The bending region near the belt in the experimental jet is small in comparison to the whole jet and it does not contribute significantly to the difference in  $x_{\text{end}}$ .

The comparison of the jet shapes for the viscous flow is based on Figure 4.13. In the experimental jet shape a small bending region appears near the nozzle, where the jet bends from the nozzle orientation to some preferred orientation. This orientation is closer to the vertical than our theory predicts. The middle part of the experimental jet is almost straight, clearly less curved than the one obtained from the model. Near the belt the experimental jet bends to the horizontal more rapidly than the one from the model. The theoretical shape is curved more uniformly than the experimental one. All this results in a larger  $x_{\text{end}}$  predicted theoretically than observed experimentally.

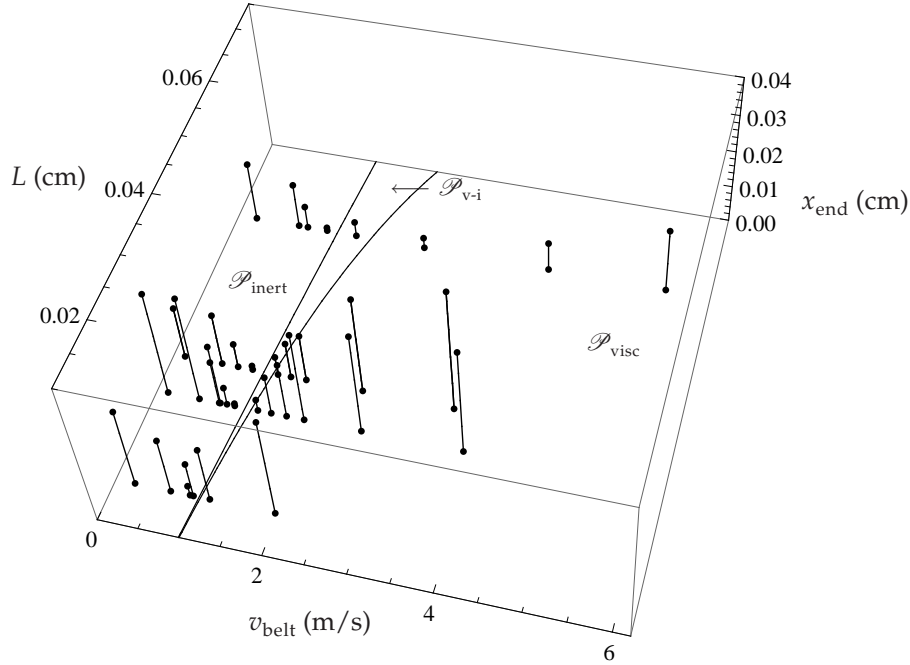


**Figure 4.11:** The regions of  $v_{\text{belt}}$  and  $L$  for the three flow regimes and the experimental values of  $x_{\text{end}}$  from Sets 3-6. Here, four values of  $L$  are used 3 cm, 3.6 cm, 6.1 cm, and 1.6 cm. The other parameters are  $\nu = 0.047 \text{ m}^2/\text{s}$ ,  $v_{\text{nozzle}} = 0.934 \text{ m/s}$ ,  $d_{\text{nozzle}} = 0.4 \text{ mm}$ , and the values of  $\alpha_{\text{nozzle}}$  vary between  $-29.7^\circ$  to  $+9^\circ$ .

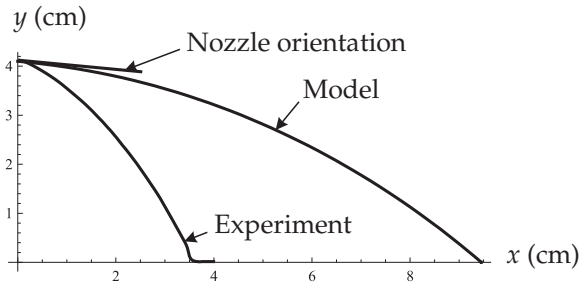


**Figure 4.12:** Comparison of the inertial jet shapes obtained theoretically and experimentally for the experiment 14 with  $L = 4.1 \text{ cm}$ ,  $\nu = 0.047 \text{ m}^2/\text{s}$ ,  $v_{\text{nozzle}} = 1.147 \text{ m/s}$ ,  $v_{\text{belt}} = 0.81 \text{ m/s}$ ,  $d_{\text{nozzle}} = 0.4 \text{ mm}$ , and  $\alpha_{\text{nozzle}} = -5^\circ$ .

### 4.3.3 Discussion about differences and similarities

From comparing the jet shapes, including  $x_{\text{end}}$ , for the two flow regimes inertial and viscous, we observe significant differences in the jet shapes obtained theoretically and experimentally. The common difference for these flow regimes is the difference in curvature of the shapes. Also differences in bending near the nozzle and the belt are found. The theoretical predictions of  $x_{\text{end}}$  are larger than the experimental ones.



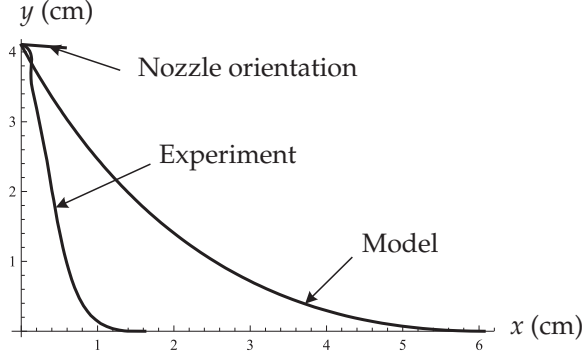


**Figure 4.13:** Comparison of the viscous jet shapes obtained theoretically and experimentally for the experiment 23 with  $L = 4.1$  cm,  $\nu = 0.047$  m<sup>2</sup>/s,  $v_{\text{nozzle}} = 1.147$  m/s,  $v_{\text{belt}} = 4.398$  m/s,  $d_{\text{nozzle}} = 0.4$  mm, and  $\alpha_{\text{nozzle}} = -5^\circ$ .

The steep bending downwards near the nozzle of the inertial jet in the experiment, and the differences in the jet orientation near the nozzle in the viscous flow play a significant role in the observed shape differences. However for the thicker jet (experiments in Set 10 with  $d_{\text{nozzle}} = 1$  mm), we do not observe a steep bending of the inertial jet near the nozzle; see Figures 4.2(a), 4.2(b) and 4.3. By analyzing the results of the comparison we found that the differences mentioned above in  $x_{\text{end}}/L$  are smaller for the thicker jet falling from a smaller height  $L$ ; see Figures 4.8 4.9, and Table 4.2.

We look for the cause of these differences in the effects which we did not include in our model, such as air drag, bending stiffness and surface tension. The jet shapes obtained from the models [13, 90] (surface tension coefficient is 0.027 N/m), which incorporate surface tension or bending stiffness, do not explain the differences; see Figures 4.14(a), 4.14(b), 4.16(a), and 4.16(b).

The model with air drag [114, p. 54] does not explain the differences in jet shapes as well; see Figures 4.15 and 4.17. The air drag is modeled by adding the term

$$-\frac{1}{2}C_N\rho_{\text{air}}v^2\pi d\mathbf{r}_s,$$

to the right hand side of the conservation of momentum (1.6). Here,  $\rho_{\text{air}}$  is the air density,  $C_N$  is the drag coefficient, and  $d$  is the jet diameter. The value  $C_N$  is usually obtained heuristically; see for example [96, p. 4070] and [76, p. 43].

To illustrate the influence of the air drag we present the jet shapes for several values of  $C_N$ . For small values of  $C_N$  the jet shape remains concave for the inertial jet and convex for the viscous jet; see Figures 4.15 and 4.17. With increase  $C_N$  for the viscous and inertial jets, the inertia starts to dominate at the nozzle and viscosity at the belt. In this case the jet is aligned with the nozzle orientation and concave near the nozzle, and convex near the belt touching the belt tangentially. At the point where  $\xi = 0$  the jet is vertical. However, changing  $C_N$  does not allow us to fit the jet shapes obtained from the model with air drag, and obtained from the experiments.

Hence, surface tension, air drag, or bending stiffness alone do not explain the difference in the jet shapes obtained theoretically and experimentally. Additional research is

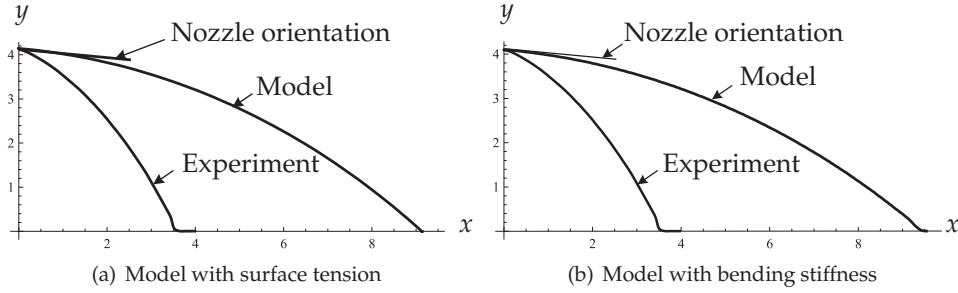


**Figure 4.14:** The inertial jet shapes from the models with surface tension (the surface tension coefficient is  $0.027 \text{ N/m}$ ), or bending stiffness, and from the experiment 14 with  $L = 4.1 \text{ cm}$ ,  $\nu = 0.047 \text{ m}^2/\text{s}$ ,  $v_{\text{nozzle}} = 1.147 \text{ m/s}$ ,  $v_{\text{belt}} = 0.81 \text{ m/s}$ ,  $d_{\text{nozzle}} = 0.4 \text{ mm}$ , and  $\alpha_{\text{nozzle}} = -5^\circ$ .

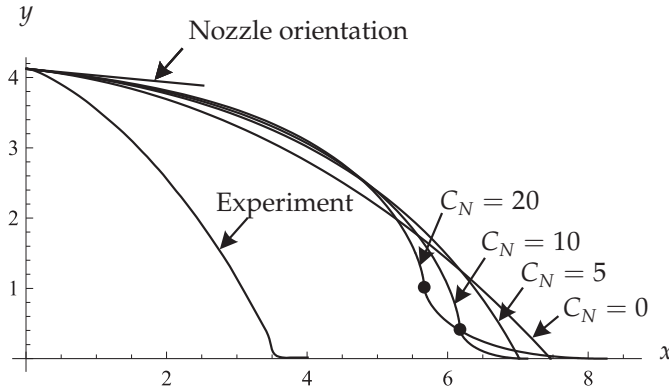


**Figure 4.15:** The inertial jet shapes obtained from the model with air drag and from the experiment 14 with  $L = 4.1 \text{ cm}$ ,  $\nu = 0.047 \text{ m}^2/\text{s}$ ,  $v_{\text{nozzle}} = 1.147 \text{ m/s}$ ,  $v_{\text{belt}} = 0.81 \text{ m/s}$ ,  $d_{\text{nozzle}} = 0.4 \text{ mm}$ , and  $\alpha_{\text{nozzle}} = -5^\circ$ . The dimensionless drag coefficient  $C_N$  has values 0, 5, 10, and 20; and the air density is  $\rho_{\text{air}} = 1.204 \text{ kg/m}^3$ . The solid dots indicate the positions in which  $\xi = 0$  and the jets are vertical.

required (i.e. considering viscoelastic constitutive law for the fluid, or using different fluid in experiments) to get a better agreement between experimental and theoretical results.

To conclude, we state that our model predicts correctly the transitions between the parameter regions for the three flow regimes. Also the tendencies in the (partial) monotonic behavior of  $x_{\text{end}}$  as  $v_{\text{belt}}$  increases are predicted well, yielding a satisfactory qualitative agreement. However, significant quantitative differences are obtained.

#### 4.4 Summary of the three flow regimes

Using our knowledge about the three flow regimes from model and experiment, we describe typical features of each flow regime. In the model, the three flow regimes are

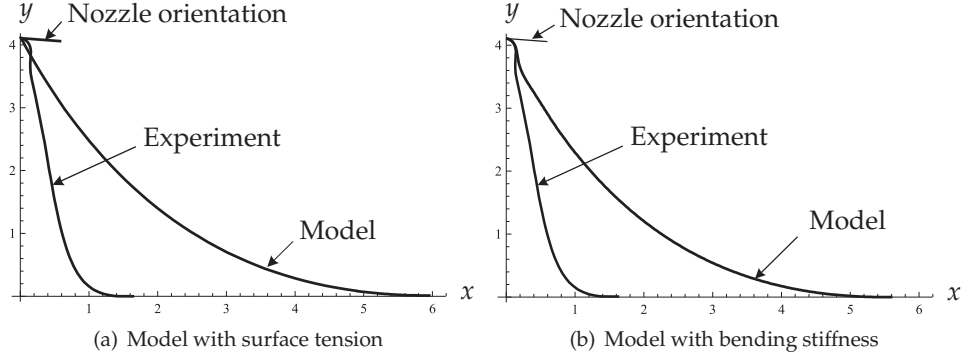


**Figure 4.16:** The viscous jet shapes from the models with surface tension (the surface tension coefficient is  $0.027 \text{ N/m}$ ), or bending stiffness, and from the experiment 23 with  $L = 4.1 \text{ cm}$ ,  $\nu = 0.047 \text{ m}^2/\text{s}$ ,  $v_{\text{nozzle}} = 1.147 \text{ m/s}$ ,  $v_{\text{belt}} = 4.398 \text{ m/s}$ ,  $d_{\text{nozzle}} = 0.4 \text{ mm}$ , and  $\alpha_{\text{nozzle}} = -5^\circ$ .

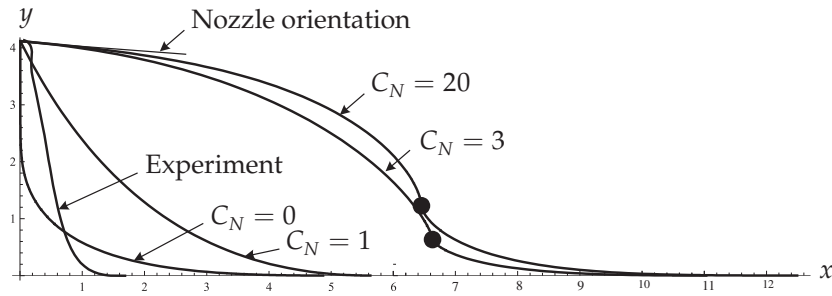


**Figure 4.17:** The viscous jet shapes obtained from the model with air drag and from the experiment 23 with  $L = 4.1 \text{ cm}$ ,  $\nu = 0.047 \text{ m}^2/\text{s}$ ,  $v_{\text{nozzle}} = 1.147 \text{ m/s}$ ,  $v_{\text{belt}} = 4.398 \text{ m/s}$ ,  $d_{\text{nozzle}} = 0.4 \text{ mm}$ , and  $\alpha_{\text{nozzle}} = -5^\circ$ . The dimensionless drag coefficient  $C_N$  has values 0, 1, 3, and 20; and the air density is  $\rho_{\text{air}} = 1.204 \text{ kg/m}^3$ . The solid dots indicate the positions in which  $\xi = 0$  and the jets are vertical.

characterized by the sign of the dimensionless variable  $\xi$ . The value of  $\xi$  represents the momentum transfer through a cross-section of the jet and describes the balance between the inertia and viscous terms in the conservation of momentum equation (2.21). Flow characterization using experimental jet shape features is possible as well. Below, we describe each flow regime separately:

- **Inertial flow.** In this flow regime  $\xi$  is positive. This means that the momentum transfer due to inertia is larger than that due to viscosity. This is reflected in the concave shape of the jet, comparable to a ballistic trajectory. The nozzle orientation is important for the jet shape. When the nozzle points vertically down the jet shape in this flow regime is vertical, no matter the flow regime is inertial or viscous-inertial. Therefore, in this case the characterization of the flow regime using the jet shape does not distinguish between inertial and viscous-inertial jets.

- **Viscous-inertial flow.** In this flow regime  $\xi$  changes sign from negative near the nozzle to positive near the belt. Hence, the momentum transfer due to viscosity is larger near the nozzle and the one due to inertia is so near the belt. The belt and nozzle orientations are now irrelevant for the jet shape, which is straight vertical in the experiments (except a possible bending region near the nozzle and bending or unstable region near the belt) as well as in the model.
- **Viscous flow.** In this flow regime  $\xi$  is negative, which means that the momentum transfer due to viscosity is larger than that due to inertia. Both in the experiments and the model the jet shape is convex (disregarding a small bending region near the nozzle in the experiment) and the jet touches the belt tangentially.

Summarizing, we conclude that the flow regimes can be characterized by the sign of the momentum transfer through the cross-section of the jet or by the convexity of the jet shape. However, for  $\alpha_{\text{nozzle}} = -\pi/2$ , the inertial jet shape is vertical, which makes it then impossible to distinguish between the inertial and viscous-inertial flow regimes. Additional shape features such as the tangency condition at the belt for the viscous flow, and the relevance of the nozzle orientation for the inertial flow can be used to distinguish between these flow regimes.

## 4.5 Concluding remarks

In this chapter we presented the experimental investigation of a jet in drag spinning. In the experiments we distinguished three flow regimes characterized by the convexity of the jet shape, i.e. concave, vertical, and convex. As we saw in Chapter 3 the jet is concave in the inertial regime, vertical in the viscous-inertial regime, and convex in the viscous regime. The monotonic behaviour of the touchdown point  $x_{\text{end}}$  is analyzed for different  $v_{\text{belt}}$ . With increasing  $v_{\text{belt}}$  from a value close to zero we first notice that  $x_{\text{end}}$  decreases towards zero, while the jet is in the inertial regime; then  $x_{\text{end}}$  reaches its minimum close to zero and stays there, while the jet is in the viscous-inertial regime; after that  $x_{\text{end}}$  increases while the jet is in the viscous regime. Some additional observations of influences of  $L$  and  $v_{\text{nozzle}}$  on  $x_{\text{end}}$  are reported as well.

For the upwards pointing nozzle an unsteady jet is observed. The evolution of  $x_{\text{end}}$  in time for the unsteady jet is not periodic. The values of  $x_{\text{end}}(t)$  are generally smaller for larger  $v_{\text{belt}}$ .

Our experimental study of the jet in drag spinning was restricted, and therefore we mainly focus on those results which can be used for further comparison with the theory. A detailed experimental study of the jet in drag spinning is beyond the scope of this work, which is mainly theoretical. Experiments are used only to qualitatively support our theory. In Appendix C we present the parameters for all the experiments for the steady jets with the values of  $x_{\text{end}}$  and the pictures of the jets.

Comparison of the relations between the horizontal position of the touchdown point  $x_{\text{end}}$  and the belt velocity  $v_{\text{belt}}$ , obtained from experiments and from the model, shows that:

1. The model and experiments show similar monotonic behavior of  $x_{\text{end}}$  as  $v_{\text{belt}}$  is changed.

2. The parameter regions in the  $(v_{\text{belt}}, L)$ -plane for the three flow regimes predicted by the model agree with the experimental data.
3. Quantitatively the relations between  $x_{\text{end}}$  and  $v_{\text{belt}}$  show a significant mismatch (experiments give substantially smaller  $x_{\text{end}}$ ) due to differences in the shapes of calculated and experimentally observed jets.

As a final conclusion, we state that our model, which includes viscous tension and inertia, but disregards air resistance, bending stiffness, and surface tension, describes in a qualitative sense the fall of a jet of a Newtonian fluid under gravity.



## Chapter 5

# Rotary fiber spinning

In this chapter we derive the equations for the steady jet string model in rotary spinning with respect to the co-rotating reference frame of the rotor. The equations are described by the three dimensionless parameters. We analyse the equations and obtain the three possible situations. These situations are: a) the viscous-inertial, b) the inertial jet, c) no steady solution exists. In rotary spinning with a non-moving coagulator, the viscous jet does not occur. The partitioning of the parameters between the three situations is described, and changes of the jet shape if the parameters leave the inertial region and enter the viscous-inertial region or try to enter the nonexistence region are illustrated. We shortly discuss the possibility of a viscous jet in case the coagulator rotates, and a situation in which we expect that the jet does not reach the coagulator. Finally, we give some conclusions.

### 5.1 Derivation of equations

We model the rotary spinning process (see Section 1.3.2) by considering the steady jet (see Figure 5.1) in two dimensions (neglecting the vertical motion due to gravity). The jet moves in a fixed horizontal frame from the nozzle of the rotor to the contact point with the coagulator. In a fixed reference frame the rotor rotates counter-clockwise with angular velocity  $\Omega$ . However we describe the motion with respect to a reference frame  $\tilde{\mathbf{e}}_x, \tilde{\mathbf{e}}_y$  rotating with the rotor. In this frame the rotor stands still and the coagulator rotates clock-wise with angular velocity  $\Omega$ . The radii of the rotor and the coagulator are  $R_{\text{rot}}$  and  $R_{\text{coag}}$ , respectively. The jet is parameterized by its length  $s$  with  $s = 0$  at the nozzle and  $s = s_{\text{end}}$  at the contact with the coagulator. The flow velocity at the nozzle is  $v_{\text{nozzle}}$ , and at the contact with the coagulator the jet sticks to it having the flow velocity  $\Omega R_{\text{coag}}$ . To describe the jet position in the rotating reference frame of the rotor, we use two coordinates : the polar coordinate system  $R(s), \beta(s)$ , with the origin at the center of the rotor and the Cartesian coordinate system  $\tilde{\mathbf{e}}_x, \tilde{\mathbf{e}}_y$ . In the rotating reference frame, two (inertial) body forces act on the jet, i.e the centrifugal,  $\mathbf{F}_C$ , and Coriolis,  $\mathbf{F}_C$ , force.

We want to derive the momentum conservation equation in the rotating reference frame, but we start with the conservation of momentum equation (1.8) in the fixed ref-

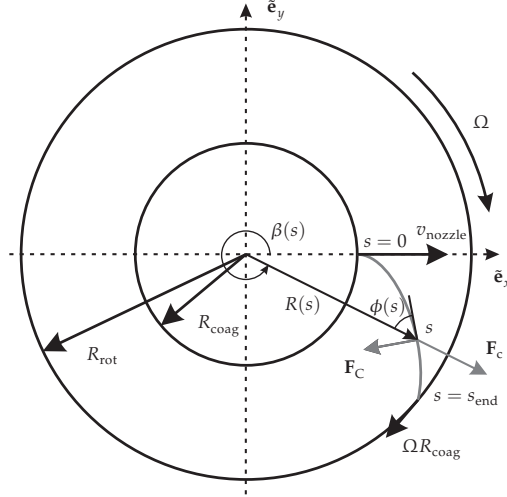


Figure 5.1: A schematic picture of the rotary spinning process.

reference frame without external body forces:

$$\mathbf{r}_{tt} + (v_t + vv_s)\mathbf{r}_s + v^2\mathbf{r}_{ss} + 2v\mathbf{r}_{st} = 3v\frac{(\mathcal{A}v_s\mathbf{r}_s)_s}{\mathcal{A}}. \quad (5.1)$$

The position vectors in the rotating reference frame,  $\tilde{\mathbf{r}}$ , and the fixed reference frame,  $\mathbf{r}$ , are related to each other according to

$$\tilde{\mathbf{r}} = \begin{pmatrix} \cos(\Omega t) & -\sin(\Omega t) \\ \sin(\Omega t) & \cos(\Omega t) \end{pmatrix} \mathbf{r}. \quad (5.2)$$

Eliminating  $\mathbf{r}$  in favor of  $\tilde{\mathbf{r}}$  in (5.1), we obtain

$$\tilde{\mathbf{r}}_{tt} + (v_t + vv_s)\tilde{\mathbf{r}}_s + v^2\tilde{\mathbf{r}}_{ss} + 2v\tilde{\mathbf{r}}_{st} = 3v\frac{(\mathcal{A}v_s\tilde{\mathbf{r}}_s)_s}{\mathcal{A}} + \Omega^2\tilde{\mathbf{r}} + 2\Omega(\tilde{\mathbf{r}}_t^\perp + v\tilde{\mathbf{r}}_s^\perp), \quad (5.3)$$

where  $\tilde{\mathbf{r}}^\perp$  is perpendicular to  $\tilde{\mathbf{r}} = (\tilde{x}, \tilde{y})$ , and given by  $\tilde{\mathbf{r}}^\perp = (\tilde{y}, -\tilde{x})$ . Further on we omit tildes. By use of (1.9)-(1.10), we rewrite (5.3) as

$$\mathbf{v}_t + v\mathbf{v}_s = 3v\frac{(\mathcal{A}v_s\mathbf{r}_s)_s}{\mathcal{A}} + \mathbf{a}_c + \mathbf{a}_C, \quad (5.4)$$

$$\mathbf{v} = \mathbf{r}_t + v\mathbf{r}_s, \quad (5.5)$$

where  $\mathbf{a}_c = \Omega^2\mathbf{r}$  and  $\mathbf{a}_C = 2\Omega\mathbf{v}^\perp$  are the centrifugal and Coriolis forces divided by  $\rho\mathcal{A}$ , respectively. The equations (1.11), (5.4)-(5.5) are studied in [40,71,77,78].

The equations for the steady jet in rotary spinning follow from (5.4)-(5.5). By using (1.11), (2.16), and (2.19), we get

$$\mathcal{A}(s) = \mathcal{A}_{\text{nozzle}}v_{\text{nozzle}}/v(s),$$



which we use to obtain

$$vv_s \mathbf{r}_s + v^2 \mathbf{r}_{ss} = 3v \left( \frac{v_s}{v} \right)_s \mathbf{r}_s + \Omega^2 \mathbf{r} + 2\Omega v \mathbf{r}_s^\perp. \quad (5.6)$$

Further on we use the polar coordinates  $R(s), \beta(s)$  to describe  $\mathbf{r}$ . By use of the angle  $\phi(s)$  (i.e. the angle between the radius vector and the tangent to the jet at the point  $s$ ) and using the arc-length condition (1.4), we write

$$\mathbf{r}_s = (\cos(\phi(s)), \sin(\phi(s))). \quad (5.7)$$

Then  $R(s), \beta(s)$ , and  $\phi(s)$  are related as

$$R'(s) = \cos(\phi(s)), \quad (5.8)$$

$$\beta'(s) = -\sin(\phi(s))/R(s). \quad (5.9)$$

Part of the boundary conditions for the steady jet follow from (2.16)-(2.18), (2.20), and they prescribe the flow velocity at the jet ends, nozzle position vector, and the position of the touchdown point at the coagulator. Boundary conditions for the jet orientation are obtained in Section 2.2. In such a way the boundary conditions for the jet in rotary spinning are

$$v(0) = v_{\text{nozzle}}, \quad (5.10)$$

$$v(s_{\text{end}}) = \Omega R_{\text{coag}}, \quad (5.11)$$

$$R(0) = R_{\text{rot}}, \quad (5.12)$$

$$\beta(0) = 0, \quad (5.13)$$

$$R(s_{\text{end}}) = R_{\text{coag}}, \quad (5.14)$$

$$\text{if } \xi(0) > 0, \text{ then } \phi(0) = 0, \quad (5.15)$$

$$\text{if } \xi(s_{\text{end}}) < 0, \text{ then } \phi(s_{\text{end}}) = \pi/2. \quad (5.16)$$

We scale the flow velocity  $v$  with respect to  $\Omega R_{\text{coag}}$ , both  $R$  and  $s$  with respect to  $R_{\text{coag}}$ . Moreover, we write (5.6) in the local coordinate system  $\mathbf{r}_s, \mathbf{r}_s^\perp$ , and make use of  $\xi$ , (1.14), which together with (5.8) and (5.9) gives

$$\xi'(s) = \cos(\phi(s))R(s)/v(s), \quad (5.17)$$

$$\xi(s)\phi'(s) = -R(s)\sin(\phi(s))/v(s) - \sin(\phi(s))\xi(s)/R(s) + 2, \quad (5.18)$$

$$v'(s) = (v(s)^2 - \xi(s)v(s))/B, \quad (5.19)$$

$$R'(s) = \cos(\phi(s)), \quad (5.20)$$

$$\beta'(s) = -\sin(\phi(s))/R(s), \quad (5.21)$$

for  $s \in (0, s_{\text{end}})$ . In dimensionless form the boundary conditions (5.10)-(5.16) become

$$v(0) = \text{Dr}, \quad (5.22)$$

$$v(s_{\text{end}}) = 1, \quad (5.23)$$

$$R(0) = R_0, \quad (5.24)$$

$$\beta(0) = 0 \quad (5.25)$$

$$R(s_{\text{end}}) = 1. \quad (5.26)$$

$$\text{if } \xi(0) > 0, \text{ then } \phi(0) = 0, \quad (5.27)$$

$$\text{if } \xi(s_{\text{end}}) < 0, \text{ then } \phi(s_{\text{end}}) = \pi/2. \quad (5.28)$$

The system of equations is fully described by the three dimensionless parameters

$$B = \frac{3\nu}{\omega R_{\text{coag}}^2},$$

the ration of the radii

$$R_0 = \frac{R_{\text{rot}}}{R_{\text{coag}}},$$

and the draw ratio

$$\text{Dr} = \frac{v_{\text{nozzle}}}{\Omega R_{\text{coag}}}.$$

Here,  $s_{\text{end}}$  is the dimensionless length of the jet, which is unknown in advance. The dimensionless parameter space consists of positive  $B$  and  $\text{Dr}$ , while the ratio  $R_0$  is bounded between 0 and 1 (i.e. the rotor is placed inside the coagulator), so

$$\mathcal{P} := \{(B, \text{Dr}, R_0) : B > 0, \text{Dr} > 0, R_0 \in (0, 1)\}. \quad (5.29)$$

By multiplying (5.17) by  $\sin(\phi(s))$  and (5.18) by  $\cos(\phi(s))$ , adding them and integrating the results with the aid of (5.20) we receive

$$\sin(\phi(s))\xi(s) = \frac{R(s)^2 - C_1}{R(s)}, \quad (5.30)$$

where  $C_1$  is an integration constant.

It is convenient to use the radius vector  $r = R(s)$  as independent variable, which transforms (5.17)-(5.21) into

$$\xi'(r) = r/v(r), \quad (5.31)$$

$$\xi(r)\phi'(r) = \frac{-\sin(\phi(r))r^2 - v(r)(\xi(r)\sin(\phi(r)) - 2r)}{v(r)r\cos(\phi(r))}, \quad (5.32)$$

$$v'(r) = (v(r)^2 - \xi(r)v(r))/(B\cos(\phi(r))), \quad (5.33)$$

$$\beta'(r) = -\tan(\phi(r))/r \quad (5.34)$$

while (5.30) becomes

$$\sin(\phi(r))\xi(r) = (r^2 - C_1)/r. \quad (5.35)$$

An advantage of this variable change is that it makes the interval for the independent variable  $r$  fixed,  $r \in [R_0, 1]$ . However, it is valid only for  $\cos(\phi(r)) \neq 0$  (i.e. the jet does not become perpendicular to the radius vector) for  $r \in [R_0, 1]$ . The boundary conditions after the change of variables are

$$v(R_0) = Dr, \quad (5.36)$$

$$v(1) = 1, \quad (5.37)$$

$$\beta(R_0) = 0, \quad (5.38)$$

$$\text{if } \xi(R_0) > 0, \text{ then } \phi(R_0) = 0, \quad (5.39)$$

$$\text{if } \xi(1) < 0, \text{ then } \phi(1) = \pi/2. \quad (5.40)$$

The equations for  $\beta$ , (5.21) or (5.34), are decoupled from the rest of the system, and are often left out of consideration. In the next section, we analyse the model equations (5.31)-(5.34) and (5.36)-(5.40).

## 5.2 Analysis

In this section, we determine possible situation for the jet and partition the parameter region between these situations. Unless indicated otherwise, we work with the system (5.31)-(5.33), (5.36), (5.37), (5.39), and (5.40), where  $r$  is the independent variable.

From the equation for  $\xi$ , (5.31), we conclude that  $\xi(r)$  is a strictly increasing function because the right-hand side of (5.31) is strictly positive. Thus, three situations are possible for the sign of  $\xi(r)$  at the jet ends, i.e.

$$0 < \xi(R_0) < \xi(1), \quad (5.41)$$

$$\xi(R_0) \leq 0 \leq \xi(1), \quad (5.42)$$

$$\xi(R_0) < \xi(1) < 0. \quad (5.43)$$

This situation is the same as for the drag spinning described in Section 3.1. Next we analyse each of the three situations (5.41), (5.42), and (5.43), separately.

The first case is (5.41).

**Definition 5.1.** *A solution to the system (5.31)-(5.33), (5.36), (5.37), (5.39), and (5.40) is called **inertial jet** if (5.41) holds.*

*The parameter region for the inertial jet is*

$$\mathcal{P}_{\text{inert}} := \{(B, Dr, R_0) \in \mathcal{P} : \text{if there exists an inertial jet}\}. \quad (5.44)$$

The term inertial jet is used because if (5.41) is true then inertia is the dominant effect in the momentum transfer through the jet cross-section. Because  $\xi$  is positive we prescribe one boundary condition for  $\phi$  at the nozzle (i.e the radial nozzle direction), and no boundary condition at the coagulator; see (5.39) and (5.40),

$$\phi(R_0) = 0. \quad (5.45)$$

Moreover, because of (5.45) the constant  $C_1$  in (5.35) becomes  $C_1 = R_0^2$ .

The second case is (5.42).

**Definition 5.2.** A solution to the system (5.31)–(5.33), (5.36), (5.37), (5.39), and (5.40) is called *viscous-inertial jet* if (5.42) holds.

The parameter region for the viscous-inertial jet is

$$\mathcal{P}_{v-i} := \{(B, Dr, R_0) \in \mathcal{P} : \text{if there exists a viscous-inertial jet}\}. \quad (5.46)$$

The term viscous-inertial jet is used because if (5.42) is true then viscosity dominates in the momentum transfer through the jet cross-section at the nozzle, whereas inertia dominates at the coagulator. The variable  $\xi$  is negative at the nozzle and positive at the coagulator and then we prescribe no boundary condition for  $\phi$ ; see (5.39) and (5.40). However, there exist a point  $r_0 \in [R_0, 1]$  in the jet so that  $\xi(r_0) = 0$ , and  $\xi$  changes sign from negative to positive. At this point the jet should be aligned with the direction of the external forces, which follows from the conservation of momentum equation (5.6) when the jet is steady. This means that at  $r_0$  we have the condition

$$\phi(r_0) = \arcsin(2v(r_0)/r_0), \quad \xi(r_0) = 0. \quad (5.47)$$

Moreover, because of (5.47) the constant  $C_1$  in (5.35) becomes  $C_1 = r_0^2$  and the jet direction does not become radial at any point in the jet. In addition, for viscous-inertial jets a restriction on  $v(r_0)$  follows from (5.47), saying that

$$v(r_0) \leq r_0/2. \quad (5.48)$$

Thus a viscous-inertial jet is only possible for  $Dr \leq R_0/2$ , regardless of the value of  $B$ .

**Remark 5.3.** It would be natural that there exists a solution to the system (5.31)–(5.33), (5.36), (5.37), (5.39), and (5.40), which also satisfies (5.43) and is called *viscous jet*. However, this is not possible. From the forthcoming Lemma 5.7, it follows that if  $\xi(1) < 0$ , then the boundary condition (5.37) can not be satisfied.

We proceed with analysis of the system (5.31)–(5.33), (5.36), (5.37), (5.45), and (5.47) in case of the inertial and viscous-inertial regimes only. We reformulate the problem by replacing the boundary condition for  $v$  at the coagulator (5.37) by a boundary condition for  $\xi$  at the rotor, i.e.

$$\xi(R_0) = w, \quad (5.49)$$

with  $w > 0$  for the inertial jet and  $w \leq 0$  for the viscous-inertial jet. In such a way, for a given  $w$ , the system (5.31)–(5.33), (5.36), (5.49), (5.45), and (5.47) has a solution  $v(r; w)$ ,  $\phi(r; w)$ ,  $\xi(r; w)$ . This solution is only considered within the range:  $R_0 < r < r_m(w)$ , where  $r_m(w)$  is so that either  $v$  becomes zero there ( $v(r_m(w); w) = 0$ ), or the jet becomes perpendicular to the radius vector ( $\phi(r_m(w); w) = \pi/2$ ).

By the introduction of  $w$  a problem is transformed into finding a  $w$  so that

$$v(1, w) = 1. \quad (5.50)$$

The phase planes  $v(r, w)$  and  $\phi(r; w)$  are depicted in Figure 5.2. For a jet in the inertial regime, (i.e.  $\xi(r; w) > 0$ ). The situation is similar for a jet in the viscous-inertial regime, when  $\xi(r; w)$  changes sign. The only difference is that in the viscous-inertial regime  $\phi(R_0; w)$  is not zero, increases with decreasing  $w$ . The gray curve  $\mathcal{C}_{\max}$  in Figure 5.2(a)

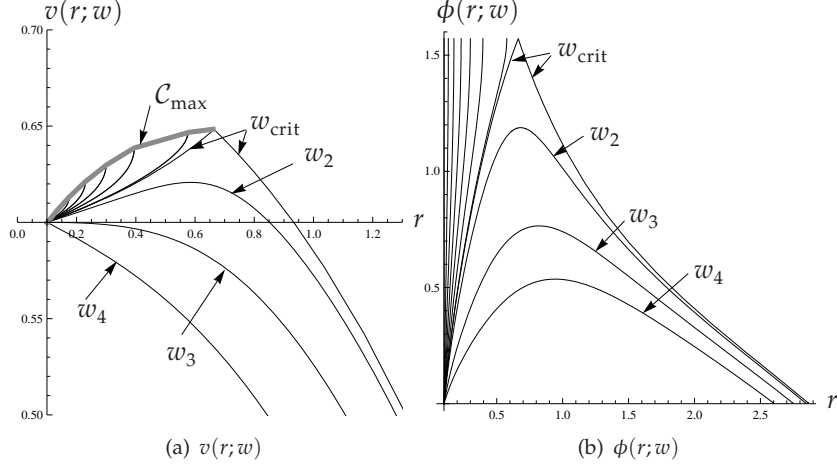


**Figure 5.2:** Phase planes for  $v(r; w)$  and  $\phi(r; w)$ , with  $B = 3$ ,  $Dr = 0.6$ , and  $R_0 = 0.1$ , and for increasing values of  $w$ :  $w_{\text{crit}}$ ,  $w_2 \in (w_{\text{crit}}, Dr)$ ,  $w_3 = Dr$ ,  $w_4 > Dr$ .

is defined as

$$\mathcal{C}_{\max} := \{(r, v(r; w)) : \phi(r; w) = \pi/2\}. \quad (5.51)$$

Note that  $v(r; w)$  can not grow above  $\mathcal{C}_{\max}$ , because it breaks down  $v(r; w)$  when reaches  $\mathcal{C}_{\max}$  due to  $\phi(r; w) = \pi/2$ .

Next, we formulate monotonicity properties of  $v(r; w)$  with respect to  $w$ .

**Lemma 5.4.** *The function  $w \mapsto v(r; w)$  is strictly decreasing if  $(r, w) \in \{(r, w) : v(r; w) > \xi(r; w) > 0\}$  and  $w > 0$*

*Proof.* In this case (5.31), (5.33), (5.35), (5.36), and (5.49), yield the system

$$\xi'(r; w) = r/v(r; w), \quad (5.52)$$

$$v'(r; w) = (v(r; w)^2 - \xi(r; w)v(r; w))/(B \cos(\phi(r; w))), \quad (5.53)$$

$$\sin(\phi(r; w))\xi(r; w) = (r^2 - R_0^2)/r, \quad (5.54)$$

$$v(R_0; w) = Dr, \quad (5.55)$$

$$\xi(R_0; w) = w. \quad (5.56)$$

At  $r = R_0$ , we have then, with  $\phi(R_0; w) = 0$  (see (5.39))

$$v'(R_0; w) = \frac{Dr^2 - wDr}{B},$$

showing that  $v'(R_0; w)$  decreases as  $w$  increases. From this follows that for  $w_1 > w_2$  we have that  $v(r; w_1) < v(r; w_2)$  for  $r$  close enough to  $R_0$ , and, consequently,  $\xi(r; w_1) > \xi(r; w_2)$ , and  $\phi(r; w_1) < \phi(r; w_2)$ . The monotonicity of  $\xi(r; w)$  follows from (5.56) (and (5.52)) and that of  $\phi(r; w)$  from (5.54).

Suppose that there exists  $r_1$  so that  $v(r_1; w_1) = v(r_1; w_2)$  with  $v'(r_1; w_1) > v'(r_1; w_2) > 0$ . Moreover, at  $r_1$  holds  $\xi(r_1; w_1) > \xi(r_1; w_2)$ , and  $\phi(r_1; w_1) < \phi(r_1; w_2)$ . But from (5.53)

we receive a contradiction

$$\begin{aligned} v'(r_1; w_1) &= (v(r_1; w_1)^2 - \xi(r_1; w_1)v(r_1; w_1)) / (B \cos(\phi(r_1; w_1))) < \\ &= (v(r_1; w_2)^2 - \xi(r_1; w_2)v(r_1; w_2)) / (B \cos(\phi(r_1; w_2))) = v'(r_1; w_2), \end{aligned}$$

because

$$v(r_1; w_1) - \xi(r_1; w_1) < v(r_1; w_2) - \xi(r_1; w_2),$$

and

$$\frac{1}{\cos(\phi(r_1; w_1))} < \frac{1}{\cos(\phi(r_1; w_2))}.$$

This contradiction completes the proof.  $\square$

Lemma 5.4 provides monotonicity of  $v(r; w)$  with respect to  $w$  only for a part of  $r$  and  $w$ . Next we formulate conjecture for all  $r$  and  $w$ .

**Conjecture 5.5.** *The function  $w \mapsto v(r; w)$  is strictly decreasing for all values of  $r$  and  $w$ .*

This conjecture is confirmed by numerical simulations and Lemma 5.4. From this conjecture it would follow that a jet solution is unique. The monotonic behavior of  $v(r; w)$  in  $w$  is depicted in Figure 5.2(a). We consider below the behaviour of  $v(r; w)$  in  $r$  for increasing values of  $w$ .

The monotonic behaviour of  $v(r; w)$  with respect to  $r$  is following:

- For small  $w$  close to zero,  $v(r; w)$  strictly increases for all  $r$ , eventually hitting the curve  $\mathcal{C}_{\max}$ , while  $\phi(r; w)$  strictly increases and becomes  $\pi/2$  for finite  $r$  (see the graphs of  $v(r; w)$  hitting  $\mathcal{C}_{\max}$  in Figure 5.2(a) and the graphs of  $\phi(r; w)$  hitting  $\phi = \pi/2$  in Figure 5.2(b)).
- The value  $w_{\text{crit}}$  of  $w$  so that  $v(r; w_{\text{crit}})$  increases, reaches its maximum at the end of  $\mathcal{C}_{\max}$ , and then decreases to zero. The angle  $\phi(r; w_{\text{crit}})$  increases having its maximum at  $\phi = \pi/2$  and then decreases to zero; see the graphs of  $v(r; w)$  and  $\phi(r; w)$  indicated by  $w_{\text{crit}}$  in Figure 5.2.

It is also possible that  $v(r; w_{\text{crit}})$  increases and never reaches its maximum and  $\phi(r; w_{\text{crit}})$  approaches to  $\pi/2$  asymptotically as  $r \rightarrow \infty$ .

- If  $w_{\text{crit}} < w < Dr$  the velocity  $v(r; w)$  increases, reaches its maximum and then decreases towards zero; see the graph of  $v(r; w)$  indicated by  $w_2$  in Figure 5.2(a). The angle  $\phi(r, w)$  increases, reaches its maximum, which is less than  $\pi/2$ , and then decreases towards zero; see the graph of  $\phi(r; w)$  indicated by  $w_2$  in Figure 5.2(b).
- If  $w \geq Dr$  the velocity  $v(r; w)$  decreases towards zero see the graph of  $v(r; w)$  indicated by  $w_3 = Dr$  and  $w_4 > Dr$  in Figure 5.2(a). The angle  $\phi(r, w)$  increases reaches its maximum, which is less than  $\pi/2$ , and then decreases towards zero; see the graph of  $\phi(r; w)$  indicated by  $w_3 = Dr$  and  $w_4 > Dr$  in Figure 5.2(b).

In view of the behaviour of  $v(r; w)$  described above a solution to (5.50) exists if the point  $(r = 1, v = 1)$  either lies below the curve  $\mathcal{C}_{\max}$  or the decreasing part of  $v(r; w_{\text{crit}})$ . The curve  $\mathcal{C}_{\max}$  can be described by an increasing function of  $r$ ,  $\mathcal{C}_{\max}(r)$ , which starts at

$r = R_0$  and ends at the maximum of  $v(r; w_{\text{crit}})$  at  $r = r_{\text{max}}$ ,

$$\max_r v(r; w_{\text{crit}}) = v(r_{\text{max}}; w_{\text{crit}}).$$

This enables us to define a region in the  $\{rv\}$ -plane

$$\mathcal{V}_{\text{reach}} = \{(r, v) : (R_0 < r < r_{\text{max}} \text{ and } v \leq C_{\text{max}}(r)) \text{ or } (r > r_{\text{max}} \text{ and } v < v(r; w_{\text{crit}}))\}, \quad (5.57)$$

that contains all the possible values of  $v$  and  $r$ ; see the grey region in Figure 5.3. Thus,

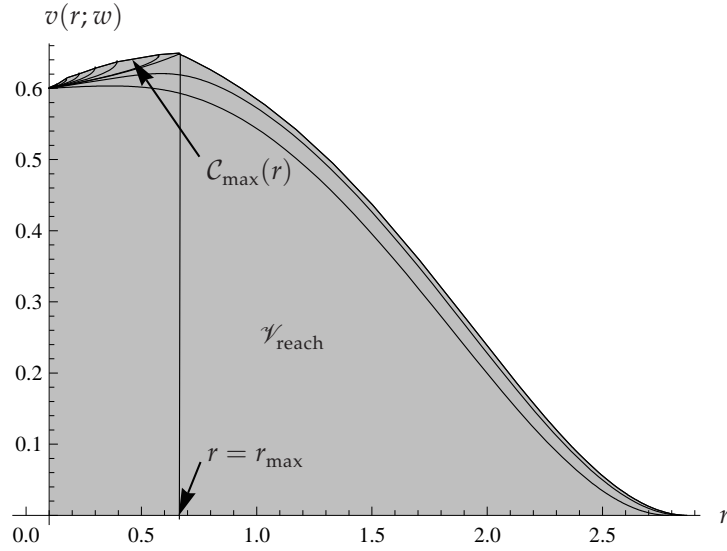


**Figure 5.3:** The region  $\mathcal{V}_{\text{reach}}$  for  $B = 3$ ,  $Dr = 0.6$ , and  $R_0 = 0.1$ .

in view of (5.50) a jet solution exists iff

$$(1, 1) \in \mathcal{V}_{\text{reach}}(B, Dr, R_0). \quad (5.58)$$

All this leads us to the definition of a parameter region in which no jet solution exists.

$$\mathcal{P}_{\text{NE}} := \{(B, Dr, R_0) \in \mathcal{P} : (1, 1) \notin \mathcal{V}_{\text{reach}}(B, Dr, R_0)\}. \quad (5.59)$$

By this the problem of partitioning of the parameter space  $\mathcal{P}$  is transformed to determining the regions  $\mathcal{P}_{\text{inert}}$ ,  $\mathcal{P}_{v-i}$ , and  $\mathcal{P}_{\text{NE}}$ . The border  $\mathcal{B}_{\text{exist}}$  between  $\mathcal{P}_{\text{NE}}$  and  $\mathcal{P}_{\text{inert}} \cup \mathcal{P}_{v-i}$  is determined by the condition

$$C_{\text{max}}(1) = 1, \text{ or } v(1; w_{\text{crit}}) = 1 \text{ and } r_{\text{max}} < 1, \quad (5.60)$$

where  $C_{\text{max}}$ ,  $v$ ,  $w_{\text{crit}}$ , and  $r_{\text{max}}$  depend on the parameters  $B$ ,  $Dr$ , and  $R_0$ . In order to obtain the  $\mathcal{B}_{\text{exist}}$  we have to determine the point  $(r_{\text{max}}, v(r_{\text{max}}; w_{\text{crit}}))$ . At this point  $v(r; w_{\text{crit}})$  reaches its maximum and as follows from, (5.19) or (5.33),

$$v(r_{\text{max}}; w_{\text{crit}}) = \xi(r_{\text{max}}; w_{\text{crit}}),$$

and, as follows from the definition of  $r_{\max}$   $\phi(r_{\max}; w_{\text{crit}}) = \pi/2$ . After substituting the result above into (5.18) for  $s = s_{\max}$  (with  $\xi \rightarrow v$ ,  $R \rightarrow r = r_{\max}$ ,  $\phi \rightarrow \pi/2$ ), we find

$$\phi'(s_{\max}) = -\frac{(r_{\max} - v(r_{\max}; w_{\text{crit}}))^2}{r_{\max} v(r_{\max}; w_{\text{crit}})^2} \leq 0.$$

Because  $\phi \leq \pi/2$  we demand that  $\phi'(s_{\max}) \geq 0$  (otherwise the jet penetrates the coagulator), which is only possible if

$$r_{\max} = v(r_{\max}; w_{\text{crit}}) \text{ and } \phi'(s) = 0. \quad (5.61)$$

This means that the condition (5.58) is satisfied only if

$$r_{\max} \geq 1. \quad (5.62)$$

Otherwise if  $r_{\max} < 1$  we have that  $v(1; w_{\text{crit}}) < v(r_{\max}; w_{\text{crit}}) < 1$  and  $\mathcal{V}_{\text{reach}}(\text{B}, \text{Dr}, \text{R}_0)$  lies below the line  $v = 1$ , so the condition (5.58) is never satisfied. Combining (5.62) and (5.60) we have that the boundary of the nonexistence region  $\mathcal{B}_{\text{exist}}$  is computed as

$$\mathcal{B}_{\text{exist}} = \{(\text{B}, \text{Dr}, \text{R}_0) : \mathcal{C}_{\max}(1; \text{B}, \text{Dr}, \text{R}_0) = 1\}. \quad (5.63)$$

The border  $\mathcal{B}_{\text{ivi}}$  between  $\mathcal{P}_{\text{inert}}$  and  $\mathcal{P}_{\text{v-i}}$  is given by the condition

$$\xi(\text{R}_0; \text{B}, \text{Dr}, \text{R}_0) = 0, \quad (5.64)$$

where  $\xi$  is a solution solution of (5.31)-(5.33), (5.36), (5.37), and (5.47).

In the next section we describe the results of partitioning of the parameter space and illustrate the jet evolution while flow regime changes.

## 5.3 Results

In this section we present some examples of the partitioning of the parameter regions between the flow regimes. The change of the steady jet shape is described when the parameters are varied so they leave the inertial regime and enter the viscous-inertial regime or the region where no solution exists.

### Parameter regions

In Figure 5.4 we present the partitioning of the parameter space for fixed  $\text{B} = 0.15$  different  $\text{Dr} > 0$  and  $0 < \text{R}_0 < 1$ . The partitioning results in four regions one inertial,  $\mathcal{P}_{\text{inert}}$ , one viscous-inertial,  $\mathcal{P}_{\text{v-i}}$ , and two separate regions where no solution is possible,  $\mathcal{P}_{\text{NE},1}$  and  $\mathcal{P}_{\text{NE},2}$ ; see Figure 5.4. These regions are separated from each other by the curves  $\mathcal{B}_{\text{exist},1}$  (connects  $\text{C}_1$  and  $\text{C}_2$ ),  $\mathcal{B}_{\text{exist},2}$  (connects  $\text{C}_3$  and  $\text{C}_4$ ),  $\mathcal{B}_{\text{exist},3}$  (connects  $\text{C}_6$  and  $\text{C}_2$ ),  $\mathcal{B}_{\text{exist},4}$  (connects  $\text{C}_5$  and  $\text{C}_3$ ), and  $\mathcal{B}_{\text{ivi}}$  (connects  $\text{C}_2$  and  $\text{C}_3$ ). The points  $\text{C}_4 = (1, 1)$  and  $\text{C}_6 = (0, 0)$ , while the point  $\text{C}_1$  has  $\text{R}_0 = 0$  and the point  $\text{C}_5$  has  $\text{Dr} = 0$ .

In order to obtain the curves  $\mathcal{B}_{\text{exist},1} - \mathcal{B}_{\text{exist},4}$ , we demand that  $\mathcal{C}_{\max}(1) = 1$  (i.e. for the parameters from these curves the jet has to touch the coagulator tangentially,  $\phi(1) = \pi/2$ ).



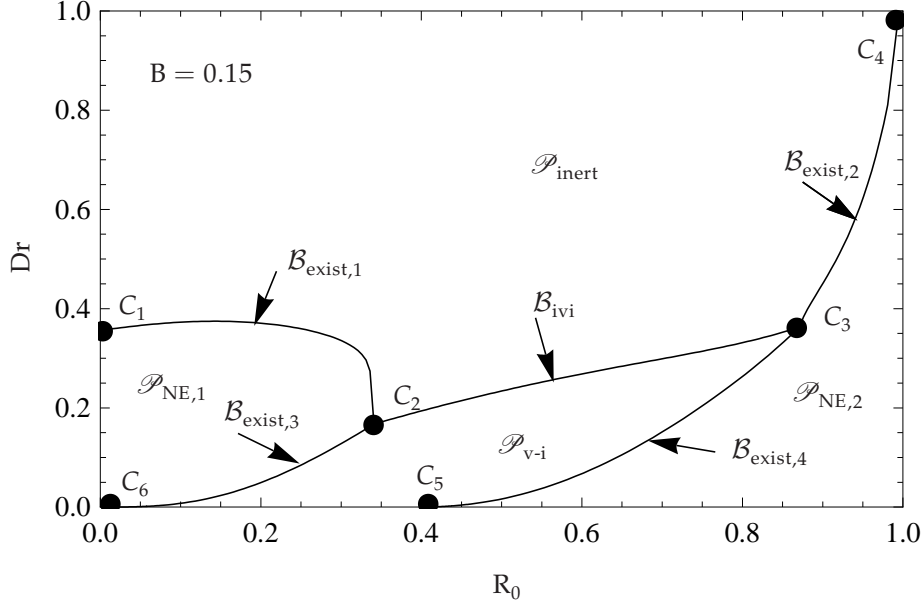


Figure 5.4: Parameter regions  $\mathcal{P}_{inert}$ ,  $\mathcal{P}_{v-i}$ , and  $\mathcal{P}_{NE}$  in the  $R_0, Dr$ -plane for  $B = 0.15$ .

The curves  $\mathcal{B}_{exist,1}$  and  $\mathcal{B}_{exist,2}$  are calculated from  $\phi(1; B, Dr, R_0) = \pi/2$  where  $\phi(r; B, Dr, R_0)$  follows from the inertial jet solution of the system (5.31) -(5.33), (5.36), (5.37), and (5.45).

The curves  $\mathcal{B}_{exist,3}$  and  $\mathcal{B}_{exist,4}$  are the parts of  $v(r; B, Dr, R_0)$  for  $r < r_0(B, Dr, R_0)$  for which  $Dr \rightarrow 0$ , ( $r_0$  is the solution of  $\xi(r_0) = 0$ ) with  $\phi(1) = \pi/2$ , where  $v, \xi, \phi$  are viscous-inertial jet solutions of the system (5.31) -(5.33), (5.36), (5.37), and (5.47). It appears that one of such solutions has  $R_0 = 0$ , so  $C_6 = (0, 0)$ , and the other has  $R_0 > 0$ , so  $C_5 = (R_0 > 0, 0)$ . The points  $C_2$  and  $C_3$  are  $(r_0, v(r_0))$  with  $\xi(r_0) = 0$ .

The curve  $\mathcal{B}_{ivi}$  is characterized by the condition that  $r_0$  in (5.47) becomes equal to  $R_0$ . This implies that  $\mathcal{B}_{ivi}$  in the  $Dr - R_0$ -plane can be found from the relation  $\xi(R_0; B, Dr, R_0) = 0$ , where  $\xi(R_0; B, Dr, R_0) = 0$  is a solution of the system (5.31) -(5.33), (5.36), (5.37), and (5.47). At the end points  $C_2$  and  $C_3$  of  $\mathcal{B}_{ivi}$  the additional relation  $\phi(1; B, Dr, R_0) = \pi/2$  holds.

The parameters region for the inertial jet  $\mathcal{P}_{inert}$  lies above the curves  $\mathcal{B}_{exist,1}$ ,  $\mathcal{B}_{ivi}$ , and  $\mathcal{B}_{exist,2}$ . It is contiguous to the two regions  $\mathcal{P}_{NE}$ , where no solution exists, and to the viscous-inertial jet region  $\mathcal{P}_{v-i}$ .

The parameter region for the viscous-inertial jet,  $\mathcal{P}_{v-i}$ , is below  $\mathcal{B}_{ivi}$  and bounded by the curves  $\mathcal{B}_{exist,3}$  and  $\mathcal{B}_{exist,4}$ .

The first region  $\mathcal{P}_{NE,1}$ , where no jet solution exists, is bounded by the curves  $\mathcal{B}_{exist,1}$ ,  $\mathcal{B}_{exist,3}$ . In this region we distinguish two causes of nonexistence: the first one is that  $C_{max}(1) < 1$ , and the second one is that the  $r_{max}$ -coordinate of the end position of  $C_{max}$  is less than 1. An example of the second cause is given in Section 5.5.

The second region  $\mathcal{P}_{NE,2}$ , where no jet solution exists, is bounded by the curves  $\mathcal{B}_{exist,2}$ ,  $\mathcal{B}_{exist,4}$ . Hence, solutions with  $Dr < 1$  do not exist if  $R_0$  is too close to 1. In this

region the cause of nonexistence is that  $(1, 1)$  lies above the curve  $C_{\max}$ .

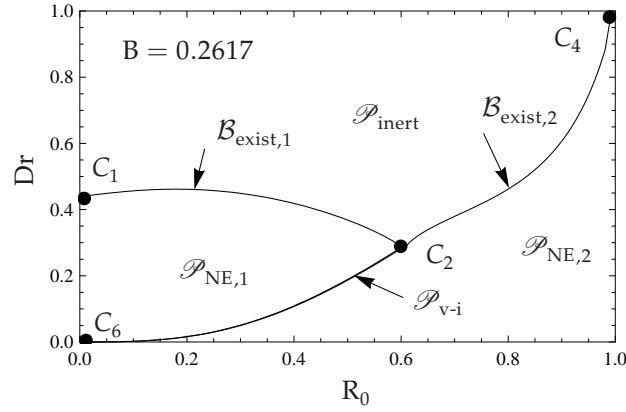


**Figure 5.5:** Parameter regions  $\mathcal{P}_{inert}$ ,  $\mathcal{P}_{v-i}$ , and  $\mathcal{P}_{NE}$  in the  $R_0, Dr$ -plane for  $B = 0.2617$ .

In case  $B$  increases, the borders  $\mathcal{B}_{exist,1}$ ,  $\mathcal{B}_{ivi}$ , and  $\mathcal{B}_{exist,2}$  go up<sup>1</sup> and the inertial jet regime shrinks to larger  $Dr$ . The curves  $\mathcal{B}_{exist,1}$  and  $\mathcal{B}_{exist,2}$  become longer, and the curve  $\mathcal{B}_{ivi}$  shorter because the points  $C_2$  and  $C_3$  come closer to each other. As a consequence, the viscous-inertial jet region  $\mathcal{P}_{v-i}$  shrinks and the nonexistence regions  $\mathcal{P}_{NE,1}$  and  $\mathcal{P}_{NE,2}$  expand.

As the result of this behaviour, we see in Figure 5.5 that when  $B$  becomes  $B = 0.2617$ , the curves  $\mathcal{B}_{exist,3}$  and  $\mathcal{B}_{exist,4}$  merge and the points  $C_3$  and  $C_2$  as well as  $C_5$  and  $C_6$  coincide, while  $C_6$  stays the same  $C_6 = (0, 0)$ ; see Figure 5.5. Now, the viscous-inertial jet region  $\mathcal{P}_{v-i}$  has diminished to only one curve starting at  $C_6$  and ending at  $C_2$ .

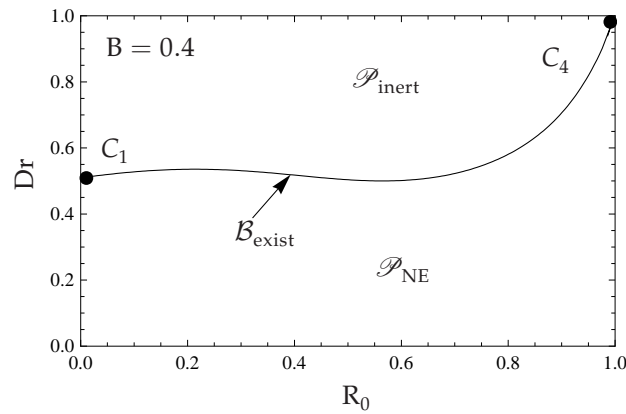


**Figure 5.6:** Parameter regions  $\mathcal{P}_{inert}$  and  $\mathcal{P}_{NE}$  in the  $R_0, Dr$ -plane for  $B = 0.4$ .

For  $B > 0.2617$ , the viscous-inertial jet region  $\mathcal{P}_{inert}$  disappears and the regions  $\mathcal{P}_{NE,1}$  and  $\mathcal{P}_{NE,2}$  merge to form  $\mathcal{P}_{NE}$ ; see Figure 5.6 for  $B = 0.4$ . The nonexistence

<sup>1</sup>The points  $C_1$ ,  $C_2$ , and  $C_3$  have larger  $Dr$  coordinates and  $C_4$  remains  $(1,1)$

region  $\mathcal{P}_{NE}$  becomes larger and  $\mathcal{P}_{inert}$  shrinks further to higher  $Dr$ , as the border  $\mathcal{B}_{exist}$  between  $\mathcal{P}_{NE}$  and  $\mathcal{P}_{inert}$  goes up. The  $Dr$ -coordinate of the point  $C_1$  increases while  $C_4$  remains the same  $C_4 = (1, 1)$ .

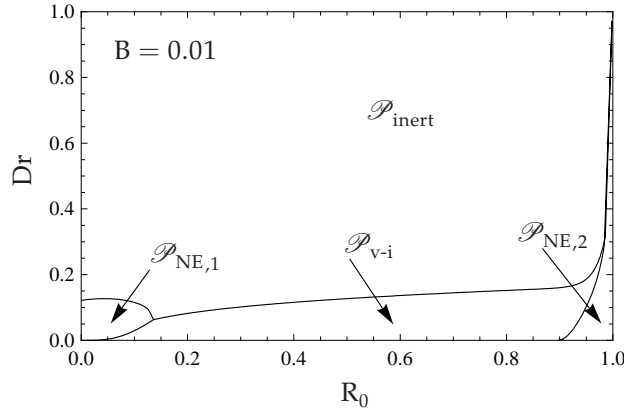


**Figure 5.7:** Parameter regions  $\mathcal{P}_{inert}$ ,  $\mathcal{P}_{v-i}$ ,  $\mathcal{P}_{NE,1}$ , and  $\mathcal{P}_{NE,2}$  in the  $R_0, Dr$ -plane for  $B = 0.01$

When  $B$  approaches zero (e.g. fluid becomes less viscous and  $\nu$  decreases) the inertial jet region  $\mathcal{P}_{inert}$  expands to lower  $Dr$ , the viscous-inertial jet region  $\mathcal{P}_{v-i}$  becomes wider and lower, and the nonexistence regions,  $\mathcal{P}_{NE,1}$  and  $\mathcal{P}_{NE,2}$ , shrink; see Figure 5.7 for  $B = 0.01$ , and compare this to the parameter regions for  $B = 0.15$  in Figure 5.4.

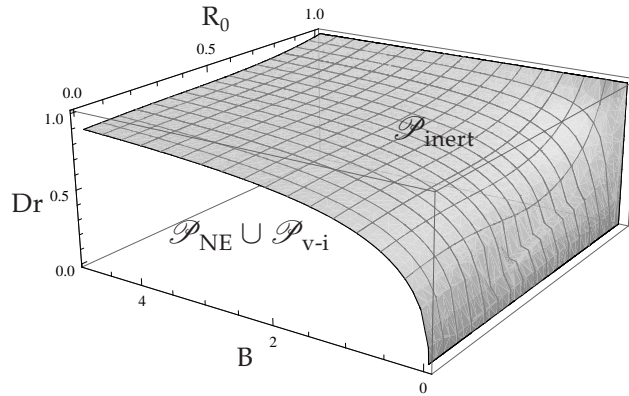


**Figure 5.8:** The border surface  $\partial\mathcal{P}_{inert}$  of the parameter region for the inertial jet  $\mathcal{P}_{inert}$  (above the surface) in the 3D space  $B, R_0, Dr$ . The parameter regions for the viscous-inertial jet and the region where no solution exists  $\mathcal{P}_{NE} \cup \mathcal{P}_{v-i}$  are below the surface.

The surface  $\partial\mathcal{P}_{inert}$  separating the inertial jet region  $\mathcal{P}_{inert}$  from the rest is depicted in Figure 5.9 in a 3D parameter space. The region  $\mathcal{P}_{inert}$  is above the surface and the

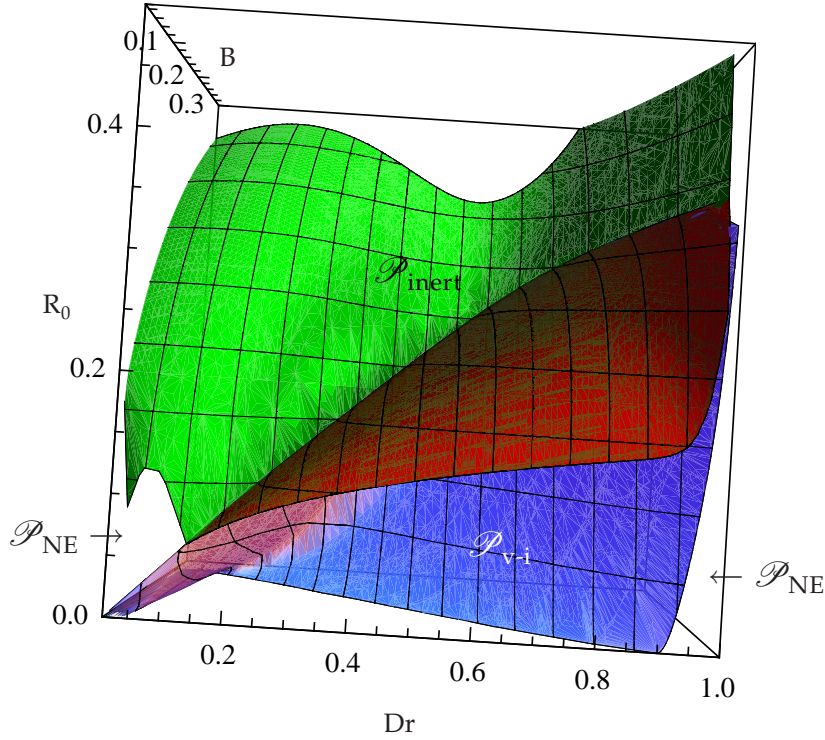


**Figure 5.9:** The parameter regions  $\mathcal{P}_{\text{inert}}$ ,  $\mathcal{P}_{\text{v-i}}$ , and  $\mathcal{P}_{\text{NE}}$  in the 3D parameter space  $B$ ,  $R_0$ ,  $Dr$ . The green surface is the border between  $\mathcal{P}_{\text{inert}}$  and  $\mathcal{P}_{\text{NE}}$ , the red surface is the border between  $\mathcal{P}_{\text{inert}}$  and  $\mathcal{P}_{\text{v-i}}$ , and the blue surface is the border between  $\mathcal{P}_{\text{v-i}}$  and  $\mathcal{P}_{\text{NE}}$ . The region  $\mathcal{P}_{\text{inert}}$  is above the green and the red surfaces, the region  $\mathcal{P}_{\text{v-i}}$  is below the red surface and in front of the blue surface, and the region  $\mathcal{P}_{\text{NE}}$  is behind the green and the blue surfaces.

regions  $\mathcal{P}_{\text{NE}}$  and  $\mathcal{P}_{\text{v-i}}$  are below the surface. For increasing  $B$  the surface  $\partial\mathcal{P}_{\text{inert}}$  rises towards  $Dr = 1$  and for  $B$  decreasing to zero,  $\partial\mathcal{P}_{\text{inert}}$  approaches to  $Dr = 0$ . In the limiting case  $B = 0$ , corresponding to an inviscid fluid,  $\partial\mathcal{P}_{\text{inert}}$  coincides with the line  $Dr = 0$  and the inertial jet is possible for all  $R_0$  and  $Dr$ .

The results about the parameter regions presented above are put together in Figure 5.9, where we present the parameter regions  $\mathcal{P}_{\text{inert}}$ ,  $\mathcal{P}_{\text{v-i}}$ , and  $\mathcal{P}_{\text{NE}}$  in the 3D parameter space. The green and blue surfaces separate the nonexistence region  $\mathcal{P}_{\text{NE}}$  from the inertial jet,  $\mathcal{P}_{\text{inert}}$  and viscous-inertial,  $\mathcal{P}_{\text{v-i}}$  regimes, respectively, and the red surface is the border between  $\mathcal{P}_{\text{inert}}$  and  $\mathcal{P}_{\text{v-i}}$ . In Figure 5.9 we observe that with increasing  $B$  the jet is inertial for larger  $Dr$ . The viscous-inertial region  $\mathcal{P}_{\text{v-i}}$  becomes narrower for increasing  $B$  and disappears for  $B$  large enough.

### Numerical simulations

To illustrate the results above, we present here some results of numerical simulations of jet shapes in  $\mathcal{P}_{\text{inert}}$  or  $\mathcal{P}_{\text{v-i}}$ . We start by showing the transition between the flow regimes by taking an initial parameter setting from the inertial regime, and by decreasing  $\text{Dr}$ , so that the parameters enter the viscous-inertial regime.

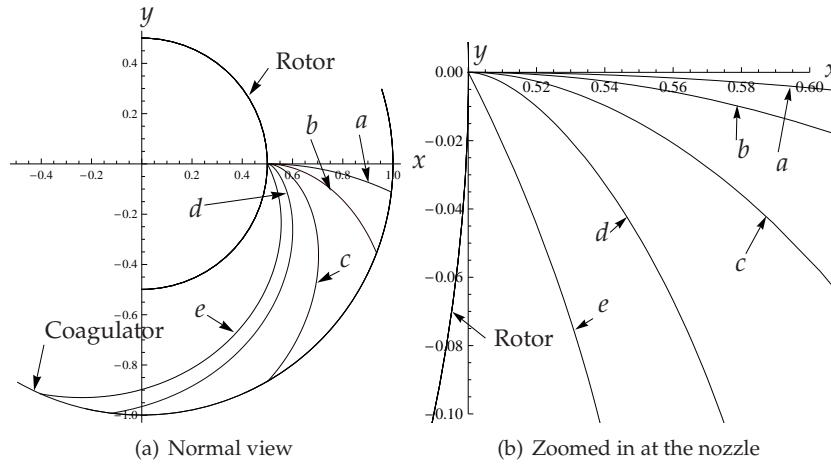


**Figure 5.10:** Numerical simulations of the inertial jet becoming viscous-inertial by decreasing  $\text{Dr}$ . The parameters  $B = 0.1$  and  $R_0 = 0.5$  are the same for all the simulations. The jet shape between the rotor and the coagulator is depicted at the right and the zoomed-in situation at the nozzle at the left. The parameter  $\text{Dr}$  has the values  $\text{Dr} = 2.2$ ,  $\text{Dr} = 0.7$ ,  $\text{Dr} = 0.35$ ,  $\text{Dr} = 0.26$ , and  $\text{Dr} = 0.22$ , corresponding to the jets  $a$ ,  $b$ ,  $c$ ,  $d$ , and  $e$ , respectively. The jets  $a$ ,  $b$ ,  $c$ , and  $d$  are inertial and leave the nozzle with the radial nozzle orientation. The jet  $e$  is viscous-inertial and the jet orientation at the nozzle does not coincide with the radial nozzle orientation.

In Figure 5.10 we present the computed jet shape for five parameter choices (the shapes between the rotor and the coagulator in the left figure, and the zoomed-in situation at the rotor in the right figure). The first four jets  $a$ ,  $b$ ,  $c$ , and  $d$ , for  $\text{Dr}$  decreasing from 2.2 to 0.26, are inertial and they leave the nozzle with the radial nozzle orientation. The touchdown point moves away from the nozzle (see Figure 5.10(a)) and the jet bends near the nozzle steeper for smaller  $\text{Dr}$ . At  $\text{Dr} = 0.22$ , the jet  $e$  becomes viscous-inertial and the nozzle exit angle is now determined by the jet itself; see Figure 5.10(b). In this figure we also see that the closer  $\text{Dr}$  is to the border with  $\mathcal{P}_{\text{v-i}}$  the steeper the jet near the nozzle changes its orientation towards the viscous-inertial jet orientation for  $\text{Dr}$  on this border.

In our next simulations we consider the inertial jet with such initial parameters that by decreasing  $\text{Dr}$  the parameter setting leaves  $\mathcal{P}_{\text{inert}}$  and enters the nonexistence region  $\mathcal{P}_{\text{NE}}$ . We illustrate this situation by four simulations presented in Figure 5.11. In the first three simulations  $a$ ,  $b$ ,  $c$  for  $\text{Dr} = 1.1$ ,  $0.96$ ,  $0.9247$  the jet is inertial. In Figure 5.11(a) we observe that for smaller  $\text{Dr}$  the touchdown point moves away from the nozzle. For the jet  $c$ , the parameters are at the border of  $\mathcal{P}_{\text{inert}}$ , and in this limit case the jet touches the coagulator tangentially; see Figure 5.11(a). To illustrate why a jet solution is not possible

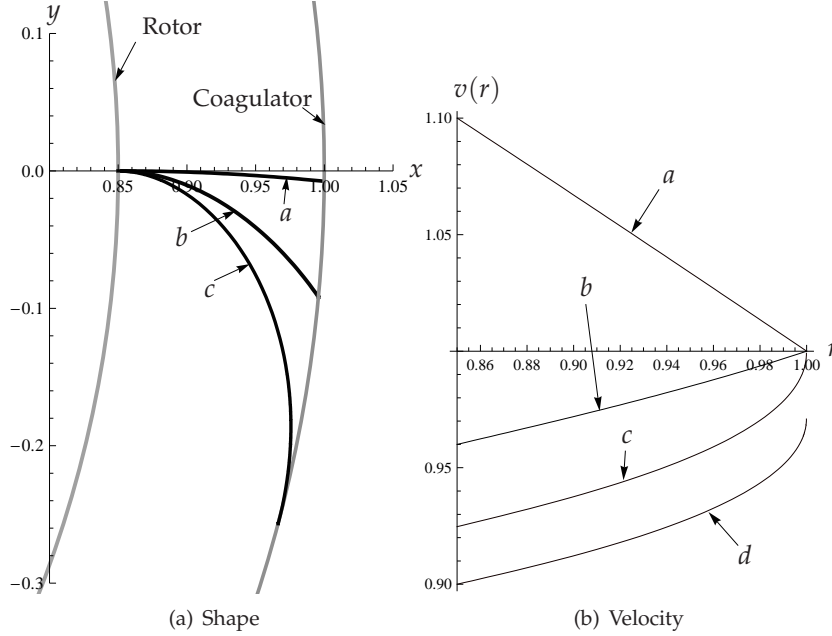


**Figure 5.11:** Numerical simulations of the inertial jet stopping to exist because by decreasing  $Dr$  the parameters leave  $\mathcal{P}_{\text{inert}}$  and enter  $\mathcal{P}_{\text{NE}}$ . The jet shape is depicted in the right figure and the flow velocity in the left figure. The parameters  $B = 3$  and  $R_0 = 0.85$  are the same for all the simulations. The parameter  $Dr$  decreases (i.e.  $Dr = 1.1$ ,  $Dr = 0.96$ , and  $Dr = 0.9247$  correspond to the jets  $a$ ,  $b$ , and  $c$ , respectively). The curve  $d$  with  $Dr = 0.9$  in the right figure indicates that the maximum velocity is less than 1 at  $r = 1$ .

in  $\mathcal{P}_{\text{NE}}$ , we analyse the flow velocity  $v$  in the jet versus the radius vector  $r$ , as presented in Figure 5.11(b), and we focus our attention at the velocity near the coagulator. For the jets  $a$  and  $b$  the functions  $v(r)$  have finite derivatives at the coagulator  $r = 1$ , and they are larger for smaller  $Dr$ . In the limit case  $c$ , the derivative of  $v(r)$  at  $r = 1$  becomes infinite. For even smaller  $Dr$ , than the one of the jet  $c$ , the flow velocity  $v(r)$  is illustrated by the curve  $d$ . In the case  $d$  the value  $v(1)$  is less than 1, and thus the boundary condition (5.37) is not satisfied. Therefore, no steady jet solution exists then.

In the numerical simulations above we observe that for larger  $Dr$  the jet shape approaches to the straight line coinciding with the radial orientation of the nozzle; see jets  $a$  in Figures 5.10(a) and 5.11(a).

### Change of the dimensional parameters

The traces of the dimensional parameters  $R_{\text{rot}}$ ,  $R_{\text{coag}}$ ,  $\nu$ ,  $v_{\text{nozzle}}$ , and  $\Omega$ , as one of them varies in the 3D dimensionless parameter space  $B$ ,  $R_0$ ,  $Dr$ , are depicted in Figure 5.12.

We start from the point corresponding to a real spinning situation with  $R_{\text{rot}} = 0.15$  m,  $R_{\text{coag}} = 0.3$  m,  $\nu = 0.7$  m<sup>2</sup>/s,  $v_{\text{nozzle}} = 1$  m/s, and  $\Omega = 262$  rad/s. For these parameters the jet is viscous-inertial. Then we decrease or increase one physical parameter

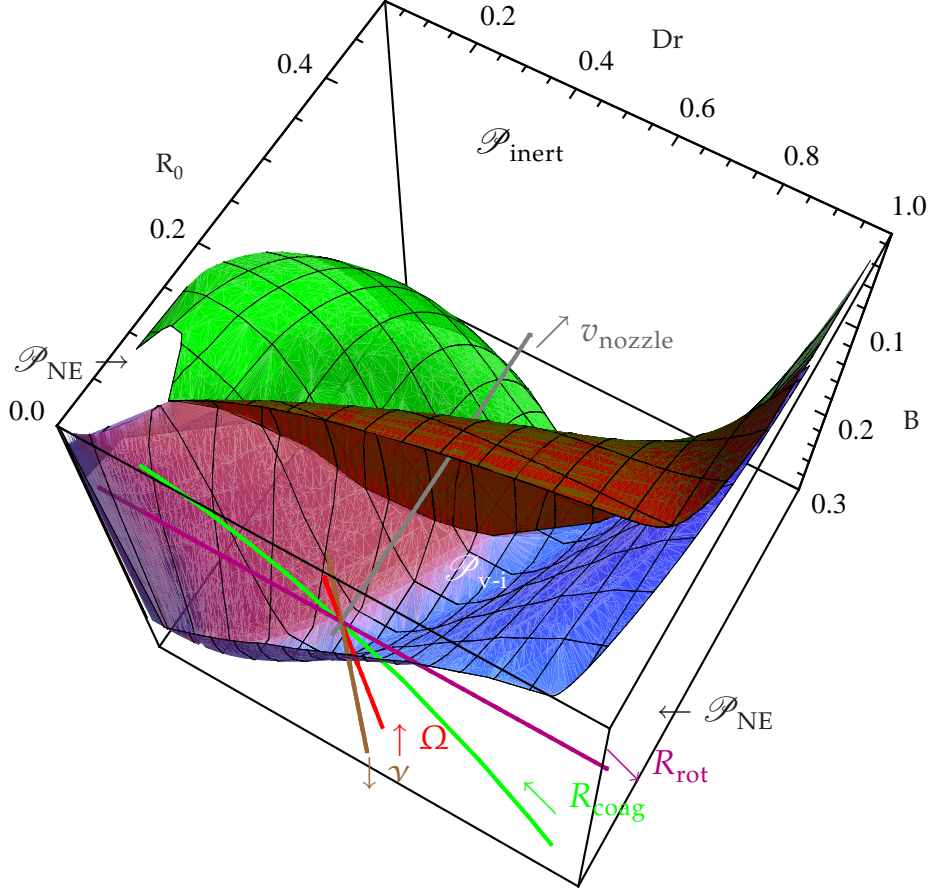


**Figure 5.12:** The trajectories in the 3D parameter space  $B$ ,  $R_0$ ,  $Dr$  (see Figure 5.9) when one of the physical parameters varies ( $R_{rot}$ ,  $R_{coag}$ ,  $\nu$ ,  $v_{nozzle}$ ,  $\Omega$ ). The trajectories starts at the point:  $B = 0.0898$ ,  $R_0 = 0.5$ , and  $Dr = 0.0127$  in  $\mathcal{P}_{v-i}$  (this corresponds to  $R_{rot} = 0.15$  m,  $R_{coag} = 0.3$  m,  $\nu = 0.7$  m<sup>2</sup>/s,  $v_{nozzle} = 1$  m/s, and  $\Omega = 262$  rad/s). Then each physical parameter varies while the rest remains the same. The trajectories corresponding to the changes of  $R_{rot}$ ,  $R_{coag}$ ,  $\nu$ ,  $v_{nozzle}$ , and  $\Omega$  are pink, green, brown, gray, and red curves, respectively. The directions of the trajectories corresponding to the parameter increase are indicated by the arrows.

from its original value while the other parameters remain constant. This leaves a trace in the space  $B$ ,  $R_0$ ,  $Dr^2$  and we focus on the situations when the traces enter another parameter regime.

The viscous-inertial jet solution ceases to exist, because the parameters enter the region  $\mathcal{P}_{NE}$ , if  $\Omega$ ,  $R_{rot}$  or  $R_{coag}$  decreases, and if  $R_{rot}$  or  $\nu$  increases. In case we increase  $v_{nozzle}$  the jet becomes inertial but if  $v_{nozzle} \rightarrow 0$ , the jet remains viscous-inertial. All these observations can be seen in Figure 5.12. Decreasing  $\nu$  will make the jet inertial

<sup>2</sup>The relations between the dimensional and dimensionless parameters are  $B = 3\nu/(\omega R_{coag}^2)$ ,  $R_0 = R_{rot}/R_{coag}$ , and  $Dr = v_{nozzle}/(\Omega R_{coag})$ .

because in the limit case  $\nu = 0$ ,  $B = 0$ ,  $Dr = 0.0127$  and  $R_0 = 0.5$  and this parameter setting is in  $\mathcal{P}_{\text{inert}}$ ; see Figure 5.8.

In the limit case  $\Omega \rightarrow \infty$  we have that  $B \rightarrow 0$ ,  $Dr \rightarrow 0$ , and  $R_0 = 0.5$ , so the jet can be either inertial or viscous-inertial. In the other limit case  $R_{\text{coag}} \rightarrow \infty$  we have that  $B \rightarrow 0$ ,  $Dr \rightarrow 0$ , and  $R_0 \rightarrow 0$ , so the jet can be either inertial or viscous-inertial, or no jet solution exists.

## 5.4 Rotating coagulator and viscous jet

In this section we shortly describe a way how to expand the parameter regions where a steady jet solution exists in such a way that the viscous jet becomes possible. We do this by changing the boundary condition for the velocity at the coagulator, (5.37), by demanding the dimensionless flow velocity at the coagulator  $v(1)$  to be less than 1. Practically this can be done by rotating the coagulator in the counterclockwise direction, in the same direction as the rotor rotates, with angular velocity  $\Omega_{\text{coag}}$ ; see Figure 5.13. We restrict ourselves to  $0 < \Omega_{\text{coag}} < \Omega$ .

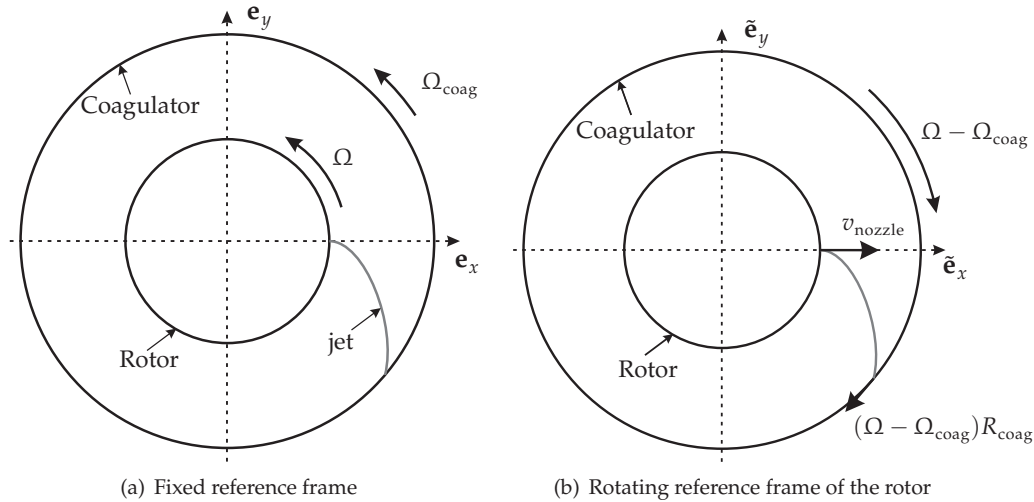


**Figure 5.13:** Rotary spinning with the rotating coagulator. The coagulator rotates with the angular velocity  $\Omega_{\text{coag}}$  in the counterclockwise direction, the same of the rotor.

The system describing the jet is (5.31)-(5.34), (5.36), and (5.38)-(5.40) together with a different boundary condition for  $v(1)$  replacing (5.37). At the coagulator the fluid sticks to it, and because the coagulator rotates, for the flow velocity  $v$  at the coagulator must be

$$v(1) = v_{\text{coag}} = \frac{\Omega - \Omega_{\text{coag}}}{\Omega}. \quad (5.65)$$

Here,  $v_{\text{coag}}$  can have values between one and zero. We also restrict ourselves to the cases



where  $\xi(r) < 0$ ; see (5.43). Thus, the system becomes

$$\xi'(r) = r/v(r), \quad (5.66)$$

$$\xi(r)\phi'(r) = \frac{-\sin(\phi(r))r^2 - v(r)(\xi(r)\sin(\phi(r)) - 2r)}{v(r)r\cos(\phi(r))}, \quad (5.67)$$

$$v'(r) = (v(r)^2 - \xi(r)v(r))/(B\cos(\phi(r))), \quad (5.68)$$

$$\phi(1) = \pi/2, \quad (5.69)$$

$$v(1) = v_{\text{coag}}, \quad (5.70)$$

$$v(R_0) = Dr, \quad (5.71)$$

where we omitted the decoupled equation for  $\beta$ , (5.34). Moreover, because  $\xi$  is negative we prescribe one boundary condition for  $\phi$  at the coagulator (i.e the tangency with the coagulator), and no boundary condition at the nozzle; see (5.39) and (5.40).

**Definition 5.6.** A solution to the system (5.66)-(5.71) is called *viscous jet* if (5.43) holds.

The parameter region for the viscous jet is

$$\mathcal{P}_{\text{visc}} := \{(B, Dr, R_0) \in \mathcal{P} : \text{if viscous jet exists}\}. \quad (5.72)$$

The term viscous jet is used because if (5.43) is true then viscosity is the dominant effect in the momentum transfer through the jet cross-section.

From the next lemma it follows that a viscous jet is possible only for  $v_{\text{coag}} < 0.5$

**Lemma 5.7.** A viscous jet solution is only possible for  $v_{\text{coag}} < 0.5$

*Proof.* By substituting the boundary conditions (5.28), (5.23) and (5.26) into (5.18), taken at the rotor we receive

$$\phi'(s_{\text{end}}) = \frac{-\xi(s_{\text{end}})v(s_{\text{end}}) + 2v(s_{\text{end}}) - 1}{v(s_{\text{end}})\xi(s_{\text{end}})}.$$

The geometrical constraint, which prevent the jet to penetrate the coagulator wall, requires  $\phi'(s_{\text{end}}) \geq 0$ . This gives us the inequality

$$0 < v(s_{\text{end}}) \leq \frac{1}{2 - \xi(s_{\text{end}})} < \frac{1}{2}, \quad (5.73)$$

because according to (5.43),  $\xi$  at the coagulator is negative.  $\square$

We replace the boundary condition (5.71) by

$$\xi(1) = \hat{w}, \quad (5.74)$$

and consider the initial-value problem (5.66)-(5.70) and (5.73) which has the solution  $v(r; \hat{w})$ ,  $\xi(r; \hat{w})$ ,  $\phi(r; \hat{w})$ . We consider this solution till  $v(r; \hat{w}) = 0$ . Thus, the boundary-value problem (5.66)-(5.71) is transformed into the initial-value problem (5.66)-(5.70) and (5.74) plus the algebraic equation for  $\hat{w}$

$$v(R_0; \hat{w}) = Dr. \quad (5.75)$$

From the inequality (5.73) we find the minimum of  $\hat{w}$  for which a viscous jet is possible as

$$\hat{w}_{\min} = -\frac{1 - 2v_{\text{coag}}}{v_{\text{coag}}}. \quad (5.76)$$

Hence in accordance with (5.73),  $\hat{w}_{\min} < 0$ .

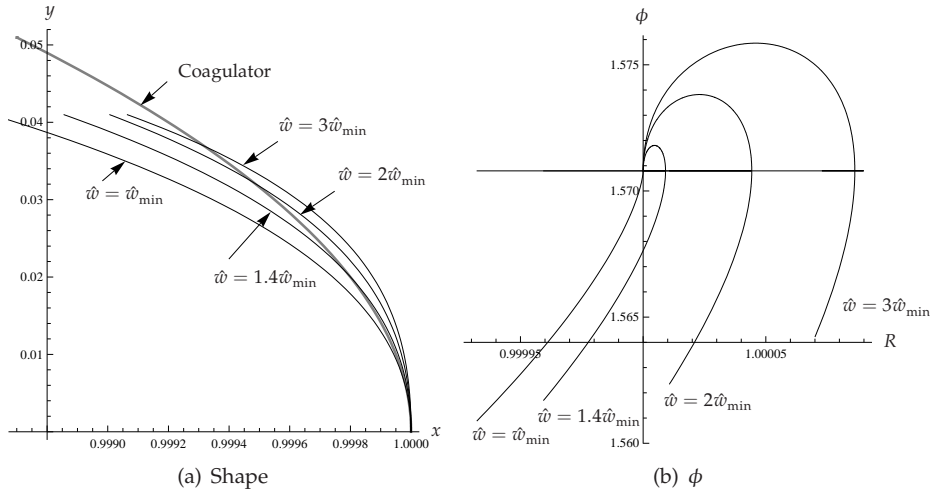


**Figure 5.14:** Solutions for the jet shape near the coagulator and the angle  $\phi$  in case  $\hat{w} < \hat{w}_{\min}$ . Here,  $B = 0.1$ ,  $v_{\text{coag}} = 0.3$ , and  $\hat{w}_{\min} = -1.3333$ .

If  $\hat{w} < \hat{w}_{\min}$ , the angle  $\phi$  first increases, reaches its maximum (which is larger for smaller  $\hat{w}$ ) and then decreases; see Figure 5.14(b). In this case the jet penetrates the coagulator and the penetration is larger for smaller  $\hat{w}$ ; see Figure 5.14(a).

Next we formulate some properties of  $v(r; \hat{w})$ .

**Conjecture 5.8.** The function  $\hat{w} \mapsto v(r; \hat{w})$  strictly increases for  $\hat{w}_{\min} \leq \hat{w} \leq 0$ .

This conjecture is illustrated in Figure 5.15, where we depict  $v(r; \hat{w})$  for several  $\hat{w}$ , varying from 0 to  $\hat{w}_{\min}$ . Note that if  $\hat{w} = 0$ , the jet is viscous-inertial and then no tangency with the coagulator is required. This means that  $v_r(1; \hat{w} = 0)$  is finite whereas  $v_r(1; \hat{w} < 0) = \infty$ ; see Figure 5.15 at  $r = 1$  and  $v = v_{\text{coag}}$ . By Conjecture 5.8, equation (5.75) has a solution only if  $(R_0, Dr)$  lies in the region bounded by the curves  $v(r; \hat{w} = 0)$  and  $v(r; \hat{w}_{\min})$ . The parameter region for the viscous jet  $\mathcal{P}_{\text{visc}}$  is defined as

$$\mathcal{P}_{\text{visc}} := \{(R_0, Dr) : v(R_0; \hat{w} = 0) > Dr \text{ and } Dr > v(R_0; \hat{w}_{\min})\}. \quad (5.77)$$

Numerical simulations of the shape of a viscous jet for increasing values of  $Dr$  are presented in Figure 5.16. When  $Dr$  becomes too large, the viscous jet becomes viscous-inertial. In the first three simulations, *a*, *b* and *c*, the jet is viscous touching the coagulator tangentially. In the simulation *d* the jet is viscous-inertial with  $\xi(1) = 0$  and the jet does not touch the coagulator tangentially. With increasing  $Dr$  the viscous jet shape approaches to the jet shape *d* and close to the coagulator the viscous jet bends steeply to

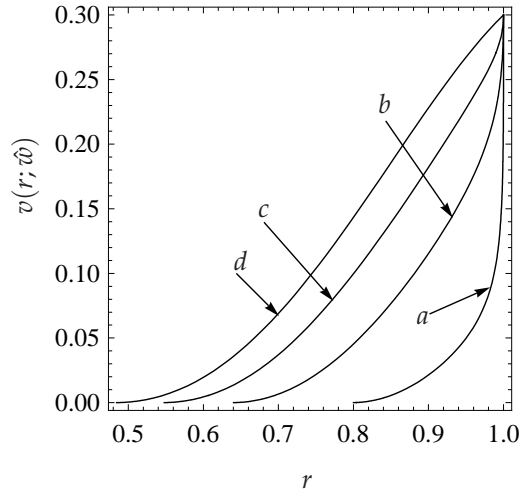


**Figure 5.15:** Flow velocities in the jet,  $v(r; \hat{w})$ , with  $v_{\text{coag}} = 0.3$  and  $B = 0.2$ , for different  $\hat{w}$  (i.e. curves  $a$ ,  $b$ ,  $c$ , and  $d$  for  $\hat{w} = \hat{w}_{\text{min}}$ ,  $\hat{w} = 0.3\hat{w}_{\text{min}}$ ,  $\hat{w} = 0.1\hat{w}_{\text{min}}$ , and  $\hat{w} = 0$ , respectively).

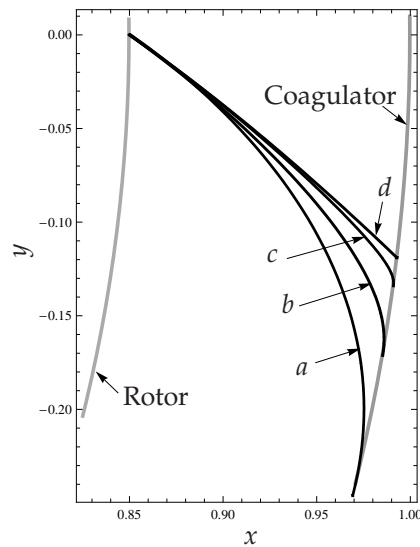


**Figure 5.16:** Numerical simulations of the jet shape for the parameters  $v_{\text{coag}} = 0.3$ ,  $B = 0.2$ ,  $R_0 = 0.85$ . The jets  $a$ ,  $b$ , and  $c$  with  $\text{Dr} = 0.10$ ,  $\text{Dr} = 0.16$ , and  $\text{Dr} = 0.18$ , respectively, are viscous, and the jets touch the coagulator tangentially. The jet  $d$ , with  $\text{Dr} = 0.185$ , is viscous-inertial, and the jet does not touch the coagulator tangentially.

the direction tangent to the coagulator; see the jet shape  $c$  in Figure 5.16. Moreover, the touchdown point with the coagulator moves away from the nozzle if  $\text{Dr}$  decreases.

The regions  $\mathcal{P}_{\text{visc}}$  for different  $v_{\text{coag}}$  and  $B$  are depicted in Figures 5.17 and 5.18. In these figures we distinguish the viscous jet region  $\mathcal{P}_{\text{visc}}$ , the nonexistence region  $\mathcal{P}_{\text{NE},2}$ ,

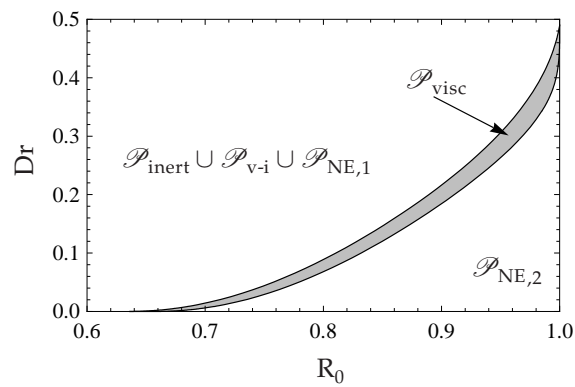
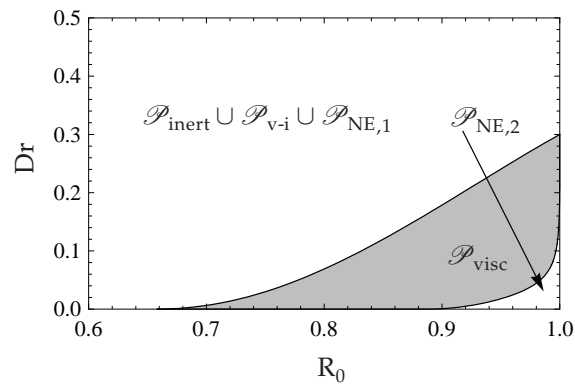
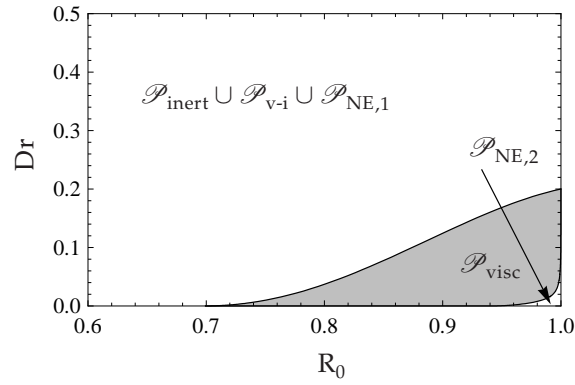


**Figure 5.17:** Parameter regions for viscous jet (grey region) for  $B = 0.1$ , and different  $v_{\text{coag}}$  (i.e.  $v_{\text{coag}} = 0.2$ ,  $v_{\text{coag}} = 0.3$ , and  $v_{\text{coag}} = 0.49$ ).

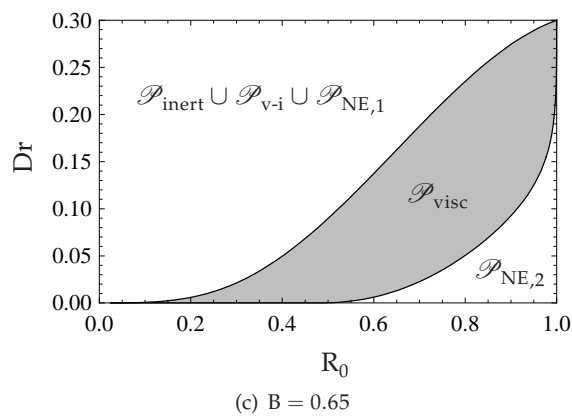
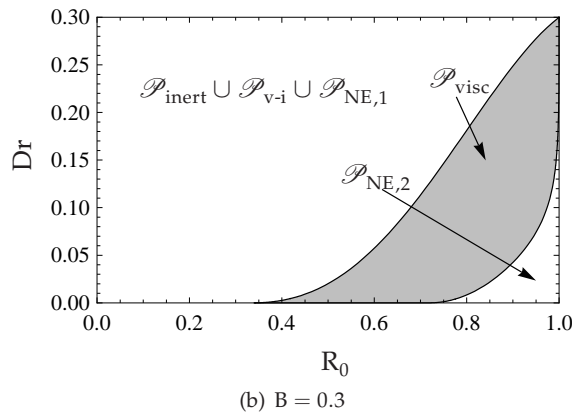
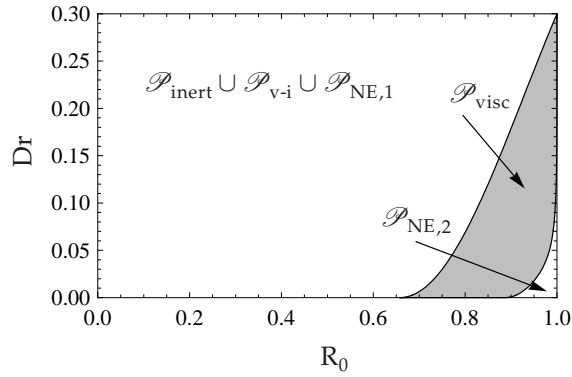


**Figure 5.18:** Parameter regions for viscous jet (grey region) for  $v_{\text{coag}} = 0.3$ , and different  $B$  (i.e.  $B = 0.1$ ,  $B = 0.3$ , and  $B = 0.65$ ).

which is below  $\mathcal{P}_{\text{visc}}$  at the corner  $(1, 0)$ , and the rest region  $\mathcal{P}_{\text{inert}} \cup \mathcal{P}_{\text{v-i}} \cup \mathcal{P}_{\text{NE},1}$ , which is above  $\mathcal{P}_{\text{visc}}$ . The region  $\mathcal{P}_{\text{NE},2}$  is smaller than the one for the non-rotating coagulator

described in Section 5.3.

The regions  $\mathcal{P}_{\text{visc}}$  for different  $v_{\text{coag}}$  are depicted in Figure 5.17. The nonexistence region  $\mathcal{P}_{\text{NE},2}$  shrinks for smaller  $v_{\text{coag}}$  because then the function  $v(R_0; \hat{w}_{\text{min}})$  becomes smaller. On the other hand the function  $v(R_0; 0)$  decreases as  $v_{\text{coag}}$  decreases and there is no clear behaviour of the size of  $\mathcal{P}_{\text{visc}}$  as  $v_{\text{coag}}$  changes. If  $v_{\text{coag}}$  approaches 0.5, the region  $\mathcal{P}_{\text{visc}}$  becomes narrow; see Figure 5.17(c) and  $\mathcal{P}_{\text{visc}}$  disappears if  $v_{\text{coag}} = 0.5$ .

The regions  $\mathcal{P}_{\text{visc}}$  for different  $B$  are depicted in Figure 5.18. The nonexistence region  $\mathcal{P}_{\text{NE},2}$  expands for larger  $B$ , because then  $v(R_0; \hat{w}_{\text{min}})$  increases. The border of the other side of the region  $\mathcal{P}_{\text{visc}}$ , the curve  $v(R_0; 0)$  increases if  $B$  increases. The region  $\mathcal{P}_{\text{visc}}$  expands for larger  $B$  as we see if we compare  $B = 0.1$  and  $B = 0.3$  in Figures 5.18(a) and 5.18(b). For  $B = 0.3$  and  $B = 0.65$  the change of size of  $\mathcal{P}_{\text{visc}}$  is not evident from the Figures 5.18(b) and 5.18(c). For  $B = 0.65$  the curve  $v(R_0; 0)$  ends at the point  $(0,0)$ . Additional investigation involving a study of a situation when the jet does not reach the coagulator, which is beyond the scope of this study, is required to determine  $\mathcal{P}_{\text{visc}}$  for  $B > 0.65$ .

## 5.5 Remark: jet does not reach the coagulator

In this section we shortly discuss a situation, in which, we expect that the jet does not hit the coagulator wall but stays at a certain distance  $R_{\text{end}}$  from the center of the rotor. It appears that there exists a steady jet which becomes perpendicular to radius vector at some distance from the rotor. At this point the viscous force is zero and the fluid particle velocity in the fixed reference frame is zero as well. This means that at  $r = R_{\text{end}}$  the jet leaves a ring trace of motionless fluid. Here, we only describe an example of this situation which is possible for the parameter setting form  $\mathcal{P}_{\text{NE},1}$  for  $B \leq 0.2617$  and from  $\mathcal{P}_{\text{NE}}$  otherwise.

The equations describing this situation are (5.31)-(5.33), and the boundary conditions at the rotor are (5.36) and (5.39). We consider only the part of the jet from  $r = R_0$  to the point  $r = R_{\text{end}}$ , where it reaches the maximum distance from the rotor, and we consider this point as a free point. At the free jet end we prescribe a zero viscous force and we demand the jet to be perpendicular to the radius vector in  $r = R_{\text{end}}$ . The viscous force is defined in (1.7), and this shows that this force is zero if  $v_s = 0$ , which is by (5.19) equivalent to  $\xi = v$ . The system for the three unknown functions  $\xi$ ,  $\phi$ , and  $v$ , and one unknown scalar free end position  $R_{\text{end}}$  is given by

$$\xi'(r) = r/v(r), \quad (5.78)$$

$$\xi(r)\phi'(r) = \frac{-\sin(\phi(r))r^2 - v(r)(\xi(r)\sin(\phi(r)) - 2r)}{v(r)r\cos(\phi(r))}, \quad (5.79)$$

$$v'(r) = (v(r)^2 - \xi(r)v(r))/(B\cos(\phi(r))), \quad (5.80)$$

$$v(R_0) = Dr, \quad (5.81)$$

$$\text{if } \xi(R_0) > 0, \text{ then } \phi(R_0) = 0, \quad (5.82)$$

$$\xi(R_{\text{end}}) = v(R_{\text{end}}), \quad (5.83)$$

$$\phi(R_{\text{end}}) = \pi/2. \quad (5.84)$$

Here, (5.83) follows from the definition of  $\xi$ , (1.14), if  $v_s = 0$  (zero viscous force), while

(5.84) expresses that the jet is perpendicular to the radius in  $r = R_{\text{end}}$ . Moreover, by demanding  $\phi'(R_{\text{end}}) \leq 0$  from (5.79) with (5.83) and (5.84) it follows that

$$R_{\text{end}} = \xi(R_{\text{end}}) = v(R_{\text{end}}). \quad (5.85)$$

Next, we calculate the dimensional fluid particle velocity  $\mathbf{v}$  in the fixed reference frame at  $r = R_{\text{end}}$ . Because of (5.84), (5.5) and (5.7) the fluid at  $r = R_{\text{end}}$  does not move in the radial direction. For the circumferential direction we have that

$$\mathbf{v}_{\mathbf{r}_s} = v(R_{\text{end}})\Omega R_{\text{coag}} - \Omega R_{\text{end}}R_{\text{coag}} \stackrel{(5.85)}{=} 0,$$

where the first term in the difference is the dimensional flow velocity in the rotating reference frame and the second one is the velocity due to the rotating frame.

An example of the jet not reaching the coagulator and staying at some distance from the rotor is given in Figure 5.19. In Figure 5.19(a) we present  $v(r)$  and  $\xi(r)$ , which cross

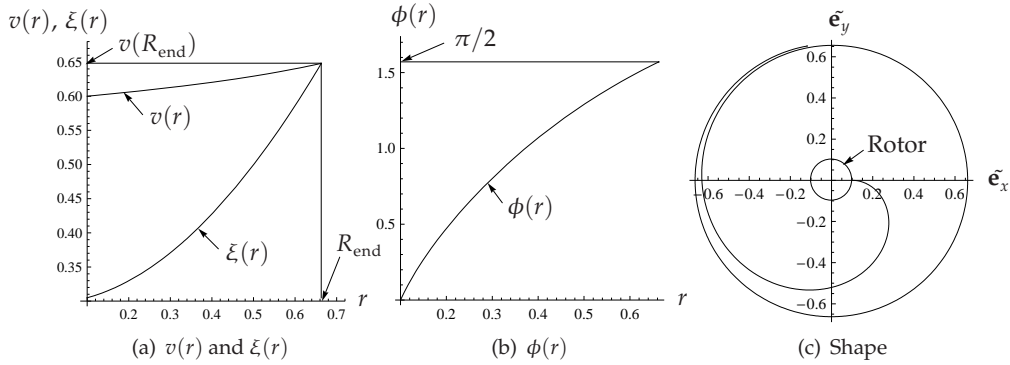


**Figure 5.19:** Numerical simulation of the jet staying at some distance from the rotor. The parameters are  $B = 3$ ,  $R_0 = 1$ ,  $Dr = 0.6$ .

each other at  $r = R_{\text{end}}$ , so the viscous force at the jet free end is zero. At the jet end we have  $R_{\text{end}} = 0.6630$ ,  $v(R_{\text{end}}) = 0.6483$ , and  $\xi(R_{\text{end}}) = 0.6479$ , and (5.85) is satisfied with a relative error of 2% because of our numerical approximation<sup>3</sup>. The angle  $\phi(r)$  reaches  $\pi/2$  at  $r = R_{\text{end}}$ ; see Figure 5.19(b). The jet shape staying at some distance from the rotor is presented in Figure 5.19(c).

A conclusion from the system above is that the jet can propagate away from the rotor to a maximum distance  $R_{\text{end}}$  and, hence, it will never reach the coagulator if  $R_{\text{end}} < 1$ . A solution to (5.78)-(5.84) is  $v(r; w_{\text{crit}})$ ,  $\xi(r; w_{\text{crit}})$ ,  $\phi(r; w_{\text{crit}})$ , and  $R_{\text{end}} = r_{\text{max}}$  in described in Section 5.2. The point  $(R_{\text{end}}, v(R_{\text{end}}))$  is the end point of the curve  $\mathcal{C}_{\text{max}}$  (5.51), which states that a solution for a jet reaching the coagulator does not exist for  $r_{\text{max}} < 1$ . In this respect, the additional restriction should be put on the region  $\mathcal{V}_{\text{reach}}$  and should read  $r_{\text{max}} < 1$ . This restriction is accounted for in our partitioning of the parameter regions in rotary spinning because of (5.63).

A detailed investigation of the system (5.78)-(5.84) describing the jet staying at some distance from the rotor and not reaching the coagulator is beyond the scope of this

<sup>3</sup>We use the shooting method based on the solver `NDSolve` from Mathematica 6.0

thesis. This problem can be put in a broader context for a setup without the coagulator saying that “When does a finite  $R_{\text{end}}$  exist?”. In a limit case  $\nu \rightarrow 0$  the inviscid jet propagates towards infinity and there is no finite  $R_{\text{end}}$ , whereas in the example of this section  $R_{\text{end}}$  is finite.

## 5.6 Conclusions

In this chapter we study the string model of a jet in rotary spinning. The jet is described by three dimensionless parameters. We distinguish the three possible situations for the jet in rotary spinning: inertial jet, viscous-inertial jet, and no steady jet exists. The dimensionless parameter space is partitioned between these three situations. A situation in which the jet is viscous is only possible if the coagulator rotates in the same direction as the rotor with angular velocity large then the half of the angular velocity of the rotor. Finally, we shortly describe a situation in which we find that there exists a steady jet which does not reach the coagulator, but reaches a certain distance from the rotor and stays there.



## Chapter 6

# A numerical method for the dynamic jet

In this chapter we develop a numerical method for the string model of the dynamic jet in drag and rotary spinning. First we formulate the equations and the boundary conditions in a suitable form for the numerical method. Then we discuss a relaxation approach of some equations and boundary conditions. For the numerical method we discretize the equations in the space variable  $s$  and use the MATLAB ODE-solver `ode15s` to integrate in the time variable  $t$ . If the dynamic jet evolves to a steady one we compare the results of the numerical simulation with the solution for the steady jet obtained in drag and rotary spinning. Simulations for the dynamic jet in drag spinning, in which the parameters are changed so that they leave one steady jet regime and enter another one, thus changing the boundary conditions for the jet orientation are performed, and their results are analyzed. Finally we run simulations for the dynamic jet in rotary spinning in the parameter region where the steady jet does not exist because the desired flow velocity at the coagulator is not reached.

### 6.1 Numerical method

In this section we rewrite the equations and the boundary conditions in drag and rotary spinning in a more convenient form. To this end, we introduce a relaxation of some of the equations and boundary conditions. Finally, we discretize the equations in the space variable  $s$ .

#### 6.1.1 Equations for dynamic jet in drag spinning

The equations for the dynamic jet in drag spinning follow from (1.2), (1.8), and (1.4) with gravity as the body force ( $\mathbf{a}_B = \mathbf{g}$ )

$$\mathcal{A}_t(s, t) + (\mathcal{A}(s, t)v(s, t))_s = 0, \quad (6.1)$$

$$\mathbf{r}_{tt} + (v_t + vv_s)\mathbf{r}_s + v^2\mathbf{r}_{ss} + 2v\mathbf{r}_{st} = \frac{(\mathcal{A}v_s\mathbf{r}_s)_s}{\mathcal{A}} - A\mathbf{e}_y, \quad (6.2)$$

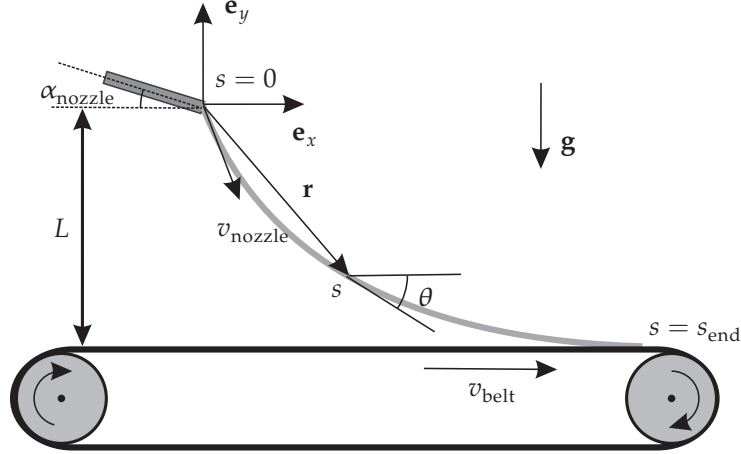


**Figure 6.1:** A schematic picture of the dynamic jet model in drag spinning. The jet emerges from the nozzle with the flow velocity  $v_{\text{nozzle}}$  and falls under the gravity  $\mathbf{g}$  onto the belt moving with the velocity  $v_{\text{belt}}$ . The jet is parameterized by its length  $s$  with  $s = 0$  at the nozzle and  $s = s_{\text{end}}$  at the belt. The jet position  $\mathbf{r}$  is described in the Cartesian coordinate system  $\mathbf{e}_x \mathbf{e}_y$ . The angle  $\theta$  is the angle between the horizontal and the jet. The distance between the belt and the nozzle is  $L$ , the nozzle orientation is  $\alpha_{\text{nozzle}}$ .

$$\|\mathbf{r}_s\| = 1, \quad (6.3)$$

for  $s \in (0, s_{\text{end}}(t))$  and  $t \in (0, \infty)$ . Here we present the system after scaling<sup>1</sup>, where  $s$  is the arc length,  $t$  the time,  $\mathbf{r}$  the position vector,  $v$  the flow velocity in the jet,  $\mathcal{A}$  the cross-sectional area of the jet, and  $s_{\text{end}}(t)$  is the jet length. The schematic picture of the model is presented in Figure 6.1. The angle  $\theta$  is the angle between the jet direction  $\mathbf{r}_s$  and the horizontal, and it is defined as

$$\theta(s, t) = \arctan \left( \frac{y(s, t)}{x(s, t)} \right). \quad (6.4)$$

The unknowns of the problem are one vector function  $\mathbf{r}(s, t)$ , two scalar functions  $v(s, t)$  and  $\mathcal{A}(s, t)$ , and one scalar function  $s_{\text{end}}(t)$ .

<sup>1</sup>We scale the system in the same way as for the steady jet in Section 3.1, i.e. the length  $s$  is scaled with respect to  $3\nu/v_{\text{nozzle}}$  ( $\nu$  is the kinematic viscosity), the cross-sectional area  $\mathcal{A}$  with respect to  $\mathcal{A}_{\text{nozzle}}$ , and the velocity  $v$  with respect to  $v_{\text{nozzle}}$ . Similarly to the steady jet, the system is fully characterized by the three dimensionless numbers  $A = 3g\nu/v_{\text{nozzle}}^3$   $\text{Re} = v_{\text{nozzle}}L/(3\nu)$  the Reynolds number,  $\text{Dr} = v_{\text{belt}}/v_{\text{nozzle}}$  the draw ratio.

The boundary conditions for (6.1)- (6.3) are given in (2.11)- (2.15) and Remark 2.2

$$v(0, t) = 1, \quad (6.5)$$

$$v(s_{\text{end}}(t), t) = D\mathbf{r} - x_t(s_{\text{end}}(t), t) + s'_{\text{end}}(t), \quad (6.6)$$

$$\mathbf{r}(0, t) = \mathbf{r}_{\text{nozzle}} = \mathbf{0}, \quad (6.7)$$

$$\mathcal{A}(0, t) = 1, \quad (6.8)$$

$$y(s_{\text{end}}(t), t) = -\text{Re}, \quad (6.9)$$

$$\text{if } \xi(0, t) > 0, \text{ then } \theta(0, t) = \alpha_{\text{nozzle}}, \quad (6.10)$$

$$\text{if } \xi(s_{\text{end}}(t), t) < 0, \text{ then } \theta(s_{\text{end}}(t), t) = 0. \quad (6.11)$$

Here  $\xi = v - v_s/v$ , (2.22). The remaining model parameters are described in Section 2.1. Next, we write  $\mathbf{r}_s = (\cos(\theta), \sin(\theta))$ , and then the components  $x$  and  $y$  of  $\mathbf{r}$  are written in terms of the angle  $\theta$  (with use of (6.7)) as

$$x(s, t) = \int_0^s \cos(\theta(\tilde{s}, t)) d\tilde{s}, \quad y(s, t) = \int_0^s \sin(\theta(\tilde{s}, t)) d\tilde{s}. \quad (6.12)$$

Consequently

$$x_t(s, t) = - \int_0^s \sin(\theta(\tilde{s}, t)) \zeta(\tilde{s}, t) d\tilde{s}, \quad y_t(s, t) = \int_0^s \cos(\theta(\tilde{s}, t)) \zeta(\tilde{s}, t) d\tilde{s}, \quad (6.13)$$

and

$$\begin{aligned} x_{tt}(s, t) &= - \int_0^s \left[ \cos(\theta(\tilde{s}, t)) \zeta(\tilde{s}, t)^2 + \sin(\theta(\tilde{s}, t)) \zeta_t(\tilde{s}, t) \right] d\tilde{s}, \\ y_{tt}(s, t) &= \int_0^s \left[ -\sin(\theta(\tilde{s}, t)) \zeta(\tilde{s}, t)^2 + \cos(\theta(\tilde{s}, t)) \zeta_t(\tilde{s}, t) \right] d\tilde{s}, \end{aligned} \quad (6.14)$$

where

$$\zeta = \theta_t. \quad (6.15)$$

By taking the inner products of (6.2) with  $\mathbf{r}_s$  and  $\mathbf{r}_s^\perp$  footnoteHere  $\mathbf{r}_s^\perp$  is a perpendicular vector to  $\mathbf{r}_s$  defined as  $\mathbf{r}_{ss} = \mathbf{r}_s^\perp \theta_s$ , i.e.  $\mathbf{r}_s^\perp = (-\sin(\theta), \cos(\theta))$ , we obtain

$$v_t + (\mathbf{r}_{tt}, \mathbf{r}_s) = v_{ss} - \left( v - \frac{\mathcal{A}_s}{\mathcal{A}} \right) v_s - A \sin(\theta), \quad (6.16)$$

and

$$(\mathbf{r}_{tt}, \mathbf{r}_s^\perp) = -2v\zeta - v\xi\theta_s - A \cos(\theta). \quad (6.17)$$

A differential equation for  $s_{\text{end}}(t)$  we derive by differentiation of (6.9) with respect to  $t$

$$s'_{\text{end}}(t) = - \frac{y_t(s_{\text{end}}(t), t)}{\sin(\theta(s_{\text{end}}(t), t))}. \quad (6.18)$$

We scale the arc length  $s$  according to  $\hat{s} = s/s_{\text{end}}(t)$ , so that  $\hat{s} \in (0, 1)$ . We illustrate the result of scaling on the differentiation with respect to the time and the space variables

by taking as an example of the unknown function of  $s$   $v(s, t) = \hat{v}(\hat{s}, t)$ , so

$$v_s(s, t) = \frac{1}{s_{\text{end}}(t)} \hat{v}_{\hat{s}}(\hat{s}, t)$$

and

$$v_t(s, t) = v_t(\hat{s}, t) - \frac{\hat{s}s'_{\text{end}}}{s_{\text{end}}} v_{\hat{s}}(\hat{s}, t).$$

Further on we omit the hats. The system (6.16), (6.17), (6.15), (6.1), (6.18), (6.5), (6.6), (6.8), (6.10), and (6.11) after scaling and with use of (6.12), (6.13), and (6.14) becomes

$$\begin{aligned} v_t + s_{\text{end}} \mathcal{J}_a(\zeta_t, \theta) &= -s_{\text{end}} \cos(\theta) \mathcal{J}_c(\zeta_s, \zeta, \theta) - s_{\text{end}} \sin(\theta) \mathcal{J}_d(\zeta_s, \zeta, \theta) \\ &\quad + v_{ss}/s_{\text{end}}^2 + \left( \frac{\mathcal{A}_s}{s_{\text{end}} \mathcal{A}} + s s'_{\text{end}} - v \right) v_s/s_{\text{end}} - A \sin(\theta), \end{aligned} \quad (6.19)$$

$$\begin{aligned} s_{\text{end}} \mathcal{J}_b(\zeta_t, \theta) &= s_{\text{end}} \sin(\theta) \mathcal{J}_c(\zeta_s, \zeta, \theta) - s_{\text{end}} \cos(\theta) \mathcal{J}_d(\zeta_s, \zeta, \theta) \\ &\quad - v \xi \theta_s/s_{\text{end}} - 2v\zeta - A \cos(\theta), \end{aligned} \quad (6.20)$$

$$\theta_t = \zeta + s \theta_s s'_{\text{end}}/s_{\text{end}}, \quad (6.21)$$

$$\mathcal{A}_t = (s \mathcal{A}_s s'_{\text{end}} - \mathcal{A} v_s - v \mathcal{A}_s)/s_{\text{end}}, \quad (6.22)$$

$$s'_{\text{end}}(t) = - \frac{s_{\text{end}}(t) \int_0^1 \cos(\theta(\tilde{s}, t)) \zeta(\tilde{s}, t) d\tilde{s}}{\sin(\theta(1, t))}, \quad (6.23)$$

$$v(0, t) = 1, \quad (6.24)$$

$$v(1, t) = v_{\text{d,b}}(t), \quad (6.25)$$

$$\mathcal{A}(0, t) = 1, \quad (6.26)$$

$$\text{if } \xi(0, t) > 0 \text{ then } \theta(0, t) = \alpha_{\text{nozzle}}, \quad (6.27)$$

$$\text{if } \xi(1, t) < 0 \text{ then } \theta(1, t) = 0, \quad (6.28)$$

where  $\xi = v - v_s/(s_{\text{end}} v)$ , and

$$\mathcal{J}_a(\zeta_t, \theta) = \int_0^s [\sin(\theta(s, t) - \theta(\tilde{s}, t)) \zeta_t(\tilde{s}, t)] d\tilde{s},$$

$$\mathcal{J}_b(\zeta_t, \theta) = \int_0^s [\cos(\theta(s, t) - \theta(\tilde{s}, t)) \zeta_t(\tilde{s}, t)] d\tilde{s},$$

$$\mathcal{J}_c(\zeta_s, \zeta, \theta) = \int_0^s [-\cos(\theta(\tilde{s}, t)) \zeta(\tilde{s}, t)^2 + \tilde{s} \sin(\theta(\tilde{s}, t)) \zeta_s(\tilde{s}, t) s'_{\text{end}}(t)/s_{\text{end}}] d\tilde{s},$$

$$\mathcal{J}_d(\zeta_s, \zeta, \theta) = \int_0^s [-\sin(\theta(\tilde{s}, t)) \zeta(\tilde{s}, t)^2 - \tilde{s} \cos(\theta(\tilde{s}, t)) \zeta_s(\tilde{s}, t) s'_{\text{end}}(t)/s_{\text{end}}] d\tilde{s},$$

$$v_{\text{d,b}}(t) = \text{Dr} + s_{\text{end}}(t) \int_0^1 \sin(\theta(\tilde{s}, t)) \zeta(\tilde{s}, t) d\tilde{s} - s'_{\text{end}}(t) (\cos(\theta(1, t)) - 1),$$

for  $s \in (0, 1)$ , and  $t > 0$ .

### 6.1.2 Relaxation forms of some equations and boundary conditions

The system (6.19)-(6.28), as it is now, is not applicable for a numerical method because of following reasons. The ODE for  $s'_{\text{end}}(t)$  (6.23), which originates from the condition (6.9), becomes singular when the jet touches the belt tangentially  $\theta(1, t) = 0$ . If  $\xi$  at  $s = 0$  or  $s = 1$  changes a sign the boundary conditions for  $\theta$  (6.27) and (6.28) changes, which can cause a jump of  $\theta$  at  $s = 0$  or  $s = 1$  causing difficulties for a numerical method. It also appears that the boundary condition for  $v$  at the belt (6.25)  $v_{\text{d,b}}(t)$  changes suddenly at the initial phase of our simulations, and the solver can not cope with this change producing a non-convergent result. All these problems require relaxations of (6.23), (6.25), (6.27), and (6.28), which is done in this subsection.

#### Relaxation form of (6.23)

The equation (6.23) has a singularity when  $\theta(1, t) = 0$ , occurring when the jet touches the belt tangentially. To avoid this singularity we replace (6.23) by an alternative equation

$$s'_{\text{end}}(t) = p_1 \left( \text{Re} + s_{\text{end}}(t) \int_0^1 \sin(\theta(\tilde{s}, t)) d\tilde{s} \right) + \begin{cases} -\frac{s_{\text{end}}(t) \int_0^1 \cos(\theta(\tilde{s}, t)) \zeta(\tilde{s}, t) d\tilde{s}}{\sin(\theta(1, t))} & \text{if } \theta(1, t) > \epsilon_0, \\ 0 & \text{if } \theta(1, t) \leq \epsilon_0. \end{cases} \quad (6.29)$$

The first term in (6.29) penalizes the deviation of  $y(1, t)$  from  $\text{Re}$  and changes  $s_{\text{end}}$  so that (6.9) is satisfied. In the second term in (6.29) we cut off a possible singularity at  $\theta(1, t) = 0$  in (6.23) by introducing a small parameter  $\epsilon_0$ . The first term in 6.29 prevents a numerical drift appearing due to differentiation of the original condition (6.9) if  $\theta(1, t) > \epsilon_0$ , and replaces (6.23) by an equivalent condition if  $\theta(1, t) \leq \epsilon_0$ . In such a way the value of  $s'_{\text{end}}(t)$  is always well defined.

When using (6.29) to calculate  $s_{\text{end}}(t)$ , we introduce an error in the boundary condition (6.9) due to the differentiation (numerical drift) of (6.9), and the modification of (6.23). The relative error is calculated from

$$\mathcal{E}_{\text{belt}} = \frac{\text{Re} + y(1, t)}{\text{Re}}. \quad (6.30)$$

To make the error as small as possible we need to choose a value of  $p_1$  as large as possible and a value of  $\epsilon_0$  as small as possible.

#### Relaxation form of (6.25)

The boundary condition (6.25) is replaced by the differential equation

$$v_t(1, t) = p_2(v_{\text{d,b}}(t) - v(1, t)), \quad (6.31)$$

where  $p_2$  is a constant. We do this replacement to avoid problems during time integration appearing due to fast jet end movements in our simulations, causing sudden change of  $v_{\text{d,b}}(t)$ . The equation (6.31) forces  $v(1, t)$  exponentially approach to  $v_{\text{d,b}}(t)$ .

The relative error introduced by (6.31) is calculated from

$$\mathcal{E}_v = \frac{v_{d,b}(t) - v(1, t)}{v(1, t)}. \quad (6.32)$$

To make this error as small as possible we need to choose a value of  $p_2$  as large as possible.

### Relaxation forms of (6.27) and (6.28)

The boundary conditions (6.27) and (6.28) are replaced by the differential equations

$$\text{if } \xi(0, t) > 0 \text{ then } \theta_t(0, t) = p_3(\alpha_{\text{nozzle}} - \theta(0, t)), \quad (6.33)$$

$$\text{if } \xi(1, t) < 0 \text{ then } \theta_t(1, t) = -p_4\theta(1, t), \quad (6.34)$$

where  $p_3$  and  $p_4$  are constants to be chosen as large as possible. This should avoid a sudden change of  $\theta$  at the boundaries which can occur due to sudden change of boundary conditions when the sign of  $\xi$  at the jet ends changes.

Errors to  $\theta$  introduced by (6.33)-(6.34) occurs only when the sign of  $\xi$  at the jet ends changes, and they decay in time to zero after the sign change. This decay is faster if  $p_3$  and  $p_4$  are larger.

### Another way of avoiding a singularity in (6.23)

Another way of avoiding a singularity while computing  $s'_{\text{end}}(t)$  is to replace the boundary condition (6.28) by

$$\text{if } \xi(1, t) < 0 \text{ then } \theta(1, t) = \epsilon_0, \quad (6.35)$$

where  $\epsilon_0$  is the same as in (6.29). In this case if  $\xi(1, t) < 0$  we avoid using the “if” statement in (6.29), and (6.34) becomes

$$\text{if } \xi(1, t) < 0 \text{ then } \theta_t(1, t) = p_4(\epsilon_0 - \theta(1, t)). \quad (6.36)$$

Situations where  $\theta(1, t) < \epsilon_0$  for arbitrarily small  $\epsilon_0$  if  $\xi(1, t) \geq 0$  are not possible for the steady jet. We expect that by using (6.36)  $\theta(1, t) \geq \epsilon_0$  for all  $t$ , and as a consequence we avoid using the “if” statement in (6.29) provided that we do not start with an initial shape with  $\theta(1, 0) < \epsilon_0$ . Therefore, whenever possible we use (6.36) instead of (6.34) in drag spinning simulations.

## 6.1.3 Numerical scheme for the dynamic jet in drag spinning

We construct a numerical method for the system (6.19), (6.20), (6.21), (6.22), (6.24), (6.26), (6.29), (6.31), (6.33), and (6.36) by discretization in  $s$  and use ODE-solver `od15s` from MATLAB to integrate in time; see [72].

We discretize functions of  $s$  as follows: the functions  $v(s, t)$ ,  $\zeta(s, t)$ ,  $\theta(s, t)$  are  $\mathcal{A}(s, t)$  approximated by  $v_i(t) \approx v(s_i, t)$ ,  $\zeta_i(t) \approx \zeta(s_i, t)$ ,  $\theta_i(t) \approx \theta(s_i, t)$ , and  $\mathcal{A}_i(t) \approx \mathcal{A}(s_i, t)$ , where  $s_i = (i - 1)h$ ,  $h = 1/n$ , and  $i = 1 \dots n + 1$ , and  $n \in \mathbb{N}$ . To approximate  $v_s$  and  $v_{ss}$

we use a forward difference for  $v_s$  and a central difference for  $v_{ss}$

$$v_s(s_i) \approx \frac{v_{i+1} - v_i}{h}, \quad i = 1 \dots n, \quad \text{and} \quad v_{ss}(s_i) \approx \frac{v_{i+1} - 2v_i + v_{i-1}}{h^2}, \quad i = 2 \dots n. \quad (6.37)$$

The value  $v_s(s_{n+1})$  is linearly extrapolated as

$$v_s(s_{n+1}) \approx 2v_s(s_n) - v_s(s_{n-1}). \quad (6.38)$$

We approximate  $\mathcal{A}_s$  using a first-order upwind scheme which results in a backward difference because  $v > 0$ , and linearly extrapolate  $\mathcal{A}_s(s_1)$ :

$$\mathcal{A}_s(s_i) \approx \frac{\mathcal{A}_i - \mathcal{A}_{i-1}}{h}, \quad i = 2 \dots n + 1, \quad \text{and} \quad \mathcal{A}_s(s_1) \approx 2\mathcal{A}_s(s_2) - \mathcal{A}_s(s_3). \quad (6.39)$$

The values of  $\xi_i$  are computed as

$$\xi_i = v_i - v_s(s_i) / (s_{\text{end}} v_i). \quad (6.40)$$

To approximate  $\theta_s$  and  $\zeta_s$  we use a first-order upwind scheme, which follows from the characteristic direction in the equation for  $\theta$  (2.28),

$$\theta_s(s_i) \approx H(\xi_i) \frac{\theta_i - \theta_{i-1}}{h} + (1 - H(\xi_i)) \frac{\theta_{i+1} - \theta_i}{h}, \quad (6.41)$$

and

$$\zeta_s(s_i) \approx H(\xi_i) \frac{\zeta_i - \zeta_{i-1}}{h} + (1 - H(\xi_i)) \frac{\zeta_{i+1} - \zeta_i}{h}, \quad (6.42)$$

where

$$H(s) = \begin{cases} 1, & s > 0 \\ 1/2, & s = 0 \\ 0, & s < 0 \end{cases} \quad (6.43)$$

is the Heaviside function. The integrals  $\mathcal{J}_a$ ,  $\mathcal{J}_b$ ,  $\mathcal{J}_c$ , and  $\mathcal{J}_d$  are approximated using a composite midpoint rule on a shifted mesh<sup>2</sup> as

$$\mathcal{J}_a(s_i) \approx \frac{h}{2} \sin(\theta_i - \theta_1) \zeta_{1,t} + h \sum_{j=2}^{i-1} \sin(\theta_i - \theta_j) \zeta_{j,t}, \quad i = 2 \dots n, \quad (6.44)$$

<sup>2</sup>This approximation allows us to keep the unknown  $\zeta_{1,t}$  and  $\zeta_{n+1,t}$  in the resulting system in such a form that makes it possible to explicitly find them after inverting the matrix  $\mathbb{M}(\mathbf{Y})$  in the system (6.54). The same is not possible for a rectangle rule. In such a way we can use an explicit numerical integration in  $t$ .

$$\mathcal{J}_b(s_1) \approx \frac{h}{2} \zeta_{1,t}, \quad (6.45)$$

$$\mathcal{J}_b(s_i) \approx \frac{h}{2} (\cos(\theta_i - \theta_1) \zeta_{i,t} + 2\zeta_{i,t}) + h \sum_{j=2}^{i-1} \cos(\theta_i - \theta_j) \zeta_{j,t}, \quad i = 2 \dots n, \quad (6.46)$$

$$\mathcal{J}_b(s_{n+1}) \approx \frac{h}{2} (\cos(\theta_{n+1} - \theta_1) \zeta_{n+1,t} + \zeta_{n+1,t}) + h \sum_{j=2}^n \cos(\theta_i - \theta_j) \zeta_{j,t}. \quad (6.47)$$

$$\mathcal{J}_c(s_1) \approx -\frac{h}{2} \cos(\theta_1) \zeta_1^2, \quad (6.48)$$

$$\mathcal{J}_c(s_i) \approx \mathcal{J}_{c,1} + h \sum_{j=2}^i \left( -\cos(\theta_j) \zeta_j^2 + s_j \sin(\theta_j) \zeta_{j,s'_{\text{end}}}/s_{\text{end}} \right), \quad i = 2 \dots n, \quad (6.49)$$

$$\mathcal{J}_c(s_{n+1}) \approx \mathcal{J}_{c,n} + \frac{h}{2} (-\cos(\theta_{n+1}) \zeta_{n+1}^2 + \sin(\theta_{n+1}) \zeta_{n+1,s'_{\text{end}}}/s_{\text{end}}), \quad (6.50)$$

and

$$\mathcal{J}_d(s_1) \approx -\frac{h}{2} \sin(\theta_1) \zeta_1^2, \quad (6.51)$$

$$\mathcal{J}_d(s_i) \approx \mathcal{J}_{d,1} - h \sum_{j=2}^i \left( \sin(\theta_j) \zeta_j^2 + s_j \cos(\theta_j) \zeta_{j,s'_{\text{end}}}/s_{\text{end}} \right), \quad i = 2 \dots n, \quad (6.52)$$

$$\mathcal{J}_d(s_{n+1}) \approx \mathcal{J}_{d,n} - \frac{h}{2} (\sin(\theta_{n+1}) \zeta_{n+1}^2 + \cos(\theta_{n+1}) \zeta_{n+1,s'_{\text{end}}}/s_{\text{end}}). \quad (6.53)$$

In the next formulas of this section we use the subindex  $i$  to indicate an approximation of the corresponding function or its  $s$  derivatives at the point  $s_i$ . After the space discretization we obtain a system of ODEs in time, written as

$$\mathbb{M}(\mathbf{Y}) \mathbf{Y}_t = \mathbf{G}(\mathbf{Y}). \quad (6.54)$$

Here  $\mathbf{Y}$  is a column vector of length  $4n + 5$ ,

$$\mathbf{Y} = (\zeta_1, \dots, \zeta_{n+1}, v_1, \dots, v_{n+1}, \theta_1, \dots, \theta_{n+1}, \mathcal{A}_1, \dots, \mathcal{A}_{n+1}, s_{\text{end}})^T, \quad (6.55)$$

and the matrix  $\mathbb{M}(\mathbf{Y}, t)$ , of size  $4n + 5 \times 4n + 5$ , has the block form

$$\mathbb{M}(\mathbf{Y}) = \begin{pmatrix} \mathbb{B}_{a,n+1 \times n+1}(\mathbf{Y}) & \mathbb{Z}_{n+1 \times n+1} & \mathbb{Z}_{2n+2 \times 2n+3} \\ \mathbb{B}_{b,n+1 \times n+1}(\mathbf{Y}) & \mathbb{I}_{n+1 \times n+1} & \\ & \mathbb{Z}_{2n+3 \times 2n+2} & \mathbb{I}_{2n+3 \times 2n+3} \end{pmatrix},$$

where  $\mathbb{I}$  denotes the identity matrix, and  $\mathbb{Z}$  the zero matrix. The structure of the matrix  $\mathbb{B}_{a,n+1 \times n+1}(\mathbf{Y})$  is given by  $\mathcal{J}_b(s_i)$  and it depends on the signs of  $\xi_1$  and  $\xi_{n+1}$ . When  $\xi_1 \leq 0$



and  $\xi_{n+1} \geq 0$   $\mathbb{B}_{a,n+1 \times n+1}(\mathbf{Y})$  has the form

$$\mathbb{B}_{a,n+1 \times n+1}(\mathbf{Y}) = h s_{\text{end}} \begin{pmatrix} 1/2 & & & & & \\ \cos(\theta_2 - \theta_1) & 1 & & & & 0 \\ \vdots & \ddots & & \ddots & & \\ \cos(\theta_n - \theta_1) & \dots & \cos(\theta_n - \theta_{n-1}) & & & 1 \\ \cos(\theta_{n+1} - \theta_1) & \dots & \cos(\theta_{n+1} - \theta_{n-1}) & \cos(\theta_{n+1} - \theta_n) & 1/2 & \end{pmatrix}. \quad (6.56)$$

If  $\xi_1 > 0$ , the first row in  $\mathbb{B}_{a,n+1 \times n+1}(\mathbf{Y})$  is replaced by

$$(1, 0, \dots, 0),$$

and if  $\xi_{n+1} < 0$ , the last row in  $\mathbb{B}_{a,n+1 \times n+1}(\mathbf{Y})$  is replaced by

$$(0, \dots, 0, 1),$$

The structure of the matrix  $\mathbb{B}_{b,n+1 \times n+1}(\mathbf{Y})$  follows from  $\mathcal{J}_a(s_i)$  as

$$\mathbb{B}_{b,n+1 \times n+1}(\mathbf{Y}) = h s_{\text{end}} \begin{pmatrix} 0 & 0 & & & & \\ \frac{\sin(\theta_2 - \theta_1)}{2} & 0 & 0 & & & 0 \\ \frac{\sin(\theta_3 - \theta_1)}{2} & \sin(\theta_3 - \theta_2) & 0 & & & \\ \vdots & \vdots & \ddots & \ddots & & \ddots \\ \frac{\sin(\theta_n - \theta_1)}{2} & \sin(\theta_n - \theta_2) & \dots & \sin(\theta_n - \theta_{n-1}) & 0 & 0 \\ 0 & 0 & \dots & 0 & 0 & 0 \end{pmatrix}. \quad (6.57)$$

Finally the right-hand-side column vector  $\mathbf{G}(\mathbf{Y})$  in (6.54) follows from the right-hand-sides of (6.19), (6.20), (6.21), (6.22), (6.24), (6.26), (6.29), (6.31), (6.33), and (6.34) as

$$\mathbf{G}(\mathbf{Y})_1 = \begin{cases} s_{\text{end}} \sin(\theta_1) \mathcal{J}_{c,1} - s_{\text{end}} \cos(\theta_1) \mathcal{J}_{d,1} & \xi_1 \leq 0, \\ -\frac{v_1 \xi_1 \theta_{1,s}}{s_{\text{end}}} - 2v_1 \zeta_1 - A \cos(\theta_1), & \xi_1 > 0, \\ 0, & \xi_1 > 0, \end{cases}$$

$$\mathbf{G}(\mathbf{Y})_i = s_{\text{end}} \sin(\theta_i) \mathcal{J}_{c,i} - s_{\text{end}} \cos(\theta_i) \mathcal{J}_{d,i} - \frac{v_i \xi_i \theta_{i,s}}{s_{\text{end}}} - 2v_i \zeta_i - A \cos(\theta_i), \quad i = 2, \dots, n,$$

$$\mathbf{G}(\mathbf{Y})_{n+1} = \begin{cases} s_{\text{end}} \sin(\theta_{n+1}) \mathcal{J}_{c,n+1} - s_{\text{end}} \cos(\theta_{n+1}) \mathcal{J}_{d,n+1} & \xi_{n+1} \geq 0, \\ -\frac{v_{n+1} \xi_{n+1} \theta_{n+1,s}}{s_{\text{end}}} - 2v_{n+1} \zeta_{n+1} - A \cos(\theta_{n+1}), & \xi_{n+1} < 0, \\ 0, & \xi_{n+1} < 0, \end{cases}$$

$$\begin{aligned}
\mathbf{G}(\mathbf{Y})_{n+2} &= 0, \\
\mathbf{G}(\mathbf{Y})_{n+1+i} &= -s_{\text{end}} \cos(\theta_i) \mathcal{J}_{c,i} - s_{\text{end}} \sin(\theta_i) \mathcal{J}_{d,i} \\
&+ \frac{v_{i,ss}}{s_{\text{end}}^2} + \left( \frac{\mathcal{A}_{i,s}}{s_{\text{end}} \mathcal{A}_i} + s_i s'_{\text{end}} - v_i \right) \frac{v_{i,s}}{s_{\text{end}}} - A \sin(\theta_i), \quad i = 2, \dots, n, \\
\mathbf{G}(\mathbf{Y})_{2n+2} &= p_2 \left( \text{Dr} - s'_{\text{end}} (\cos(\theta_{n+1}) - 1) \right. \\
&\left. + s_{\text{end}} h \left( \sum_{j=1}^n (\sin(\theta_j) \zeta_j) + \frac{\sin(\theta_1) \zeta_1 + \sin(\theta_{n+1}) \zeta_{n+1}}{2} \right) - v_{n+1} \right), \\
\mathbf{G}(\mathbf{Y})_{2n+3} &= \begin{cases} \zeta_1, & \xi_1 \leq 0, \\ p_3 (\alpha_{\text{nozzle}} - \theta_1), & \xi_1 > 0, \end{cases} \\
\mathbf{G}(\mathbf{Y})_{2n+2+i} &= \zeta_i + \frac{s_i \theta_{i,s} s'_{\text{end}}}{s_{\text{end}}}, \quad i = 2, \dots, n, \\
\mathbf{G}(\mathbf{Y})_{3n+3} &= \begin{cases} \zeta_{n+1} + \frac{\theta_{n+1,s} s'_{\text{end}}}{s_{\text{end}}}, & \xi_{n+1} \geq 0, \\ p_4 (\epsilon_0 - \theta_{n+1}), & \xi_{n+1} < 0, \end{cases} \\
\mathbf{G}(\mathbf{Y})_{3n+4} &= 0, \\
\mathbf{G}(\mathbf{Y})_{3n+4+i} &= \frac{1}{s_{\text{end}}} (s_i \mathcal{A}_{i,s} s'_{\text{end}} - \mathcal{A}_i v_{i,s} - v_i \mathcal{A}_{i,s}), \quad i = 2, \dots, n+1, \\
\mathbf{G}(\mathbf{Y})_{4n+5} &= s'_{\text{end}},
\end{aligned}$$

where

$$\begin{aligned}
s'_{\text{end}} &= p_1 \left( \text{Re} + s_{\text{end}} \left( \frac{\sin(\theta_1) + \sin(\theta_{n+1})}{2} + \sum_{j=2}^n \sin(\theta_j) \right) \right) \\
&+ \begin{cases} -\frac{s_{\text{end}}}{\sin(\theta_{n+1})} \left( \frac{\zeta_1 \cos(\theta_1) + \zeta_{n+1} \cos(\theta_{n+1})}{2} + \sum_{j=2}^n \zeta_j \cos(\theta_j) \right), & \theta_{n+1} > \epsilon_0, \\ 0, & \theta_{n+1} \leq \epsilon_0. \end{cases}
\end{aligned}$$

Note, that the formulation above incorporates all boundary conditions for the dynamic problem. Therefore, the initial conditions for  $\mathbf{Y}_{n+2}$  should be equal to 1 (this follows from (6.24):  $v(0, t) = \mathbf{Y}_1(t) \equiv 1$ ), and the initial condition for  $\mathbf{Y}_{3n+4}$  should be equal to 1 (this follows from (6.26):  $\mathcal{A}(0, t) = \mathbf{Y}_{3n+4}(t) \equiv 1$ ).

The system of ODEs in time, (6.54), is solved in MATLAB using `ode15s` solver. For this we need to compute the matrix  $\mathbb{M}(\mathbf{Y})$  and the vector  $\mathbf{G}(\mathbf{Y})$ , and supply them into the `ode15s` solver together with the initial values  $\mathbf{Y}(0)$ . The initial values follow from the initial jet configuration together with the boundary conditions. In Section 6.2.1, we perform some simulations for a set of chosen initial conditions.

#### 6.1.4 Equations for dynamic jet in rotary spinning

In this subsection we derive the equations for the dynamic jet in rotary spinning to be used in a numerical method. First we formulate the equations and boundary conditions derived in a form convenient for discretization in the space variable  $s$ . After this, we

relax the equation for  $s_{\text{end}}(t)$  and some boundary conditions for  $\theta$  making them suitable for our numerical method. In Section 6.2.2 we discuss the effects of these relaxations. The dynamic jet configuration in rotary spinning is depicted in Figure 6.2. A system

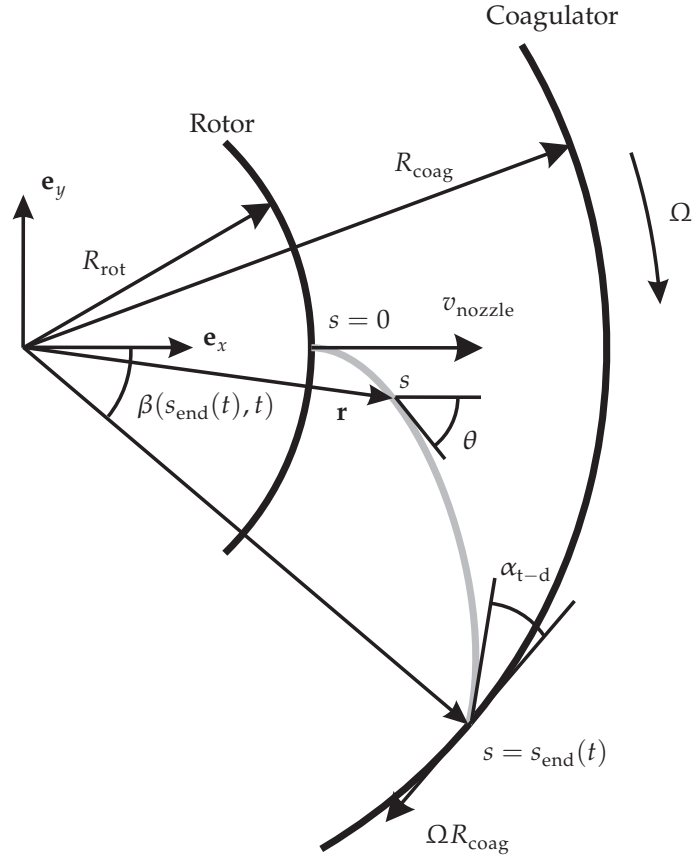


**Figure 6.2:** The dynamic jet in rotary spinning in the rotating frame of the rotor. The jet emerges from the nozzle at the rotor with the velocity  $v_{\text{nozzle}}$  and flows towards the coagulator, which rotates clockwise with the angular velocity  $\Omega$ . The fluid velocity at the coagulator is  $\Omega R_{\text{coag}}$ . The jet is parameterized by its arc-length  $s$  with  $s = 0$  at the nozzle and  $s = s_{\text{end}}(t)$  at the coagulator. The polar angle of the contact point is  $\beta(s_{\text{end}}(t), t)$  and the touchdown angle (i.e. the angle between the jet and the coagulator at  $s = s_{\text{end}}(t)$ ) is  $\alpha_{\text{t-d}}(t)$ . The jet position is described by the vector  $\mathbf{r}$  in the Cartesian coordinate system  $\mathbf{e}_x \mathbf{e}_y$  with the origin at the centers of the rotor and the coagulator and the basis vector  $\mathbf{e}_x$  directed towards the nozzle. The angle between the jet and  $\mathbf{e}_x$  is  $\theta$ . The radii of the rotor and the coagulator are  $R_{\text{rot}}$  and  $R_{\text{coag}}$ .

describing the dynamic jet consists of the conservation of momentum and mass together with the condition for  $s$  being the arc-length (5.4), (5.5), (1.2), and (1.4), which after

scaling<sup>3</sup> become

$$\mathbf{r}_{tt} + (v_t + vv_s)\mathbf{r}_s + v^2\mathbf{r}_{ss} + 2v\mathbf{r}_{st} = B \frac{(\mathcal{A}v_s\mathbf{r}_s)_s}{\mathcal{A}} + \mathbf{a}_c + \mathbf{a}_C, \quad (6.58)$$

$$\mathcal{A}_t(s, t) + (\mathcal{A}(s, t)v(s, t))_s = 0, \quad (6.59)$$

$$\|\mathbf{r}_s\| = 1, \quad (6.60)$$

for  $s \in (0, s_{\text{end}}(t))$  and  $t \in (0, \infty)$ . Here  $\mathbf{v} = \mathbf{r}_t + v\mathbf{r}_s$  is the fluid particle velocity with  $\mathbf{v} = (v_x, v_y)$  (1.10),  $\mathbf{a}_c = \mathbf{r}$  is the scaled centrifugal force, and  $\mathbf{a}_C = 2\mathbf{v}^\perp$  is the scaled Coriolis force<sup>4</sup>. The boundary conditions for (6.59)- (6.60) are given in (2.16)- (2.20) and Remark 2.2

$$v(0, t) = D\mathbf{r}, \quad (6.61)$$

$$v(s_{\text{end}}(t), t) = 1 + \beta_t(s_{\text{end}}(t), t) + s'_{\text{end}}(t), \quad (6.62)$$

$$\mathbf{r}(0, t) = (R_0, 0), \quad (6.63)$$

$$\mathcal{A}(0, t) = 1, \quad (6.64)$$

$$|\mathbf{r}(s_{\text{end}}(t), t)| = 1, \quad (6.65)$$

$$\text{if } \xi(0, t) > 0 \text{ then } \theta(0, t) = 0, \quad (6.66)$$

$$\text{if } \xi(s_{\text{end}}(t), t) < 0 \text{ then } \theta(s_{\text{end}}(t), t) = -\pi/2 + \beta(s_{\text{end}}(t), t). \quad (6.67)$$

Here,  $\xi = v^2 - Bv_s$ ,  $\beta(s_{\text{end}}(t), t)$  is the angular coordinate of the jet end

$$\beta(s_{\text{end}}(t), t) = \arctan(y(s_{\text{end}}(t), t)/x(s_{\text{end}}(t), t)), \quad (6.68)$$

and the angle  $\theta$  is the angle between  $\mathbf{e}_x$  and the jet orientation defined as

$$\theta = \arctan(y/(x - R_0)). \quad (6.69)$$

By taking the inner product of (6.58) with  $\mathbf{r}_s$  and  $\mathbf{r}_s^\perp$ <sup>5</sup>, we obtain (compare with (6.16) and (6.17))

$$v_t + (\mathbf{r}_{tt}, \mathbf{r}_s) = v_{ss} - \left(v - \frac{\mathcal{A}_s}{\mathcal{A}}\right) v_s + (\mathbf{a}_c + \mathbf{a}_C, \mathbf{r}_s), \quad (6.70)$$

and

$$(\mathbf{r}_{tt}, \mathbf{r}_s^\perp) = -2v\zeta - v\xi\theta_s + (\mathbf{a}_c + \mathbf{a}_C, \mathbf{r}_s^\perp). \quad (6.71)$$

<sup>3</sup>Here we scale time  $t$  with respect to  $1/\Omega$ ,  $R$  and  $s$  with respect to  $R_{\text{coag}}$ , cross-sectional area  $\mathcal{A}$  with respect to  $\mathcal{A}_{\text{nozzle}}$ , and flow velocity  $v$  with respect to  $\Omega R_{\text{coag}}$ . Thus, our system is fully characterized by the three dimensionless numbers  $B = 3\nu/(\Omega R_{\text{coag}}^2)$ , the radii ratio  $R_0 = R_{\text{rot}}/R_{\text{coag}}$  and the draw ratio  $D\mathbf{r} = v_{\text{nozzle}}/(\Omega R_{\text{coag}})$ .

<sup>4</sup>The vector  $\mathbf{v}^\perp$  is perpendicular to  $\mathbf{v}$  and is defined as  $\mathbf{v}^\perp = (v_y, -v_x)$ . This definition corresponds to the counter-clockwise rotating rotor in the fixed coordinate frame; see Section 5.1 for details.

<sup>5</sup>Here  $\mathbf{r}_s^\perp$  is a perpendicular vector to  $\mathbf{r}_s$  defined as  $\mathbf{r}_{ss} = \mathbf{r}_s^\perp \theta_s$ , i.e.  $\mathbf{r}_s^\perp = (-\sin(\theta), \cos(\theta))$

We write  $\mathbf{r}_s = (\cos(\theta), \sin(\theta))$ , so the components  $x$  and  $y$  of  $\mathbf{r}$  in terms of the angle  $\theta$  and (6.63) are

$$x(s, t) = R_0 + \int_0^s \cos(\theta(\tilde{s}, t)) d\tilde{s}, \quad y(s, t) = \int_0^s \sin(\theta(\tilde{s}, t)) d\tilde{s}. \quad (6.72)$$

Then

$$x_t(s, t) = - \int_0^s \sin(\theta(\tilde{s}, t)) \zeta(\tilde{s}, t) d\tilde{s}, \quad y_t(s, t) = \int_0^s \cos(\theta(\tilde{s}, t)) \zeta(\tilde{s}, t) d\tilde{s}. \quad (6.73)$$

and

$$\begin{aligned} x_{tt}(s, t) &= - \int_0^s \left[ \cos(\theta(\tilde{s}, t)) \zeta(\tilde{s}, t)^2 + \sin(\theta(\tilde{s}, t)) \zeta_t(\tilde{s}, t) \right] d\tilde{s}, \\ y_{tt}(s, t) &= \int_0^s \left[ -\sin(\theta(\tilde{s}, t)) \zeta(\tilde{s}, t)^2 + \cos(\theta(\tilde{s}, t)) \zeta_t(\tilde{s}, t) \right] d\tilde{s}, \end{aligned} \quad (6.74)$$

where

$$\zeta = \theta_t. \quad (6.75)$$

A differential equation for  $s_{\text{end}}(t)$  is obtained after differentiation of (2.20) with respect to  $t$

$$s'_{\text{end}}(t) = - \frac{x(s_{\text{end}}(t), t) x_t(s_{\text{end}}(t), t) + y(s_{\text{end}}(t), t) y_t(s_{\text{end}}(t), t)}{x(s_{\text{end}}(t), t) \cos(\theta(s_{\text{end}}(t), t)) + y(s_{\text{end}}(t), t) \sin(\theta(s_{\text{end}}(t), t))}. \quad (6.76)$$

We scale the arc length parameter  $s$  according to  $\hat{s} = s/s_{\text{end}}(t)$ , so the interval for  $\hat{s} \in (0, 1)$  is fixed. From now on we omit the hats. After scaling and using (6.72), (6.73), and (6.74) the system (6.70), (6.71), (6.75), (6.59), (6.76), (6.61), (6.62), (6.64), (6.66), and (6.67) becomes

$$\begin{aligned} v_t + s_{\text{end}} \mathcal{J}_a(\zeta_t, \theta) &= -s_{\text{end}} \cos(\theta) \mathcal{J}_c(\zeta_s, \zeta, \theta) - s_{\text{end}} \sin(\theta) \mathcal{J}_d(\zeta_s, \zeta, \theta) + B v_{ss}/s_{\text{end}}^2 \\ \left( B \frac{\mathcal{A}_s}{s_{\text{end}} \mathcal{A}} + s s'_{\text{end}} - v \right) v_s/s_{\text{end}} &+ (x + 2v_y) \cos(\theta) + (y - 2v_x) \sin(\theta), \end{aligned} \quad (6.77)$$

$$\begin{aligned} s_{\text{end}} \mathcal{J}_b(\zeta_t, \theta) &= s_{\text{end}} \sin(\theta) \mathcal{J}_c(\zeta_s, \zeta, \theta) - s_{\text{end}} \cos(\theta) \mathcal{J}_d(\zeta_s, \zeta, \theta) - v \xi \theta_s/s_{\text{end}} - 2v \zeta \\ &- (x + 2v_y) \sin(\theta) + (y - 2v_x) \cos(\theta), \end{aligned} \quad (6.78)$$

$$\theta_t = \zeta + s \theta_s s'_{\text{end}}/s_{\text{end}}, \quad (6.79)$$

$$\mathcal{A}_t = (s \mathcal{A}_s s'_{\text{end}} - \mathcal{A} v_s - v \mathcal{A}_s)/s_{\text{end}}, \quad (6.80)$$

$$s'_{\text{end}}(t) = - \frac{x(1, t) x_t(1, t) + y(1, t) y_t(1, t)}{x(1, t) \cos(\theta(1, t)) + y(1, t) \sin(\theta(1, t))}, \quad (6.81)$$

$$v(0, t) = D r, \quad (6.82)$$

$$v(1, t) = v_{d,c}(t), \quad (6.83)$$

$$\mathcal{A}(0, t) = 1, \quad (6.84)$$

$$\text{if } \xi(0, t) > 0 \text{ then } \theta(0, t) = 0, \quad (6.85)$$

$$\text{if } \xi(1, t) < 0 \text{ then } \theta(1, t) = -\pi/2 + \beta(1, t) \quad (6.86)$$

where  $\beta(1, t) = \arctan(y(1, t)/x(1, t))$ ,  $\xi = v - Bv_s/(s_{\text{end}}v)$ ,

$$x(s, t) = R_0 + s_{\text{end}}(t) \int_0^s \cos(\theta(\tilde{s}, t)) d\tilde{s}, \quad y(s, t) = s_{\text{end}}(t) \int_0^s \sin(\theta(\tilde{s}, t)) d\tilde{s},$$

$$x_t(s, t) = -s_{\text{end}}(t) \int_0^s \sin(\theta(\tilde{s}, t)) \zeta(\tilde{s}, t) d\tilde{s}, \quad y_t(s, t) = s_{\text{end}}(t) \int_0^s \cos(\theta(\tilde{s}, t)) \zeta(\tilde{s}, t) d\tilde{s},$$

$$v_x = x_t + v \cos(\theta), \quad v_y = y_t + v \sin(\theta),$$

$$\mathcal{J}_a(\zeta_t, \theta) = \int_0^s \sin(\theta(s, t) - \theta(\tilde{s}, t)) \zeta_t(\tilde{s}, t) d\tilde{s},$$

$$\mathcal{J}_b(\zeta_t, \theta) = \int_0^s \cos(\theta(s, t) - \theta(\tilde{s}, t)) \zeta_t(\tilde{s}, t) d\tilde{s},$$

$$\mathcal{J}_c(\zeta_s, \zeta, \theta) = \int_0^s \left[ -\cos(\theta(\tilde{s}, t)) \zeta(\tilde{s}, t)^2 + \tilde{s} \sin(\theta(\tilde{s}, t)) \zeta_s(\tilde{s}, t) s'_{\text{end}}(t) / s_{\text{end}}(t) \right] d\tilde{s},$$

$$\mathcal{J}_d(\zeta_s, \zeta, \theta) = \int_0^s \left[ -\sin(\theta(\tilde{s}, t)) \zeta(\tilde{s}, t)^2 - \tilde{s} \cos(\theta(\tilde{s}, t)) \zeta_s(\tilde{s}, t) s'_{\text{end}}(t) / s_{\text{end}}(t) \right] d\tilde{s},$$

$$v_{d,c}(t) = 1 + s'_{\text{end}}(t) + x(1, t) (\sin(\theta(1, t)) s'_{\text{end}}(t) + y_t(1, t)) \\ - y(1, t) (\cos(\theta(1, t)) s'_{\text{end}}(t) + x_t(1, t)).$$

### 6.1.5 Relaxation forms of some equations and boundary conditions

Similarly to the case of drag spinning (see Section 6.1.2) we need to change some equations and boundary conditions of the system (6.77)-(6.86) describing the dynamic jet in rotary spinning so it becomes applicable for a numerical method. We change the ODE for  $s_{\text{end}}(t)$  (6.81) to avoid a singularity occurring if the jet touches the coagulator tangentially. We replace the boundary conditions for  $\theta$  (6.85) and (6.86) by differential equations to avoid jumps in  $\theta$  at the jet ends if the sign of  $\xi$  at the jet ends changes.

We do not relax the boundary condition for  $v(1, t)$  (6.83) for rotary spinning, in contrary to drag spinning (6.31). Direct use of the boundary condition (6.83) appears to be manageable for a numerical scheme. It is also not possible to avoid a possibility of singularity in (6.81) by modifying the boundary condition for  $\theta$  at the coagulator (6.86). In Chapter 5 we show that it is possible that the steady jet can touch the coagulator tangentially even though we do not demand tangency with the coagulator.

Next we describe the relaxations in detail.

#### Relaxation form of (6.81)

We modify the equations for  $s_{\text{end}}(t)$  (6.81) in such a way that division by zero is avoided if the jet is tangent to the coagulator. To achieve this we perform two steps. First we choose a small parameter  $\epsilon_0$  and introduce an "if" statement so if the touchdown angle  $\alpha_{t-d} < \epsilon_0$  we use (6.81) to compute  $s'_{\text{end}}(t)$ , otherwise we take  $s'_{\text{end}}(t) = 0$ . Secondly we add to the expression above a term  $p_1 \left(1 - \sqrt{x(1, t)^2 + y(1, t)^2}\right)$  with the parameter  $p_1 > 0$ . The action of this term is to decrease the jet length  $s_{\text{end}}(t)$  if the jet end is outside the coagulator and increase  $s_{\text{end}}(t)$  if the jet end is inside the coagulator so the condition

that the jet end lays at the coagulator (6.65) is asymptotically satisfied. The resulting expression for  $s'_{\text{end}}(t)$  is following

$$s'_{\text{end}}(t) = p_1 \left( 1 - \sqrt{x(1,t)^2 + y(1,t)^2} \right) + \begin{cases} -\frac{x(1,t)x_i(1,t)+y(1,t)y_i(1,t)}{x(1,t)\cos(\theta(1,t))+y(1,t)\sin(\theta(1,t))} & \text{if } \theta(1,t) - \beta(1,t) + \pi/2 > \epsilon_0, \\ 0 & \text{if } \theta(1,t) - \beta(1,t) + \pi/2 \leq \epsilon_0. \end{cases} \quad (6.87)$$

By use of (6.87) to calculate  $s_{\text{end}}(t)$  we have introduced an error to the boundary condition (6.65) due to the differentiation (6.65), and modification (6.81). The relative error is calculated as

$$\mathcal{E}_{\text{coag}} = 1 - \sqrt{x(1,t)^2 + y(1,t)^2}. \quad (6.88)$$

To make this error as small as possible we need to choose  $p_1$  as large as possible.

### Relaxation forms of (6.85) and (6.86)

We relax the boundary conditions for  $\theta$  (6.85) and (6.86) as follows

$$\text{if } \xi(0,t) > 0 \text{ then } \theta_t(0,t) = -p_3\theta(0,t), \quad (6.89)$$

$$\text{if } \xi(1,t) < 0 \text{ then } \theta_t(1,t) = p_4(\beta(1,t) - \pi/2 - \theta(1,t)), \quad (6.90)$$

so they are suitable for our numerical method. This is done to avoid a sudden change of  $\theta$  at the boundaries due to the "if" statements in (6.85) and (6.86). The relaxed conditions smoothly change the jet orientation, so jet exponentially approaches to be aligned with the nozzle if  $\xi(0,t) > 0$ ; see (6.89), and to be tangent with the coagulator if  $\xi(1,t) < 0$ ; see (6.90).

In the next subsection we describe a discretization  $s$  of the dynamic jet system in rotary spinning (6.77)-(6.80), (6.87), (6.82)-(6.84), (6.89), and (6.90).

## 6.1.6 Numerical scheme for dynamic jet in rotary spinning

In this subsection we develop a numerical scheme for the dynamic jet equations in rotary spinning in a similar way as for drag spinning in Subsection 6.1.3.

We discretize functions of  $s$  as follows: the functions  $v(s,t)$ ,  $\zeta(s,t)$ ,  $\theta(s,t)$  are  $\mathcal{A}(s,t)$  approximated by  $v_i(t) \approx v(s_i,t)$ ,  $\zeta_i(t) \approx \zeta(s_i,t)$ ,  $\theta_i(t) \approx \theta(s_i,t)$ , and  $\mathcal{A}_i(t) \approx \mathcal{A}(s_i,t)$ , where  $s_i = (i-1)h$ ,  $h = 1/n$ ,  $i = 1 \dots n+1$ , and  $n \in \mathbb{N}$ . We approximate  $v_s$ ,  $v_{ss}$ ,  $\mathcal{A}_s$ ,  $\theta_s$ ,  $\zeta_s$ ,  $\mathcal{J}_a$ ,  $\mathcal{J}_b$ ,  $\mathcal{J}_c$ , and  $\mathcal{J}_d$  as in (6.37)-(6.39), (6.41), (6.41) and (6.44)-(6.53). We also replace the Heaviside function  $H(s)$  in (6.41) and (6.42) by its smoothed-out version

$$H(s) = 1/2 + \arctan(100s)/\pi. \quad (6.91)$$

Next in this subsection we use subindex  $i$  to denote the approximation of the functions or their derivatives at the point  $s_i$ . The values of  $\xi(s_i,t)$  are computed as

$$\xi_i = v_i - Bv_s(s_i)/v_i. \quad (6.92)$$

Coordinates  $x$  and  $y$ , and their time derivatives  $x_t$  and  $y_t$  are computed as

$$x_i = R_{\text{rot}} + h \sum_{j=2}^i \cos(\theta_j), \quad y_i = h \sum_{j=2}^i \sin(\theta_j), \quad (6.93)$$

$$x_{t,i} = -h \sum_{j=2}^i \sin(\theta_j) \zeta_j, \quad \text{and} \quad y_{t,i} = h \sum_{j=2}^i \cos(\theta_j) \zeta_j. \quad (6.94)$$

The components of  $\mathbf{v}$  are

$$\mathbf{v}_{x,i} = x_{t,i} + v_i \cos(\theta_i) \quad \text{and} \quad \mathbf{v}_{y,i} = y_{t,i} + v_i \sin(\theta_i) \quad (6.95)$$

After the space discretization we obtain a system of ODEs in time, written as

$$\mathbb{M}(\mathbf{Y}) \mathbf{Y}_t = \mathbf{G}(\mathbf{Y}). \quad (6.96)$$

Here  $\mathbf{Y}$  is a column vector of length  $4n + 2$ ,

$$\mathbf{Y} = (\zeta_1, \dots, \zeta_{n+1}, v_2, \dots, v_n, \theta_1, \dots, \theta_{n+1}, \mathcal{A}_2, \dots, \mathcal{A}_{n+1}, s_{\text{end}})^T, \quad (6.97)$$

and the matrix  $\mathbb{M}(\mathbf{Y}, t)$  of size  $4n + 2 \times 4n + 2$ , has the block form

$$\mathbb{M}(\mathbf{Y}) = \begin{pmatrix} \mathbb{B}_{a,n+1 \times n+1}(\mathbf{Y}) & \mathbb{Z}_{n+1 \times n-1} & \mathbb{Z}_{2n \times 2n+2} \\ \mathbb{B}_{b,n-1 \times n+1}(\mathbf{Y}) & \mathbb{I}_{n-1 \times n-1} & \\ & \mathbb{Z}_{2n+2 \times 2n} & \mathbb{I}_{2n+2 \times 2n+2} \end{pmatrix}$$

where  $\mathbb{I}$  denotes the identity matrix,  $\mathbb{Z}$  denotes the zero matrix. The matrix  $\mathbb{B}_{a,n+1 \times n+1}(\mathbf{Y})$  is given by (6.56), and the matrix  $\mathbb{B}_{b,n-1 \times n+1}(\mathbf{Y})$ <sup>6</sup> follows from  $\mathcal{J}_a(s_i)$  as

$$\mathbb{B}_{b,n-1 \times n+1}(\mathbf{Y}) = h s_{\text{end}} \begin{pmatrix} \frac{\sin(\theta_2 - \theta_1)}{2} & 0 & 0 & 0 & 0 \\ \frac{\sin(\theta_3 - \theta_1)}{2} & \sin(\theta_3 - \theta_2) & 0 & 0 & \\ \vdots & \vdots & \ddots & \ddots & \ddots \\ \frac{\sin(\theta_n - \theta_1)}{2} & \sin(\theta_n - \theta_2) & \dots & \sin(\theta_n - \theta_{n-1}) & 0 & 0 \end{pmatrix}. \quad (6.98)$$

Finally the right-hand-side column vector  $\mathbf{G}(\mathbf{Y})$  in (6.54) follows from the right-hand-

<sup>6</sup>The matrix  $\mathbb{B}_{b,n-1 \times n+1}(\mathbf{Y})$  in rotary spinning follows from the matrix  $\mathbb{B}_{b,n+1 \times n+1}(\mathbf{Y})$  (6.57) in drag spinning by removing from it the first and the last rows.



sides of (6.77)-(6.80), (6.89), (6.90), and (6.87) as

$$\mathbf{G}(\mathbf{Y})_1 = \begin{cases} s_{\text{end}} \sin(\theta_1) \mathcal{J}_{c,1} - s_{\text{end}} \cos(\theta_1) \mathcal{J}_{d,1} & \xi_1 \leq 0, \\ -\frac{v_1 \xi_1 \theta_{1,s}}{s_{\text{end}}} - 2v_1 \zeta_1 - (x_1 + 2v_{y,1}) \sin(\theta_1) + (y_1 - 2v_{x,1}) \cos(\theta_1), & \xi_1 > 0, \\ 0, & \end{cases}$$

$$\mathbf{G}(\mathbf{Y})_i = s_{\text{end}} \sin(\theta_i) \mathcal{J}_{c,i} - s_{\text{end}} \cos(\theta_i) \mathcal{J}_{d,i} - \frac{v_i \xi_i \theta_{i,s}}{s_{\text{end}}} - 2v_i \zeta_i$$

$$- (x_i + 2v_{y,i}) \sin(\theta_i) + (y_i - 2v_{x,i}) \cos(\theta_i), \quad i = 2, \dots, n,$$

$$\mathbf{G}(\mathbf{Y})_{n+1} = \begin{cases} s_{\text{end}} \sin(\theta_{n+1}) \mathcal{J}_{c,n+1} - s_{\text{end}} \cos(\theta_{n+1}) \mathcal{J}_{d,n+1} - \frac{v_{n+1} \xi_{n+1} \theta_{n+1,s}}{s_{\text{end}}} - 2v_{n+1} \zeta_{n+1} & \xi_{n+1} \geq 0, \\ -(x_{n+1} + 2v_{y,n+1}) \sin(\theta_{n+1}) + (y_{n+1} - 2v_{x,n+1}) \cos(\theta_{n+1}), & \xi_{n+1} < 0, \\ 0, & \end{cases}$$

$$\mathbf{G}(\mathbf{Y})_{n+i} = -s_{\text{end}} \cos(\theta_i) \mathcal{J}_{c,i} - s_{\text{end}} \sin(\theta_i) \mathcal{J}_{d,i} + \left( \frac{\mathcal{A}_{i,s}}{s_{\text{end}} \mathcal{A}_i} + s_i s'_{\text{end}} - v_i \right) \frac{v_{i,s}}{s_{\text{end}}}$$

$$+ \frac{v_{i,ss}}{s_{\text{end}}^2} + (x_i + 2v_{y,i}) \cos(\theta_i) + (y_i - 2v_{x,i}) \sin(\theta_i), \quad i = 2, \dots, n,$$

$$\mathbf{G}(\mathbf{Y})_{2n+1} = \begin{cases} \zeta_1, & \xi_1 \leq 0, \\ -p_3 \theta_1, & \xi_1 > 0, \end{cases}$$

$$\mathbf{G}(\mathbf{Y})_{2n+i} = \zeta_i + \frac{s_i \theta_{i,s} s'_{\text{end}}}{s_{\text{end}}}, \quad i = 2, \dots, n,$$

$$\mathbf{G}(\mathbf{Y})_{3n+1} = \begin{cases} \zeta_{n+1} + \frac{\theta_{n+1,s} s'_{\text{end}}}{s_{\text{end}}} & \xi_{n+1} \geq 0, \\ p_4 (\beta_{n+1} - \pi/2 - \theta_{n+1}), & \xi_{n+1} < 0, \end{cases}$$

$$\mathbf{G}(\mathbf{Y})_{3n+1+i} = \frac{1}{s_{\text{end}}} (s_i \mathcal{A}_{i,s} s'_{\text{end}} - \mathcal{A}_i v_{i,s} - v_i \mathcal{A}_{i,s}), \quad i = 1, \dots, n,$$

$$\mathbf{G}(\mathbf{Y})_{4n+2} = s'_{\text{end}},$$

where

$$s'_{\text{end}} = p_1 \left( 1 - \sqrt{x_{n+1}^2 + y_{n+1}^2} \right)$$

$$+ \begin{cases} -\frac{x_{n+1} x_{t,n+1} + y_{n+1} y_{t,n+1}}{x_{n+1} \cos(\theta_{n+1}) + y_{n+1} \sin(\theta_{n+1})} & \text{if } \theta_{n+1} - \beta_{n+1} + \pi/2 > \epsilon_0, \\ 0 & \text{if } \theta_{n+1} - \beta_{n+1} + \pi/2 \leq \epsilon_0, \end{cases}$$

and  $\beta_{n+1} = \arcsin(y_{n+1}/(y_{n+1}^2 + x_{n+1}^2))$ .

The boundary conditions for  $v$  and  $\mathcal{A}$  (6.82)-(6.84) are assigned to  $v_1, v_{n+1}, \mathcal{A}_1$  i.e.

$$v_1 = \text{Dr},$$

$$v_{n+1} = 1 + s'_{\text{end}} + x_{n+1} (\sin(\theta_{n+1}) s'_{\text{end}} + y_{t,n+1}) - y_{n+1} (\cos(\theta_{n+1}) s'_{\text{end}} + x_{t,n+1}),$$

and

$$\mathcal{A}_1 = 1.$$

The boundary conditions for  $\theta$  (6.89)-(6.90) are incorporated in  $\mathbf{G}(\mathbf{Y})_{2n+1}$  and  $\mathbf{G}(\mathbf{Y})_{3n+1}$ .

The system of ODE's in time (6.96) is solved in MATLAB using a solver `ode15s`. To do this we need to compute the matrix  $\mathbb{M}(\mathbf{Y})$  and the vector  $\mathbf{G}(\mathbf{Y})$ , and supply them to the solver `ode15s` together with initial values for  $\mathbf{Y}(0)$ . The initial values follow from the initial jet configuration. In Section 6.2.2 we illustrate "How the method works?" by performing some simulations.

## 6.2 Numerical simulations

In this section we present some results of numerical simulations for the dynamic jet in drag and rotary spinning. For drag spinning simulations with fixed parameters the dynamic jet evolves to a steady jet in the flow regime determined by the parameter space partitioning. Next, we perform simulations with changing  $v_{\text{nozzle}}$ , so jet regime moves from one steady regime to another. For rotary spinning we perform simulations where the dynamic jet evolves to a steady one in one of the three flow regimes. Finally we perform a simulation in which the jet regime approaches the region where a steady jet solution does not exist.

### 6.2.1 Results for dynamic jet in drag spinning

#### Evolution to steady jet

For the dynamic jet in drag spinning, we start with three numerical simulations where the jet evolves to the steady one for fixed parameters. We take three sets of parameters from the three steady flow regimes, and let the jet evolve to the steady one in the corresponding flow regime.

In all the three cases we choose the initial jet configuration as follow:

- The initial jet shape is straight aligned with the nozzle orientation i.e.

$$\theta(s, 0) = \alpha_{\text{nozzle}}.$$

- Initially the jet does not move, so

$$\zeta(s, 0) = 0.$$

- The initial flow velocity in the jet  $v$  has a linear profile between the nozzle velocity at  $s = 0$ ,  $v(0, 0) = v_{\text{nozzle}}$ , and the belt velocity at  $s = s_{\text{end}}(0)$ ,  $v(s_{\text{end}}(0), 0) = v_{\text{belt}}$

$$v(s, 0) = v_{\text{nozzle}} + \frac{s}{s_{\text{end}}(0)}(v_{\text{belt}} - v_{\text{nozzle}}).$$

- The initial jet cross-section area has the same value  $\mathcal{A}_{\text{nozzle}}$  for all  $s$ . Consequently, in scaled version, the initial condition for  $\mathcal{A}$  becomes

$$\mathcal{A}(s, 0) = \mathcal{A}_{\text{nozzle}} = 1.$$

- The initial jet length is calculated from the initial jet shape as

$$s_{\text{end}}(0) = L/|\sin(\alpha_{\text{nozzle}})|.$$

Therefore, the belt velocity  $v_{\text{belt}}$ , the flow velocity at the nozzle  $v_{\text{nozzle}}$ , the falling height  $L$ , and the nozzle orientation  $\alpha_{\text{nozzle}}$  determine our initial conditions. Furthermore we need to specify the kinematic viscosity of the fluid  $\nu$ , and the additional parameters  $p_1$  and  $\epsilon_0$  for the relaxed ODE for  $s_{\text{end}}(t)$ , (6.29), and  $p_2$ ,  $p_3$ , and  $p_4$  for the relaxed boundary conditions (6.31), (6.33), and (6.36). Values of  $p_1$ ,  $p_2$ ,  $p_3$ , and  $p_4$  have to be taken as larger as possible, and a value of  $\epsilon_0$  has to be taken as small as possible. We chose these values by trial and error so the solver can cope with the problem, and the errors  $\mathcal{E}_{\text{belt}}$  and  $\mathcal{E}_\nu$  introduced by the relaxations (6.29) and (6.31) are less than 1%. In the simulations below we specify only those parameters ( $p_1$ ,  $\epsilon_0$ ,  $p_2$ ,  $p_3$ , and  $p_4$ ) which are relevant for that simulation (i.e. we do not need  $p_1$ ,  $\epsilon_0$ , if the touchdown angle is away from zero during the jet evolution). For all the simulations below we take  $n = 100$ . Next, we describe in detail the numerical results for three cases in which the jet evolves to a steady one in one of the three regimes.

### Viscous regime

In the first simulation we start with parameters from the steady **viscous jet** regime  $\mathcal{P}_{\text{visc}}$ . In this case  $v_{\text{belt}} = 2 \text{ m/s}$ ,  $v_{\text{nozzle}} = 1 \text{ m/s}$ ,  $\nu = 0.11 \text{ m}^2/\text{s}$ ,  $L = 0.04 \text{ m}$ ,  $\alpha_{\text{nozzle}} = -\pi/3$ ,  $p_1 = 1$ ,  $\epsilon_0 = -0.005$ ,  $p_2 = 1000$ , and  $p_4 = 10$ . The latter four parameters are chosen in a way described above in this section. During the evolution of the jet the condition  $\xi(s, t) < 0$  holds for all  $s$  and  $t$ . In this case, the boundary condition (6.35) is prescribed at the belt. The action of this condition is to change the touchdown angle  $\theta(1, t)$  from  $-\pi/3$  to  $\epsilon_0$ .

The evolution of the jet shape is depicted in Figure 6.3(a). The grey line in Figure 6.3(a) lies in the plane  $y = 0$  and illustrates the evolution of the touchdown point in time. The jet shape evolves from an initially straight line to the convex steady shape with zero touchdown angle at the belt; see Figure 6.3(b). The flow velocity at the belt  $v(s_{\text{end}}(t), t)$  first decreases because the touchdown point moves away from the nozzle, reaches a positive minimum and then increases to  $v_{\text{belt}} = 2$ ; see Figure 6.3(c). The relative error  $\mathcal{E}_\nu$  due to relaxing the boundary condition (6.6) by (6.31) rises up to 0.02 for small  $t$  and then decreases to 0 with increasing  $t$ ; see Figure 6.3(d). The relative error  $\mathcal{E}_{\text{belt}}$  is of order  $10^{-3}$ ; see Figure 6.3(f).

From the plots in Figures 6.3 we conclude that when we start with the parameters from  $\mathcal{P}_{\text{visc}}$  the dynamic jet evolves to the steady viscous jet provided that  $\xi(s, t) < 0$  is always fulfilled. Moreover, from Figures 6.3(a), 6.3(b) and 6.3(c) we observe that after 1 second the dynamic jet is almost steady. A comparison of the steady jet shape  $y_{\text{steady}}(x)$  and the dynamic jet shape after 5 seconds  $y(x, 5)$  is presented in Figure 6.3(e), where we plot the absolute difference of the shapes, which is of order of magnitude  $10^{-4}$ . Here we present the shape as the vertical coordinate  $y$ , i.e. the shape above the belt, being a function of the horizontal coordinate  $x$ .

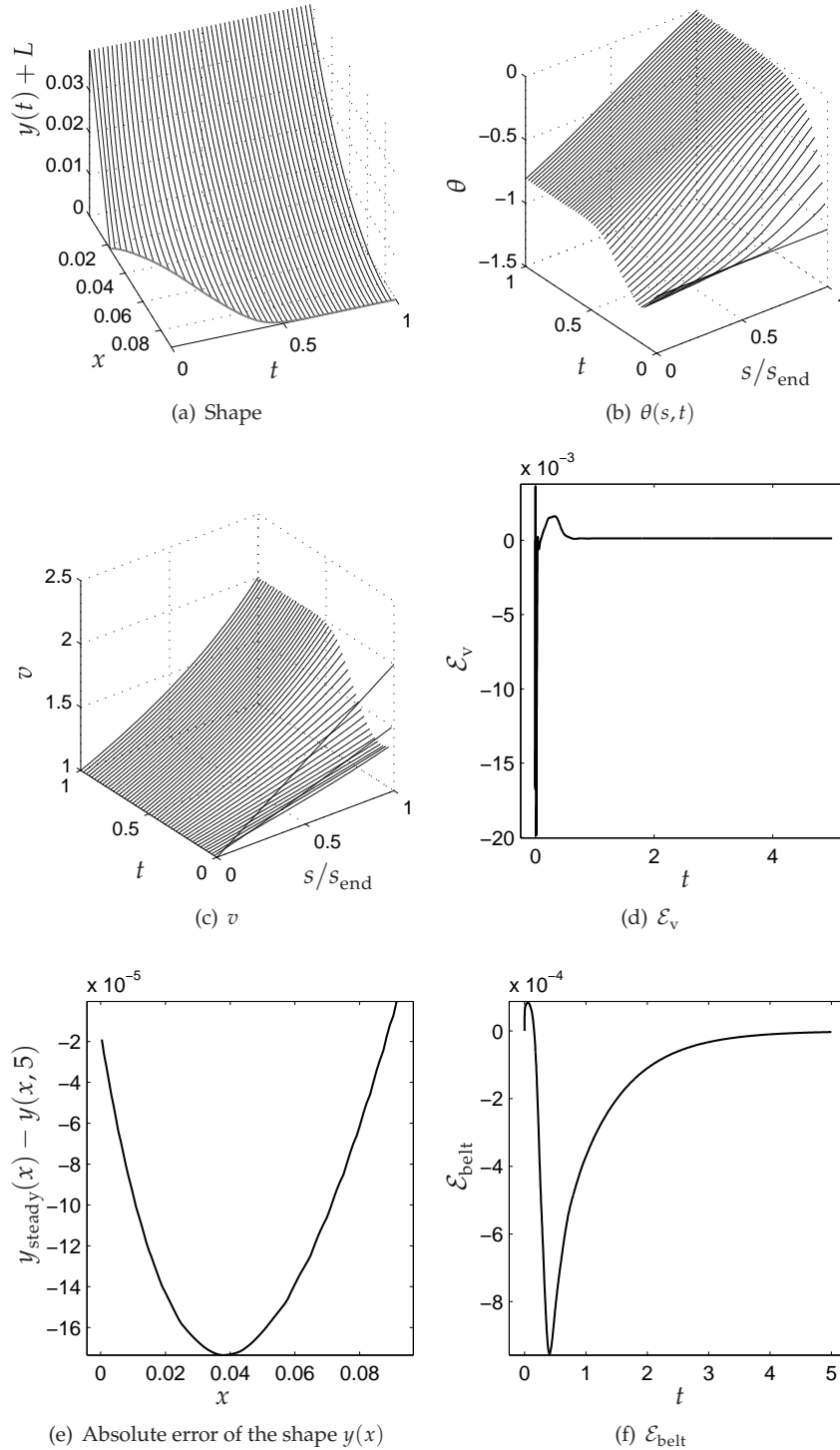


**Figure 6.3:** Results of a numerical simulation for the dynamic jet in drag spinning with the parameters taken from  $\mathcal{P}_{\text{visc}}$ ,  $v_{\text{belt}} = 2 \text{ m/s}$ ,  $v_{\text{nozzle}} = 1 \text{ m/s}$ ,  $\nu = 0.11 \text{ m}^2/\text{s}$ ,  $L = 0.04 \text{ m}$ ,  $\alpha_{\text{nozzle}} = -\pi/3$ ,  $p_1 = 1$ ,  $\epsilon_0 = -0.005$ ,  $p_2 = 1000$ , and  $p_4 = 10$ .

### Viscous-inertial regime

Results of a numerical simulation of the dynamic jet for the parameters from the **viscous-inertial jet** regime  $\mathcal{P}_{v-i}$  are depicted in Figure 6.4. The following values of the parameters are used for this simulation  $v_{\text{belt}} = 3 \text{ m/s}$ ,  $v_{\text{nozzle}} = 1 \text{ m/s}$ ,  $\nu = 0.05 \text{ m}^2/\text{s}$ ,  $L = 0.1 \text{ m}$ ,  $\alpha_{\text{nozzle}} = -\pi/3$ ,  $p_1 = 1$ , and  $p_2 = 1000$ . During the evolution of the jet the conditions  $\xi(0, t) < 0$  and  $\xi(1, t) < 0$  hold for all  $t$ , and no boundary conditions for  $\theta$  are necessary for this simulation; see (6.33) and (6.36). Therefore,  $p_3$  and  $p_4$  together with  $\epsilon_0$  are irrelevant for this simulations. The parameter  $\epsilon_0$  has no influence because, as we shall see next, the touchdown angle  $\theta(1, t)$  evolves towards  $-\pi/2$  and stays away from 0 for all  $t$ .

The evolution of the jet shape is depicted in Figure 6.4(a), where the jet evolves to a purely vertical shape, and the orientation angle  $\theta$  tends to  $-\pi/2$ ; see Figure 6.4(b). The grey line in Figure 6.4(a) in the plane  $y = 0$  illustrates the evolution of the touchdown point in time towards  $x = 0$ . The flow velocity at the belt first increases, because the touchdown point moves towards the nozzle, and afterwards decreases to  $v_{\text{belt}} = 3 \text{ m/s}$  when the jet approaches to the steady flow; see Figure 6.4(c). The relative error  $\mathcal{E}_v$ , in Figure 6.4(d), is of order  $6 \times 10^{-3}$  at the beginning of this simulation, when  $v(s_{\text{end}}(t), t)$  changes rapidly, and then decays towards zero with the jet approaching the steady flow. The relative error  $\mathcal{E}_{\text{belt}}$  is of order  $10^{-6}$ ; see Figure 6.4(e).

In Figures 6.4 we observe that the jet approaches the steady one with a purely vertical shape provided that  $x(0, t) < 0$  and  $x(1, t) > 0$  for all  $t$ . In Figure 6.4(b) we observe that at  $t = 2$  the angle  $\theta(s, 2) \approx -\pi/2$  which corresponds to the vertical jet shape.

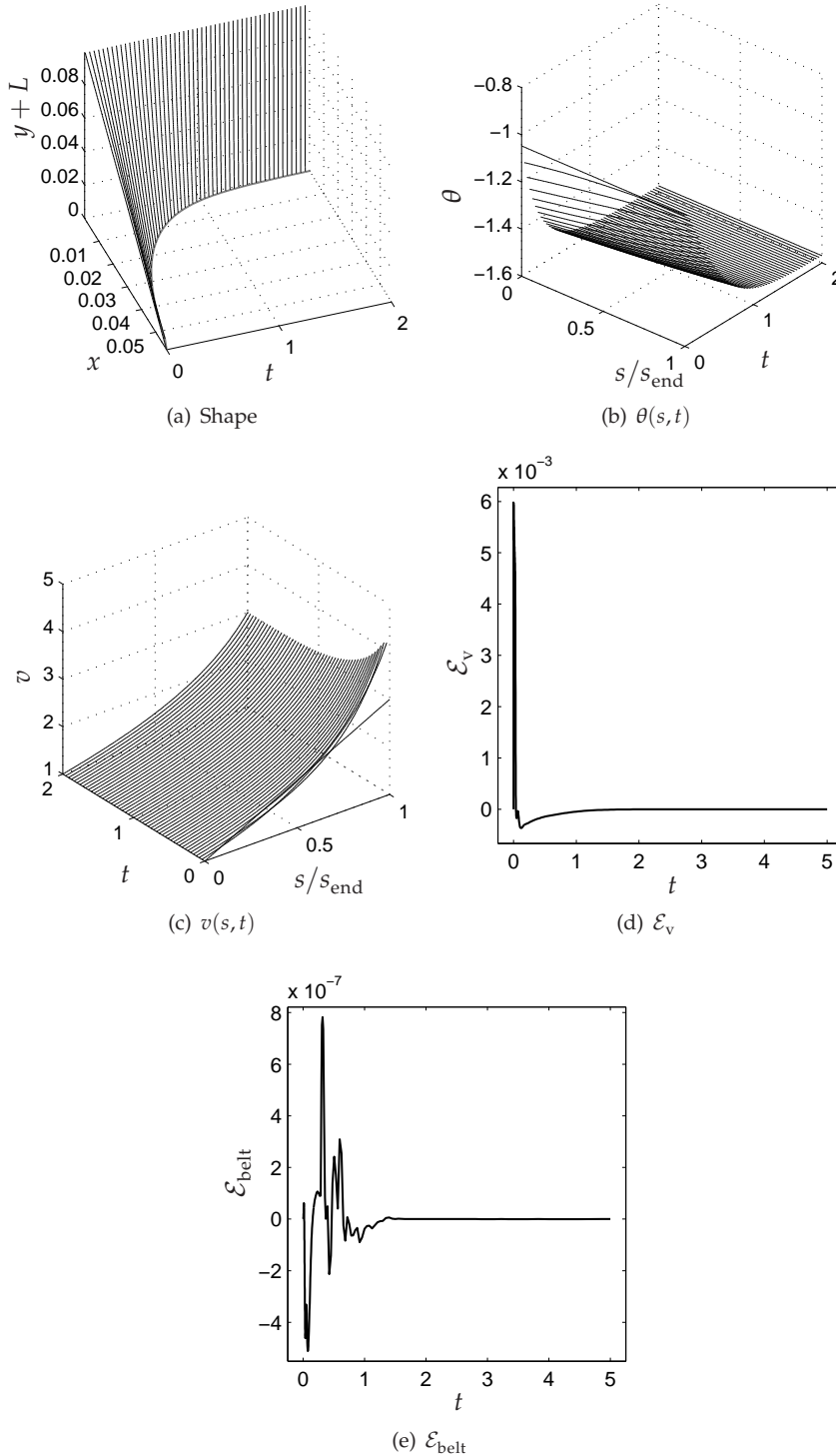


**Figure 6.4:** Results of a numerical simulation for the dynamic jet in drag spinning with  $v_{\text{belt}} = 3 \text{ m/s}$ ,  $v_{\text{nozzle}} = 1 \text{ m/s}$ ,  $\nu = 0.05 \text{ m}^2/\text{s}$ ,  $L = 0.1 \text{ m}$ ,  $\alpha_{\text{nozzle}} = -\pi/3$ ,  $p_1 = 1$ ,  $p_2 = 1000$ . The parameters are from the viscous-inertial jet regime  $\mathcal{P}_{\text{v-i}}$ .

### Inertial regime

Next we discuss a numerical simulation of the dynamic jet for the parameters from the **inertial jet** flow regime  $\mathcal{P}_{\text{inert}}$ ; see Figure 6.5. For this simulation we use the parameters:  $v_{\text{belt}} = 2 \text{ m/s}$ ,  $v_{\text{nozzle}} = 1 \text{ m/s}$ ,  $\nu = 0.02 \text{ m}^2/\text{s}$ ,  $L = 0.1 \text{ m}$ ,  $\alpha_{\text{nozzle}} = -\pi/6$ ,  $p_1 = 1$ , and  $p_2 = 1000$ . During the jet evolution  $\xi(s, t) > 0$  for all  $s$  and  $t$ . In this case, one boundary condition is prescribed at the nozzle for  $\theta$ , (6.33). Now, the parameters  $p_4$  and  $\epsilon_0$  are not relevant because  $\xi(1, t) > 0$  for all  $t$  and  $\theta(1, t)$  stays away from zero. Since the value of  $\theta(0, t) = -\pi/6$ , the parameter  $p_3$  is irrelevant for this simulation.

In this simulation the jet evolves from an initially straight shape to a concave shape comparable to the ballistic trajectory; see Figure 6.5(a). The jet orientation at the nozzle is constant, whereas  $\theta(s, t)$  decreases as  $s$  increases with  $\theta(1, t)$  greater than  $-\pi/2$ ; see Figure 6.5(b). The evolution of the touchdown point in the plane  $y = 0$  is depicted by the grey line in Figure 6.5(a), where  $x(1, t)$  decreases in time and asymptotically approaches a value greater than zero. Due to this movement the flow velocity at the touchdown point first increases and then decreases approaching  $v_{\text{belt}} = 2$  asymptotically; see Figure 6.5(c). The relative error  $\mathcal{E}_v$ , shown in Figure 6.5(d), is of order  $2 \times 10^{-2}$  at the beginning of this simulation, when  $v(s_{\text{end}}(t), t)$  changes rapidly, and then decays to zero with the jet approaching the steady flow. The relative error  $\mathcal{E}_{\text{belt}}$  is of order  $10^{-4}$ ; see Figure 6.4(e).

From the plots in Figures 6.5 we conclude that the dynamic jet evolves to the steady inertial jet provided that  $\xi(s, t) > 0$  for all  $s$  and  $t$ . The jet is almost steady after 0.5 s; see Figures 6.5(a), 6.5(b) and 6.5(c). A comparison of the steady jet shape  $y_{\text{steady}}(x)$  and the dynamic jet shape after 5 seconds  $y(x, 5)$  is presented in Figure 6.5(e), and it shows a difference in the shapes of order  $10^{-3}$ .

So far, we have performed numerical simulations for fixed parameters in which the jets having initially a straight still shape aligned with the nozzle orientation, a linear flow velocity profile between  $v_{\text{nozzle}}$  and  $v_{\text{belt}}$ , and a uniform thickness, evolve to steady jets. In all the simulations the dynamic jets evolved to steady jets in the same flow regime as the parameters where taken from. In case the parameters are from  $\mathcal{P}_{\text{visc}}$  or  $\mathcal{P}_{\text{inert}}$ , the comparisons between the dynamic jet shapes at  $t = 5 \text{ s}$  and the steady jet shapes computed for the same parameters, show that the difference between the shapes is at most 1 mm. In case the parameters are from  $\mathcal{P}_{\text{v-i}}$  the shape approaches the purely vertical one.

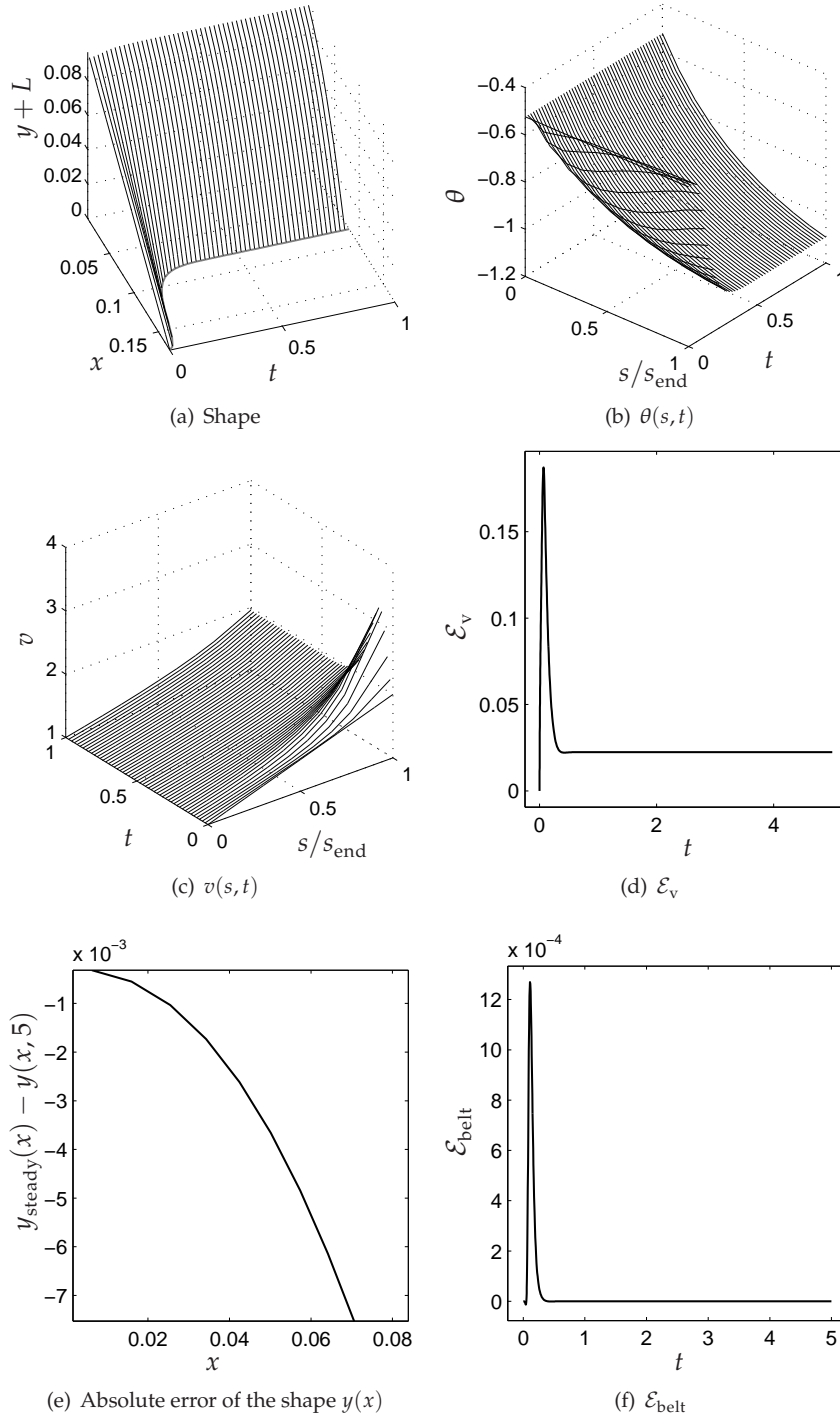


**Figure 6.5:** Results of a numerical simulation for the dynamic jet in drag spinning with  $v_{\text{belt}} = 2 \text{ m/s}$ ,  $v_{\text{nozzle}} = 1 \text{ m/s}$ ,  $\nu = 0.02 \text{ m}^2/\text{s}$ ,  $L = 0.1 \text{ m}$ ,  $\alpha_{\text{nozzle}} = -\pi/6$ ,  $p_1 = 1$ ,  $p_2 = 1000$ . The parameters are from the inertial jet regime  $\mathcal{P}_{\text{inert}}$ .



### Regime change

In all the simulations performed up to here, the signs of  $\xi$  at the nozzle and the belt were kept the same during the jet evolution, and, moreover, the boundary conditions for  $\theta$  were not changed. As a next step, we analyse situations when the sign of  $\xi$  changes at the belt or at the nozzle. We do that by starting with a steady jet in one flow regime, and then tune the parameters to enter the neighboring flow regime. Finally, we let the jet evolve to a steady jet in the new regime. The parameter tuning is done by varying  $v_{\text{nozzle}}$  in time. First, we present two simulations where the parameters move from viscous-inertial to viscous and from viscous-inertial to inertial regimes. In these simulations the expected transition results are obtained. In two other simulations we change  $v_{\text{nozzle}}$  so that the parameters leave the viscous or inertial regime and enter the viscous-inertial regime. However, these simulations are not successful due to steep change of the jet orientation at the jet ends.

### Parameter change from $\mathcal{P}_{\text{v-i}}$ to $\mathcal{P}_{\text{visc}}$

In this simulation we start with a steady, purely vertical, viscous-inertial jet with  $v_{\text{belt}} = 0.5 \text{ m/s}$ ,  $v_{\text{nozzle}} = 0.2 \text{ m/s}$ ,  $\nu = 0.0033 \text{ m}^2/\text{s}$ , and  $L = 0.02 \text{ m}$ . Then, at  $t = 0.1 \text{ s}$ , we linearly decrease the  $v_{\text{nozzle}}$  to  $v_{\text{nozzle}} = 0.1 \text{ m/s}$  during 2 s so the parameters enter the viscous regime; see Figure 6.6(f). After these 2 s we keep  $v_{\text{nozzle}} = 0.1 \text{ m/s}$ , and we then see that the jet asymptotically evolves to a steady viscous jet. The nozzle orientation  $\alpha_{\text{nozzle}}$  is irrelevant for this simulation because  $\xi(0, t)$  is always negative. The other parameters used in this simulation are  $p_1 = 1$ ,  $p_2 = 1000$ , and  $\epsilon_0 = 0.01$ . The boundary condition (6.36) is replaced here by

$$\text{if } \xi(1, t) < -0.01 \text{ then } \theta_t(1, t) = (\epsilon_0 - \theta(1, t)). \quad (6.99)$$

By this modification, we start satisfying the tangency at the belt not directly at the moment when  $\xi(1, t)$  becomes negative, but somewhat later when  $\xi(1, t)$  is a bit away from zero. The reason of this is to smooth out the change of the boundary condition at the belt when  $\xi(1, t)$  changes sign from positive to negative.

Results of the simulation are presented in Figure 6.6. The evolution of the jet shape with the initially straight vertical jet becoming convex and tangent to the belt is depicted in Figure 6.6(a). The initially vertical jet orientation  $\theta \equiv -\pi/2$  increases with time, and the touchdown angle eventually approaches zero; see Figure 6.6(b). The flow velocity at the belt  $v(1, t)$  first decreases when the touchdown point moves away from the nozzle, and then increases asymptotically to the value  $v_{\text{belt}} = 0.5 \text{ m/s}$ ; see Figure 6.6(c). The relative errors  $\mathcal{E}_{\text{belt}}$  and  $\mathcal{E}_v$  are of order  $10^{-6}$  and  $10^{-4}$ ; see Figures 6.6(e) and 6.6(d). In Figure 6.6(d) we observe one sudden jump down of the error when  $\xi(1, t)$  changes sign and a jump up, at  $t = 2 \text{ s}$ , when  $v_{\text{nozzle}}$  stops to decrease and stays  $0.1 \text{ m/s}$ ; see Figure 6.6(f).

In this simulation we observe that the initially viscous-inertial jet after transition approaches the steady viscous one, if the parameters are changed to move from  $\mathcal{P}_{\text{v-i}}$  to  $\mathcal{P}_{\text{visc}}$ . Our current numerical method is capable to cope with the change of the boundary conditions for  $\theta$  at the belt from no boundary condition to the tangency condition. However, this requires a change of the relaxed boundary condition from (6.36) to (6.99).

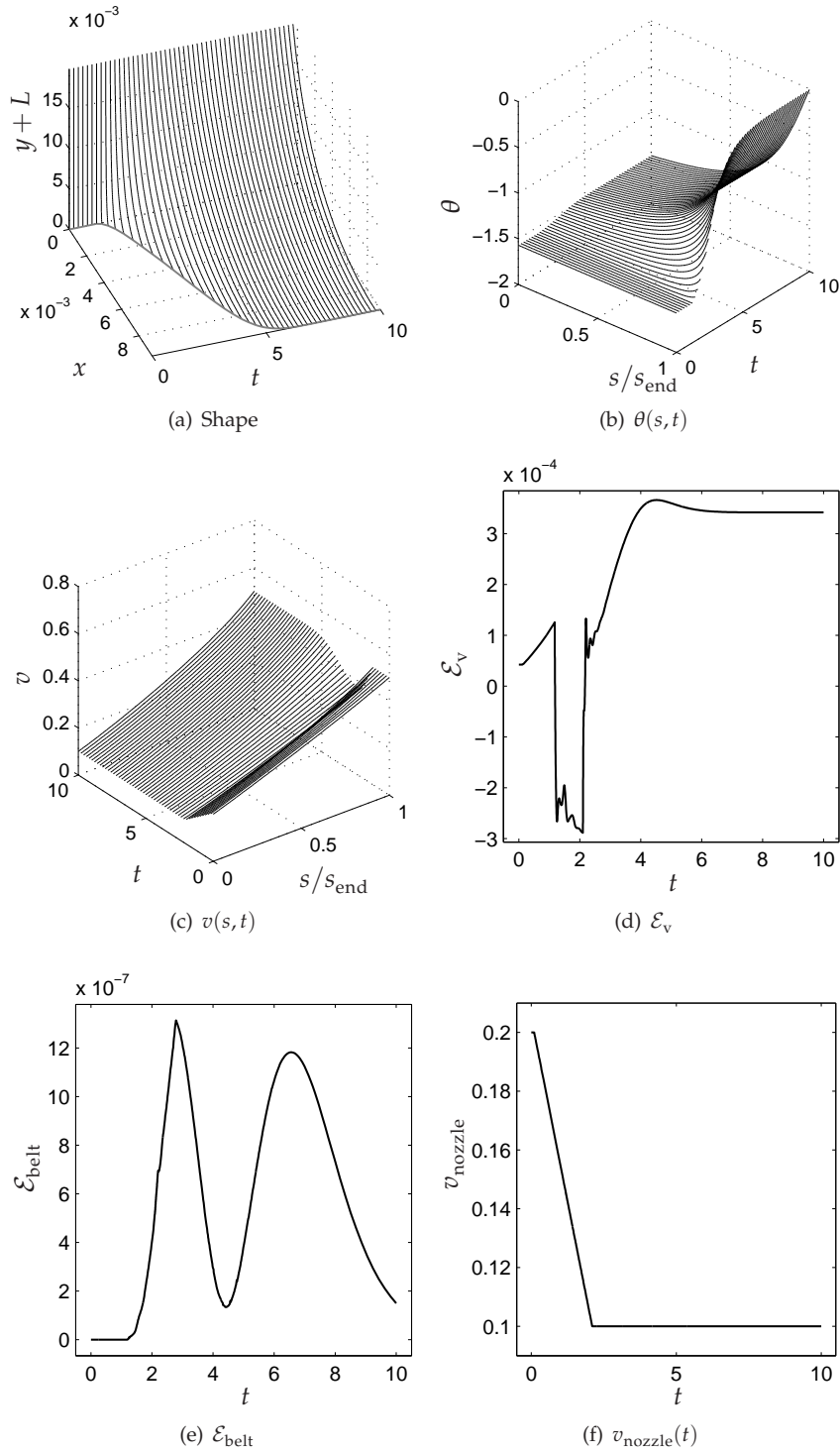


**Figure 6.6:** A numerical simulation in which we start with a steady viscous-inertial jet having the parameters:  $v_{\text{belt}} = 0.5 \text{ m/s}$ ,  $v_{\text{nozzle}} = 0.2 \text{ m/s}$ ,  $\nu = 0.0033 \text{ m}^2/\text{s}$ , and  $L = 0.02 \text{ m}$ . Next, starting at  $t = 0.1 \text{ s}$ ,  $v_{\text{nozzle}}$  linearly decreases to  $0.1 \text{ m/s}$  during  $2 \text{ s}$ , and the parameters enter  $\mathcal{P}_{\text{visc}}$ .

### Parameter change from $\mathcal{P}_{v-i}$ to $\mathcal{P}_{inert}$

We proceed with a numerical simulation similar to the preceding one, in which the initially viscous-inertial jet evolves to the inertial jet after a continuous parameter change. Hence, the parameters set leaves  $\mathcal{P}_{v-i}$  and enters  $\mathcal{P}_{inert}$ . The initial parameters for this simulation are  $v_{belt} = 2 \text{ m/s}$ ,  $v_{nozzle} = 0.5 \text{ m/s}$ ,  $\nu = 0.02 \text{ m}^2/\text{s}$ ,  $L = 0.1 \text{ m}$ , and  $\alpha_{nozzle} = -\pi/6$ . After 3 s we start to linearly increase  $v_{nozzle}$  until it becomes 1.1 m/s at  $t = 7 \text{ s}$ , and keep  $v_{nozzle} = 1.1 \text{ m/s}$  for  $t > 7 \text{ s}$ ; see Figure 6.7(f). The parameters for the relaxed conditions (6.29), (6.31), and (6.33) relevant for this simulation, are  $p_1 = 1$ ,  $p_2 = 1000$ , and  $p_3 = 3$ .

The evolution of the jet shape from purely vertical to a concave one is depicted in Figure 6.7(a). From  $t = 5 \text{ s}$  on, the angle  $\theta$  starts to increase from its uniform initial value  $\theta = -\pi/2$ . At the nozzle,  $\theta(0, t)$  asymptotically increases to the nozzle orientation  $\alpha_{nozzle} = -\pi/6$  when  $\xi(0, t)$  changes sign from negative to positive around  $t = 5 \text{ s}$ ; see Figure 6.7(b). The flow velocity at the belt  $v(s_{end}(t), t)$  suddenly decreases when the touchdown point moves away from the nozzle and then increases asymptotically approaching the value of  $v_{belt} = 2 \text{ m/s}$ ; see Figure 6.7(c). The relative errors  $\mathcal{E}_{belt}$  and  $\mathcal{E}_v$  are of order  $10^{-5}$  and  $10^{-3}$ ; see Figures 6.7(e) and 6.7(d). The errors are maximal around  $t = 5 \text{ s}$ , when  $\xi(0, t)$  changes sign.

In this simulation we see that our numerical method is capable to cope with a change of the boundary condition for  $\theta$  at the nozzle from no boundary condition to the alignment with the nozzle orientation. However, the parameter change in this transition should be performed fast enough so that a sudden change of the jet orientation at the nozzle, occurring for the steady inertial jet when  $\xi$  at the nozzle is close to zero, is avoided.

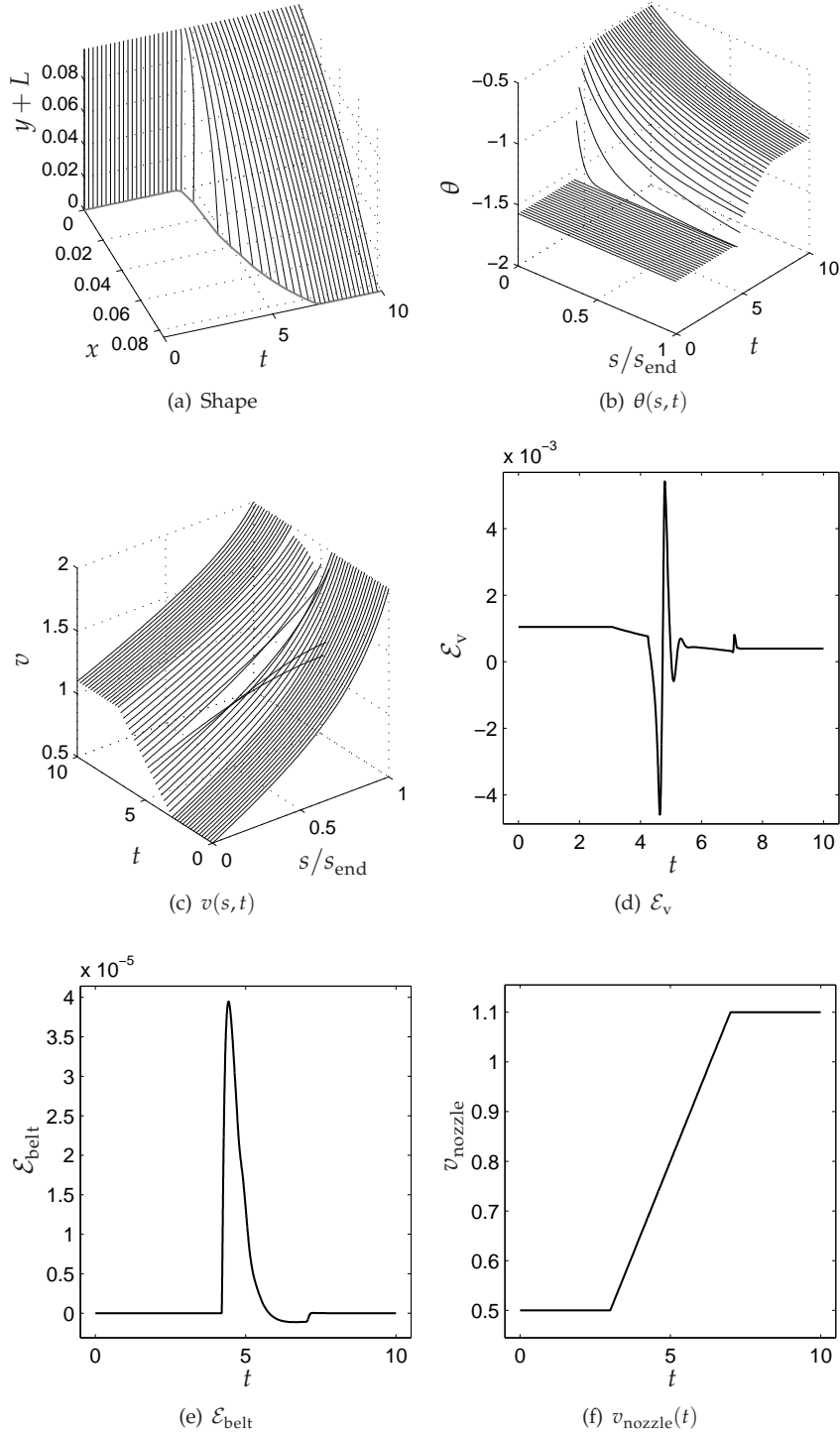


**Figure 6.7:** A numerical simulation in which we start with the steady viscous-inertial jet with the parameters  $v_{\text{belt}} = 2 \text{ m/s}$ ,  $v_{\text{nozzle}} = 0.5 \text{ m/s}$ ,  $\nu = 0.02 \text{ m}^2/\text{s}$ ,  $L = 0.1 \text{ m}$ , and  $\alpha_{\text{nozzle}} = -\pi/6$ . Then, starting at  $t = 3 \text{ s}$   $v_{\text{nozzle}}$  linearly increases to  $1.1 \text{ m/s}$  during  $4 \text{ s}$ , and the parameters enter  $\mathcal{P}_{\text{inert}}$ .

### Parameter changes from $\mathcal{P}_{\text{visc}}$ and $\mathcal{P}_{\text{inert}}$ towards $\mathcal{P}_{\text{v-i}}$

In the next two simulations we make an attempt to vary the parameters so that they leave  $\mathcal{P}_{\text{visc}}$  or  $\mathcal{P}_{\text{inert}}$  and enter  $\mathcal{P}_{\text{v-i}}$ . In this we keep all parameters fixed except  $v_{\text{nozzle}}$ . However, our simulations did not converge, because during evolution the jet shape orientation changes steeply at the nozzle or at the belt and our numerical method is not capable of overcoming these boundary layer effects.

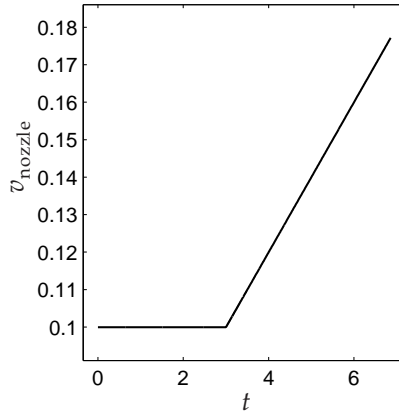


**Figure 6.8:** Change of  $v_{\text{nozzle}}$  in time so the parameters leave  $\mathcal{P}_{\text{visc}}$  and enter  $\mathcal{P}_{\text{v-i}}$

Let us start with the steady viscous jet having the parameters  $v_{\text{belt}} = 0.5 \text{ m/s}$ ,  $v_{\text{nozzle}} = 0.1 \text{ m/s}$ ,  $\nu = 0.0033 \text{ m}^2/\text{s}$ , and  $L = 0.02 \text{ m}$ . The relevant parameters for the relaxed conditions are  $p_1 = 1$ ,  $p_2 = 10000$ , and  $\epsilon_0 = 0.01$ . Then, starting at  $t = 3 \text{ s}$ , we increase  $v_{\text{nozzle}}$  with the rate  $0.02 \text{ m/s}^2$ ; see Figure 6.8. In this period the jet shape approaches the vertical shape but it never reach the purely vertical shape; see Figure 6.9(a). In this period of the evolution process the angle  $\theta$  near the belt ( $s/se \uparrow 1$ ) changes steeply from 0 to  $-\pi/2$ ; see Figure 6.9(b), and this change becomes steeper while  $\xi(1, t)$  crosses zero and becomes positive; see Figure 6.9(e). This causes the size of time steps in the MATLAB solve ode15s to decrease, resulting in an extremely steep end of the curve in Figure 6.9(d). The solver can not overcome this boundary layer effect and stops the numerical integration in time at  $t = 6.86 \text{ s}$ . In this simulation the relative errors  $\mathcal{E}_{\text{belt}}$  and  $\mathcal{E}_v$  remain small of order  $10^{-4}$ ; see Figures 6.9(f) and 6.9(c).

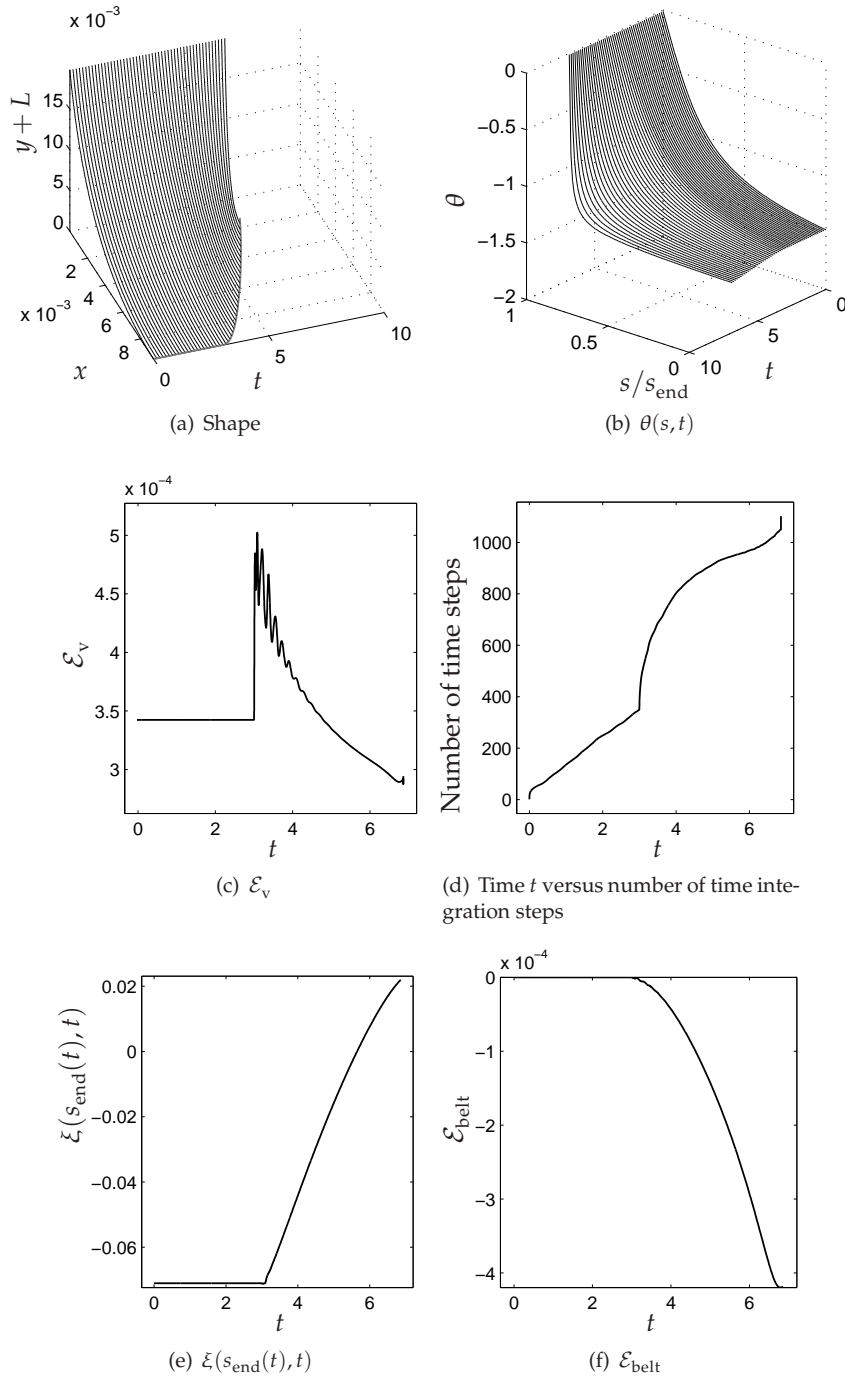


**Figure 6.9:** Results of a numerical simulation starting with the steady viscous jet having the parameters  $v_{\text{belt}} = 0.5 \text{ m/s}$ ,  $v_{\text{nozzle}} = 0.1 \text{ m/s}$ ,  $\nu = 0.0033 \text{ m}^2/\text{s}$ , and  $L = 0.02 \text{ m}$ . After  $t = 3 \text{ s}$  we increase  $v_{\text{nozzle}}$  with the rate  $0.02 \text{ m/s}^2$  until the numerical integration stops at  $t = 6.86 \text{ s}$ .

In the final simulation we start with the steady inertial jet having the parameters  $v_{\text{belt}} = 2 \text{ m/s}$ ,  $v_{\text{nozzle}} = 1.1 \text{ m/s}$ ,  $\nu = 0.02 \text{ m}^2/\text{s}$ ,  $L = 0.1 \text{ m}$ , and  $\alpha_{\text{nozzle}} = -\pi/6$ . The relevant parameters for the relaxed conditions are  $p_1 = 1$  and  $p_2 = 10000$ . Starting at  $t = 1 \text{ s}$ , we decrease  $v_{\text{nozzle}}$  with the rate  $0.1 \text{ m/s}^2$ ; see Figure 6.10. Because of this the jet shape approaches the vertical shape, but it does never reach a purely vertical shape; see Figure 6.11(a). During the evolution process the angle  $\theta$  near the nozzle ( $s_{\text{end}}/s \uparrow 0$ ) from  $\alpha_{\text{nozzle}} = -\pi/6$  to  $-\pi/2$ ; see Figure 6.11(b), and this change becomes steeper while  $\xi(0, t)$  approaches zero; see Figure 6.11(e). This causes the size of time steps in the MATLAB solve ode15s to decrease, resulting in an extremely steep end of the curve in Figure 6.11(d). Again, the solver can not overcome this boundary layer effect and stops numerical integration in time at  $t = 6.86 \text{ s}$ . In this simulation the relative errors  $\mathcal{E}_{\text{belt}}$  and  $\mathcal{E}_{\text{v}}$  are still small, of order  $10^{-3}$  and  $10^{-5}$ ; see Figures 6.11(f) and 6.11(c).

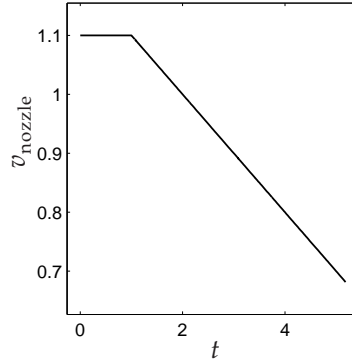


**Figure 6.10:** Change of  $v_{\text{nozzle}}$  in time so the parameters leave  $\mathcal{P}_{\text{inert}}$  and enter  $\mathcal{P}_{\text{v-i}}$

### Conclusions for drag spinning simulations

We summarize the results of the above simulations for the dynamic jet in drag spinning. The first three simulations have shown that if we start from the initially straight jet with the parameters taken from one of the three flow regimes, then the jet evolves to the steady jet in the same flow regime. However, in these three simulations the values of  $\xi$  at the belt and at the nozzle have the same sign during the whole evolution. Comparisons of the steady jet shape with the dynamic jet after 5 s of evolution has shown a good agreement for the parameters from the viscous and inertial regimes.

The simulations with initially the viscous-inertial jet and then changing the parameters so that they enter  $\mathcal{P}_{\text{visc}}$  or  $\mathcal{P}_{\text{inert}}$  are successfully performed. On the other hand, the opposite transition is not possible due to boundary layer effects for  $\theta$  at the belt or at the nozzle appearing during these transitions for initially viscous and inertial steady jets.

The absolute errors  $\mathcal{E}_{\text{belt}}$  and  $\mathcal{E}_{\text{v}}$  caused by the relaxed equation for  $s_{\text{end}}(t)$  and the boundary condition for  $v(1, t)$  (6.29) and (6.31) are on average  $10^{-4}$ . Also the relaxed boundary conditions for  $\theta$  (6.33) and (6.36) are working fine, so the numerical method is capable of making a transition to the jet aligned with the belt or the nozzle.

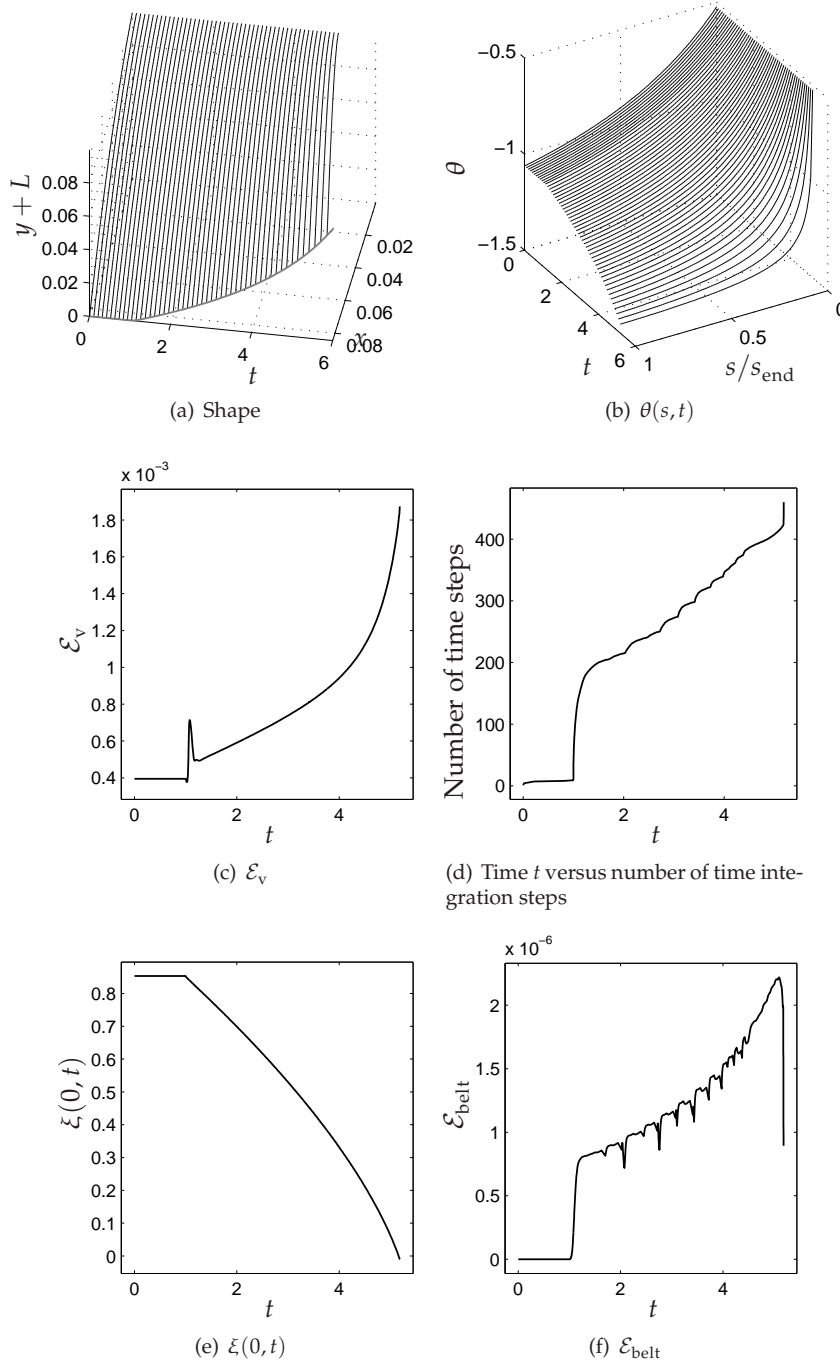


**Figure 6.11:** Results of a numerical simulation starting having the steady inertial jet with the parameters  $v_{\text{belt}} = 2 \text{ m/s}$ ,  $v_{\text{nozzle}} = 1.1 \text{ m/s}$ ,  $\nu = 0.02 \text{ m}^2/\text{s}$ ,  $L = 0.1 \text{ m}$ , and  $\alpha_{\text{nozzle}} = -\pi/6$ . After  $t = 1 \text{ s}$  we decrease  $v_{\text{nozzle}}$  with the rate  $0.1 \text{ m/s}^2$  until the numerical integration stops at  $t = 5.18 \text{ s}$ .



### 6.2.2 Results for dynamic jet in rotary spinning

In this section we perform numerical simulations for the dynamic jet in rotary spinning. In the first three simulations the jet evolves to a steady one of the in the three flow regimes (i.e. viscous with the rotating coagulator, and viscous-inertial and inertial with the coagulator fixed). The final simulation we start initially with an inertial jet and decrease  $Dr$  so that the parameters approach the region where no steady jet between the rotor and the coagulator exists.

#### Evolution to the steady jet

In the first three simulations, we choose as an initial configuration a straight, still, and radially oriented jet of uniform thickness and with the flow velocity linearly distributed between the nozzle and the rotor. This mean that we have the following initial conditions

$$\begin{aligned}\theta(s, 0) &= 0, \quad \zeta(s, 0) = 0, \quad v(s, 0) = v_{\text{nozzle}} + \frac{s}{s_{\text{end}}(0)}((\Omega - \Omega_{\text{coag}})R_{\text{coag}} - v_{\text{nozzle}}), \\ \mathcal{A}(s, 0) &= 1, \quad \text{and } s_{\text{end}}(0) = R_{\text{coag}} - R_{\text{rot}}.\end{aligned}$$

For our numerical simulations we need to specify the parameters of the system,  $v_{\text{nozzle}}$ ,  $R_{\text{rot}}$ ,  $R_{\text{coag}}$ ,  $\Omega$ ,  $\Omega_{\text{coag}}$  (only nonzero in case of viscous jet), and  $\nu$ . In addition we need to choose the parameters  $p_1$  and  $\epsilon_0$  for the relaxed ODE for  $s_{\text{end}}(t)$  (6.87), and  $p_3$  and  $p_4$  for the relaxed boundary conditions (6.89) and (6.90). The parameters  $p_1$ ,  $p_3$ , and  $p_4$  should be taken as large as possible, and  $\epsilon_0$  as close to zero as possible.

In the next three simulations we describe evolutions of the jets shapes,  $\theta$ , and  $v$  to a steady regime. In particular we focus on the error  $\mathcal{E}_{\text{coag}}$ , touchdown angle  $\alpha_{\text{t-d}}$  and influences of the relaxed equation (6.87) and boundary conditions (6.89) and (6.90). In these simulations  $\xi$  at the nozzle and at the coagulator does not change sign, so the boundary conditions for  $\theta$  do not change during the evolution. We also compare the dynamic jet shapes after they have become steady with the corresponding steady ones. To do that we describe the jet shape in Cartesian coordinates as  $x_{\text{steady}}(y)$  for the steady jet, and so  $x(y, t)$  for the dynamic jet, in the first and the third simulation. For the second simulation we represent the shape in polar coordinates as  $R_{\text{steady}}(\beta)$  for the steady jet, and as  $R(\beta, t)$  for the dynamic jet.

We start with the simulation of a dynamic jet evolving to a steady **viscous jet**. The parameters are taken from  $\mathcal{P}_{\text{visc}}$ , and have values  $v_{\text{nozzle}} = 0.05 \text{ m/s}$ ,  $R_{\text{rot}} = 0.9 \text{ m}$ ,  $R_{\text{coag}} = 1 \text{ m}$ ,  $\Omega = 1 \text{ rad/s}$ ,  $\Omega_{\text{coagulator}} = 0.7 \text{ rad/s}$  and  $\nu = 0.033 \text{ m}^2/\text{s}$ . During the jet evolution,  $\xi$  is always negative and thus we demand tangency with the coagulator (6.90). The additional parameters relevant for this simulation are  $p_1 = 1$ ,  $\epsilon_0 = 0.001$ , and  $p_4 = 2$ .

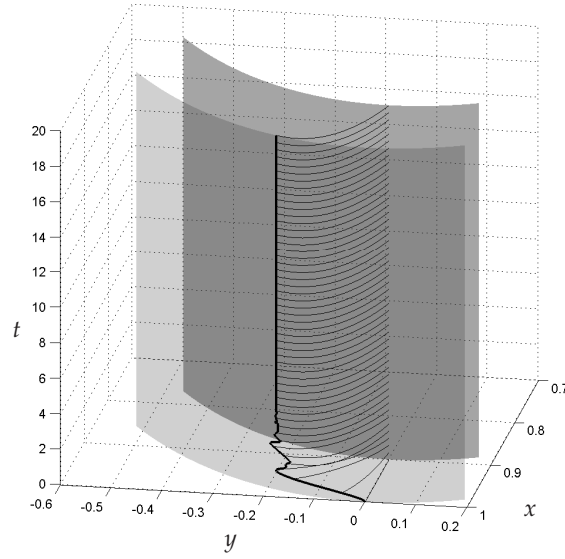


**Figure 6.12:** Evolution of the dynamic jet shape for the parameters from  $\mathcal{P}_{\text{visc}}$ . The darker grey surface represents the rotor and the lighter grey the coagulator.

The initially straight jet evolves to a steady one tangent to the coagulator after about 5 s; see Figure 6.12. Figure 6.13(a) shows how the initially zero angle  $\theta$  automatically chooses its non-radial orientation at the nozzle. At the coagulator the jet tends to become tangent at the belt as be seen in Figure 6.13(e) where the initial touchdown angle  $\alpha_{\text{t-d}} = \pi/2$  goes asymptotically to zero. After 5 s the jet is steady due to the action of the relaxed boundary condition (6.90). A zoom-in of  $\alpha_{\text{t-d}}(t)$  near zero is presented in Figure 6.13(f), where the dashed line corresponds to the value of  $\epsilon_0$ . The touchdown angle  $\alpha_{\text{t-d}}(t)$  crosses this line a couple of times, indicates a change in ODE for  $s_{\text{end}}(t)$  due to the “if” statement in (6.87). The touchdown error  $\mathcal{E}_{\text{coag}}$  is about  $10^{-3}$ ; see Figure 6.13(c), and it has jumps around  $t = 4 \text{ s}$  and  $t = 5 \text{ s}$ , at the same points where  $\alpha_{\text{t-d}}(t)$  crosses  $\epsilon_0$ ; see Figures 6.13(c) and 6.13(f). A comparison between the steady jet shape  $x_{\text{steady}}(y)$  and the dynamic jet shape  $x(y, 20)$  after 20 s of evolution is done in Figure 6.13(d), where we plot the relative error of the shapes  $(x_{\text{steady}}(y) - x(y, 20))/x(y, 20)$ , which is of order  $10^{-4}$ . The flow velocity in the dynamic jet is depicted in Figure 6.13(b), where we see that at the coagulator the flow velocity decreases, because the end point moves away from the nozzle and then after a couple of decaying oscillations approaches to the value of  $(\Omega - \Omega_{\text{coag}})R_{\text{coag}} = 0.3 \text{ m/s}$ .

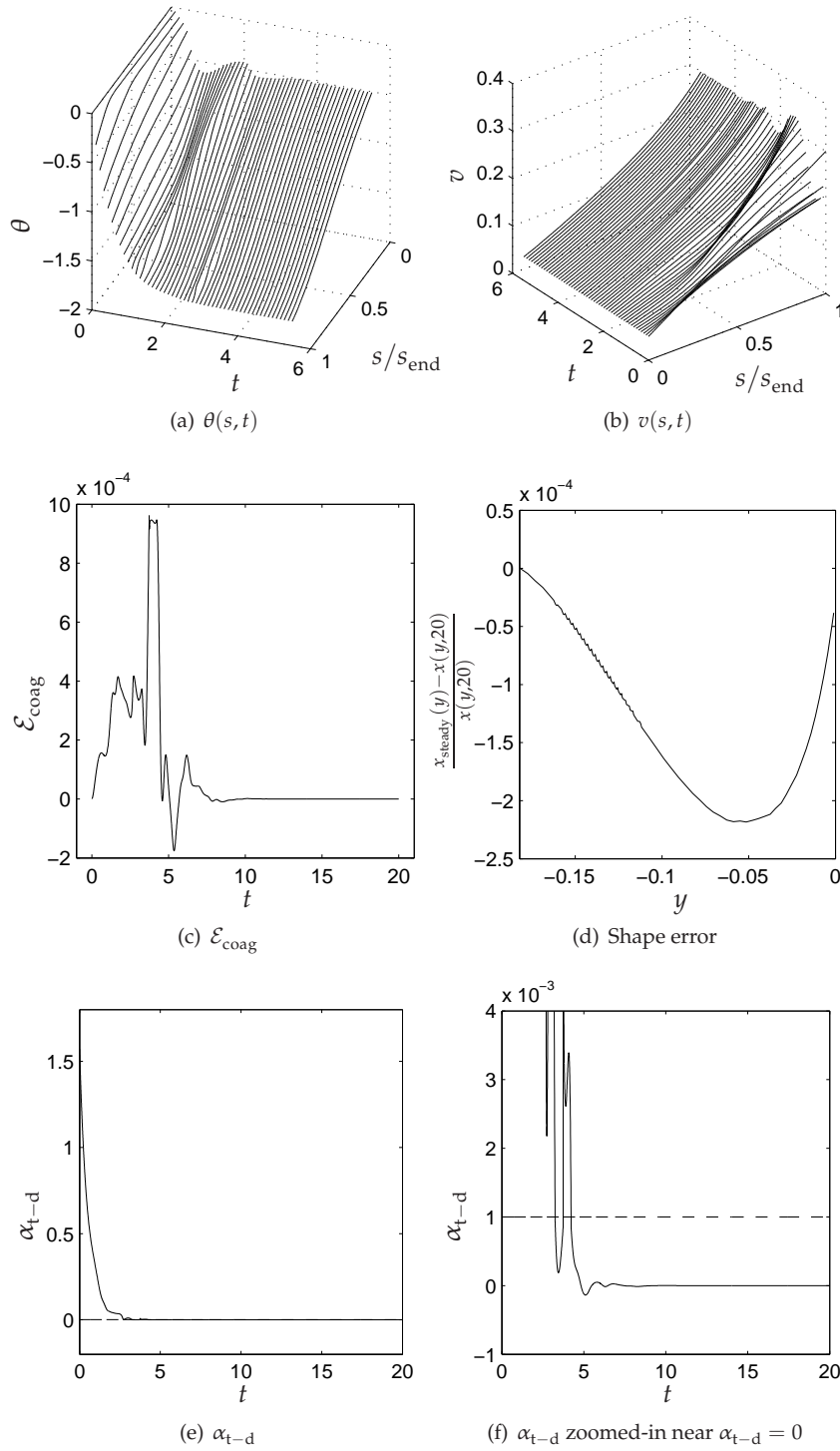


**Figure 6.13:** Simulation results of the dynamic jet with the parameters from  $\mathcal{P}_{\text{visc}}$ .

In our second simulation we calculate how a dynamic jet evolves to a steady **viscous-inertial jet**. The parameters are taken from  $\mathcal{P}_{v-i}$ , and have values  $v_{\text{nozzle}} = 0.17$  m/s,  $R_{\text{rot}} = 0.5$  m,  $R_{\text{coag}} = 1$  m,  $\Omega = 1$  rad/s and  $\nu = 0.04$  m<sup>2</sup>/s. During the jet evolution  $\xi$  is negative at the nozzle and positive at the coagulator so we can not prescribe boundary conditions for  $\theta$ . There is only one additional parameter relevant for this simulation, namely  $p_1 = 1$ . The parameter  $\epsilon_0$  is not needed because  $\alpha_{t-d}$  is away from zero, and  $p_3$  and  $p_4$  are irrelevant, because the jet itself determines its orientations at the nozzle and at the coagulator.

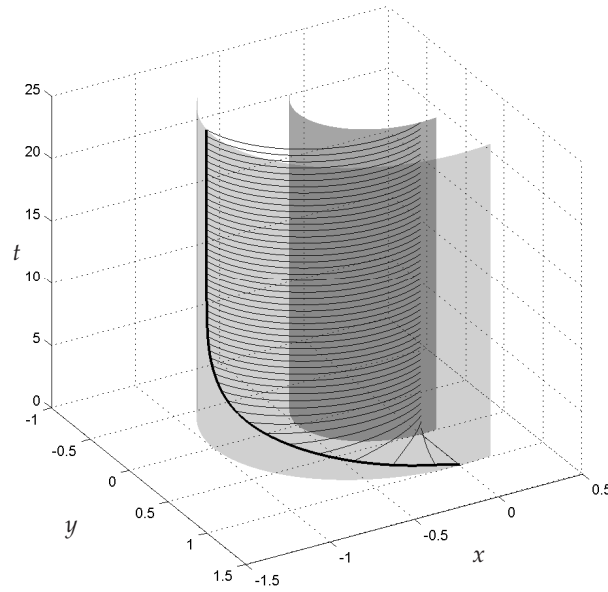


**Figure 6.14:** Evolution of the dynamic jet shape for the parameters from  $\mathcal{P}_{v-i}$ . The red surface represents the rotor and the blue the coagulator.

The initially straight jet evolves to the steady one after  $t = 10$  s; see Figure 6.14. The jet orientation  $\theta$  at the nozzle is determined by the jet itself; see Figure 6.15(a). The touchdown angle  $\alpha_{t-d}$  initial value  $\pi/2$ , goes asymptotically to some positive value determined the jet itself, which is away from zero; see Figure 6.15(e). The relative error  $\mathcal{E}_{\text{coag}}$  is of order  $10^{-3}$ ; see Figure 6.15(c). Contrary to the simulations with the parameters from  $\mathcal{P}_{\text{visc}}$  and  $\mathcal{P}_{\text{inert}}$  this error does not go to zero. Hence, here the extra term in (6.89) does not prevent a numerical drift. A comparison of the steady jet shape,  $R_{\text{steady}}(\beta)$ , and the dynamic one after 25 s,  $R(\beta, 25)$ , is done in Figure 6.15(d). The relative error  $(R_{\text{steady}}(\beta) - R(\beta, 25))/R(\beta, 25)$  is of order  $10^{-3}$ . The flow velocity in the dynamic jet  $v$  is depicted in Figure 6.15(b), where we observe that initially at the coagulator the flow velocity decreases because the jet end moves away from the nozzle, reaches its minimum, and consequently increases, asymptotically approaching from below a value of  $\Omega R_{\text{coag}} = 1$  m/s.

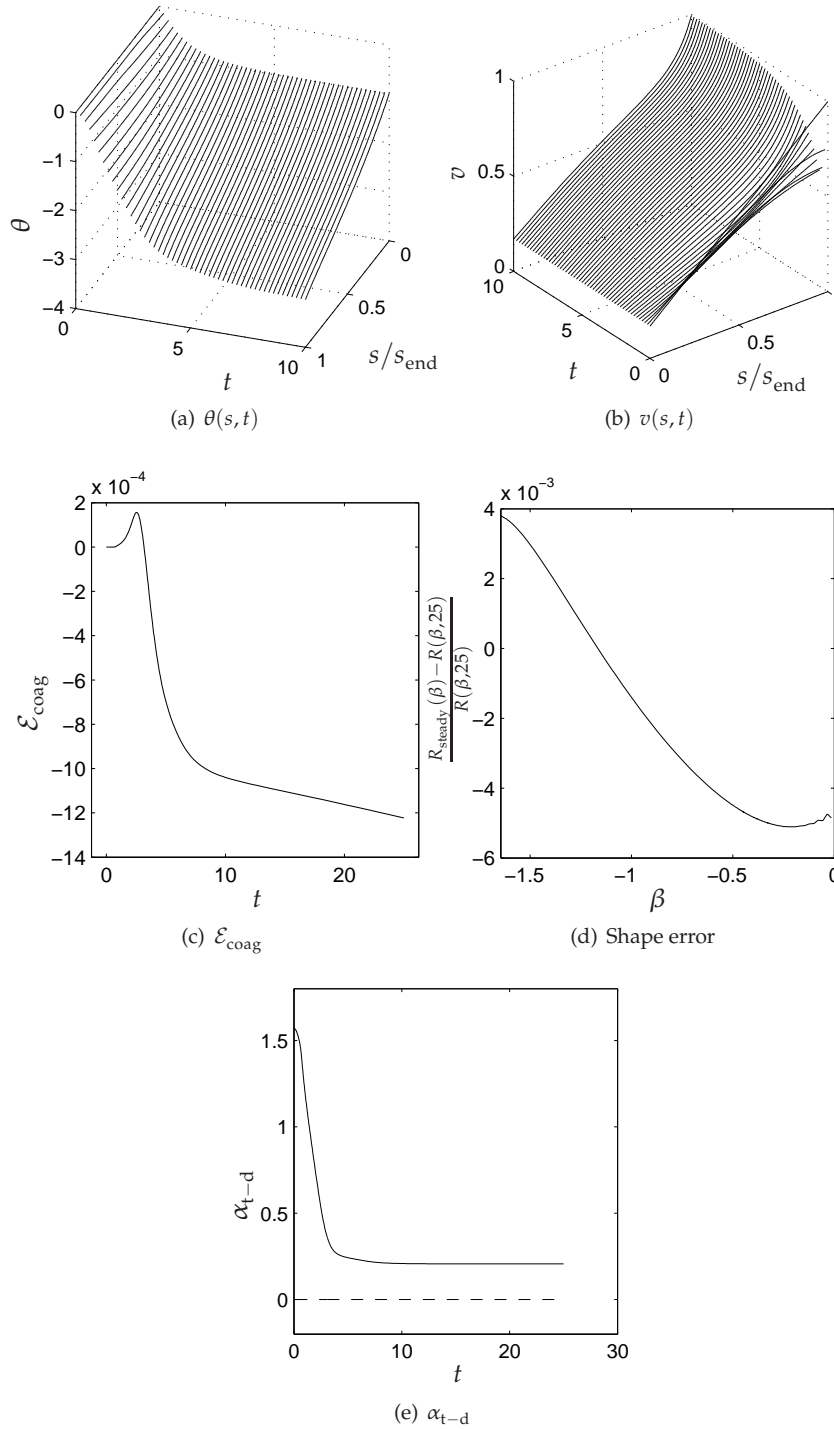
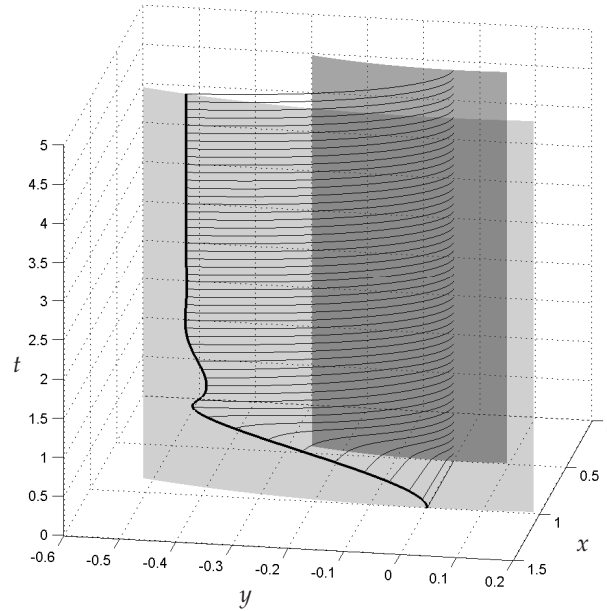


Figure 6.15: Simulation results of the dynamic jet for the parameters from  $\mathcal{P}_{v-i}$ .

In the third simulation we calculate how a straight jet evolves to a steady **inertial jet**. The parameters are taken from  $\mathcal{P}_{\text{inert}}$  and the values are  $v_{\text{nozzle}} = 0.6 \text{ m/s}$ ,  $R_{\text{rot}} = 0.5 \text{ m}$ ,  $R_{\text{coag}} = 1 \text{ m}$ ,  $\Omega = 1 \text{ rad/s}$ , and  $\nu = 0.04 \text{ m}^2/\text{s}$ . The parameter  $p_4$  is not needed for this simulation, because  $\xi$  is positive everywhere in the jet for all  $t$ , and in particular at the coagulator. Since we start with the jet aligned with the nozzle,  $\theta(0,0)$ , yielding  $\theta(0,t) = 0$ , for all  $t > 0$ , and then  $p_3$  does not affect the simulation. There is now only one additional parameter relevant for this simulation, namely  $p_1 = 10$ . The value of  $\epsilon_0$  is irrelevant because the jet touchdown angle  $\alpha_{t-d}$  does not become zero during the evolution.



**Figure 6.16:** Evolution of the dynamic jet shape for the parameters from  $\mathcal{P}_{\text{inert}}$ . The darker grey surface represents the rotor and the lighter grey the coagulator.

The initially straight jet evolves to the steady one after  $t = 3 \text{ s}$ ; see Figure 6.16. This jet is aligned with the radial nozzle orientation:  $\theta(0,t) = 0$ ; see Figure 6.17(a). At the coagulator the touchdown angle decreases from  $\pi/2$  to a nonzero value and it always stay away from zero; see Figure 6.17(e). The error  $\mathcal{E}_{\text{coag}}$  is of order  $10^{-3}$  and after having a peak at  $t = 1 \text{ s}$  it decays exponentially to zero; see Figure 6.17(c). A shape comparison of the steady inertia jet,  $x_{\text{steady}}(y)$ , and the dynamic jet after 5 s of evolution,  $x(y,5)$ , is presented in Figure 6.17(d), and the maximum relative difference is of order  $10^{-2}$ . The flow velocity in the jet  $v$  first decreases, because the jet end moves away from the nozzle, and then increases to a value larger than  $\Omega R_{\text{coag}} = 1$  and eventually approaches the value  $\Omega R_{\text{coag}} = 1$ .

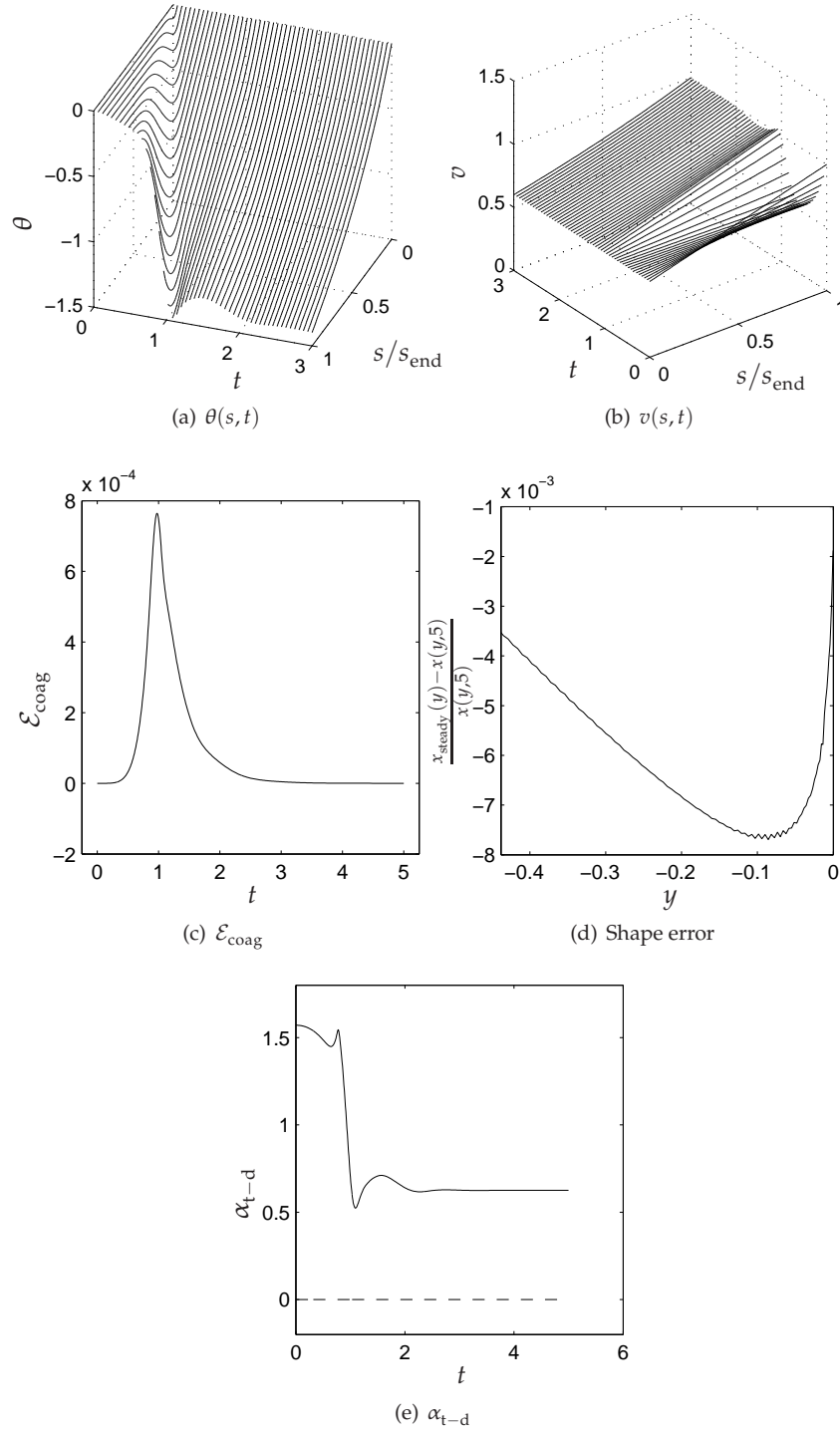


Figure 6.17: Simulation results of the dynamic jet for the parameters from  $\mathcal{P}_{\text{inert}}$ .

### Unsteady jet in rotary spinning

In our final simulations we start with a steady inertial jet. The dimensional parameters are  $v_{\text{nozzle}} = 0.7 \text{ m/s}$ ,  $R_{\text{rot}} = 0.85 \text{ m}$ ,  $R_{\text{coag}} = 1 \text{ m}$ ,  $\Omega = 1 \text{ rad/s}$ , and  $\nu = 0.066 \text{ m}^2/\text{s}$ ; and the dimensionless parameters are  $B = 0.2$ ,  $R_0 = 0.85$ , and  $\text{Dr} = 0.7$ . The space parametrization for  $B = 0.2$  is presented in Figure 6.18, where the point  $A$  indicates the initial position in the parameter space for the steady jet.

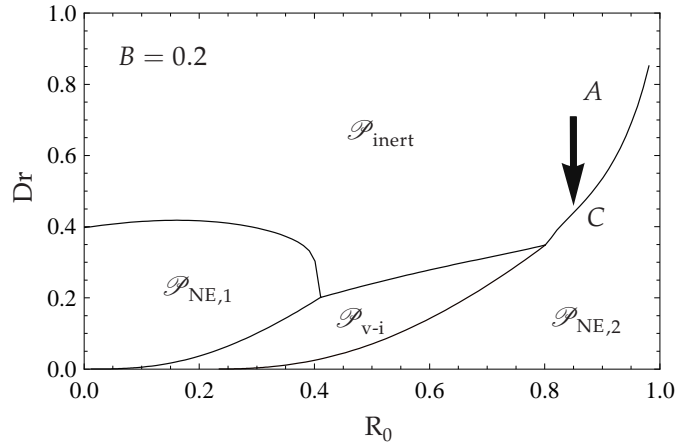


Figure 6.18: Partitioning of the parameter space for  $B = 0.2$ .

To obtain an unsteady jet we gradually decrease  $\text{Dr}$  by decreasing  $v_{\text{nozzle}}$  so that the parameters approach the non-existence jet region  $\mathcal{P}_{\text{NE},2}$ , as indicated by the arrow  $AC$  in Figure 6.18. We do that by gradually decreasing  $v_{\text{nozzle}}$  during 20 s; see Figure 6.20(c) for a typical velocity profile. We use five different decelerations  $-0.011$ ,  $-0.01195$ ,  $-0.012$ ,  $-0.0121$ ,  $-0.0122$ , so at the end we reach the following points in the parameter space along the  $AC$  direction:  $C_1$  with  $v_{\text{nozzle}} = 0.48 \text{ m/s}$ ,  $C_2$  with  $v_{\text{nozzle}} = 0.461 \text{ m/s}$ ,  $C_3$  with  $v_{\text{nozzle}} = 0.46 \text{ m/s}$ ,  $C_4$  with  $v_{\text{nozzle}} = 0.458 \text{ m/s}$ , and  $C_5$  with  $v_{\text{nozzle}} = 0.456 \text{ m/s}$ , respectively. Further on, in Figure 6.21, we use these symbols to refer to the corresponding points in the parameter space. The additional parameters relevant for all the simulations are  $p_1 = 1$  and  $\epsilon_0 = 10^{-3}$ . Since the jet is initially aligned with the nozzle,  $p_3$  is irrelevant for these simulations.

The critical value of  $v_{\text{nozzle}}$  to leave  $\mathcal{P}_{\text{inert}}$  (and to enter  $\mathcal{P}_{\text{NE},2}$ ) is 0.43923. Hence in all the cases considered, the parameters are still in  $\mathcal{P}_{\text{inert}}$ . Nevertheless we observe some an behaviour for the points  $C_i$ , which we describe next.

First we describe the simulation  $C_3$  in detail. We start with the steady jet and after one second we begin to decrease  $v_{\text{nozzle}}$  with the rate 0.012 during 20 s. After 21 s the nozzle velocity  $v_{\text{nozzle}} = 0.46 \text{ m/s}$  and is kept constant. The shape of the dynamic jet, inclusive the position of the touchdown point on the lateral surface of the coagulator, is depicted in Figure 6.19. Here we observe that starting from the steady inertial jet, after 1 s the touchdown point moves away from the nozzle and after 21 s the jet end starts to oscillate with increasing amplitude; see the angular coordinate of the touchdown point  $\beta(s_{\text{end}}(t), t)$  in Figure 6.20(b).

The computation stops at  $t = 81.7997 \text{ s}$ , because the integration time step in the



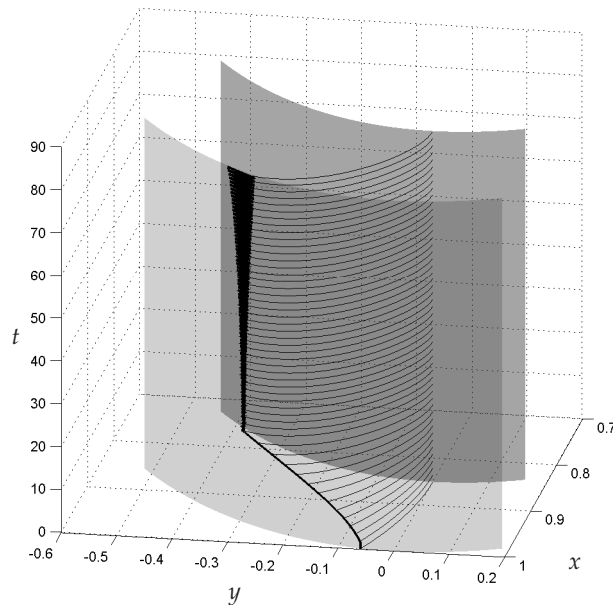


**Figure 6.19:** Shape of the dynamic jet for the case  $C_3$ ; the bold line indicates the position of the touchdown point at the coagulator (the horn-shape region represents the rapid oscillations of the touchdown point). The darker grey surface represents the rotor and the lighter grey the coagulator.

MATLAB solver `ode15s` becomes extremely small and the integration tolerance is not met, while further decrease of the integration step is not possible. This can be observed in the plot of the number of time integration steps versus the reached time in Figure 6.20(f), where the end of the curve is vertical. This means that the time steps become extremely small at the end of calculations.

A possible explanation of the integration stop can be found in studying the behaviour of the touchdown angle  $\alpha_{t-d}$ . In Figure 6.20(d) we observe that  $\alpha_{t-d}$  first decreases and after  $t = 21$  s starts to oscillate with increasing amplitude. Hence at some point  $\alpha_{t-d}$  becomes smaller than  $\epsilon_0$ ; see Figure 6.20(e) for a zoomed-in situation, where the horizontal dashed line indicates  $\epsilon_0$ . At that time the ODE for  $s_{end}(t)$  (6.87) changes due to the “if” statement. After that  $\alpha_{t-d}$  becomes negative so the jet exceeds the coagulator, which is not physical. Then  $\alpha_{t-d}$  increases and crosses  $\epsilon_0$  so the ODE for  $s_{end}(t)$  changes back, and shortly afterwards the calculations stop. The error  $\mathcal{E}_{coag}$  is of order  $10^{-4}$  everywhere except at the end of the calculations when  $\mathcal{E}_{coag}$  jumps to the value  $-6.2 \times 10^{-3}$ ; see Figure 6.20(a). All this brings us to the conclusion that this switching in (6.87) possibly explains the failure of further numerical integration.

Next we analyse the relation between the magnitudes of  $v_{nozzle}$  in  $C_i$  and the oscillating behaviour of the dynamic jet. For all the five cases the flow velocity at the nozzle  $v_{nozzle}(t)$  is plotted in Figure 6.21(a) and, correspondingly, the angular coordinate of the touchdown point  $\beta(s_{end}(t), t)$  is plotted at in Figure 6.21(b). The plots start

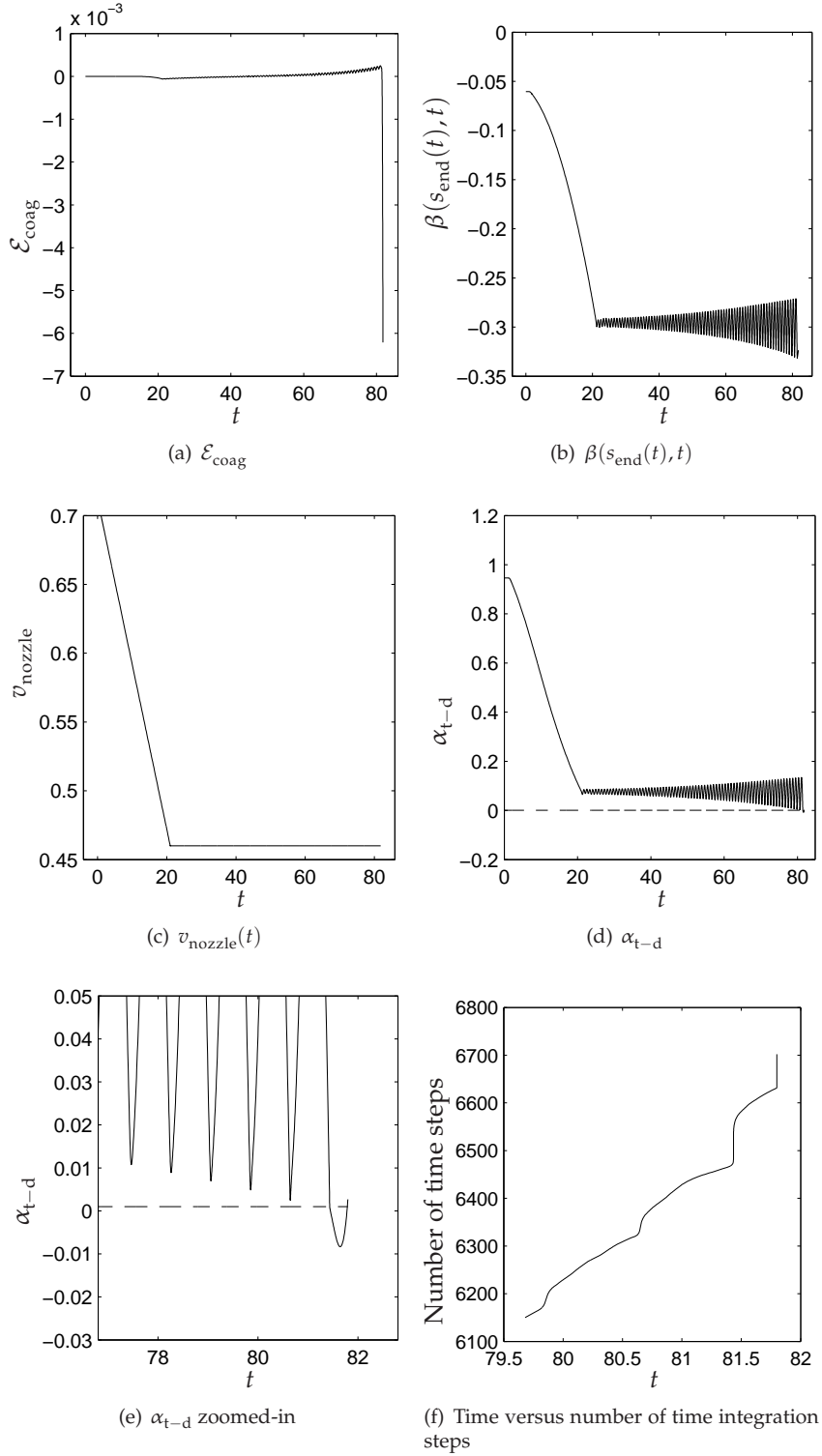
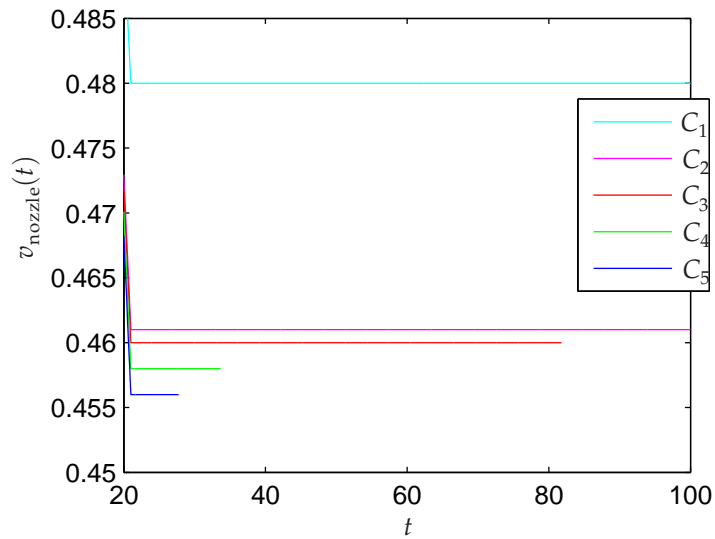
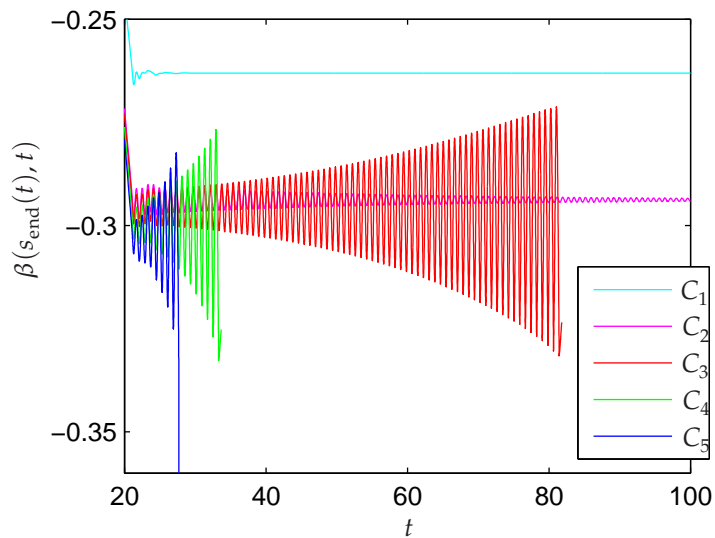


**Figure 6.20:** Simulation results of the dynamic jet for the case  $C_3$ .



(a)



(b)

**Figure 6.21:** (a) The flow velocity at the nozzle  $v_{\text{nozzle}}(t)$ , and (b) the angular coordinate of the touchdown point  $\beta(s_{\text{end}}(t), t)$  versus time for the dynamic jets in the situations  $C_1$ - $C_5$ .

from  $t = 20$  s (just before the deceleration of  $v_{\text{nozzle}}$  ends). In all the simulations we intend to reach  $t = 100$  s. However we only succeeded for  $C_1$  and  $C_2$ . In the simulation  $C_1$  having the largest final value of  $v_{\text{nozzle}}$ , just after the deceleration stops at  $t = 21$  s  $\beta(s_{\text{end}}(t), t)$  makes couple of fast decaying oscillations, but after that it becomes steady;

Figure 6.21(b). In the simulation  $C_2$ , for a smaller  $v_{\text{nozzle}}$ , we observe very slowly decaying oscillations of  $\beta(s_{\text{end}}(t), t)$ . Further decrease of  $v_{\text{nozzle}}$  in the cases  $C_3$ ,  $C_4$ , and  $C_5$  results in growing oscillations and the computations stop before the desired time is reached. In Figures 6.21(a) and 6.21(b) we see that oscillations grow faster and computations stop earlier for smaller  $v_{\text{nozzle}}$ .

From the five simulations above we conclude that if the parameters are close to the region  $\mathcal{P}_{\text{NE},2}$ , the dynamic jet starts to oscillate and the closer we are to that region the faster the oscillations grow, whereas farther away from  $\mathcal{P}_{\text{NE},2}$  the dynamic jet tends to the steady one. When oscillations grow, we are not capable to produce arbitrary long jet simulations and a precise picture is missing. The difference between the critical value of  $v_{\text{nozzle}}$  to enter  $\mathcal{P}_{\text{NE},2}$  and the value of  $v_{\text{nozzle}}$  for which jet oscillations grow is of order 0.02 m/s, which is comparable to the order of accuracy of our numerical method. Numerical simulations of the dynamic jet with a smaller number of space discretization points show that this difference increases. So there is a correlation between these two numbers and therefore we relate this difference to a numerical error. Our final conclusion is that the results of simulations with growing jet oscillations reflect a situation in  $\mathcal{P}_{\text{NE},2}$ .

### 6.3 Conclusions

In this chapter we have constructed a numerical method to simulate the dynamic jet in drag and rotary spinning based on the string jet model developed in Section 1.5. For the sake of the numerical method we relax some equations and boundary conditions. More specifically we relax the ODE in time for the jet length  $s_{\text{end}}(t)$  and the boundary conditions for the jet orientation for drag and rotary spinning. For drag spinning, we also relax the boundary condition for  $v$  at the belt. We discretize the equations in the space variable and integrate in the time variable using the MATLAB ODE solver `ode15s`. A key issue for the appropriate space discretization is the use of an upwind scheme for the jet orientation angle  $\theta$  in accordance with the characteristic directions of the equation for the position vector  $\mathbf{r}$  described in Section 2.2.

Simulations of the dynamic jet in drag and rotary spinning show that if the sign of  $\xi$  does not change at the jet ends during simulations, then the jet evolves to the steady one. Simulations in drag spinning where the sign of  $\xi$  changes are successful when the parameters are moved from  $\mathcal{P}_{\text{v-i}}$  to  $\mathcal{P}_{\text{visc}}$  or  $\mathcal{P}_{\text{inert}}$ . If the parameters are moved to  $\mathcal{P}_{\text{v-i}}$  the simulations fail due to a steep change of the jet orientations at the nozzle or at the belt appearing during the jet evolution. In rotary spinning when the jet enters the region  $\mathcal{P}_{\text{NE},2}$ , where a steady jet does not exist, we observe growing oscillations until the numerical time integration fails.

Final conclusions from this chapter are

- Successful simulations in which a dynamic jet evolves to a steady jet in one of the three flow regimes, and the use of the upwind scheme in our numerical method, confirm the theory about characteristic directions in Section 2.2.
- For rotary spinning, and when the parameters become very close (order of the discretization error of our numerical method) to  $\mathcal{P}_{\text{NE},2}$ , the dynamic jet starts to oscillate with increasing amplitude until the touchdown angle  $\alpha_{\text{t-d}}$  becomes zero. After that the simulations fail to continue.

## Chapter 7

# Conclusions and outlook

In this thesis we study curved thin jets of viscous Newtonian fluid in two separate configurations. The first one we call drag spinning where the jet emerges from an oriented nozzle and falls under gravity onto a horizontal moving belt. The second one we call rotary spinning where the jet emerges from a rotating cylindrical rotor and flows towards a cylindrical coagulator due to centrifugal and Coriolis forces.

The jet is described by a string model. Our model consists of the conservation laws of mass and momentum, and incorporates effects of viscosity, inertia, and external forces to describe the jet; see Section 1.5. Some more effects, which are typically used in the modeling of thin jets and fiber spinning processes, but neglected here are: surface tension, air drag, temperature dependent fluid properties, viscous shear and bending.

A key issue is to determine the boundary conditions for the model equations (see Chapter 2) in order to ensure existence of a jet solution for all admissible model parameters. In this context we are faced with two nontrivial boundary conditions, which we formulate for a dynamic jet.

The first one is the boundary condition for the flow velocity at the contact with the moving surface. By demanding the flow continuity inside the dynamic jet, we derive the boundary condition at the moving surface in Section 2.1.

The second one is the boundary conditions for the jet shape  $\mathbf{r}$  follow from the momentum conservation for the dynamic jet; see Section 2.2. This equation is hyperbolic for  $\mathbf{r}$  if the jet is under tension and elliptic if the jet is under compression. In case the jet is under compression the Cauchy problem is ill-posed, and the jet can be unstable. Therefore, we restrict our attention to the jet under extension. For hyperbolic equations the number of boundary conditions should be equal to the number of characteristics pointing into the domain. The characteristic directions are fully determined by the sign of the balance between the viscous and inertial momentum transfer through the jet cross-section,  $\xi$ . According to this we always prescribe the nozzle position for  $\mathbf{r}$ . In addition if inertia dominates at the nozzle we prescribe the nozzle orientation and if viscosity dominates at the surface we demand tangency with the surface.

In Chapter 3 we study the steady jet in drag spinning theoretically. A scaling allows us to characterize the system in terms of three dimensionless parameters. For the steady jet we distinguish the three flow regimes, which are characterized by the dominant effect in the momentum transfer through the jet cross-section, i.e. viscous, viscous-inertial,

and inertial. In the viscous regime viscosity dominates in the momentum transfer, and the jet has a convex shape tangent to the belt. In the viscous-inertial regime viscosity dominates at the nozzle and inertia at the belt, and the jet is vertical. The reason for the vertical jet shape is: at the point where the momentum transfer due to viscosity equals the one due to inertia the jet orientation should coincide with the direction of the external force at this point. In this case this is the vertical direction of gravity. The last regime is called inertial because inertia dominates everywhere in the jet. The jet shape is concave, comparable to a ballistic trajectory, with the jet aligned with the nozzle.

The steady jet equations in drag spinning are partly solved so that the problem becomes a first-order ODE with a free boundary. We transform the free-boundary problem into an equivalent algebraic equation. Next, we determine the parameter regions for the three flow regimes in the 3D dimensionless parameter space. For each flow regime we prove existence and investigate uniqueness. The viscous and viscous-inertial jet solutions are unique for the parameters from the corresponding flow region, whereas, if the nozzle does not point vertically downwards, up to two inertial jet solutions can coexist with one viscous or viscous-inertial jet solution. In case the nozzle points upwards the inertial jet is possible for the belt placed above the nozzle; see Section 3.7. We analyse the three parameter regions, and the changes of the jet shape as dimensional parameters vary so that the flow regime changes are illustrated in Section 3.8.

Experiments of jets in drag spinning are described in Chapter 4. In the experiments we observe steady jets in each of the three flow regimes. For the nozzle pointing upwards we observe unsteady jets. For the steady jet we measure the horizontal distance between the nozzle and the touchdown point  $x_{\text{end}}$  for different belt velocities  $v_{\text{belt}}$ . A comparison of the relations between  $x_{\text{end}}$  and  $v_{\text{belt}}$  obtained from the model and from the experiments gives a qualitative agreement and shows that the model correctly predicts the regions of the three flow regimes. A quantitative disagreement is large because of the effects not included in our model. A cause of this disagreement is an open question at the moment.

The steady jet model in rotary spinning is studied in Chapter 5. The scaled system describing the jet is characterized by three dimensionless parameters. For the jet in rotary spinning we distinguish three situations: the inertial jet, the viscous-inertial jet, and a steady jet solution does not exist. If the coagulator rotates in the same direction as the rotor with at least half of the angular velocity of the rotor the viscous jet becomes possible. A situation in which the jet does not reach the coagulator and stays at some distance from the rotor is shortly discussed in Section 5.5.

We develop a numerical method for the dynamic jet in drag and rotary spinning in Chapter 6. Numerical simulations show that if the steady jet exists the dynamic jet evolves to the steady one. Using this method, we observe that for the parameters from the nonexistence region in rotary spinning the dynamic jet starts to oscillate with increasing amplitude.

## Outlook

Possible future development of this work is to study influences of the effects neglected in our model though normally used to model the drag and rotary spinings. One can think of air drag, surface tension, or a nonlinear viscoelastic constitutive law for the fluid. Here we mean existence and uniqueness of a solution to the model.

A jet model with bending and shear is more complicated, because in addition to the conservation of momentum and mass it contains the conservation of angular momentum. This type of model is called a rod model, and a correct way of prescribing boundary conditions for this model such that for any admissible parameters a solution exists and adequately describes the thread is an open question at this moment. We illustrate this using the following example.

Consider a thread of viscous fluid vertically falling onto a moving surface, depicted in Figure 7.1. In Figure 7.1(a) the surface moves fast enough for the thread to bend and

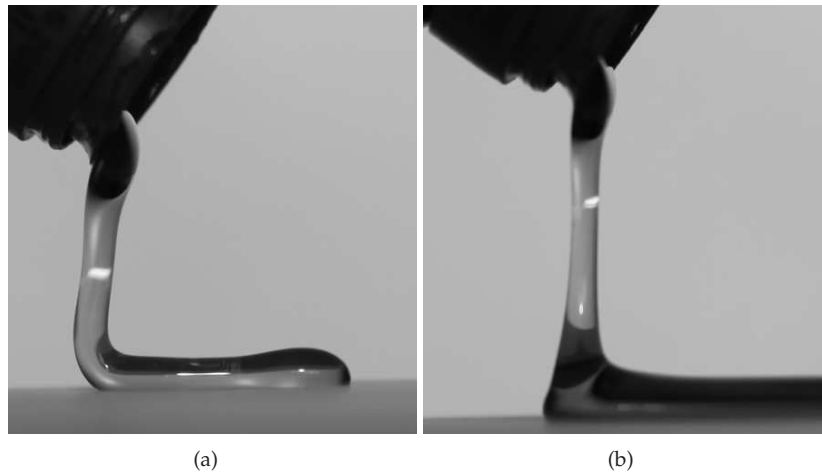


**Figure 7.1:** *A thread of viscous fluid hits a moving surface.*

touch the surface tangentially. In this situation it is natural to demand tangency with the belt as a boundary condition for the jet orientation. This choice is made in [90]. However, if the surface moves slowly the fluid at the surface forms a puddle, which is gradually transported away; see Figure 7.1(b). In this case the thread hits the surface perpendicularly. Therefore, it is not clear whether demanding tangency at the belt as a boundary condition in the second case leads to an adequate description of the thread.





# Appendix A

## Surfaces $S_1$ and $S_2$

### A.1 Surface $S_1$

Consider the initial value problem for the vertical jet following from (3.16) and (3.18)

$$v_{v-i,s} - \left( \frac{v_{v-i,s}}{v_{v-i}} \right)_s - \frac{A}{v_{v-i}} = 0, \quad (\text{A.1})$$

$$v_{v-i}(0) = 1, \quad (\text{A.2})$$

$$v_{v-i,s}(0) = 1 - w, \quad (\text{A.3})$$

Where the boundary condition (A.3) follows from  $\xi(0) = w$ . The system (A.1)-(A.3) has an analytical solution [15], which for  $w = 0$  we present as a fraction

$$v_{v-i}(s; 0, A) = \frac{N_1(s; A)}{N_2(s; A)},$$

where

$$N_1(s; A) = \beta \left( \text{Ai}(\beta(s-1)) - \frac{\text{Ai}'(-\beta)\text{Bi}(\beta(s-1))}{\text{Bi}'(-\beta)} \right)^2,$$

and

$$N_2(s; A) = \left( \text{Ai}'(\beta(s-1)) - \frac{\text{Ai}'(-\beta)\text{Bi}'(\beta(s-1))}{\text{Bi}'(-\beta)} \right)^2 \quad (\text{A.4})$$
$$- \beta(s-1) \left( \frac{\text{Ai}'(-\beta)\text{Bi}(\beta(s-1))}{\text{Bi}'(-\beta)} - \text{Ai}(\beta(s-1)) \right)^2.$$

Here  $\beta = \sqrt[3]{A/2}$ , Ai and Bi are Airy functions. The solution  $v_{v-i}(s; 0, A)$  is considered until the smallest  $s$  such that  $N_1(s; A) = 0$  or  $N_2(s; A) = 0$ . The numerator  $N_1(s_0; A) = 0$  and  $v_{v-i}(s_0; 0, A) = 0$  first if  $A > A^*$ , and the denominator  $N_2(s_\infty; A) = 0$  and  $v_{v-i}(s_\infty; 0, A) = \infty$  first if  $A < A^*$ , see Figure A.1. Consequently the solution  $v_{v-i}(s; 0, A^*)$  does not become zero or infinity at finite  $s$ , see Figure A.1. The value of  $A^*$  is found from

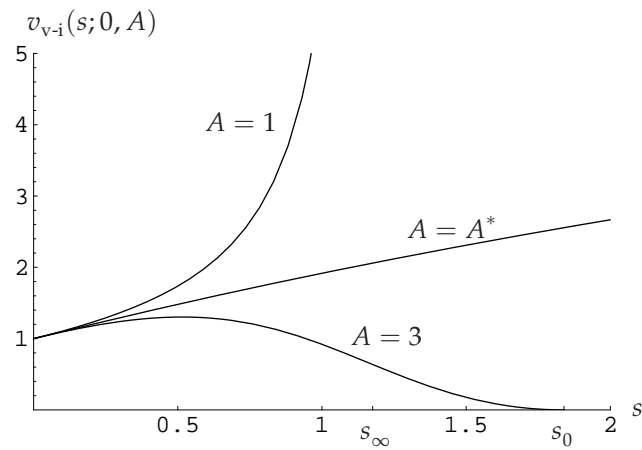


**Figure A.1:**  $v_{v-i}(s; 0, A)$  for  $A = 1$ ,  $A = A^*$ , and  $A = 3$ . The solution  $v_{v-i}(s; 0, 1)$  becomes infinite at  $s = s_{\infty}$ , the solution  $v_{v-i}(s; 0, 3)$  becomes zero at  $s = s_0$ , and  $v_{v-i}(s; 0, A^*)$  does not become infinite or zero for finite  $s$ .

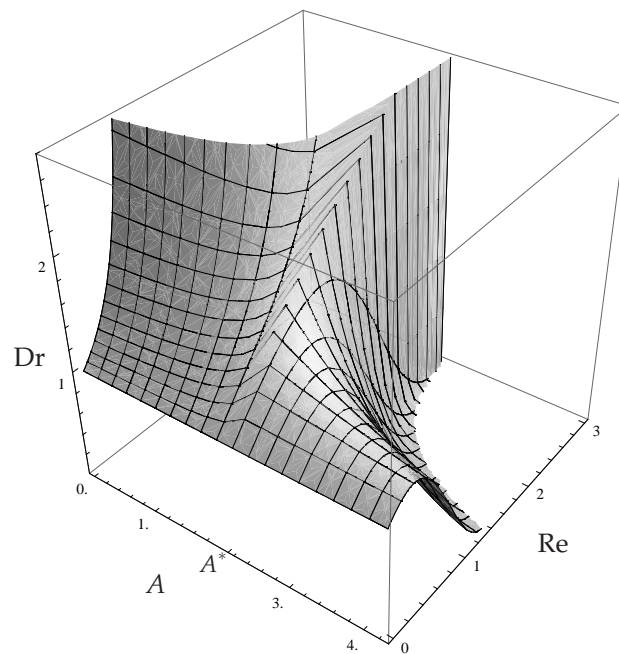


**Figure A.2:** The surface  $S_1$

$$\text{Ai}'\left(-\sqrt[3]{\frac{A^*}{2}}\right) = 0$$

as

$$A^* = 2.11489.$$

The surface  $S_1$  is defined as follow

$$S_1 = \begin{cases} v_{v-i}(\text{Re}; 0, A), & \text{for } A > A^* \text{ and } \text{Re} < s_0, \\ v_{v-i}(\text{Re}; 0, A), & \text{for } A < A^* \text{ and } \text{Re} < s_\infty, \\ v_{v-i}(\text{Re}; 0, A), & \text{for } A = A^*, \end{cases}$$

see Figure A.2.

## A.2 Surface $S_2$

In this appendix we present calculation of the surface  $I(0; \hat{A}, \hat{D}r)$ . A surface  $S_2$  is calculated using (3.64) as

$$S_2 = \{(A, Dr, \text{Re}) : \text{Re} = I(0; A/Dr^3, 1/Dr)/Dr\}. \quad (\text{A.5})$$

First we calculate  $\hat{v}(\hat{\tau}; 0)$  analytically. The differential equation for  $\hat{v}(\hat{\tau}; 0)$  follows from (3.65) and (3.66),

$$\hat{v}'(\hat{\tau}; 0) = -\hat{v}^2(\hat{\tau}; 0)(\hat{A}\hat{\tau} + \hat{v}(\hat{\tau}; 0)), \quad \hat{v}(0; 0) = 1. \quad (\text{A.6})$$

By replacing  $\hat{v}(\hat{\tau}; 0)$  by  $Z(\hat{\tau}) = 1/\hat{v}(\hat{\tau}; 0)$ , we find

$$Z'(\hat{\tau})Z(\hat{\tau}) = \hat{A}Z(\hat{\tau})\hat{\tau} + 1, \quad Z(0) = 1. \quad (\text{A.7})$$

We seek for a solution of (A.7) in parametric form. With the substitution

$$Z(z) = z + \hat{A}/2\hat{\tau}^2(z), \quad (\text{A.8})$$

where  $z$  is a parameter, (A.7) becomes

$$\hat{\tau}'(z) = \hat{A}\hat{\tau}^2(z) + z, \quad \hat{\tau}(1) = 0. \quad (\text{A.9})$$

Here the initial condition is deduced from (A.8) by setting  $\hat{\tau}(z) = 0$  and  $Z(z) = 1$ . This differential equation is known as the special Riccati equation [82, p. 4, type 4] and has the solution

$$\hat{\tau}(z) = \frac{\sqrt{2z} \left( J_{\frac{2}{3}} \left( \frac{\sqrt{2\hat{A}z^{3/2}}}{3} \right) c_1 - J_{-\frac{2}{3}} \left( \frac{\sqrt{2\hat{A}z^{3/2}}}{3} \right) \right)}{\sqrt{\hat{A}} \left( J_{\frac{1}{3}} \left( \frac{\sqrt{2\hat{A}z^{3/2}}}{3} \right) + J_{-\frac{1}{3}} \left( \frac{\sqrt{2\hat{A}z^{3/2}}}{3} \right) c_1 \right)}, \quad (\text{A.10})$$

with

$$c_1 = \frac{J_{-\frac{2}{3}}(\alpha)}{J_{\frac{2}{3}}(\alpha)}, \quad \alpha = \sqrt{2\hat{A}}/3. \quad (\text{A.11})$$

Here the functions  $J_\alpha$  are the Bessel functions of the first kind. The velocity  $\hat{v}$  is given by

$$\hat{v}(z) = \frac{1}{z} \left( 1 + \left( \frac{J_{\frac{2}{3}}\left(\frac{\sqrt{2\hat{A}}z^{3/2}}{3}\right)c_1 - J_{-\frac{2}{3}}\left(\frac{\sqrt{2\hat{A}}z^{3/2}}{3}\right)}{J_{\frac{1}{3}}\left(\frac{\sqrt{2\hat{A}}z^{3/2}}{3}\right) + J_{-\frac{1}{3}}\left(\frac{\sqrt{2\hat{A}}z^{3/2}}{3}\right)c_1} \right)^2 \right)^{-1}. \quad (\text{A.12})$$

To write the result in a more elegant form we replace the parameter  $z$  by  $\tilde{z} = \sqrt{2\hat{A}}z^{3/2}/3$  (we then omit tildes)

$$\hat{\tau}(z) = \frac{(6z)^{1/3} J_{\frac{2}{3}}(z)c_1 - J_{-\frac{2}{3}}(z)}{A^{2/3} J_{\frac{1}{3}}(z) + J_{-\frac{1}{3}}(z)c_1}, \quad (\text{A.13})$$

$$\hat{v}(z) = \frac{(2\hat{A})^{1/3}}{(3z)^{2/3}} \left( 1 + \left( \frac{J_{\frac{2}{3}}(z)c_1 - J_{-\frac{2}{3}}(z)}{J_{\frac{1}{3}}(z) + J_{-\frac{1}{3}}(z)c_1} \right)^2 \right)^{-1}. \quad (\text{A.14})$$

To calculate  $\hat{\tau}_{\text{end}}(0)$  from the solution (A.13) and (A.14) it is necessary to find  $z^*$  satisfying

$$\hat{D}r = \frac{(2\hat{A})^{1/3}}{(3z^*)^{2/3}} \left( 1 + \left( \frac{J_{\frac{2}{3}}(z^*)c_1 - J_{-\frac{2}{3}}(z^*)}{J_{\frac{1}{3}}(z^*) + J_{-\frac{1}{3}}(z^*)c_1} \right)^2 \right)^{-1}, \quad (\text{A.15})$$

and then substitute  $z = z^*$  into (A.13).

The equation (A.15) has many solutions. A correct solution  $z^*$  is the first solution of (A.15) after the point  $\alpha$ . It is convenient to search for  $z^*$  in the interval  $(\alpha, z_0)$  using the bisection method [83]. Here,  $z_0$  is the first zero of  $\hat{v}(z)$  according to (A.14) after the point  $\alpha$ .

Next, we have to find a correct  $z_0$ . Because zeros of  $\hat{v}(z)$  coincide with zeros of

$$J_{\frac{1}{3}}(z) + J_{-\frac{1}{3}}(z)c_1, \quad (\text{A.16})$$

we can look for the first zero of (A.16) after  $\alpha$ . Using (A.11), we can rewrite the latter as

$$J_{\frac{1}{3}}(z_0)J_{\frac{2}{3}}(\alpha) + J_{-\frac{1}{3}}(z_0)J_{-\frac{2}{3}}(\alpha) = 0. \quad (\text{A.17})$$

This equation can be rewritten in terms of Airy functions [1, 10.4.22 and 10.4.27] as

$$Bi(-\hat{z}_0)Ai'(-\hat{\alpha}) - Ai(-\hat{z}_0)Bi'(-\hat{\alpha}) = 0, \quad \hat{z}_0 = \left(\frac{3z_0}{2}\right)^{\frac{2}{3}}, \quad \hat{\alpha} = \left(\frac{3\alpha}{2}\right)^{\frac{2}{3}}. \quad (\text{A.18})$$

Using the representation of Airy functions via modulus and phase [1, 10.4.69 and 10.4.70]

$$Ai(-\hat{z}_0) = M(\hat{z}_0) \cos \theta(\hat{z}_0), \quad Bi(-\hat{z}_0) = M(\hat{z}_0) \sin \theta(\hat{z}_0),$$

$$Ai'(-\hat{\alpha}) = N(\hat{\alpha}) \cos \phi(\hat{\alpha}), \quad Bi'(-\hat{\alpha}) = N(\hat{\alpha}) \sin \phi(\hat{\alpha}),$$

we see that (A.18) becomes

$$\sin(\theta(\hat{z}_0) - \phi(\hat{\alpha})) = 0. \quad (\text{A.19})$$

For large  $\hat{z}_0 \gg 1$  and  $\hat{\alpha} \gg 1$  the asymptotic expressions for  $\theta(\hat{z}_0)$  and  $\phi(\hat{\alpha})$  [1, 10.4.79 and 10.4.81] are given by

$$\theta(\hat{z}_0) = \frac{\pi}{4} - \frac{3}{2}\hat{z}_0^{2/3} \left( 1 - \frac{5}{32\hat{z}_0^3} + \frac{1105}{6144\hat{z}_0^6} + \dots \right),$$

and

$$\phi(\hat{\alpha}) = \frac{3\pi}{4} - \frac{3}{2}\hat{\alpha}^{2/3} \left( 1 + \frac{7}{32\hat{\alpha}^3} - \frac{1463}{6144\hat{\alpha}^6} + \dots \right),$$

or in terms of  $z_0$  and  $\alpha$  (A.18)

$$\theta(z_0) = \frac{\pi}{4} - z_0 \left( 1 - \frac{5}{72z_0^2} + \frac{1105}{31104z_0^4} + \dots \right), \quad (\text{A.20})$$

and

$$\phi(\alpha) = \frac{3\pi}{4} - \alpha \left( 1 + \frac{7}{72\alpha^2} - \frac{1463}{31104\alpha^4} \right). \quad (\text{A.21})$$

After substituting (A.20) and (A.21) into (A.19) for  $\alpha \gg 1$  we find

$$z_0 \approx \alpha + \pi/2. \quad (\text{A.22})$$

When  $\alpha$  is not large we can find  $z_0$  numerically by looking for a solution of (A.17) in the interval  $(\alpha, \alpha + \pi)$ .

Once  $z_0$  is found we find  $z^*$  and consequently compute  $\hat{\tau}_{\text{end}}(0)$ . Knowing  $\hat{\tau}_{\text{end}}(0)$  we can compute  $I(0)$ . To avoid computation of the integral

$$I(0) = \int_0^{\hat{\tau}_{\text{end}}(0)} \hat{\vartheta}(\hat{\tau}; 0) d\hat{\tau},$$

we can calculate this integral using the differential equation (A.6), when written as

$$\left( \frac{1}{\hat{\vartheta}(\hat{\tau}; 0)} \right)' = \hat{A}\hat{\tau} + \hat{\vartheta}(\hat{\tau}; 0). \quad (\text{A.23})$$

By integrating this equation from 0 to  $\hat{\tau}_{\text{end}}(0)$ , we get

$$\left( \frac{1}{\hat{\vartheta}(\hat{\tau}_{\text{end}}(0); 0)} - \frac{1}{\hat{\vartheta}(0; 0)} \right) = \hat{A} \frac{\hat{\tau}_{\text{end}}(0)^2}{2} + \int_0^{\hat{\tau}_{\text{end}}(0)} \hat{\vartheta}(\hat{\tau}; 0) d\hat{\tau}. \quad (\text{A.24})$$

We use the definitions of  $I(0)$  and  $\hat{\tau}_{\text{end}}(0)$ , together with the initial condition  $\hat{\vartheta}(0; 0) = 1$  to obtain

$$I(0) = \frac{1 - \hat{D}_r}{\hat{D}_r} - \hat{A} \frac{\hat{\tau}_{\text{end}}(0)^2}{2}. \quad (\text{A.25})$$



# Appendix B

## Proof of lemmas from Chapter 3

### B.1 Proof of Lemma 3.4

*Proof.* To prove this lemma consider a problem in the variable  $\tau$ , which follows (3.49) and (3.50)

$$v - \frac{v_\tau}{v^2} = A\tau, \quad (\text{B.1})$$

$$v(0) = 1. \quad (\text{B.2})$$

Here and throughout this prove we use  $v(\tau)$  instead of  $v_{v-i}(\tau)$ . The value  $v_{v-i}(s; 0, A)$  is computed as

$$(s, v_{v-i}(s; 0, A)) = \left( \int_0^\tau v(\tilde{\tau}; 0, A) d\tilde{\tau}, v(\tau; 0, A) \right). \quad (\text{B.3})$$

The continuity of  $v_{v-i}(s; 0, A)$  with respect to  $s$  and  $A$  can be proved in the same way as in Lemma 3.18, while its monotonicity with respect to  $A$  follows from the monotonicity properties of  $v(\tau; A)$  and the integral in (B.3).

The monotonicity of  $v(\tau; 0, A)$  is proved in two steps in a similar way as in Lemma 3.18, i.e. we first show that around  $\tau = 0$ ,  $v(\tau; A)$  is larger for smaller  $A$ , and secondly that away from  $\tau = 0$  for any  $A_1 > A_2$ ,  $v(\tau; A_1)$  does not cross  $v(\tau; A_2)$ . The second step is done in the same way as in the proof of Lemma 3.18.

To show that in a vicinity of zero,  $v(\tau; 0, A)$  increases as  $A$  decreases we use a Taylor series expansion of  $v(\tau; 0, A)$  around zero. The first two coefficients in this expansion are 1 and the second derivative at  $\tau = 0$  is  $3 - A$ . Therefore, initially for smaller  $A$ ,  $v(\tau; 0, A)$  is larger.

Now we need to show that for any  $A_1 > A_2$ , and such  $\tau_1$  and  $\tau_2$  that

$$\int_0^{\tau_1} v(\tilde{\tau}; 0, A_1) d\tilde{\tau} = \int_0^{\tau_2} v(\tilde{\tau}; 0, A_2) d\tilde{\tau}, \quad (\text{B.4})$$

the following is true

$$v(\tau_1; 0, A_1) < v(\tau_2; 0, A_2). \quad (\text{B.5})$$

Note that due to the monotonicity of  $v(\tau; 0, A)$  with respect to  $A$  and (B.4) we have that

$\tau_2 < \tau_1$ . We integrate the system (B.1)-(B.2) from 0 to  $\tau_1$ , with  $A = A_1$ , and then we integrate the same system from 0 to  $\tau_2$  with  $A = A_2$ . After subtraction of the second expression from the first one and making use of (B.4), we obtain

$$\frac{v(\tau_1; 0, A_1) - v(\tau_2; 0, A_2)}{v(\tau_1; 0, A_1)v(\tau_2; 0, A_2)} = (A_2\tau_2^2 - A_1\tau_1^2) < 0,$$

which is negative due to  $A_1 > A_2$  and  $\tau_2 < \tau_1$ . Thus, we have proved the part 2 of this lemma.

To prove part 3 of this lemma we first describe the possible monotonicity properties of  $v(\tau; 0, A)$ . They are the same as those for  $v_{v-i}(s; 0, A)$ , because  $v > 0$ . The proofs of these properties directly follow from part 3 of Lemma 3.18. In the first case,  $v(\tau; 0, A)$  strictly increases and blows up for finite  $\tau$ , (example with  $A = 0$  is straightforward to check that  $v(\tau; 0, 0) = 1/\sqrt{1-2\tau}$  blows up at  $\tau_\infty = 0.5$ ). In the second case,  $v(\tau; 0, A)$  increases and has an oblique asymptote  $A\tau$  as  $\tau \rightarrow \infty$ . This holds only for one value of  $A = A^*$  (a prove of this is similar to the proof of part 4 of Lemma 3.18). The third situation occurs when  $v(\tau; A)$  first increases, reaches its maximum when  $v(\tau; 0, A)$  crosses  $A\tau$ , and then decreases asymptotically towards zero. To show that there exists a value of  $A_3$  such that  $v(\tau; A_3)$  is in the third situation, we take for example  $\tau = 0.2$  and  $A_3 = v(0.2; 0, 0)/0.2$ . In this case, because of part 2 of this lemma, we obtain that at  $\tau = 0.2$  the function  $v(\tau; A_3)$  decreases because  $v(\tau; A_3) < A_3\tau$ .

We show that if  $v(\tau; A)$  is in the first situation (i.e.  $v(\tau; A)$  blows up at finite  $\tau_\infty$ ) then  $v_{v-i}(s; 0, A)$  blows up for finite  $s_\infty$ , with

$$s_\infty = \int_0^{\tau_\infty} v(\tilde{\tau}; A) d\tilde{\tau}.$$

To show this we integrate the system (B.1)-(B.2) from 0 to  $\tau_\infty$ , which gives

$$1 = s_\infty - A\tau_\infty^2/2.$$

So, because  $\tau_\infty$  is finite we have that  $s_\infty$  is finite as well, which proves (3.58).

In the second situation when  $v(\tau; 0, A^*)$  is defined for all  $\tau > 0$  and increases towards infinity,  $v_{v-i}(s; 0, A)$  is defined for all  $s > 0$  and increases to infinity as well, which proves (3.59).

In the situation when  $v(\tau; A)$  is defined for all  $\tau > 0$  and decreases asymptotically towards 0, we show that  $v_{v-i}(s; 0, A)$  becomes zero for finite  $s_0$ . For this we need to show that the integral

$$s_0 = \int_0^\infty v(\tilde{\tau}; 0, A) d\tilde{\tau}$$

is finite. This follows from the estimate (B.11). Hence,  $v(\tau; 0, A)$  approaches 0 with the rate  $1/\tau^2$ , and  $s_0$  is finite. This proves (3.60), and completes the proof of this lemma.  $\square$



## B.2 Proof of Lemmas 3.6, 3.9, 3.10, and 3.11

### Proof of Lemma 3.6

*Proof.* The right-hand side of (3.65) is  $C(\Omega)$  and Lipschitz continuous in  $\hat{v}$  uniformly on  $\Omega$ , where  $\Omega = (\{\hat{\tau}, \hat{v}, \hat{w}\} : \tau \in [0, \infty), \hat{v} \in (0, 1], \hat{w} \geq 0)$ . Therefore, locally there exists a unique solution of (3.65) satisfying (3.66), which continuously depends on  $\hat{w}$  [17, Theorem 7.4].

From (3.65) it follows that  $\hat{v}'(\hat{\tau}; \hat{w}) < 0$  whenever  $\hat{v}(\hat{\tau}; \hat{w}) > 0$  and that  $\hat{v} \equiv 0$  is a solution of this equation. Thus, because of (3.66),  $\hat{v}'(\hat{\tau}; \hat{w})$  is always negative and  $\hat{v}(\cdot; \hat{w})$  is strictly decreasing. Since  $\hat{v} \equiv 0$  is a solution of (3.65),  $\hat{v}(\hat{\tau}; \hat{w})$  remains positive for  $\hat{\tau} \geq 0$ . Therefore,  $\hat{v}(\hat{\tau}; \hat{w}) \in (0, 1] \forall \hat{\tau} \geq 0$ ; this proves the existence and uniqueness of  $\hat{v}$  and the monotonicity in  $\hat{\tau}$ .

For the monotonicity in  $\hat{w}$ , fix  $\hat{w}_1 > \hat{w}_2 \geq 0$ . Then  $\hat{v}'(0; \hat{w}_1) = -(\sqrt{\hat{w}_1} + 1) < \hat{v}'(0; \hat{w}_2) = -(\sqrt{\hat{w}_2} + 1)$ , and  $\hat{v}(\hat{\tau}; \hat{w}_1) < \hat{v}(\hat{\tau}; \hat{w}_2)$  for small  $\hat{\tau} > 0$ . Suppose that there exists a  $\hat{\tau}^* > 0$  such that  $\hat{v}(\hat{\tau}^*; \hat{w}_1) = \hat{v}(\hat{\tau}^*; \hat{w}_2)$ , then  $\hat{v}'(\hat{\tau}^*; \hat{w}_1) \geq \hat{v}'(\hat{\tau}^*; \hat{w}_2)$ , which leads to a contradiction with  $\hat{w}_1 > \hat{w}_2$ . This completes the proof of part 1 of the Lemma.

Because  $\hat{v}(\hat{\tau}; \hat{w}) > 0$  we have

$$\hat{v}'(\hat{\tau}; \hat{w}) < -\hat{v}(\hat{\tau}; \hat{w})^2 \sqrt{\hat{A}^2 \hat{\tau}^2 + \hat{w}},$$

or

$$\left( \frac{1}{\hat{v}(\hat{\tau}; \hat{w})} \right)' > \sqrt{\hat{A}^2 \hat{\tau}^2 + \hat{w}}. \quad (\text{B.6})$$

We integrate (B.6) from 0 to  $\hat{\tau}$  and apply the initial condition  $\hat{v}(0; \hat{w}) = 1$  to find the following estimate of  $\hat{v}(\hat{\tau}; \hat{w})$ :

$$\hat{v}(\hat{\tau}; \hat{w}) < \frac{2\hat{A}}{2\hat{A} + \hat{A}\hat{\tau} \sqrt{\hat{A}^2 \hat{\tau}^2 + \hat{w}} + \hat{w} \log \left( \frac{\hat{A}\hat{\tau} + \sqrt{\hat{A}^2 \hat{\tau}^2 + \hat{w}}}{\sqrt{\hat{w}}} \right)} < \frac{2}{2 + \hat{\tau} \sqrt{\hat{A}^2 \hat{\tau}^2 + \hat{w}}}.$$

This estimate proves part 2 and shows that  $\hat{v}(\hat{\tau}; \hat{w}) \rightarrow 0$  as  $\hat{\tau} \rightarrow \infty$ .

The right-hand side of (3.65) depends continuously on  $\hat{w}$ . This together with the estimate (3.69) of  $\hat{v}(\hat{\tau}; \hat{w})$  at  $\hat{\tau} = \infty$  proves part 3.  $\square$

### Proof of Lemma 3.9

*Proof.* Choose  $\hat{w}_1$  and  $\hat{w}_2$  with

$$\hat{w}_1 > \hat{w}_2 \geq 0. \quad (\text{B.7})$$

From part 1 of Lemma 3.6 it follows that

$$\hat{\tau}_{\text{end}}(\hat{w}_1) < \hat{\tau}_{\text{end}}(\hat{w}_2). \quad (\text{B.8})$$

Combining (B.8) with statement 1 of Lemma 3.6 and (B.7) with the definition of  $I(\hat{w})$ , we have

$$\begin{aligned} I(\hat{w}_1) &= \int_0^{\hat{\tau}_{\text{end}}(\hat{w}_1)} \frac{\hat{A}\hat{\tau}\hat{\vartheta}(\hat{\tau}; \hat{w}_1)}{\sqrt{\hat{A}^2\hat{\tau}^2 + \hat{w}_1}} d\hat{\tau} < \int_0^{\hat{\tau}_{\text{end}}(\hat{w}_2)} \frac{\hat{A}\hat{\tau}\hat{\vartheta}(\hat{\tau}; \hat{w}_1)}{\sqrt{\hat{A}^2\hat{\tau}^2 + \hat{w}_1}} d\hat{\tau} \\ &< \int_0^{\hat{\tau}_{\text{end}}(\hat{w}_2)} \frac{\hat{A}\hat{\tau}\hat{\vartheta}(\hat{\tau}; \hat{w}_2)}{\sqrt{\hat{A}^2\hat{\tau}^2 + \hat{w}_2}} d\hat{\tau} = I(\hat{w}_2), \end{aligned}$$

which proves the Lemma.  $\square$

### Proof of Lemma 3.10

*Proof.* Fix  $\hat{w} \geq 0$  and let

$$\hat{w}_n \rightarrow \hat{w} \quad \text{as } n \rightarrow \infty. \quad (\text{B.9})$$

Then

$$\begin{aligned} I(\hat{w}) - I(\hat{w}_n) &= \int_0^{\hat{\tau}_{\text{end}}(\hat{w})} \frac{\hat{A}\hat{\tau}\hat{\vartheta}(\hat{\tau}; \hat{w})}{\sqrt{\hat{A}^2\hat{\tau}^2 + \hat{w}}} d\hat{\tau} - \int_0^{\hat{\tau}_{\text{end}}(\hat{w}_n)} \frac{\hat{A}\hat{\tau}\hat{\vartheta}(\hat{\tau}; \hat{w}_n)}{\sqrt{C^2\hat{\tau}^2 + \hat{w}_n}} d\hat{\tau} \\ &= \int_0^{\hat{\tau}_{\text{end}}(\hat{w}_n)} \left[ \frac{\hat{A}\hat{\tau}\hat{\vartheta}(\hat{\tau}; \hat{w})}{\sqrt{\hat{A}^2\hat{\tau}^2 + \hat{w}}} - \frac{\hat{A}\hat{\tau}\hat{\vartheta}(\hat{\tau}; \hat{w}_n)}{\sqrt{\hat{A}^2\hat{\tau}^2 + \hat{w}_n}} \right] d\hat{\tau} + \int_{\hat{\tau}_{\text{end}}(\hat{w}_n)}^{\hat{\tau}_{\text{end}}(\hat{w})} \frac{\hat{A}\hat{\tau}\hat{\vartheta}(\hat{\tau}; \hat{w})}{\sqrt{\hat{A}^2\hat{\tau}^2 + \hat{w}}} d\hat{\tau} \\ &= J_1 + J_2. \end{aligned}$$

Both  $J_1$  and  $J_2$  converge to zero as  $n \rightarrow \infty$ ; for  $J_1$  this follows from the continuity of  $\hat{\vartheta}(\hat{\tau}; \hat{w})$  in  $\hat{w}$  (Lemma 3.6) and for  $J_2$  from the continuity of  $\hat{\tau}_{\text{end}}(\hat{w})$  in  $\hat{w}$ , which we prove next.

From Lemma 3.6 we have that  $\hat{\vartheta}(\cdot; \hat{w}) \in C^1([0, \infty))$  and  $-\infty < \hat{\vartheta}'(\hat{\tau}; \hat{w}) < 0$ . Therefore, by the Inverse Function Theorem (e.g. [94, Theorem 9.24]) there exists a function  $\hat{\tau} = \hat{\tau}(\cdot; \hat{w}) \in C^1((0, 1])$  such that  $\hat{\tau}(\hat{\vartheta}(\hat{t}; \hat{w})) = \hat{t}$  for all  $\hat{t} \geq 0$ .

Next note that

$$\hat{\vartheta}_n := \hat{\vartheta}(\hat{\tau}_{\text{end}}(\hat{w}_n); \hat{w}) \longrightarrow \hat{D}r \quad \text{as } n \rightarrow \infty, \quad (\text{B.10})$$

since

$$\begin{aligned} |\hat{\vartheta}(\hat{\tau}_{\text{end}}(\hat{w}_n); \hat{w}) - \hat{D}r| &= |\hat{\vartheta}(\hat{\tau}_{\text{end}}(\hat{w}_n); \hat{w}) - \hat{\vartheta}(\hat{\tau}_{\text{end}}(\hat{w}_n); \hat{w}_n)| \\ &\leq \|\hat{\vartheta}(\cdot; \hat{w}) - \hat{\vartheta}(\cdot; \hat{w}_n)\|_{\infty} \longrightarrow 0 \end{aligned}$$

by part 3 of Lemma 3.6. Therefore, by continuity of  $\hat{\tau}(\cdot; \hat{w})$  we have

$$\hat{\tau}_{\text{end}}(\hat{w}_n) = \hat{\tau}(\hat{\vartheta}(\hat{\tau}_{\text{end}}(\hat{w}_n); \hat{w}); \hat{w}) = \hat{\tau}(\hat{\vartheta}_n; \hat{w}) \longrightarrow \hat{\tau}(\hat{D}r; \hat{w}) = \hat{\tau}_{\text{end}}(\hat{w}),$$

which completes the proof.  $\square$

**Proof of Lemma 3.11**

*Proof.* From the definition of  $I(\hat{w})$  and  $\hat{v}(\hat{\tau}; \hat{w}) \in (0, 1]$  (Lemma 3.6) we have

$$\begin{aligned} I(\hat{w}) &= \int_0^{\hat{\tau}_{\text{end}}(\hat{w})} \frac{\hat{A}\hat{\tau}\hat{v}(\hat{\tau}; \hat{w})}{\sqrt{\hat{A}^2\hat{\tau}^2 + \hat{w}}} d\hat{\tau} < \int_0^{\hat{\tau}_{\text{end}}(\hat{w})} \frac{\hat{A}\hat{\tau}}{\sqrt{\hat{A}^2\hat{\tau}^2 + \hat{w}}} d\hat{\tau} \\ &= \frac{\sqrt{\hat{w} + \hat{A}^2\hat{\tau}_{\text{end}}(\hat{w})^2} - \sqrt{\hat{w}}}{\hat{A}} = \frac{\hat{A}\hat{\tau}_{\text{end}}(\hat{w})^2}{\sqrt{\hat{w} + \hat{A}^2\hat{\tau}_{\text{end}}(\hat{w})^2} + \sqrt{\hat{w}}}. \end{aligned}$$

Because  $\hat{\tau}_{\text{end}}(\hat{w})$  decreases in  $\hat{w}$ , by letting  $\hat{w} \rightarrow \infty$  we find

$$\lim_{\hat{w} \rightarrow \infty} I(\hat{w}) = 0.$$

□

**B.3 Proof of Lemmas 3.18 and 3.22****Proof of Lemma 3.18**

*Proof.* The right-hand side of (3.82) is Lipschitz continuous on any bounded set for  $v$  and  $\tau$ . Therefore,  $v(\tau; w)$  exists and is unique on the domain of definition. Part 1 follows directly from [17, Theorem 7.4] if  $(v(\tau; w), \tau) \in \Omega$ .

For  $w_1 > w_2 \geq 0$ , from (3.82)-(3.83) we have that  $v_\tau(0; w_1) = 1 - w_1$  and  $v_\tau(0; w_2) = 1 - w_2$ , which gives  $v_\tau(0; w_1) < v_\tau(0; w_2)$ . Therefore,  $v(\tau; w_2) > v(\tau; w_1)$  in the vicinity of zero and  $\tau > 0$ . Next we show that the curves  $v(\tau; w_1)$  and  $v(\tau; w_2)$  do not cross each other for all  $\tau > 0$ . Assume the opposite, namely the existence of a point  $\tau^*$  so that  $v(\tau^*; w_1) = v(\tau^*; w_2)$  and  $v_\tau(\tau^*; w_1) \geq v_\tau(\tau^*; w_2)$ . Then, from (3.82) at  $\tau = \tau^*$  we have

$$v_\tau(\tau^*; w_1) - v_\tau(\tau^*; w_2) = v(\tau^*; w_1)^2 (f(\tau^*, w_2) - f(\tau^*, w_1)) < 0,$$

because  $f(\tau, w)$  is a strictly increasing function in  $w$ . This leads to a contradiction and completes the proof of part 2.

There are three possibilities for asymptotic behavior of  $v(\tau; w)$ , which follow when one of the three terms in

$$\frac{v_\tau}{v^2} = v - f(\tau, w)$$

becomes much smaller than the other two. In case 3a, we assume that there exists an  $\epsilon > 0$  so that  $v(\tau; w) > f(\tau, w) + \epsilon$ , for all  $\tau$ . From this, we get an estimate for  $v(\tau; w)$  from

$$\frac{v_\tau}{v^2} > \epsilon$$

which yields  $v(\tau; w) > 1/(c_1 - \epsilon\tau)$ , where  $c_1$  is some positive constant. Thus  $v(\tau; w)$  goes asymptotically to infinity.

Suppose that  $v(\tau; w)$  for  $\tau \geq 0$  has a maximum (crosses the curve  $f(\tau, w)$ , or strictly decreases). Then there exists a positive constant  $C_m > 0$  so that  $v(\tau; w) < C_m$ . This give

the supper estimate of  $v(\tau; w)$ , following from

$$\frac{v_\tau}{v^2} < C_m - f(\tau, w),$$

as

$$v(\tau; w) < 2A \left/ \left( w^2 \log(2(At + f(\tau, w) - w \sin(\alpha_{\text{nozzle}}))) \cos^2(\alpha_{\text{nozzle}}) - \right. \right. \quad (\text{B.11}) \\ \left. \left. 2A(C_m \tau + c_1) + f(\tau, w)(A\tau - w \sin(\alpha_{\text{nozzle}})) \right) \right.,$$

which goes to zero as  $\tau$  goes to infinity. We estimate  $v(\tau; w)$  from below using

$$\frac{v_\tau}{v^2} > -f(\tau, w),$$

as

$$v(\tau; w) > 2A \left/ \left( w^2 \log(2(At + f(\tau, w) - w \sin(\alpha_{\text{nozzle}}))) \cos^2(\alpha_{\text{nozzle}}) - \right. \right. \\ \left. \left. 2Ac_1 + f(\tau, w)(A\tau - w \sin(\alpha_{\text{nozzle}})) \right) \right.,$$

which also goes to zero as  $\tau$  goes to infinity. From the last two estimates on  $v(\tau; w)$  it follows that when  $v(\tau; w)$  has a maximum, it has the asymptotic behavior 3c.

If 3a and 3c do not hold, then

$$\lim_{\tau \rightarrow \infty} v(\tau; w) = \infty$$

and there exists a sequence  $\tau_n \rightarrow \infty$  as  $n \rightarrow \infty$  so that

$$\lim_{n \rightarrow \infty} |v(\tau_n, w) - f(\tau_n, w)| = 0. \quad (\text{B.12})$$

Note that either  $v(\tau; w) > f(\tau, w)$  for all  $\tau \geq 0$ , or  $v(\tau; w)$  has a maximum. Next we show that

$$\lim_{\tau \rightarrow \infty} |v(\tau, w) - f(\tau, w)| = 0$$

holds. Suppose the opposite, then there exists a sequence  $\tau_m \rightarrow \infty$  as  $m \rightarrow \infty$  so that

$$\lim_{m \rightarrow \infty} |v(\tau_m, w) - f(\tau_m, w)| = \epsilon, \quad 0 < \epsilon < \infty. \quad (\text{B.13})$$

Then, from (3.82), (B.13) and  $v(\tau_m, w) > f(\tau_m, w)$

$$\lim_{m \rightarrow \infty} v'(\tau_m, w) = \infty. \quad (\text{B.14})$$

For inflection points  $\tau_{\text{infl}}$  of  $v(\tau; w)$ , we notice that

$$\text{if } \tau_{\text{infl}} \rightarrow \infty, \text{ then } |v(\tau_{\text{infl}}; w) - f(\tau_{\text{infl}}, w)| \rightarrow 0. \quad (\text{B.15})$$

It follows from (B.15) that there exists an  $m$  so that there is no inflection point, meaning that

$$v - f(\tau, w) > \epsilon \text{ and } \tau > \tau_m. \quad (\text{B.16})$$

Moreover,

$$v'(\tau_m, w) > \max_{\tau} f(\tau, w),$$

follows from (B.14) and the fact that  $f_{\tau}$  is bounded. Because  $v(\tau; w)$  is strictly convex in (B.16),  $v'(\tau, w) > \max_{\tau} f(\tau, w)$  for  $\tau > \tau_m$ , which leads to a contradiction with (B.12). To show that (B.15) holds, and that  $v(\tau; w)$  is strictly convex in (B.16), we calculate  $v_{\tau\tau}(\tau, w)$  from (3.82) as

$$v_{\tau\tau} = 2(v - f)^2 v^3 + (v^2(v - f) - f_{\tau})v^2 \quad (\text{B.17})$$

and thus inflection points are found from

$$2(v - f)^2 v + v^2(v - f) = f_{\tau}. \quad (\text{B.18})$$

Because  $f_{\tau}$  is bounded (B.15) holds for inflection points, and  $v_{\tau\tau} > 0$  for  $\tau > \tau_m$  and  $v - f > \epsilon$ . This completes the proof of part 3b.

Define sets  $W_1 = \{w > 0 : 3a \text{ holds}\}$  and  $W_3 = \{w > 0 : 3c \text{ holds}\}$ , and consider the case when  $v(\tau, 0)$  has the asymptotic behavior 3a ( $A < A^*$ ). Then  $W_1$  is nonempty. The set  $W_3$  is nonempty, because  $v(\tau; w)$  is a strictly decreasing function for  $w > 1$  and has asymptotic behavior 3c.

For any  $w_1 \in W_3$  a  $\tau^*$  exists so that  $f(\tau^*; w_1) > v(\tau^*; w_1)$ . From the continuity of  $v(\tau; w)$  in  $w$  (part 1 of this Lemma) and monotonicity of  $f(\tau, w)$  with respect to  $w$ , we can find  $w_2 < w_1$  so that  $f(\tau^*; w_2) > v(\tau^*; w_2) > v(\tau^*; w_1)$ . From what follows,  $v(\tau, w_2)$  has a maximum, and as a consequence it has the asymptotic behaviour 3c. Therefore  $(w_2, w_1] \subset W_3$  and the set  $W_3$  is open.

To show that  $W_1$  is open, we take  $w_1 \in W_1$ . From part 2 it follows that  $[0, w_1] \subset W_1$  and we need to show that there exists  $w_2 > w_1$  so that  $w_2 \in W_1$ . Then from the continuity of  $v(\tau; w)$  in  $w$  (part 1 of this Lemma) it follows that  $W_1$  is open.

We describe only the main steps of the proof and omit the technical details. For any  $\tau^*$  and  $\epsilon$  we can find  $w_2 > w_1$  so that  $v(\tau^*; w_1) - v(\tau^*; w_2) < \epsilon$ . We choose  $\tau^*$  and  $\epsilon$  so that  $v(\tau; w_2)$  is strictly convex for  $\tau > \tau^*$ , and  $v_{\tau}(\tau^*; w_2) > \max_{\tau} f_{\tau}(\tau, w_2)$ . These issues follow from the analysis of (B.17) and the asymptotical and monotonicity properties of  $v(\tau; w_1)$ . Then there exists  $\epsilon^* > 0$  so that  $v(\tau; w_2) > f(\tau, w_2) + \epsilon^*$  for all  $\tau$  and, therefore  $w_2 \in W_1$ .

A set  $W_2 = \{w > 0 : 3b \text{ holds}\}$  is closed and nonempty because  $W_2 = [0, \infty) \setminus (W_1 \cup W_3)$ . We show that the set  $W_2$  consists of one element. From part 2 we have that  $v(\tau; w) - f(\tau, w)$  strictly decreases as  $w$  increases. Take  $w \in W_2$  and integrate (3.82), to get

$$\int_0^{\infty} \frac{v_{\tau}(\tau; w)}{v(\tau; w)^2} d\tau = \int_0^{\infty} (v(\tau; w) - f(\tau, w)) d\tau. \quad (\text{B.19})$$

Using (3.83), we see the right-hand side of (B.19) is equal to 1, the left hand side of (B.19) is a strictly decreasing function of  $w$ . Therefore, (B.19) can hold only for one value of  $w$   $\square$

### Proof of Lemma 3.22

*Proof.* First we show that  $I_{\text{inert}}(w)$  is continuous. Fix  $w^* \in \mathcal{D}(I_{\text{inert}}(w))$  and consider a sequence

$$w_n \rightarrow w^* \quad \text{as } n \rightarrow \infty.$$

Then

$$\begin{aligned}
I_{\text{inert}}(w^*) - I_{\text{inert}}(w_n) &= \int_0^{\tau_{\text{end}}(w^*)} g(\tau, w^*)v(\tau; w^*) d\tau - \int_0^{\tau_{\text{end}}(w_n)} g(\tau, w_n)v(\tau; w_n) d\tau \\
&= \int_0^{\tau_{\text{end}}(w_n)} [g(\tau, w^*)v(\tau; w^*) - g(\tau, w_n)v(\tau; w_n)] d\tau \\
&\quad + \int_{\tau_{\text{end}}(w_n)}^{\tau_{\text{end}}(w^*)} g(\tau, w^*)v(\tau; w^*) d\tau \\
&= J_1 + J_2.
\end{aligned}$$

The integrals  $J_1$  and  $J_2$  converge to zero as  $n \rightarrow \infty$ ; for  $J_1$  this follows from the continuity of  $v(\tau; w)$  in  $w$  (part 1 of Lemma 3.18) and for  $J_2$  from the continuity of the curve  $\tau_{\text{end}}(w)$ , which we prove next.

Because of  $v_w(t, w) < 0$  (part 2 of Lemma 3.18) and part 1 of the same Lemma we can apply the Implicit Function Theorem (e.g. [6, Theorem 3.2]) to  $v(\tau_{\text{end}}, w(\tau_{\text{end}})) - v_{\text{belt}} = 0$ . Then  $w(\tau_{\text{end}})$  is a  $C^1$ -function and

$$w'(\tau_{\text{end}}) = -\frac{v_\tau(\tau_{\text{end}}, w(\tau_{\text{end}}))}{v_w(\tau_{\text{end}}, w(\tau_{\text{end}}))}.$$

The function  $w'(\tau_{\text{end}})$  is zero only at a point when  $v(\tau_{\text{max}}, w(\tau_{\text{max}}))$  has a maximum, and this critical point is at most one. When  $w(\tau_{\text{end}})$  does not have critical points we apply the Inverse Function Theorem (e.g. [6, Theorem 3.1]) to  $w(\tau_{\text{end}})$  to prove that  $\tau_{\text{end}}(w)$  is a  $C^1$ -function.

If  $\tau_{\text{max}}$  exists, then on the interval  $\tau_{\text{end}} < \tau_{\text{max}}$  because  $v_\tau(\tau_{\text{end}}, w(\tau_{\text{end}})) > 0$  we have that  $w'(\tau_{\text{end}}) < 0$  and by applying the Inverse Function Theorem to  $w(\tau_{\text{end}})$  we obtain  $\tau_{\text{end},1}(w)$ , which is a  $C^1$ -function. Similarly, if  $\tau_{\text{end}} > \tau_{\text{max}}$ , then  $w'(\tau_{\text{end}}) > 0$ , and we obtain  $\tau_{\text{end},2}(w)$ , which is a  $C^1$ -function. Moreover, because  $\tau_{\text{max}}$  is unique and  $w(\tau_{\text{end}})$  is continuous for  $w_{\text{max}} = w(\tau_{\text{max}})$  it follows that

$$\lim_{w \rightarrow -w_{\text{max}}} \tau_{\text{end},1}(w) = \lim_{w \rightarrow +w_{\text{max}}} \tau_{\text{end},2}(w) = \tau_{\text{end}}(w_{\text{max}}). \quad (\text{B.20})$$

This finishes the proof of part 1.

To prove part 2, we first show that

$$\lim_{w \rightarrow +w_{\text{crit}}} \tau_{\text{end},2}(w) = \infty. \quad (\text{B.21})$$

In other words,  $\forall \epsilon > 0, \exists \delta > 0 : 0 < w - w_{\text{crit}} < \delta, \tau_{\text{end},2}(w) > \epsilon$ . By part 1 of Lemma 3.18 for  $\epsilon_1 = f(\epsilon; w_{\text{crit}}) - v_{\text{belt}}, \exists \delta_1 > 0 : 0 < w - w_{\text{crit}} < \delta_1, |v(\tau; w) - v(\tau; w_{\text{crit}})| < \epsilon_1$  for  $\tau < \epsilon$  and as a consequence of part 3 of Lemma 3.18, we conclude that  $\tau_{\text{end},2}(w) > \epsilon$ . Therefore, by taking  $\delta = \delta_1$  we prove (B.21).

Because  $g(\tau; w)$  has a horizontal asymptote  $\lim_{\tau \rightarrow \infty} g(\tau; w) = 1$  and  $v(\tau; w) > \min\{1, v_{\text{belt}}\}$  for  $0 < \tau < \tau_{\text{end},2}(w)$ , we have that

$$\lim_{w \rightarrow w_{\text{crit}}} I_{\text{inert},2}(w) = \lim_{w \rightarrow w_{\text{crit}}} \tau_{\text{end},2}(w) = \infty.$$

Next we prove part 3. Consider  $w > 1$ , then  $v(\tau; w)$  is strictly decreasing. From (3.82), (3.83) we estimate  $v_\tau(\tau; w)$  as

$$\frac{v_\tau(\tau; w)}{v(\tau; w)^2} < 1 - w, \quad v(0; w) = 1,$$

because  $f(\cdot, w)$  is strictly increasing. This estimates  $v(\tau; w)$  as

$$v(\tau; w) < \frac{1}{(w-1)\tau + 1},$$

which together with the definition of  $\tau_{\text{end}}(w)$  gives an upper estimate

$$\tau_{\text{end}}(w) < \frac{1 - v_{\text{belt}}}{v_{\text{belt}}(w-1)}. \quad (\text{B.22})$$

Then, using  $g(\tau, w) \leq 1$  and  $v(\tau; w) \leq 1$  (for  $w > 1$ ), we obtain

$$\lim_{w \rightarrow \infty} I_{\text{inert}}(w) < \lim_{w \rightarrow \infty} \tau_{\text{end}}(w) = 0,$$

by (B.22).

Choose  $w_1 < w_2$ , for which  $\tau_{\text{end},1}$  exists. By part 2 of Lemma 3.18, monotonicity properties of  $v(\tau; w)$ , and the definition  $\tau_{\text{end},1}$  it follows that  $\tau_{\text{end},1}(w_1) < \tau_{\text{end},1}(w_2)$ . Next, consider the difference

$$\begin{aligned} I_{\text{inert},1}(w_2) - I_{\text{inert},1}(w_1) &= \int_0^{\tau_{\text{end},1}(w_2)} v(\tau; w_2) d\tau - \int_0^{\tau_{\text{end},1}(w_1)} v(\tau; w_1) d\tau \\ &> \int_{\Delta\tau}^{\tau_{\text{end},1}(w_2)} v(\tau; w_2) d\tau - \int_0^{\tau_{\text{end},1}(w_1)} v(\tau; w_1) d\tau \\ &> \int_0^{\tau_{\text{end},1}(w_1)} \Delta v(\tau) d\tau > 0, \end{aligned}$$

where  $\Delta\tau = \tau_{\text{end},1}(w_2) - \tau_{\text{end},1}(w_1)$  and  $\Delta v(\tau) = v(\tau + \Delta\tau; w_2) - v(\tau; w_1)$ , because

$$\Delta v(\tau) > 0 \text{ for } \tau \in [0, \tau_{\text{end},1}(w_1)], \quad (\text{B.23})$$

which will be shown next. Here,  $\Delta v(\tau_{\text{end},1}(w_1)) = 0$  follows from the definition of  $\tau_{\text{end}}(w)$ . From (3.82) we have

$$\Delta v'(\tau_{\text{end},1}(w_1)) = v_{\text{belt}}^2(f(\tau_{\text{end},1}(w_1), w_1) - f(\tau_{\text{end},1}(w_2), w_2)) < 0,$$

and from Lemma 3.18 it follows that  $\Delta v(\tau) > 0$  in a vicinity of  $\tau_{\text{end},1}(w_1)$  for  $\tau < \tau_{\text{end},1}(w_1)$ . Suppose that there exist a point  $\tau^* < \tau_{\text{end},1}(w_1)$  so that  $\Delta v(\tau^*) = 0$  and  $\Delta v'(\tau^*) > 0$  with  $v_* = v(\tau^* + \Delta\tau; w_2) = v(\tau^*; w_1)$ . Then

$$0 < \Delta v'(\tau^*) = v_*^2(f(\tau^*, w_1) - f(\tau^* + \Delta, w_2)) < 0.$$

This leads to a contradiction, which proves (B.23) and completes the proof of part 4.

To prove part 5, we take  $w_1 < w_2$  so that  $\tau_{\text{end},2}$  exists. By part 2 of Lemma 3.18 and the definition  $\tau_{\text{end},2}$  it follows that  $\tau_{\text{end},2}(w_1) > \tau_{\text{end},2}(w_2)$ , and  $v(\tau; w_1) > v(\tau; w_2)$ . We use that  $g(\tau, w)$  is non-increasing in  $w$  and consider the difference

$$\begin{aligned} I_{\text{inert},2}(w_2) - I_{\text{inert},2}(w_1) &= \int_0^{\tau_{\text{end},2}(w_2)} g(\tau, w_2)v(\tau; w_2)d\tau \\ &\quad - \int_0^{\tau_{\text{end},2}(w_1)} g(\tau, w_1)v(\tau; w_1)d\tau \\ &< \int_0^{\tau_{\text{end},2}(w_2)} (g(\tau, w_2)v(\tau; w_2) - g(\tau, w_1)v(\tau; w_1))d\tau \\ &< \int_0^{\tau_{\text{end},2}(w_2)} v(\tau; w_2)(g(\tau, w_2) - g(\tau, w_1))d\tau \leq 0, \end{aligned}$$

which proves part 5.

From Lemma 3.18 it follows that  $\tau_{\text{end},2}(w)$  and  $\tau_{\text{end},1}(w)$  can exist for the same  $w$  only if  $v(\tau; w)$  first increases and then decrease, (part 3 of Lemma 3.18 which gives  $\tau_{\text{end},2}(w) > \tau_{\text{end},1}(w)$ ). Now the difference

$$\begin{aligned} I_{\text{inert},2}(w) - I_{\text{inert},1}(w) &= \int_0^{\tau_{\text{end},2}(w)} g(\tau, w)v(\tau; w)d\tau \\ &\quad - \int_0^{\tau_{\text{end},1}(w)} g(\tau, w)v(\tau; w)d\tau \\ &= \int_{\tau_{\text{end},1}(w)}^{\tau_{\text{end},2}(w)} g(\tau, w)v(\tau; w)\tau > 0, \end{aligned}$$

proves part 6. □



## Appendix C

# Experimental measurements

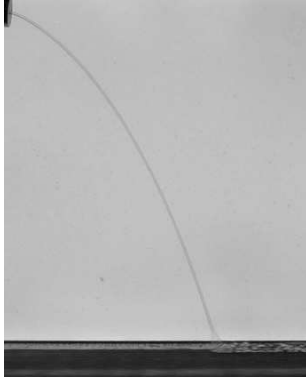
Parameters values of the experiments and values of the touchdown points  $x_{\text{end}}$

Set	Exp. N.	$v_{\text{belt}}$ m/s	$v_{\text{nozzle}}$ m/s	$d_{\text{nozzle}}$ m	$\alpha_{\text{nozzle}}$	$L$ m	$L/x_{\text{end}}$
Set 1	1	0.100	1.188	0.0004	-5	0.068	0.620763
	2	0.223	1.148	0.0004	-5	0.068	0.623529
	3	0.535	1.148	0.0004	-5	0.068	0.639066
	4	0.537	1.148	0.0004	-5	0.068	0.622601
	5	0.933	1.148	0.0004	-5	0.068	0.609244
	6	1.427	1.148	0.0004	-5	0.068	0.498947
	7	2.050	1.148	0.0004	-5	0.068	0.354974
	8	2.800	1.148	0.0004	-5	0.068	0.154412
	9	3.767	1.148	0.0004	-5	0.068	0.127637
	10	4.450	1.148	0.0004	-5	0.068	0.187764
	11	5.083	1.148	0.0004	-5	0.068	0.142857
Set 2	12	0.100	1.147	0.0004	-5	0.041	0.863905
	13	0.283	1.147	0.0004	-5	0.041	0.874816
	14	0.810	1.147	0.0004	-5	0.041	0.871157
	15	1.173	1.147	0.0004	-5	0.041	0.611765
	16	1.453	1.147	0.0004	-5	0.041	0.28863
	17	1.677	1.147	0.0004	-5	0.041	0.010249
	18	2.272	1.147	0.0004	-5	0.041	0.066568
	19	2.523	1.147	0.0004	-5	0.041	0.095588
	20	2.867	1.147	0.0004	-5	0.041	0.170554
	21	3.215	1.147	0.0004	-5	0.041	0.239826
	22	3.663	1.147	0.0004	-5	0.041	0.203757
	23	4.398	1.147	0.0004	-5	0.041	0.429838
	24	5.622	1.136	0.0004	-5	0.041	0.46793

Set	Exp. N.	$v_{\text{belt}}$ m/s	$v_{\text{nozzle}}$ m/s	$d_{\text{nozzle}}$ m	$\alpha_{\text{nozzle}}$	$L$ m	$L/x_{\text{end}}$
Set 3	25	0.138	0.934	0.0004	9	0.03	0.99053
	26	0.542	0.934	0.0004	9	0.03	1.005703
	27	0.797	0.934	0.0004	9	0.03	0.421053
	28	0.812	0.934	0.0004	9	0.03	0.58034
	29	0.897	0.934	0.0004	9	0.03	0.173004
	30	0.995	0.934	0.0004	9	0.03	0.022857
	31	1.290	0.934	0.0004	9	0.03	0.111324
	32	1.460	0.934	0.0004	9	0.03	0.372137
	33	1.652	0.934	0.0004	9	0.03	0.528409
	34	1.872	0.934	0.0004	9	0.03	0.858779
	35	2.587	0.934	0.0004	9	0.03	0.954198
	36	3.833	0.934	0.0004	9	0.03	1
Set 4	37	0.140	0.934	0.0004	-29.7	0.036	0.411864
	38	0.627	0.934	0.0004	-29.7	0.036	0.411765
	39	0.833	0.934	0.0004	-29.7	0.036	0.195286
	40	1.023	0.934	0.0004	-29.7	0.036	0.031987
	41	1.350	0.934	0.0004	-29.7	0.036	0.14958
	42	1.517	0.934	0.0004	-29.7	0.036	0.287145
	43	1.712	0.934	0.0004	-29.7	0.036	0.376471
	44	2.427	0.934	0.0004	-29.7	0.036	0.764214
	45	3.565	0.934	0.0004	-29.7	0.036	0.961345
Set 5	46	0.245	0.934	0.0004	-2.6	0.061	0.264646
	47	0.828	0.934	0.0004	-2.6	0.061	0.200803
	48	0.948	0.934	0.0004	-2.6	0.061	0.101304
	49	1.212	0.934	0.0004	-2.6	0.061	0.014056
	50	1.608	0.934	0.0004	-2.6	0.061	0.067269
	51	2.522	0.934	0.0004	-2.6	0.061	0.048193
	52	4.152	0.934	0.0004	-2.6	0.061	0.129293
	53	5.645	0.934	0.0004	-2.6	0.061	0.287298
Set 6	54	0.238	0.934	0.0004	-2.6	0.016	1.405941
	55	0.685	0.934	0.0004	-2.6	0.016	1.003195
	56	0.923	0.934	0.0004	-2.6	0.016	0.186495
	57	0.965	0.934	0.0004	-2.6	0.016	0.636964
	58	1.167	0.934	0.0004	-2.6	0.016	0.980892
	59	1.965	0.931	0.0004	-2.6	0.016	1.767516
Set 7	60	0.067	0.723	0.0004	-38	0.034	0.131769
	61	0.443	0.723	0.0004	-38	0.034	0.047273
	62	0.652	0.723	0.0004	-38	0.034	0.102334
	63	0.800	0.723	0.0004	-38	0.034	0.081081
	64	1.017	0.723	0.0004	-38	0.034	0.539216
	65	1.492	0.723	0.0004	-38	0.034	0.846758
	66	2.528	0.723	0.0004	-38	0.034	1.226378

Set	Exp. N.	$v_{\text{belt}}$ m/s	$v_{\text{nozzle}}$ m/s	$d_{\text{nozzle}}$ m	$\alpha_{\text{nozzle}}$	$L$ m	$L/x_{\text{end}}$
Set 8	67	0.650	0.723	0.0004	-38	0.052	0.031407
	68	1.207	0.723	0.0004	-38	0.052	0.061481
	69	1.512	0.723	0.0004	-38	0.052	0.212766
	70	1.957	0.723	0.0004	-38	0.052	0.366162
	71	2.453	0.723	0.0004	-38	0.052	0.454774
	72	4.145	0.772	0.0004	-38	0.052	0.717528
Set 9	73	0.093	0.482	0.0004	-38	0.052	0.035194
	74	0.353	0.482	0.0004	-38	0.052	0.084848
	75	0.502	0.482	0.0004	-38	0.052	0.015644
	76	0.592	0.482	0.0004	-38	0.052	0.191283
	77	0.858	0.482	0.0004	-38	0.052	0.548736
	78	1.005	0.482	0.0004	-38	0.052	0.728365
	79	1.185	0.482	0.0004	-38	0.052	0.773109
	80	1.548	0.482	0.0004	-38	0.052	0.92883
	81	2.205	0.482	0.0004	-38	0.052	1.08082
Set 10	82	0.093	1.061	0.001	-37.3	0.054	0.572629
	83	0.750	1.061	0.001	-37.3	0.054	0.543529
	84	1.057	1.061	0.001	-37.3	0.054	0.309942
	85	1.312	1.061	0.001	-37.3	0.054	0.117919
	86	1.708	1.061	0.001	-37.3	0.054	0.076923
	87	2.717	1.061	0.001	-37.3	0.054	0.176337
	88	3.200	1.061	0.001	-37.3	0.054	0.284078

## Set 1



Experiment 1



Experiment 2



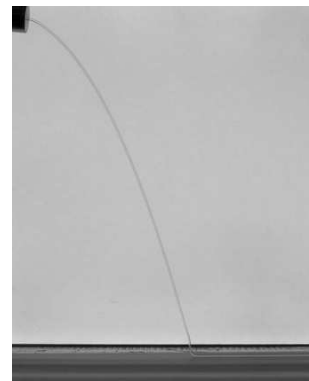
Experiment 3



Experiment 4



Experiment 5



Experiment 6



Experiment 7



Experiment 8



Experiment 9

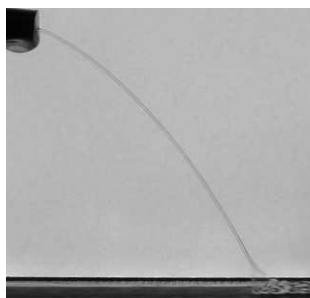


Experiment 10

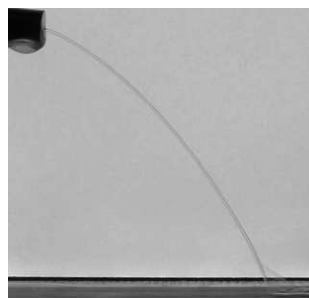


Experiment 11

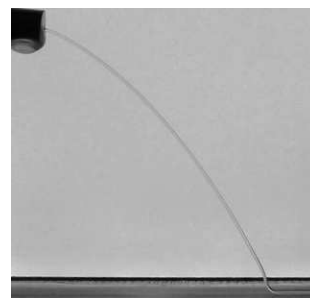
Set 2



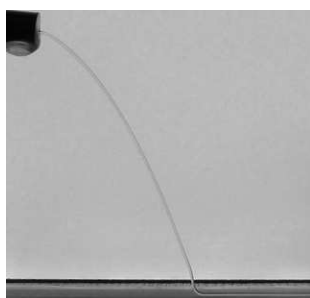
Experiment 12



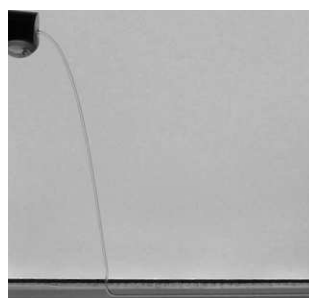
Experiment 13



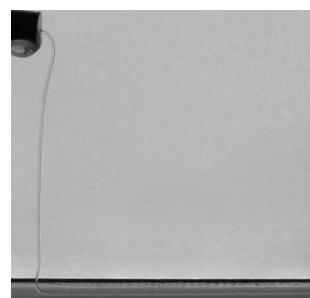
Experiment 14



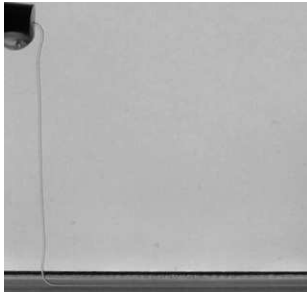
Experiment 15



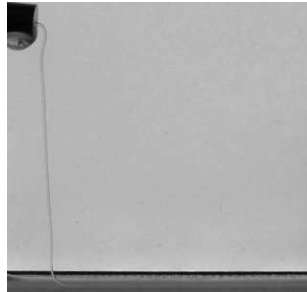
Experiment 16



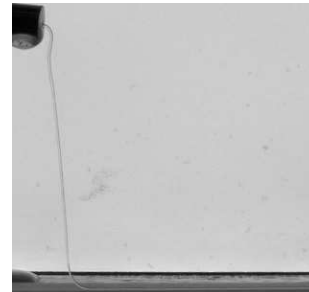
Experiment 17



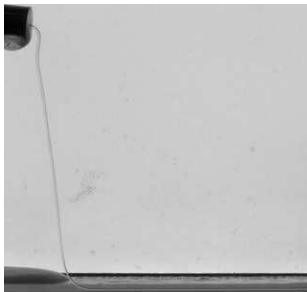
Experiment 18



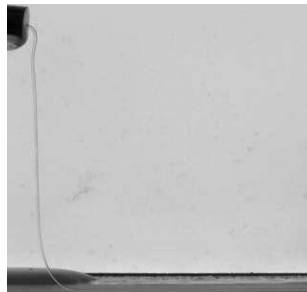
Experiment 19



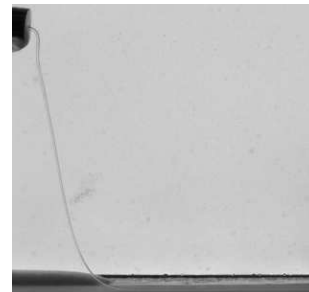
Experiment 20



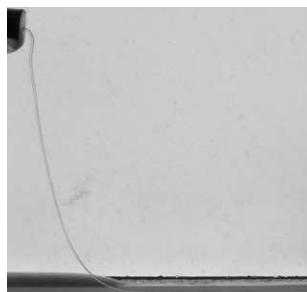
Experiment 21



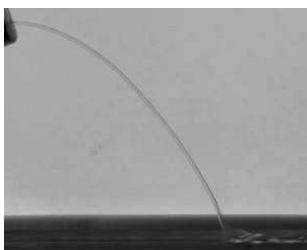
Experiment 22



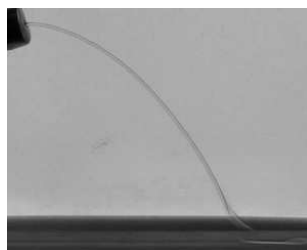
Experiment 23



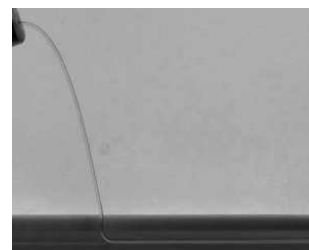
Experiment 24

**Set 3**

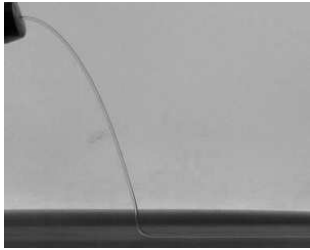
Experiment 25



Experiment 26



Experiment 27



Experiment 28



Experiment 29



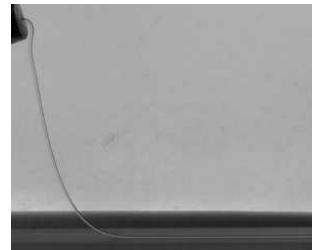
Experiment 30



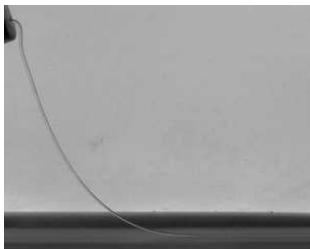
Experiment 31



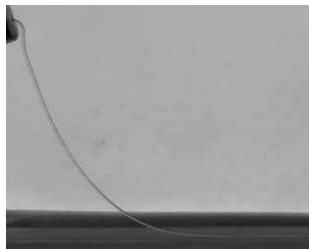
Experiment 32



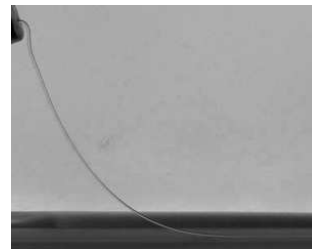
Experiment 33



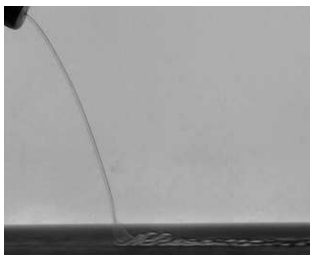
Experiment 34



Experiment 35



Experiment 36

**Set 4**

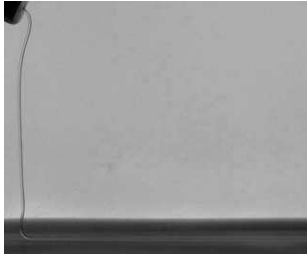
Experiment 37



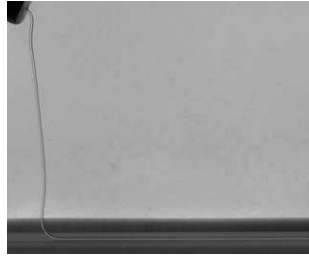
Experiment 38



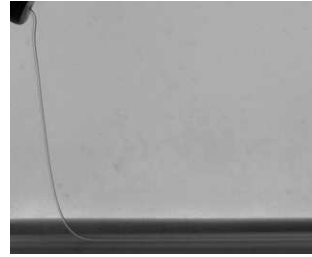
Experiment 39



Experiment 40



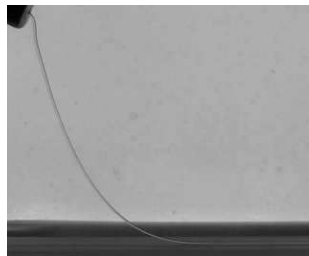
Experiment 41



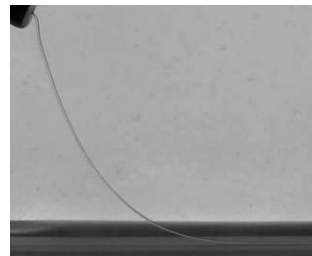
Experiment 42



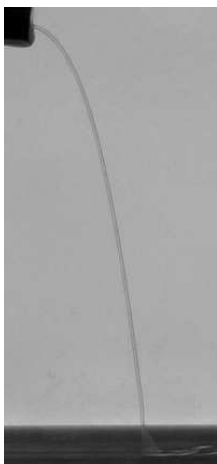
Experiment 43



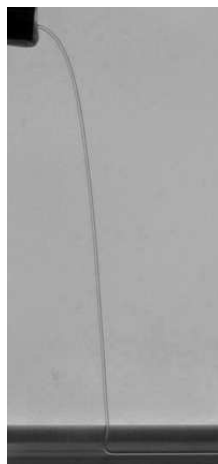
Experiment 44



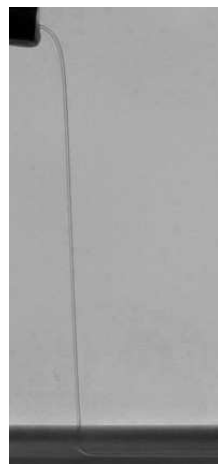
Experiment 45

**Set 5**

Experiment 46



Experiment 47



Experiment 48



Experiment 49





Experiment 50



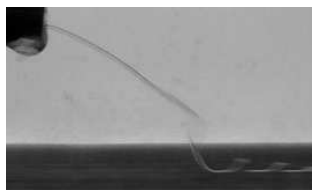
Experiment 51



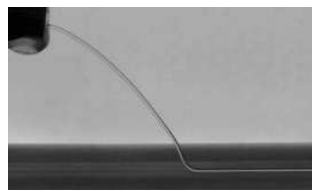
Experiment 52



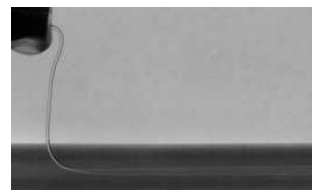
Experiment 53

**Set 6**

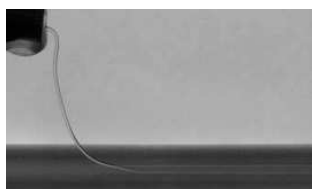
Experiment 54



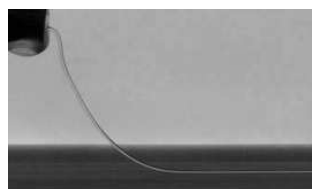
Experiment 55



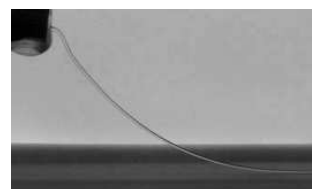
Experiment 56



Experiment 57



Experiment 58



Experiment 59

**Set 7**

Experiment 60



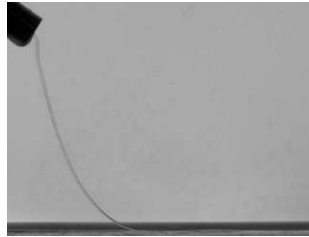
Experiment 61



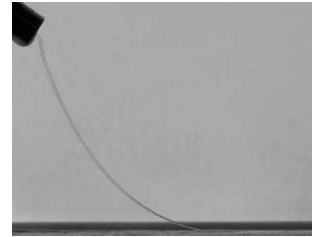
Experiment 62



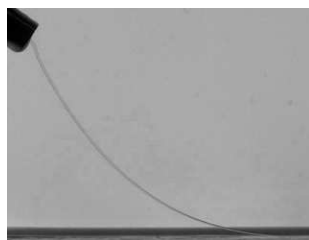
Experiment 63



Experiment 64



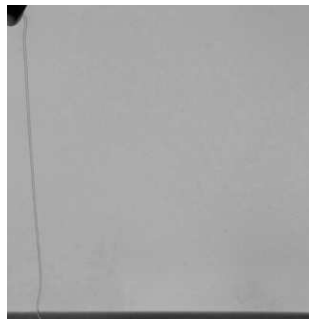
Experiment 65



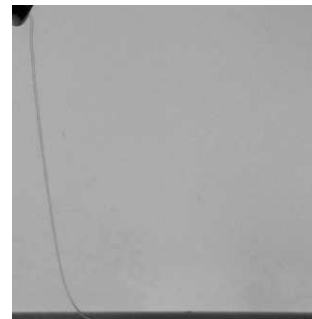
Experiment 66

**Set 8**

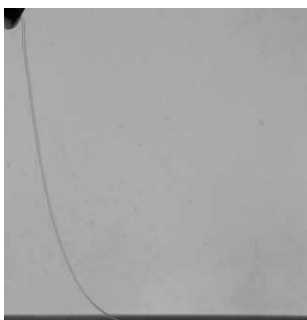
Experiment 67



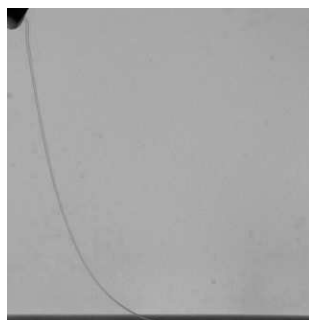
Experiment 68



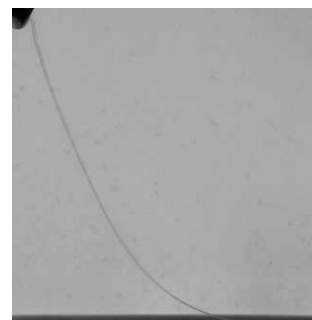
Experiment 69



Experiment 70

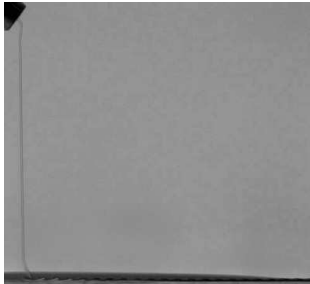


Experiment 71

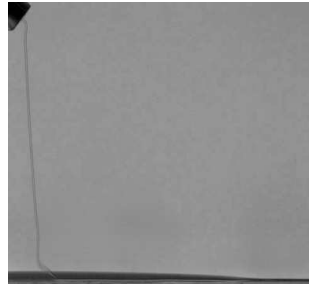


Experiment 72

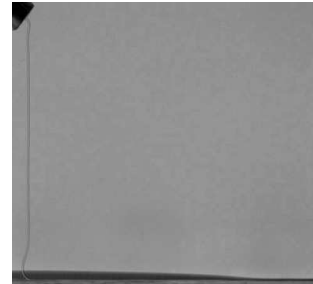
## Set 9



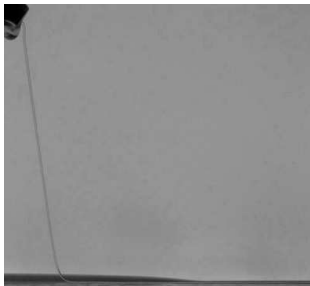
Experiment 73



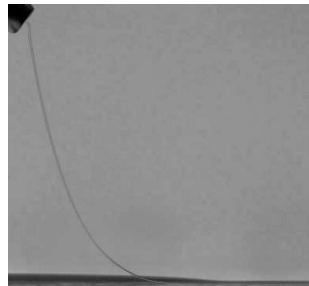
Experiment 74



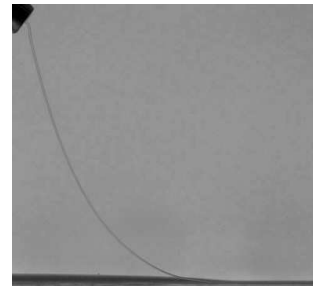
Experiment 75



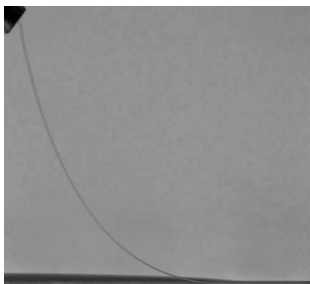
Experiment 76



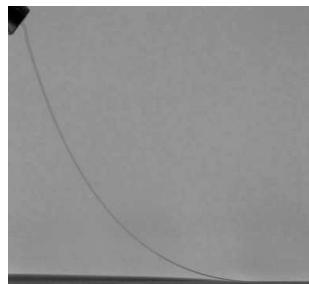
Experiment 77



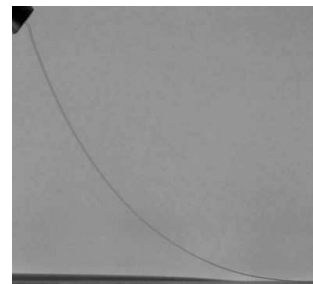
Experiment 78



Experiment 79

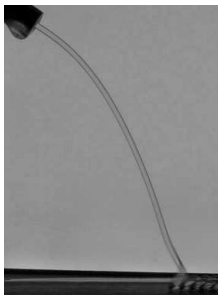


Experiment 80

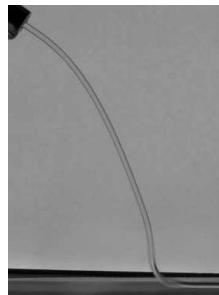


Experiment 81

## Set 10



Experiment 82



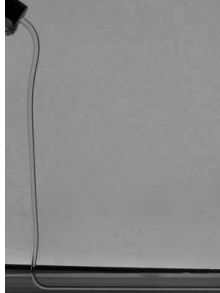
Experiment 83



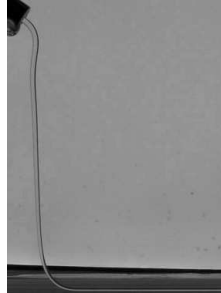
Experiment 84



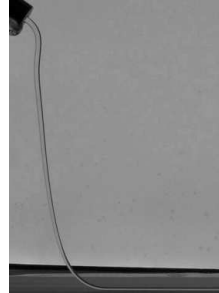
Experiment 85



Experiment 86



Experiment 87



Experiment 88

# Bibliography

- [1] ABRAMOWITZ, M., AND STEGUN, I. A. *Handbook of mathematical functions with formulas, graphs, and mathematical tables*, vol. 55 of *National Bureau of Standards Applied Mathematics Series*. For sale by the Superintendent of Documents, U.S. Government Printing Office, Washington, D.C., 1964.
- [2] ADACHI, K. Laminar jets of a plane liquid sheet falling vertically in the atmosphere. *Journal of Non-Newtonian Fluid Mechanics* 24 (1987), 11–30.
- [3] ALLEBORN, N. Progress in coating theory. *Thermal Science* 5 (2001), 131–152.
- [4] ANDASARI, V. Modeling of coiling of polymer filaments. <http://www.win.tue.nl/oowi/final%20project/archive/ViviAndasari.pdf>.
- [5] ANTMAN, S. S. *Nonlinear Problems of Elasticity*. Published by Springer-Verlag, 1995.
- [6] AVEZ, A. *Differential calculus*. A Wiley-Interscience Publication. John Wiley & Sons Ltd., Chichester, 1986. Translated from the French by D. Edmunds.
- [7] BARNES, G., AND MACKENZIE, J. Height of fall versus frequency in liquid rope-coil effect. *American Journal of Physics* 27, 2 (1959), 112–115.
- [8] BARNES, G., AND WOODCOCK, R. Liquid rope-coil effect. *American Journal of Physics* 26, 4 (1958), 205–209.
- [9] BONILLA, L. L., GÖTZ, T., KLAR, A., MARHEINEKE, N., AND WEGENER, R. Hydrodynamic limit of a Fokker–Planck equation describing fiber lay-down processes. *SIAM Journal on Applied Mathematics* 68, 3 (2007), 648–665.
- [10] BREWARD, C., DYSON, R., EDWARDS, C., METCALFE, P., PLEASE, C., AND ZYSKIN, M. Modelling of melt on spinning wheels. Study group report, European Study Group with Industry 49th ESGI (Oxford 29/3/2004 - 4/4/2004), 2005. Thermal Ceramics UK.
- [11] CHAUDHARY, K. C., AND REDEKOPP, L. G. The nonlinear capillary instability of a liquid jet. part 1. theory. *Journal of Fluid Mechanics* 96, 02 (1980), 257–274.
- [12] CHAUDHARY, K. C., AND REDEKOPP, L. G. The nonlinear capillary instability of a liquid jet. part 2. experiments on jet behaviour before droplet formation. *Journal of Fluid Mechanics* 96, 02 (1980), 275–297.

- 
- [13] CHIU-WEBSTER, S., AND LISTER, J. R. The fall of a viscous thread onto a moving surface: a 'fluid-mechanical sewing machine'. *Journal of Fluid Mechanics* 569 (2006), 89–111.
- [14] CLARKE, A., WEINSTEIN, S. J., MOON, A. G., AND SIMISTER, E. A. Time-dependent equations governing the shape of a two-dimensional liquid curtain, part 2: Experiment. *Physics of Fluids* 9, 12 (1997), 3637–3644.
- [15] CLARKE, N. S. A differential equation in fluid mechanics. *Mathematika* 13 (1966), 51–53.
- [16] CLARKE, N. S. Two-dimensional flow under gravity in a jet of viscous liquid. *Journal of Fluid Mechanics* 31 (1968), 481–500.
- [17] CODDINGTON, E. A., AND LEVINSON, N. *Theory of ordinary differential equations*. McGraw-Hill Book Company, Inc., New York-Toronto-London, 1955.
- [18] COURANT, R., AND HILBERT, D. *Methods of mathematical physics. Vol. II*. Wiley Classics Library. John Wiley & Sons Inc., New York, 1989. Partial differential equations, Reprint of the 1962 original, A Wiley-Interscience Publication.
- [19] CRUICKSHANK, J., AND MUNSON, B. Viscous fluid buckling of plane and axisymmetric jets. *Journal of Fluid Mechanics* 113, -1 (1981), 221–239.
- [20] CRUICKSHANK, J. O. *Viscous fluid buckling: a theoretical and experimental analysis with extensions to general fluid stability*. PhD thesis, Iowa State University, Ames IA, USA., 1980.
- [21] CRUICKSHANK, J. O. Low-Reynolds-number instabilities in stagnating jet flows. *Journal of Fluid Mechanics* 193, -1 (1988), 111–127.
- [22] CRUICKSHANK, J. O., AND MUNSON, B. R. An energy loss coefficient in fluid buckling. *Physics of Fluids* 25, 11 (1982), 1935–1937.
- [23] CRUICKSHANK, J. O., AND MUNSON, B. R. A theoretical prediction of the fluid buckling frequency. *Physics of Fluids* 26, 4 (1983), 928–930.
- [24] CUBAUD, T., AND MASON, T. G. Folding of viscous threads in diverging microchannels. *Physical Review Letters* 96, 11 (2006), 114501.
- [25] CUMMINGS, L. J., AND HOWELL, P. D. On the evolution of non-axisymmetric viscous fibres with surface tension, inertia and gravity. *Journal of Fluid Mechanics* 389, -1 (2000), 361–389.
- [26] DAVIS, J. L. *Mathematics of wave propagation*. Princeton University Press, Princeton, NJ, 2000.
- [27] DECENT, S. P., KING, A. C., AND WALLWORK, I. M. Free jets spun from a prilling tower. *Journal of Engineering Mathematics* 42, 3 (2002), 265 – 282.

- [28] DEN DECKER, P., KNOESTER, H., MEERMAN, H., DEKKER, K. VAN HORSEN, W., VUIK, C., WESSELING, P., PROKERT, G., VAN 'T HOF, B., AND VAN BECKUM, F. The rotor spinning process for fibre production. In *Proceedings of the 48th European Study Group Mathematics with Industry (Delft, 15-19 March 2004)* (2004), pp. 35–48.
- [29] DUBOIS, F., AND LEFLOCH, P. Boundary conditions for nonlinear hyperbolic systems of conservation laws. *J. Differential Equations* 71, 1 (1988), 93–122.
- [30] DYSON, R. J., HOWELL, P. D., BREWARD, C. J. W., HERDMAN, P., AND BRANDER, J. Mathematical modelling of curtain coating. In *Proceedings of the 6th European Coating Symposium ECS2005* (2005).
- [31] EGGERS, J., AND VILLERMAUX, E. Physics of liquid jets. *Reports on Progress in Physics* 71, 036601 (2008), 79pp.
- [32] ENTOV, V. M., AND YARIN, A. L. Dynamical equation for a liquid jet. *Translated from Izvestiya Akademii Nauk SSSR, Mekhanika Zhidkosti i Gaza*, 5 (September-October 1980), 11–18.
- [33] ENTOV, V. M., AND YARIN, A. L. The dynamics of thin liquid jets in air. *Journal of Fluid Mechanics* 140, -1 (1984), 91–111.
- [34] EVANS, L. C. *Partial differential equations*, vol. 19 of *Graduate Studies in Mathematics*. American Mathematical Society, Providence, RI, 1998.
- [35] FINNICUM, D. S., WEINSTEIN, S. J., AND RUSCHAK, K. J. The effect of applied pressure on the shape of a two-dimensional liquid curtain falling under the influence of gravity. *Journal of Fluid Mechanics* 255, -1 (1993), 647–665.
- [36] FOREST, M. G., AND WANG, Q. Dynamics of slender viscoelastic free jets. *SIAM Journal on Applied Mathematics* 54, 4 (1994), 996–1032.
- [37] FOREST, M. G., AND ZHOU, H. Unsteady analyses of thermal glass fibre drawing processes. *European Journal of Applied Mathematics* 12, 04 (2001), 479–496.
- [38] GODLEWSKI, E., AND RAVIART, P.-A. *Numerical approximation of hyperbolic systems of conservation laws*, vol. 118 of *Applied Mathematical Sciences*. Springer-Verlag, New York, 1996.
- [39] GÖTZ, T., KLAR, A., MARHEINEKE, N., AND WEGENER, R. A stochastic model and associated Fokker–Planck equation for the fiber lay-down process in non-woven production processes. *SIAM Journal on Applied Mathematics* 67, 6 (2007), 1704–1717.
- [40] GÖTZ, T., KLAR, A., UNTERREITER, A., AND WEGENER, R. Numerical evidence for the non-existence of stationary solutions of the equations describing rotational fiber spinning. *Mathematical Models and Methods in Applied Sciences* 18, 10 (2008), 1829–1844.
- [41] GUNAWAN, A. Y. *Stability of Immersed Liquid Threads*. PhD thesis, Technische Universiteit Eindhoven, 2004.

- [42] GUNAWAN, A. Y., MOLENAAR, J., AND VAN DE VEN, A. A. F. In-phase and out-of-phase break-up of two immersed liquid threads under influence of surface tension. *European Journal of Mechanics - B/Fluids* 21, 4 (2002), 399 – 412.
- [43] GUNAWAN, A. Y., MOLENAAR, J., AND VAN DE VEN, A. A. F. Does shear flow stabilize an immersed thread? *European Journal of Mechanics - B/Fluids* 24, 3 (2005), 379 – 396.
- [44] GUNAWAN, A. Y., MOLENAAR, J., AND VAN DE VEN, A. A. F. Temporal stability of a viscoelastic immersed thread in a confined region. *Journal of Non-Newtonian Fluid Mechanics* 126, 2-3 (2005), 83 – 92. Annual European Rheology Conference 2003.
- [45] HABIBI, M., MALEKI, M., GOLESTANIAN, R., RIBE, N. M., AND BONN, D. Dynamics of liquid rope coiling. *Physical Review E (Statistical, Nonlinear, and Soft Matter Physics)* 74, 6 (2006), 066306.
- [46] HABIBI, M., RIBE, N. M., AND BONN, D. Coiling of elastic ropes. *Physical Review Letters* 99, 15 (2007), 154302.
- [47] HAN, T., RENEKER, D. H., AND YARIN, A. L. Buckling of jets in electrospinning. *Polymer* 48, 20 (2007), 6064 – 6076.
- [48] HAN, T., RENEKER, D. H., AND YARIN, A. L. Pendulum-like motion of straight electrified jets. *Polymer* 49, 8 (2008), 2160 – 2169.
- [49] HENSON, G. M., CAO, D., BECHTEL, S. E., AND FOREST, M. G. A thin-filament melt spinning model with radial resolution of temperature and stress. *Journal of Rheology* 42, 2 (1998), 329–360.
- [50] HLOD, A., AARTS, A. C. T., VAN DE VEN, A. A. F., AND PELETIER, M. A. Mathematical model of falling of a viscous jet onto a moving surface. *European Journal of Applied Mathematics* 18 (2007), 659–677.
- [51] HLOD, A., AARTS, A. C. T., VAN DE VEN, A. A. F., AND PELETIER, M. A. Three flow regimes of viscous jet falling onto a moving surface. CASA Repor 08-28, Technische Universiteit Eindhoven, Eindhoven, 2008.
- [52] HLOD, A., AARTS, A. C. T., VAN DE VEN, A. A. F., AND PELETIER, M. A. Falling of a viscous jet onto a moving surface. CASA-Report 06-23, Centre for Analysis, Scientific computing and Applications, July 2006.
- [53] INGRAM, J. *The Velocity of Honey: And More Science of Everyday Life*. Thunder's Mouth Press, 2005.
- [54] KELLER, J. B. Teapot effect. *Journal of Applied Physics* 28, 8 (1957), 859–864.
- [55] KIRK, R. E., OTHMER, D. F., KROSCWITZ, J. I., AND HOWE-GRANT, M. *Encyclopedia of chemical technology*. Wiley, 1997.
- [56] KISTLER, S. F., AND SCRIVEN, L. E. The teapot effect: sheet-forming flows with deflection, wetting and hysteresis. *Journal of Fluid Mechanics* 263, -1 (1994), 19–62.



- 
- [57] KOLK, E. Mathematical models for a rotor spinning process. Interim report, TU Delft, 2005.
- [58] KOLK, E. Mathematical models for a rotor spinning process. Final report, TU Delft, 2005.
- [59] KOULAKIS, J. P., MITESCU, C. D., BROCHARD-WYART, F., DE GENNES, P.-G., AND GUYON, E. The viscous catenary revisited: experiments and theory. *Journal of Fluid Mechanics* 609, -1 (2008), 87–110.
- [60] KOWALEWSKI, T. A. On the separation of droplets from a liquid jet. *Fluid Dynamics Research* 17 (1996).
- [61] KREISS, H.-O. Initial boundary value problems for hyperbolic systems. *Communications on Pure and Applied Mathematics*. 23 (1970), 277–298.
- [62] LEE, J. K., AND SEO, G. T. The falling laminar jet of semi-dilute polymer solutions. *Korean Journal of Chemical Engineering* 12, 3 (1995), 273–276.
- [63] LIM, K.-S., AND LONGE, J. L. *How Products Are Made: An Illustrated Guide to Product Manufacturing*. Gale, 1998.
- [64] MAHADEVAN, L., AND KELLER, J. B. Coiling of flexible ropes. *Proceedings of the Royal Society A: Mathematical, Physical and Engineering Sciences* 452, 1950 (1996), 1679–1694.
- [65] MAHADEVAN, L., AND KELLER, J. B. Periodic folding of thin sheets. *SIAM Review* 41, 1 (1999), 115–131.
- [66] MAHADEVAN, L., RYU, W. S., AND SAMUEL, A. D. T. Fluid “rope trick” investigated. *Nature* 392, 6672 (1998), 140.
- [67] MAHADEVAN, L., RYU, W. S., AND SAMUEL, A. D. T. Correction: fluid “rope trick” investigated. *Nature* 403 (2000), 502.
- [68] MALEKI, M., HABIBI, M., GOLESTANIAN, R., RIBE, N. M., AND BONN, D. Liquid rope coiling on a solid surface. *Physical Review Letters* 93, 21 (Nov 2004), 214502.
- [69] MARHEINEKE, N., AND WEGENER, R. Fiber dynamics in turbulent flows: General modeling framework. *SIAM Journal on Applied Mathematics* 66, 5 (2006), 1703–1726.
- [70] MARHEINEKE, N., AND WEGENER, R. Fiber dynamics in turbulent flows: Specific Taylor drag. *SIAM Journal on Applied Mathematics* 68, 1 (2007), 1–23.
- [71] MARHEINEKE, N., AND WEGENER, R. Asymptotic model for the dynamics of curved viscous fibres with surface tension. *Journal of Fluid Mechanics* 622, -1 (2009), 345–369.
- [72] MATTHEIJ, R. M. M., RIENSTRA, S. W., AND TEN THIJE BOONKAMP, J. H. M. *Partial differential equations*. SIAM Monographs on Mathematical Modeling and Computation. Society for Industrial and Applied Mathematics (SIAM), Philadelphia, PA, 2005. Modeling, analysis, computation.

- 
- [73] MIDDLEMAN, S. *Modeling Axisymmetric Flows: Dynamics of Films, Jets, and Drops*. Academic Press, 1995.
- [74] MORRIS, S. W., DAWES, J. H. P., RIBE, N. M., AND LISTER, J. R. Meandering instability of a viscous thread. *Physical Review E (Statistical, Nonlinear, and Soft Matter Physics)* 77, 6 (2008), 066218.
- [75] NAGAIRO, S., AND HAYAKAWA, Y. Bending-filament model for the buckling and coiling instability of a viscous fluid rope. *Physical Review E (Statistical, Nonlinear, and Soft Matter Physics)* 78, 2 (2008), 025302.
- [76] NAKAJIMA, T., KAJIWARA, K., AND MCINTYRE, J. E. *Advanced fiber spinning technology*. Woodhead Publishing, 1994.
- [77] PANDA, S. *The Dynamics of Viscous Fibers*. PhD thesis, Technische Universität Kaiserslautern, 2006.
- [78] PANDA, S., MARHEINEKE, N., AND WEGENER, R. Systematic derivation of an asymptotic model for the dynamics of curved viscous fibers. *Mathematical Methods in the Applied Sciences* 31, 10 (2008), 1153–1173.
- [79] PARAU, E. I., DECENT, S., SIMMONS, M., WONG, D. C. Y., AND KING, A. C. Nonlinear viscous liquid jets from a rotating orifice. *Journal of Engineering Mathematics* 57, 2 (February 2007), 159–179.
- [80] PARAU, E. I., DECENT, S. P., KING, A. C., SIMMONS, M. J. H., AND WONG, D. C. Nonlinear travelling waves on a spiralling liquid jet. *Wave Motion* 43, 7 (August 2006), 599–618.
- [81] PARTRIDGE, L., WONG, D. C. Y., SIMMONS, M. J. H., PARAU, E. I., AND DECENT, S. P. Experimental and theoretical description of the break-up of curved liquid jets in the prilling process. *Chemical Engineering Research and Design* 83, A11 (November 2005), 1267–1275.
- [82] POLYANIN, A. D., ZAITSEV, V. F., AND MOUSSIAUX, A. *Handbook of first order partial differential equations*, vol. 1 of *Differential and Integral Equations and Their Applications*. Taylor & Francis Ltd., London, 2002.
- [83] QUARTERONI, A., SACCO, R., AND SALERI, F. *Numerical mathematics*, vol. 37 of *Texts in Applied Mathematics*. Springer-Verlag, New York, 2000.
- [84] RAYLEIGH, L. On the instability of jets. *Proceedings of the London Mathematical Society* s1-10 (1878), 4–13.
- [85] RIBE, N. M. A general theory for the dynamics of thin viscous sheets. *Journal of Fluid Mechanics* 457 (2002), 255–283.
- [86] RIBE, N. M. Periodic folding of viscous sheets. *Physical Review E* 68 (2003), 036305.
- [87] RIBE, N. M. Coiling of viscous jets. *Proceedings of the Royal Society of London A* 460 (2004), 3223–3239.

- [88] RIBE, N. M., HABIBI, M., AND BONN, D. Stability of liquid rope coiling. *Physics of Fluids* 18, 8 (2006), 084102.
- [89] RIBE, N. M., HUPPERT, H. E., HALLWORTH, M. A., HABIBI, M., AND BONN, D. Multiple coexisting states of liquid rope coiling. *Journal of Fluid Mechanics* 555, -1 (2006), 275–297.
- [90] RIBE, N. M., LISTER, J. R., AND CHIU-WEBSTER, S. Stability of a dragged viscous thread: Onset of stitching in a fluid-mechanical sewing machine. *Physics of Fluids* 18 (2006), 124105–1–8.
- [91] ROMANOWSKI, P. How products are made, volume 4, cotton candy. <http://www.madehow.com/Volume-4/Cotton-Candy.html>.
- [92] ROOS, J. P., SCHWEIGMAN, C., AND TIMMAN, R. Mathematical formulation of the laws of conservation of mass and energy and the equation of motion for a moving thread. *Journal of Engineering Mathematics* 7, 2 (April 1973), 139–146.
- [93] ROY, A., MAHADEVAN, L., AND THIFFEAULT, J.-L. Fall and rise of a viscoelastic filament. *Journal of Fluid Mechanics* 563, -1 (2006), 283–292.
- [94] RUDIN, W. *Principles of mathematical analysis*, third ed. McGraw-Hill Book Co., New York, 1976. International Series in Pure and Applied Mathematics.
- [95] RUSCHAK, K. J. Coating flows. *Annual Review of Fluid Mechanics* 17, 1 (1985), 65–89.
- [96] SALAMONE, J. C. *Polymeric Materials Encyclopedia*. CRC Press, 1996.
- [97] SAUTER, U. S., AND BUGGISCH, H. W. Stability of initially slow viscous jets driven by gravity. *Journal of Fluid Mechanics* 533 (2005), 237–257.
- [98] SCHMEITS, G. Strooppatronen wiskundig onderzocht. *Kennislink, Vakpagina Wiskunde*, [www.kennislink.nl](http://www.kennislink.nl) (12/7/2006).
- [99] SENCHENKO, S., AND BOHR, T. Shape and stability of a viscous thread. *Physical Review E (Statistical, Nonlinear, and Soft Matter Physics)* 71, 5 (2005), 056301.
- [100] SKOROBOGATIY, M., AND MAHADEVAN, L. Folding of viscous sheets and filaments. *Europhysics Letters* 52, 5 (2000), 532–538.
- [101] TAYLOR, G. I. Instability of jets, threads, and sheets of viscous fluid. In *Proceedings of the 12th International Congress of Applied mechanics (Stanford, 1968)* (1969), Springer-Verlag, pp. 382–388.
- [102] TCHAVDAROV, B., YARIN, A. L., AND RADEV, S. Buckling of thin liquid jets. *Journal of Fluid Mechanics* 253 (1993), 593–615.
- [103] TEICHMAN, J., AND MAHADEVAN, L. The viscous catenary. *Journal of Fluid Mechanics* 478, -1 (2003), 71–80.
- [104] TOME, M. F., DUFFY, B., AND MCKEE, S. A numerical technique for solving unsteady non-Newtonian free surface flows. *Journal of Non-Newtonian Fluid Mechanics* 62, 1 (1996), 9 – 34.

- 
- [105] TOME, M. F., MANGIAVACCHI, N., CUMINATO, J. A., CASTELO, A., AND MCKEE, S. A finite difference technique for simulating unsteady viscoelastic free surface flows. *Journal of Non-Newtonian Fluid Mechanics* 106, 2-3 (2002), 61 – 106.
- [106] TOME, M. F., AND MCKEE, S. Numerical simulation of viscous flow: Buckling of planar jets. *International Journal for Numerical Methods in Fluids* 29, 6 (1999), 705–718.
- [107] TROUTON, F. T. On the coefficient of viscous traction and its relation to that of viscosity. *Proceedings of the Royal Society of London. Series A, Containing Papers of a Mathematical and Physical Character* 77, 519 (May 1906), 426–440.
- [108] UDDIN, J., DECENT, S. P., AND SIMMONS, M. J. The instability of shear thinning and shear thickening spiralling liquid jets: linear theory. *Transactions of the ASME Journal of Fluids Engineering* 128, 5 (September 2006), 968–975.
- [109] VOYCE, C., FITT, A., AND MONRO, T. Mathematical model of the spinning of microstructured fibres. *Opt. Express* 12, 23 (2004), 5810–5820.
- [110] WALLWORK, I. M., DECENT, S. P., KING, A. C., AND SCHULKES, R. M. S. M. The trajectory and stability of a spiralling liquid jet. part 1. inviscid theory. *Journal of Fluid Mechanics* 459 (2002), 43–66.
- [111] WEINSTEIN, S. J., CLARKE, A., MOON, A. G., AND SIMISTER, E. A. Time-dependent equations governing the shape of a two-dimensional liquid curtain, part 1: Theory. *Physics of Fluids* 9, 12 (1997), 3625–3636.
- [112] WEINSTEIN, S. J., AND RUSCHAK, K. J. Coating flows. *Annual Review of Fluid Mechanics* 36, 1 (2004), 29–53.
- [113] WONG, D. C. Y., SIMMONS, M. J. H., DECENT, S. P., PARAU, E. I., AND KING, A. C. Break-up dynamics and drop size distributions created from spiralling liquid jets. *International Journal of Multiphase Flow* 30, 5 (May 2004), 499–520.
- [114] YARIN, A. L. *Free liquid jets and films: hydrodynamics and rheology*. Interaction of Mechanics and Mathematics Series. Longman Scientific & Technical, Harlow, 1993.
- [115] YARIN, A. L. Drop impact dynamics: Splashing, spreading, receding, bouncing... *Annual Review of Fluid Mechanics* 38, 1 (2006), 159–192.
- [116] YARIN, A. L., AND TCHAVDAROV, B. M. Onset of folding in plane liquid films. *Journal of Fluid Mechanics* 307 (1996), 85–99.
- [117] ZIABICKI, A. *Fundamentals of Fibre Formation: The Science of Fibre Spinning and Drawing*. Wiley, 1976.
- [118] ZIABICKI, A., AND KAWAI, H. *High-speed Fiber Spinning: Science and Engineering Aspects*. Wiley, 1985.

# Index

Symbols	
$A$ .....	30
$C_N$ .....	81
$F_L$ .....	10
$H$ .....	127
$L$ .....	17
$M_\tau$ .....	40
$O$ .....	17, 19
$R$ .....	87
$R_{\text{coag}}$ .....	18
$R_{\text{rot}}$ .....	18
$S_1$ .....	34
$S_2$ .....	35
$A^*$ .....	163
$A_i$ .....	161
$\mathcal{B}_{\text{exist}}$ .....	95
$Bi$ .....	161
$\mathcal{B}_{\text{ivi}}$ .....	96
$B$ .....	90
$p_1$ .....	117
$p_2$ .....	117
$p_3$ .....	118
$p_4$ .....	118
$C_{\text{max}}$ .....	92
$d_{\text{nozzle}}$ .....	28
$Dr$ , draw ratio .....	30, 90
$\mathcal{E}_{\text{belt}}$ .....	117
$\mathcal{E}_v$ .....	118
$F$ , mass flux .....	29
$F_N$ .....	24
$F_{R,y}$ .....	25
$I_{\text{inert}}$ .....	33
$I_{\text{inert},2}$ .....	45
$I_{\text{inert},1}$ .....	45
$I_{v-i}$ .....	33
$I_{v-i,2}$ .....	42
$I_{v-i,1}$ .....	42
$I_{\text{visc}}$ .....	33
$\mathcal{J}_a$ .....	116
$\mathcal{J}_b$ .....	116
$\mathcal{J}_c$ .....	116
$\mathcal{J}_d$ .....	116
$\Omega_{\text{coag}}$ .....	104
$\Omega$ .....	18
$\Pi$ .....	43
$R_0$ .....	90
$\mathcal{P}$ .....	30
$\mathcal{V}_{\text{reach}}$ .....	95
$\mathcal{P}_{\text{NE}}$ .....	95
$\mathcal{P}_{\text{inert}}$ .....	32
$\mathcal{P}_{\text{visc}}$ .....	31
$\mathcal{P}_{v-i}$ .....	31
$\alpha_{t-d}$ .....	123
$\alpha_{\text{nozzle}}$ .....	17
$\theta_0$ .....	25
$\beta$ .....	19, 87
$\mathcal{L}$ .....	48
$\mathcal{L}_{\text{inert}}$ .....	48
$\mathcal{L}_{v-i}$ .....	48
$\mathcal{L}_{\text{visc}}$ .....	48
$C_I$ .....	47
$C_{\text{inert}}$ .....	43
$C_{\text{inert}}^1$ .....	49
$C_{\text{inert}}^2$ .....	49
$C_{v-i}$ .....	42
$C_{v-i}^1$ .....	49
$C_{v-i}^2$ .....	49
$C_{\text{visc}}$ .....	38
$v_{d,b}$ .....	116
$\epsilon_0$ .....	24, 117
$\hat{A}$ .....	37
$\hat{Re}$ .....	37
$\hat{Dr}$ .....	37
$\hat{v}$ .....	116
$\hat{s}$ .....	115
$\hat{\tau}$ .....	36

$\hat{\tau}_{\text{end}}$ .....	37	$v_{\text{visc}}$ .....	33
$\hat{\sigma}$ .....	36	$w_{\text{crit}}$ .....	40, 44, 94
$\hat{w}$ .....	37	$w_{\text{max}}$ .....	42, 44
$\mathbb{B}_{a,n+1 \times n+1}$ .....	120	$w_1^*$ .....	55
$\mathbb{B}_{b,n+1 \times n+1}$ .....	120	$w_{\text{visc}}$ .....	47
$\mathbb{I}$ , identity matrix .....	120	$x_{\text{end}}$ .....	28
$\mathbb{M}$ .....	120, 128	$\xi$ .....	12, 19
$\mathbb{Z}$ , zero matrix .....	120	$\zeta$ .....	115
$\mathbf{0}$ .....	18	$d$ .....	81
Fr, Froude number .....	30	$f$ .....	43
Re, Reynolds number .....	30	$g$ .....	43
$\mathcal{D}$ .....	59	$r$ .....	90
$\mathcal{R}_1$ .....	57	$s$ , arc-length .....	10
$\mathcal{R}_2$ .....	57	$s^*$ .....	22
$\mathcal{R}_3$ .....	59	$s_{\text{end}}$ .....	16
$\tilde{\mathbf{f}}$ .....	12	$t$ .....	10
$\phi$ .....	89	$v$ , intrinsic flow velocity .....	11
$R_{\text{end}}$ .....	110	$v_{\text{belt}}$ .....	17
$\rho_{\text{air}}$ .....	81	$v_{\text{nozzle}}$ .....	16
$r_{\text{max}}$ .....	95	$v_{\text{surface}}$ .....	16
$\tau_{fm}$ .....	55	$v_{d,c}$ .....	126
$\theta$ .....	23, 27	$w$ .....	33
$\tilde{\mathbf{e}}_x$ .....	19	$x$ .....	17
$\tilde{\mathbf{e}}_y$ .....	19	$y$ .....	17
$\tau$ .....	30	$z$ .....	20
$\tau^*$ .....	32	$z_1$ .....	20
$\tau_{\text{end},2}(w)$ .....	42, 44	$z_2$ .....	20
$\tau_{\text{end},1}(w)$ .....	42, 44	$\mathbf{v}^\perp$ .....	124
$\tilde{\mathbf{r}}$ .....	88	$\mathbf{a}$ .....	11
$\tilde{\mathbf{r}}^\perp$ .....	88	$\mathbf{a}_B$ .....	10
$\mathbf{F}_c$ , centrifugal force .....	87	$\mathbf{e}_x$ .....	17
$\mathbf{F}_C$ , Coriolis force .....	87	$\mathbf{e}_y$ .....	17
$\mathbf{F}_N$ .....	23	$\mathbf{r}$ , position vector .....	10
$\mathbf{F}_R$ .....	24	$\mathbf{r}_{\text{nozzle}}$ .....	16
$\mathbf{F}_f$ .....	23	$\mathbf{r}_s^\perp$ .....	23
$\mathbf{G}$ .....	120, 128	$\mathbf{v}$ , fluid particle velocity .....	11
$\mathbf{F}_L$ .....	23	$\mathcal{A}$ .....	10
$\mathbf{Y}$ .....	120, 128	$\mathcal{A}_{\text{nozzle}}$ .....	16
$\mathbf{a}_c$ .....	88, 124	$\mathcal{V}$ .....	11
$\mathbf{a}_C$ .....	88, 124		
$v_{\text{inert}}$ .....	33	<b>A</b>	
$v_{\text{coag}}$ .....	104	air drag .....	81
$\mathbf{e}_n$ .....	27	Airy functions .....	161
$\mathbf{e}_t$ .....	27	algebraic equation .....	33
$\mathbf{g}$ .....	28		
$\mathbf{r}_s^\perp$ .....	115	<b>B</b>	
$v_{v-i}$ .....	33	backward difference .....	119

- 
- bending stiffness ..... 81  
boundary conditions ..... 15
- C**
- Cauchy problem ..... 23  
central difference ..... 119  
characteristic direction ..... 17  
characteristic equation ..... 20  
co-rotating reference frame ..... 19, 87  
coagulator ..... 4  
composite midpoint rule on a shifted mesh  
119  
conservation of mass ..... 11  
conservation of momentum ..... 11
- D**
- drag coefficient ..... 81  
drag spinning ..... 6, 27  
dynamic jet ..... 16, 113  
    drag spinning ..... 113  
    rotary spinning ..... 122
- E**
- elliptic PDE ..... 19  
experiment ..... 67
- F**
- forward difference ..... 119  
frequency domain ..... 75  
friction force ..... 23
- G**
- glass wool ..... 5  
gravity ..... 28
- H**
- Hadamard's example ..... 23  
Heaviside function ..... 127  
histogram ..... 76  
hyperbolic PDE ..... 17, 19
- I**
- ill-posed problem ..... 23  
inertial flow ..... 83  
inertial flow regime ..... 21  
inertial jet ..... 21, 32, 91  
initial-value problem ..... 37, 40, 43
- L**
- linear extrapolation ..... 119
- M**
- momentum flux ..... 12, 19
- N**
- numerical drift ..... 117
- P**
- parabolic PDE ..... 17, 19  
parameter regions  
    drag spinning ..... 36  
    rotary spinning ..... 96  
    rotating coagulator ..... 104  
polar coordinate system ..... 87
- R**
- relative error ..... 117  
relaxation forms  
    drag spinning ..... 117  
    rotary spinning ..... 126  
rotary spinning ..... 4, 7, 9, 87  
rotating coagulator ..... 104  
rotor ..... 4
- S**
- slenderness ..... 9  
Sobolev norm ..... 23  
steady jet ..... 27, 87  
surface tension ..... 81
- T**
- teapot effect ..... 8  
thermal isolation ..... 4  
three-dimensional polymeric mat ..... 5  
Trouton viscosity ..... 11
- U**
- upwards pointing nozzle ..... 55  
upwind scheme ..... 119
- V**
- viscous flow ..... 84  
viscous flow regime ..... 20  
viscous jet ..... 21, 31, 92  
viscous-inertial flow ..... 84  
viscous-inertial flow regime ..... 20  
viscous-inertial jet ..... 21, 31, 92

**W**

water curtain ..... 4



# Summary

In our thesis we study theoretically and experimentally a jet of viscous fluid hitting a moving wall in two setups. The first one is a jet fall under gravity from an oriented nozzle onto a horizontally moving belt. The second one is the jet in rotary spinning, which is used to produce synthetic fibers.

We start with the jet falling under gravity onto a moving belt. In experiments we distinguish three flow regimes: i) a concave shape aligned with the nozzle orientation (comparable to a ballistic trajectory), ii) a vertical shape, or iii) a convex shape aligned with the belt. The concaveness or convexity of the shape characterizes the three flow regimes. In addition to this overall structure, steady or unsteady boundary effects can be observed at the nozzle and near the belt. Moreover, when the nozzle does not point vertically down the whole jet can be unsteady.

To describe the jet we use a model which takes into account the effects of inertia, viscosity, and gravity, and disregards bending. This allows us to focus on the large-scale jet shape while avoiding the modeling of bending and buckling regions at the jet ends. Also, we neglect surface tension and assume the fluid to be isothermal and Newtonian. The key issue for this model is the boundary conditions for the jet shape. They follow from the conservation of momentum equation when interpreted as a hyperbolic equation for the shape. The correct boundary conditions follow from consideration of the characteristic directions of that equation at each end. This also provides a criterion for partitioning the parameter space into the three regimes.

The physical quantity which characterizes the three flow regimes is the momentum transfer through a jet cross-section, which has contributions from both inertia and viscosity. In a concave jet the momentum transfer due to inertia dominates the viscous one everywhere in the jet, and therefore the nozzle orientation is relevant. In the vertical jet the momentum transfer due to viscosity dominates at the nozzle and due to inertia at the belt, and in the point where they are equal the stationary jet should be aligned with the direction of gravity. From this the vertical shape follows. In the convex jet the viscous momentum transfer dominates in the jet and the tangency with the belt becomes important. This gives an alternative characterization of the three flow regimes in which the jet can be inertial, viscous-inertial, and viscous, respectively.

Moreover, for this model we prove existence and investigate uniqueness for all admissible parameters. When we have non-uniqueness of steady flows, up to three stationary solutions are possible, which is consistent with the unsteady behaviour observed experimentally. The comparison between our theory and experiments shows a qualitative agreement.

We model a setup of rotary spinning using the same approach. In this process the

jet is driven out from a rotating rotor by centrifugal and Coriolis forces towards a cylindrical surface (the 'coagulator'). The parameter space is divided into four regions. Two correspond to the inertial and the viscous-inertial jets discussed before. The two others correspond to different types of non-existence of stationary jets, one because no stationary jet can reach the coagulator (causing real-world jets to wind around the rotor), and one because a stationary jet can not match velocities at the coagulator. An interesting fact is that the viscous jet situation is not possible; this would require the coagulator to rotate in the same direction as the rotor with at least half of its angular velocity.

Finally, we develop a numerical method for the dynamic jet in both setups. In cases when the steady jet exists the dynamic jet evolves to the steady one. A simulation of the jet in rotary spinning for the parameters from the region where a steady jet does not exist but reaches the coagulator reveals that the jet oscillates with increasing amplitude.

# Samenvatting

In dit proefschrift bestuderen we theoretisch en experimenteel een straal viskeuze vloeistof die een bewegende wand raakt. We beschouwen twee opstellingen. De eerste is een straal die vanuit een gerichte spuitmond onder invloed van de zwaartekracht op een horizontale lopende band valt. De tweede opstelling is die van *rotary spinning* ('rotor-spinnen'), dat wordt gebruikt voor de productie van synthetische vezels. Hier draait de spuitmond rond en beweegt de straal onder invloed van centrifugaal- en Corioliskrachten naar een vaste wand.

We beginnen met de straal die door de zwaartekracht op een bewegende band valt. In de experimenten herkennen we drie regimes: i) een concave vorm die in lijn met de spuitmond de spuitmond verlaat (vergelijkbaar met een ballistische baan), ii) een verticale vorm, of iii) een convexe vorm die tangentiaal de band raakt. De convexiteit of concaviteit van de vorm kenmerkt de drie regimes. Naast deze algemene structuur kunnen stationaire of instationaire randeffecten worden waargenomen bij de spuitmond en in de buurt van de band. Bovendien, wanneer de spuitmond niet verticaal naar beneden wijst kan de hele straal instabiel zijn.

Voor de beschrijving van de straal gebruiken we een model dat rekening houdt met de effecten van inertie, viscositeit en zwaartekracht, en we negeren buigingseffecten. Dit stelt ons in staat ons te richten op de grootschalige vorm van de straal, en we vermijden daarmee het modelleren van de buiging en randeffecten aan de twee uiteinden. Ook verwaarlozen wij de oppervlaktespanning en we nemen aan dat de vloeistof isotherm en Newtoniaans is. Het belangrijkste aspect van dit model zijn de randvoorwaarden. Ze volgen uit de (instationaire) wet van behoud van impuls wanneer die geïnterpreteerd wordt als een hyperbolische vergelijking voor de positie. De juiste randvoorwaarden volgen uit onderzoek van de karakteristieke richtingen van die vergelijking aan de uiteinde. Dit biedt ook een criterium voor de verdeling van de parameterruimte over de drie regimes.

De fysieke grootte die de drie regimes kenmerkt is de impulsoverdracht over een dwarsdoorsnede van de straal, die bijdragen bevat van zowel inertie als viscositeit. In een concave straal domineert de inertiaële impulsoverdracht overal in de straal, waardoor de hoek van de straal continu is bij de spuitmond. In de verticale straal domineert de inertiaële impulsoverdracht bij de spuitmond en de viskeuze overdracht bij de band; op het punt waar ze in evenwicht zijn is een stationaire straal in lijn met de zwaartekracht. Hieruit volgt de verticale vorm. In de convexe straal domineert de viskeuze impulsoverdracht in de gehele straal, waardoor de hoek continu is aan het einde dat de band raakt. Dit geeft een alternatieve karakterisering van de drie regimes waar de straal respectievelijk inertiael, viskeus-inertiael en viskeus is.

Bovendien bewijzen we voor dit model het bestaan van oplossingen en onderzoeken we de eenduidigheid voor alle parameterwaarden. Wanneer uniciteit faalt, zijn maximaal drie stationaire oplossingen mogelijk, die consistent zijn met het experimenteel waargenomen instationaire gedrag. De vergelijking tussen de theorie en experimenten toont een kwalitatieve overeenkomst.

We modelleren het rotorspinnen met dezelfde aanpak. In dit proces wordt de straal vanuit een draaiende rotor door centrifugaal- en Corioliskrachten naar een cilindrisch oppervlak (de 'coagulator') toe geslingerd. De parameter ruimte is verdeeld in vier regio's. Twee komen overeen met de inertiaële en de viskeus-inertiaële stralen hierboven. De twee andere komen overeen met verschillende vormen van niet-bestaan van stationaire oplossingen, hetzij omdat geen stationaire straal de coagulator kan bereiken (in een experiment windt de straal zich dan rondom de rotor), hetzij omdat een stationaire straal de benodigde snelheid op de coagulator niet kan bereiken. Een interessant feit is dat het viskeuze regime niet mogelijk is; dit zou vereisen dat de coagulator in dezelfde richting als de rotor draait met minstens de helft van diens hoeksnelheid.

Tenslotte ontwikkelen we een numerieke methode voor het tijdsafhankelijke probleem in beide opstellingen. In gevallen waarin de stationaire straal bestaat convergeert de tijdsafhankelijke straal naar de stationaire. In een simulatie voor de parameters uit de rotorspinnen-regio waar geen stationaire oplossing is (wegens te lage snelheid bij het bereiken van de coagulator) blijkt dat de straal oscilleert met toenemende amplitude.

# Acknowledgments

A problem, which gave birth to this work, was brought to the mathematical community by Teijin Aramid at 48th ESGI. This PhD project follows up this problem, and is an example how an industrial problem produces a nice mathematics, and how mathematics can serve the community. Because of that I would like to express my deep respect to the people who make such interactions between industry and mathematics possible.

One of those people is my promotor and supervisor prof.dr. Mark Peletier. Among many problems he picked up very promising and interesting one for my PhD, which as it appeared later was a hot subject at that time. Because of that and many things that I have learned from Mark, I express my deep respect and gratitude to Mark. Especially I would like to mention the right combination of freedom and enough guidance to go a proper way, which produces a nice and open working environment. Moreover, I would like to thank Mark for many possibilities to travel around the world to make connections and spread the project results. I would like to thank my advisors dr.ir. Fons van de Ven and dr.ir. Annemarie Aarts for their contribution and support.

In addition to that I mention our fruitful meetings with Hans Meerman and Piet Den Decker from Teijin Aramid, and thank for making the experiments reported in this thesis possible. Many nice pictures in the thesis were made by Maria Rudnaya.

My defence committee is formed by prof.dr.ir. GertJan van Heijst, jun.-prof.dr. Nicole Marheineke, prof.dr. Mark Peletier, prof.dr. Han Slot, and prof. Alexander Yarin. I would like to thank them for their time investment and willingness to judge my work and for their comments and suggestions. I also want to thank prof.dr. Jos Baeten, prof.dr. Bob Mattheij, and dr.ir. Fons van de Ven for being part of the extended defence committee.

I am also indebted to my colleagues from CASA for the friendly and open working atmosphere, their support and frankness. Many thanks also to all the current and former PhD students, postdocs, and young colleagues: Aga, Ali, Bart, Berkan, Christina, Darcy, Davit, Dragan, Erwin, Evgeniya, Hans, Jan, Jos, Jurgen, Kakuba, Kamyar, Kundan, Laura, Maria, Maria, Mark, Maxim, Michiel, Miguel, Mirela, Nico, Patricio, Paul, Peter, Remko, Remo, Roxana, Schruti, Sven, Temesgen, Valeriu, Venkat, Wenqing, Yabin, Yan, Yixin, and Zoran. My special thanks to the people I have shared the office and much more Marco, Matthias, Oleg, Tasnim, and Yves. Our two secretaries Marèse and Enna deserve a special word of thank, for taking care of all administrative work.

On personal level I would like to thank my friends and family for their love and support. My special appreciation to my mother Hanna, father Vasyl, and sister Maria for their love and backing. Last but definitely not least I would like to thank my wife Oksana and my lovely daughter with curly hair Iryna.



# Curriculum Vitae

Andriy Hlod was born in Boryslav, Ukraine on April 25th, 1980. After finishing his pre-university education at the Lviv Lyceum of Physics and Mathematics in 1996, he started his studies in Mathematics at the faculty of Mechanics and Mathematics of the Ivan Franko National University of Lviv. In June 2001 he obtained his master's degree in Mathematics with master thesis entitled "Investigation of Mathematical Models of Elastic Cylindrical Solids". From October 2001 until January 2003 he was working at the Pidstryhach Institute for Applied Problems of Mechanics and Mathematics where he investigated contact interactions between two movable half-spaces.

In February 2003 he came to the Netherlands and started the post-master program, Mathematics for Industry of the Eindhoven University of Technology, which he graduated in May 2005. From June 2005 until August 2009 he has been working as a PhD student at the Eindhoven University of Technology within the Applied Analysis group. In his project he studied jets of viscous fluid hitting a moving wall under supervision of prof.dr. Mark Peletier. Moreover, dr.ir. Annemarie Aarts and dr.ir. Fons van de Ven were involved in this project, and a cooperation was made with Teijin Aramid. The result of his PhD-project is the underlying thesis.

Eindhoven, July 2009